UNIVERSITY OF CALIFORNIA SAN DIEGO

Design and Selection of Probes for In Vivo Molecular Targeting and Imaging

A dissertation submitted in partial satisfaction of the
requirements for the degree Doctor of Philosophy

in

Biomedical Sciences

by

Heather Lovae Glasgow

Committee in charge:

Professor Roger Y. Tsien, Chair
Professor Steven Dowdy
Professor Nathan Gianneschi
Professor Stephen Howell
Professor Quyen Nguyen

2015

The Dissertation of Heather Lovae Glasgow is approved, and it is acceptable in quality and form for publication on microfilm and electronically:

_____

_____

_____

_____

_____
Chair

University of California, San Diego

2015

DEDICATION

In dedication to Bobbie and Papa, Nana and Grandad (Barbara and Samuel McPheeters Glasgow, Jr. and Lovae and Forrest Eggimann)

TABLE OF CONTENTS

LIST OF FIGURES

LIST OF TABLES

ACKNOWLEDGEMENTS

I would like to thank Dr. Roger Y. Tsien for giving me the greatest opportunity - to work on projects that still make me excited to come to lab every day and to which I could dedicate entire lifetimes to, for enabling me to grow scientifically, and for his excellent insight, support, and guidance.

I would like to thank Dr. Michael A. Whitney for his mentorship, for endless hours of proofreading, for putting up with a million questions, for constantly coming up with new ideas, for troubleshooting, and for keeping an eye on the big picture.

I would also like to thank the following people without whom this research would not have been possible: Dr. Quyen Nguyen, Dr. Stephen Adams, Dr. Beth Friedman, Larry Gross, Dr. Jessica Crisp, Paul Steinbach, Qing Xiong, Dr. John Ngo, Dr. Bernd Wollscheid, Dr. Andreas Frei, Karel Novy, Dr. Timon Hussain, Melina Mastrodimos, Joan Kanter, Perla Arcaira, Rachel Levin, and Dr. Elamprakash Savariar.

I would like to thank my thesis committee members, Dr. Steven Dowdy, Dr. Nathan Gianneschi, Dr. Stephen Howell, Dr. Quyen Nguyen, and Dr. Marianne Manchester for their encouragement, insightful suggestions, and for keeping me focused.

I would like to thank Cancer Island, Casa Dwyrtle, Dinner Groupers, and John Glasgow for their friendship, emotional support, and making grad school fun.

I would like to acknowledge my parents, Sam and Diane Glasgow, for their continuous supportive and love and always staying positive.

Lastly, I would like to thank Dr. Mark Kamps, Dr. Joseph Vinetz, Dr. Carlton Evans, and the Howard Hughes Medical Institute Med-into-Grad program for giving me

the chance to experience first-hand a different side of the world and enabling me to find my next pursuit in life.

Chapter 2 is currently being submitted for publication of the material. Glasgow, H.L.; Whitney, M.A.; Gross, L.A.; Friedman, B.; Adams, S.R.; Crisp, J.L., Hussain, T.; Frei, A.P.; Wollscheid, B.; Nguyen, Q.T.; Tsien R.Y. The dissertation author was the primary author of this material.

VITA

2008 Bachelor of Arts in Molecular and Cell Biology, University of California, Berkeley

2012 Master of Science, University of California, San Diego

2015 Doctor of Philosophy, University of California, San Diego

PUBLICATIONS

Glasgow HL, Whitney MA, Gross LA, Friedman B, Adams SR, Crisp JL, Hussain T, Frei AP, Wollscheid B, Nguyen QT, and Tsien RY, "Ligand-Proximal Photoxidation to identify the binding target of a peripheral nerve-highlighting peptide" Manuscript in preparation.

Glasgow HL*, Ramos ES*, Coleman D, Tovar MA, Evans CA. "Carbendazim reduces contamination of tuberculosis cultures in the thin layer agar MDR/XDR-TB Color Test" Manuscript in preparation.
*co-first authors

Hussain T, Mastrodimos MB, Raju SC, **Glasgow HL,** Whitney M, Friedman B, Moore JD, Kleinfeld D, Steinbach P, Messer K, Pu M, Tsien RY, and Nguyen QT. "Fluorescently labeled peptide increases identification of degenerated facial nerve branches during surgery and improves functional outcome" *PLoS One*, March 2015, *10*.

Crisp JL, Savariar EN, **Glasgow HL**, Ellies LG, Whitney MA, and Tsien RY, "Dual Targeting of Integrin αvβ3 and Matrix Metalloproteinase-2 for Optical Imaging of Tumors and Chemotherapeutic Delivery" *Molecular Cancer Therapeutics*, June 2013, *13*.

Whitney M, Savariar EN, Friedman B, Levin RA, Crisp JL, **Glasgow HL**, Lefkowitz R, Adams SR, Steinbach P, Nashi N, Nguyen Q, and Tsien RY, "Ratiometric activatable cell penetrating peptides provide rapid *in vivo* readout of thrombin activation," *Angewandte Chemie* International Edition, January 2013, *52*.

ORAL AND POSTER PRESENTATIONS

Presentation, Pharmacology Department Rounds, UC San Diego, June 2014:
"Optimization of nerve-highlighting peptides for fluorescence guided surgery using a novel tool to identify ligand-protein interactions"

Poster, Society for Neuroscience, San Diego, CA, November 2013: "Nerve-highlighting Peptides for Fluorescence Guided Surgery and the Identification of Potential Binding Targets"

Poster, UCSD Biomedical Sciences Graduate Program Retreat, La Quinta, CA, September 2013: "Nerve-highlighting Peptides for Fluorescence Guided Surgery and the Identification of Potential Binding Targets"

Presentation, Pharmacology Department Rounds, UC San Diego, May 2011: “Development of Peptides for the Intracellular Delivery of Nanoparticles”

Honors thesis oral presentation, UC Berkeley, May 2008: “A new SnoN-interacting protein and its role in mammalian epithelial carcinogenesis.” Annual Biochemistry and Molecular Biology Honors Symposium

Poster, Genentech Internship Reception, South San Francisco, CA, August 2007: “Investigating a Non-Canonical Pathway of a G-protein Coupled Receptor.”

FIELDS OF STUDY

2008-2015 Targeted Peptide Development under Dr. Roger Tsien

2012-2015 Molecular Tool Development under Dr. Roger Tsien

ABSTRACT OF THE DISSERTATION

Design and Selection of Probes for In Vivo Molecular Targeting and Imaging

by

Heather Lovae Glasgow

Doctor of Philosophy in Biomedical Sciences

University of California, San Diego, 2015

Professor Roger Y. Tsien, Chair

Molecular targeting with nerve-binding peptides and activatable cell penetrating peptides (ACPPs) enables site-specific delivery of imaging agents or therapeutics *in vivo*. Nerve binding peptides conjugated to fluorescent dyes improve intraoperative identification of nerves, which should reduce accidental transection, thus reducing patient morbidities, and enhance nerve repair in pre-existing injury, improving outcomes. To enhance *in vivo* nerve contrast and advance the potential clinical application of first generation nerve-highlighting peptides, such as NP41, identifying molecular binding targets, improving affinity, reducing off-target binding, and validating function in human

nerve is needed. Laminins-421, -211, and collagen VI were identified as NP41's binding targets using a novel tool developed to improve the isolation of low affinity interacting molecules, termed Ligand-Proximal Photooxidation (ProxPhOx). This approach uses light activation of a singlet-oxygen generating (SOG) fluorophore conjugated to a ligand to create a highly localized area of oxidation that can be covalently tagged with biotin hydrazide for purification. A new NP41-derivatized peptide, NP713, had higher affinity, *in vivo* contrast, and showed higher labeling of human nerve sections than NP41. Beyond improving nerve peptides, we sought to more specifically target disease sites using ACPPs. ACPPs sensitive to matrix metalloproteinases (MMPs), particularly MMP-2/-9, have been shown to target tumors and metastases; however, improvement in the enzyme selectivity and targeting of other proteases have the potential to increase uptake and specificity of localization to these and other disease sites. Detailed characterization of the selectivity of various substrates revealed potential enzyme targets, that when coupled to their application in disease models may reveal new biological insight, as well as creating potential diagnostic and therapeutic agents. Finally, intracellular delivery of non-membrane permeable therapeutics represents a major bottleneck in molecular targeting. The development of a novel assay for cytoplasmic delivery enabled quantification of membrane translocation efficiency and may allow identification of more effective carriers. The cumulative research presented here advances the use of nerve-targeted fluorophores and of ACPP-targeted drugs and contrast agents in the clinic. These agents will allow surgeons to accomplish difficult operations more precisely and will help clinicians to better diagnose and treat many diseases.

CHAPTER 1: Introduction

1.1. Potential of molecular targeting for imaging and therapeutic development

Targeting imaging and therapeutic agents to specific disease sites is an emerging field of research that holds a great deal of promise for the detection and treatment of a large number of diseases. Agents commonly used for deep-tissue clinical imaging techniques, such as magnetic resonance imaging (MRI), computed tomography (CT), positron emission tomography (PET), ultrasound, and single photon emission computed tomography (SPECT), are currently limited in sensitivity, resolution and innate tissue contrast. Molecular targeting of such agents has the potential to enhance early detection of many diseases in patients. Optical imaging with application of targeted fluorescent dyes is a quickly-developing technology that has the potential to enable real-time fluorescence-guidance and improve a vast range of surgeries, as well as enabling disease detection. Macromolecular targeting could enable large payload delivery of imaging agents or drugs with no other disease or tissue-specific properties. Likewise, disease-specific targeting of any drug has the potential to increase its efficacy and reduce toxic off-target effects by modulating its localization.

1.2. Optical imaging

Enhanced optical imaging modalities, such as fluorescence and bioluminescence, have become common place in biomedical research; however, their clinical application is still a newly emerging field with great promise.

Fluorescence imaging has the advantage of high sensitivity of detection and may be able to generate signal-to-background higher than other imaging technologies (Luker and Luker 2008). Tissue penetrance, however, may not be as deep as other clinical imaging modalities. Wavelengths in the near-infrared spectrum, 600-1000 nm, must be used for maximal light penetration through tissues for deep imaging, as hemoglobin and other molecules absorb light at shorter wavelengths, and because of high tissue background fluorescence at shorter wavelengths (Weissleder 2001, Hadjipanayis, Jiang et al. 2011).

Fluorescence-guided surgery has the potential to excel beyond targeted therapy. In some cases, even targeted therapeutics may have low accessibility, such as poorly vascularized tumor cores and atherosclerotic plaques, the drug may be insufficiently effective, or drug efflux may result in reduced activity or resistance. However, a surgeon may be able to use to targeted fluorescent compounds to find and completely remove a tumor and involved lymph nodes from a cancer patient, or to find and repair blocked or damaged blood vessels, in atherosclerosis and ischemic stroke patients. Another potential advantage of optical imaging for diseases such as cancer is the potential for its dual use as a diagnostic and therapeutic (theranostic), using photodynamic therapy techniques, where high focused levels of light are used to excite a photo-reactive molecule capable of generating toxic reactive-oxygen to kill tissue.

1.3. Mechanisms of targeting

The concept of targeting involves the concentration of a molecule at a particular site while reducing or eliminating the biodistribution of the molecule at all other sites.

1.3.1. Passive Targeting

Passive targeting relies on natural anatomical access and barriers to create certain patterns of biodistribution. For instance, blood pool MR imaging agents using gadolinium or other molecules to enhance contrast collect and are retained in areas of high blood volume for longer periods due to their large size and inability to pass through the vasculature (Nolte-Ernsting, Adam et al. 1998, Bremerich, Bilecen et al. 2007). Macromolecular targeting of solid tumors can effectively be achieved by a phenomenon known as enhanced permeability and retention (EPR). In order to facilitate fast growth and an exchange of nutrients, tumors have more permeable vasculature with large pore size that is poorly constructed, resulting in the retention of large molecules, in the range of hundreds of nanometers (Yuan, Dellian et al. 1995, Maeda, Wu et al. 2000). Abraxane (albumin conjugated paclitaxel) and Doxil (liposome-formulated doxorubicin), for example, are two clinically approved nanoparticles used to treat different types of cancer that rely on EPR.

1.3.2. Active targeting

Actively-targeted agents are now being abundantly developed. These rely on distinct molecular environments at the site of interest and the targeting moiety's recognition of or response to them. Mechanisms include simple affinity attachment and stimulus-dependent activity.

1.3.2.1. Affinity based mechanisms

Affinity-based targeting of molecules involves the binding of the targeting agent directly with a signature molecule at the site of interest. Affinity-targeting therapeutics are now commonplace in cancer treatment and other conditions, such as macular

degeneration, utilizing antibodies that bind to overexpressed cell-surface receptors uniquely by the cancer cells or other target tissue.

1.3.2.2. Stimulus dependent mechanisms

Stimuli-sensitive probes or activatable probes also have a great deal of promise for targeting diseases or tissues that lack an abundant, unique, and typically surface-expressed molecular signature for binding. Probes have been designed that detect many different environmental cues. These include enzyme activity to which a probe may be susceptible, pH, ion concentration, oxygen concentration, reactive oxygen species or other molecules. Stimuli-based probes have the potential for greater signal than their affinity-based counterparts because one target may be able to activate multiple probes, rather than stoichiometric 1:1 binding.

1.4. Types of targeting agents

In addition to the abundance of cargos types for delivery, a variety of targeting molecules have been pursued, which have been recently reviewed in detail (Hadjipanayis, Jiang et al. 2011, Hellebust and Richards-Kortum 2012). Briefly, while antibodies have been extremely effective in therapy, smaller targeting moieties for imaging agents generally have more optimal properties, such as faster washout from circulation and lower immunogenicity. Antibody fragments, which have high affinities and range from 6-21 times smaller, have been pursued, including single chain antibodies, small antibodies naturally produced by camelids, and affibodies been used for targeting therapeutics and imaging agents (Cortez-Retamozo, Lauwereys et al. 2002, Poduslo, Ramakrishnan et al. 2007). Proteins, such as modified native ligands, which offer high affinity, have been

shown to highlight diseases in which an overexpressed receptor is present (Ke, Wen et al. 2003). Peptides, nucleic acid aptamers, and small molecules have also been used as targeting agents and offer ultra-small size of only a few <10 kD, thus potentially being able to reach more areas (Lee, Xie et al. 2010, Hong, Goel et al. 2011). Compared to proteins and antibodies, they can be cheaply and easily produced on a large scale synthetically and have low immunogenicity. The emerging field of glycobiology has demonstrated that many glycan-based interactions occur at the extracellular matrix and glycan-targeted agents have been explored, as have metabolized sugars, such as glucose derivatives for PET imaging and, recently, fluorescence (Sheth, Josephson et al. 2009, van Kasteren, Campbell et al. 2009).

Nucleic acids, peptides, proteins, and antibodies are advantageous for creating novel targeting agents because of the ease of selecting functional molecules and optimizing them from diverse libraries by protein or peptide display techniques, such as SELEX, mRNA display, ribosome display, bacterial cell surface display, and phage display.

1.5. Intraoperative nerve detection

Any surgical operation requires the identification of peripheral nerves in order to preserve their function. Accidental nerve transection or damage leads to patient morbidities, including chronic pain, numbness, loss of muscle function, or even permanent paralysis. Nerves are typically identified during surgeries by their characteristic white fiber-like appearance against other tissues, which are various shades of pink of red and by the surgeon's general anatomical knowledge. Small or buried nerves are difficult to distinguish and are most likely to be damaged.

The general location of motor nerves is identified by electromyographic (EMG) monitoring, in which an electrode is inserted and distal muscle is monitored for movement (Davis, Rea et al. 1979, Gantz 1985). However, this technique does not give visual or other cues that indicate the distance or location of the nerve, nor is it able to identify sensory nerves or sympathetic nerves, such as the cavernous nerves around the prostate gland (Kubler, Tseng et al. 2007, Walz, Graefen et al. 2007, Walz, Burnett et al. 2010). Prostate nerve injury during prostatectomy often leads to urinary and sexual dysfunction ((Kubler, Tseng et al. 2007)). Furthermore, EMG detection can not be used when nerve to muscle signaling is blocked, as occurs in the case of damage to nerves or surrounding tissues, and when local anaesthetics or neuromusclular inhibitors are used. EMG monitoring itself may damage nerves when inserted, as well.

Potential *in vivo* label-free nerve visualization technologies include optical coherence tomography and laser confocal microscopy; however, these technologies suffer from low intrinsic nerve contrast, and the lack of real-time images at the surgical field for guidance (Chitchian, Weldon et al. 2010, Zhivov, Blum et al. 2010).

1.5.1. Nerve-labeling dyes

Intraoperative nerve labeling agents are therefore highly desirable. Previously developed nerve imaging techniques for axonal tracing research in animals have included retrograde or anterograde tracing of individual axons via fluorescent dyes or protein-dye conjugates (Richmond, Gladdy et al. 1994, Kobbert, Apps et al. 2000, Marangos, Illing et al. 2001, O'Malley, Wittkopf et al. 2006). In order to highlight nerve fibers, dyes are injected into an innervated tissue, such as muscle, and the dye moves by axonal transport in a retrograde fashion through the nerve tract, or they are applied directly to nerves for

travel in both directions. However, only single nerve tracts are labeled, and dye transport requires extensive lengths of time, for instance a span of millimeters can take days. Poor fluorescence contrast is generated if excess dye is not washed out of non-nerve tissue and direct injection of nerves or other tissues may be damaging. Thus, their potential for clinical application is dubious.

Nerve and myelin-binding small molecule dyes have recently been developed that are able to bind and highlight peripheral and central nerves upon systemic injection (Gibbs-Strauss, Nasr et al. 2011, Cotero, Siclovan et al. 2012, Park, Hyun et al. 2014). However, they pose several drawbacks. Due to high lipophilicity, these dyes also show high adipose fluorescence. Non-myelinated sympathetic nerves are not likely be fluorescently labeled, and furthermore, the potential neurotoxic effects of myelin binding and penetration of the blood-brain barrier are unknown.

1.5.2. History of nerve binding peptides

A peptide sequence, nerve peptide 41 (NP-41), was found by our lab using phage display for binding to whole nerves that highlights peripheral nerves against adjacent non-nerve tissues such as muscle, fat, and organs when injected systemically in mice ((Whitney, Crisp et al. 2011). When used in models of nerve repair and tumor removal, NP-41 has led to improved intraoperative nerve detection and sparing, lower surgical time, reduced local tissue damage and inflammation, and enhanced repair of pre-existing nerve damage (Wu, Whitney et al. 2011, Hussain, Mastrodimos et al. 2015).

1.5.3. Nerve peptide developments presented in this dissertation

While NP-41 demonstrates great potential of peptide-targeted fluorophores to label nerves in patients, there remain important lingering questions and the possibility for improvement prior to its use in the clinic. Among those questions and optimizations that will be addressed in this thesis are: identification of the molecular binding target(s), derivitization and selection of new peptides, the analysis of binding to various nerve types and tissues, the characterization of other similarly-developed nerve peptides in mouse and human tissue, and the quantitation of its binding affinity.

1.6. Summary of Chapters

The chapters of this dissertation can be divided into three areas of study.

Part 1: The evolution of nerve binding molecules and their use in fluorescence-guided surgery to reduce the morbidity of nerve damage

Chapter 2 describes the development of a new methodology to uncover ligand-receptor interactions using mass spectrometry and its application in determining the binding targets of a nerve-highlighting peptide.

Chapter 3 chronicles the work to evolve and improve nerve peptides for clinical translation using phage display selections of degenerate libraries, an *ex vivo* high throughput screen for nerve binding, and characterization of peptide binding to human nerve.

Part 2: Development of selective activatable cell-penetrating peptides for molecularly-targeted delivery of therapeutics and imaging diagnostics

Chapter 4 discusses the development of a high-throughput assay to characterize enzyme cleavage of activatable cell-penetrating peptides using fluorescence resonance energy transfer and describes phage display selection of peptide

substrates of a membrane-anchored metalloproteinase for the molecular targeting of cancer.

Part 3: Introduction to macromolecular therapeutics and how enhancement of intracellular delivery could improve pharmacological efficiency

Chapter 5 details the development of an assay which measures the efficiency of endosomal escape or cytosolic translocation into cells.

Chapter 6 chronicles the attempts to find novel peptide sequences that can carry large nanoparticle-sized molecules into the cytoplasm of cells.

CHAPTER 2: Ligand-Proximal Photooxidation Identifies the Binding Targets of a Peripheral Nerve-Highlighting Peptide

2.1. Abstract

Target-blind activity-based screening of molecular libraries is often used to develop first-generation compounds and drugs, but subsequent identification of binding partners is rate-limiting to further affinity optimization. A novel method to covalently tag molecules surrounding a ligand *in vivo* was developed to identify the binding targets of NP41, a peptide identified by phage display that fluorescently highlights peripheral nerves. Ligand-Proximal Photooxidation (ProxPhOx) generates ligand-localized oxidation sites with a conjugated light-activatable singlet oxygen generator. Biotin hydrazide reacts with oxidized residues, enabling mass spectrometry identification of binding targets. ProxPhOx identified laminin-421 and laminin-211 as binding partners of NP41, confirmed by colocalization and protein binding assays. Perineurial laminin-421 showed the greatest enrichment, consistent with NP41's prominent perineurial staining. Other extracellular matrix proteins collagen VI and nidogen were also identified. These targets provide a rational explanation for the striking ability of NP41 to highlight highly degenerated nerves, which are invisible to the unaided eye.

2.2. Introduction

Molecular interactions including ligand-receptor binding are a key component of nearly every biological process. Phage display is a powerful affinity-based molecular selection tool that has enabled the identification and optimization of peptides, proteins,

and antibodies that bind to molecular targets including receptors and tissue specific antigens.(Smith and Petrenko 1997) Although typically used for selection by binding to a specific protein or molecule, selections against complex sources, such as live cells, cell extracts, or organs, have also yielded promising results.(Pasqualini and Ruoslahti 1996, Brown 2000, Whitney, Crisp et al. 2011) Despite the obvious implications of these novel ligands and binding targets as potential drugs or biomarkers, few receptors of peptides identified by affinity selection to a complex source have been defined. Affinity chromatography, cDNA library screening and yeast two-hybrid have been used to identify some binding targets of phage-selected peptides.(Rajotte and Ruoslahti 1999, Weissleder 2010) However, such methods have not been widely successful, as phage-selected ligands typically have low affinity and binding interactions are easily disrupted or may require a native context or special post-translational modifications.

A variety of methods to capture native ligand-receptor interactions use crosslinking via chemical or light-induced reactions followed by mass spectrometry.(Tanaka, Bond et al. 2008, Sinz 2010, Frei, Jeon et al. 2012) However, some require that ligand retain binding activity after harsh chemical treatment which can be disruptive.(Woodward, Young et al. 1985) In most crosslinking techniques, the ligand must reach an appropriately reactive site on the receptor for crosslinking to occur, while being conjugated to a potentially bullky purification tag, which may weaken specific binding.

In order to more efficiently capture interactions that are low affinity or easily disrupted, we have developed a novel method for light-induced covalent labeling of a high affinity tag (biotin) to receptor/proteins that are in the close proximity of a natively

bound ligand, termed Ligand-Proximal Photooxidation (ProxPhOx) is diagrammed in Figure 1. A photo-inducible singlet oxygen generating (SOG) molecule (i.e. methylene blue, dibromofluorescein, or fluorescein), is conjugated to a ligand of interest, which upon binding and exposure to light, generates a localized area of oxidation on proteins or other molecules proximal to the ligand, within ~10-50 nm of the photoactivated dye, thus only the target receptor or closely interacting proteins are oxidatively modified.(Moan and Berg 1991) Singlet oxygen reacts with several amino acids forming many products, including side-chain ketones and aldehydes such as the conversion of tryptophan into a ketone-containing kynurenine or N-formylkynurenine.(Nilsson, Merkel et al. 1972, Davies 2003, Kim, Rodriguez et al. 2008) Because these residues are normally rare in tissues and hydrazides have specific reactivity for ketones and aldehydes, oxidatively-modified molecules can be specifically reacted. Hydrazides or hydrazines containing an affinity tag, such as biotin, are incubated with the tissue, either applied exogenously (Scheme 1) or synthesized in tandem with the ligand-SOG (Scheme 2), so that chemical conjugation can be performed simultaneously *in vivo* or localized away from other potential reactive sites.(Silvester, Timmins et al. 1998, Hensley 2009) Biotin-tagged proteins can be purified from homogenized mixtures with immobilized streptavidin, then dissociated via hydrolysis of the hydrazone bond with strong acid, digested with trypsin, and identified by LC-MS/MS, using label-free quantification to compare protein abundance relative to a control.(Kalia and Raines 2008)

In this report, ProxPhOx has been successfully used to identify the molecular targets of the recently phage-display identified nerve-binding peptide NP41, which highlights nerves when labeled with fluorescent dyes and aids in the surgical repair of

transected facial nerves.(Whitney, Crisp et al. 2011), (Wu, Whitney et al. 2011, Hussain, Mastrodimos et al. 2015) ProxPhOx identification of extracellular matrix targets explains NP41's striking ability to label highly degenerated nerves many months post-transection that are invisible to the naked eye.

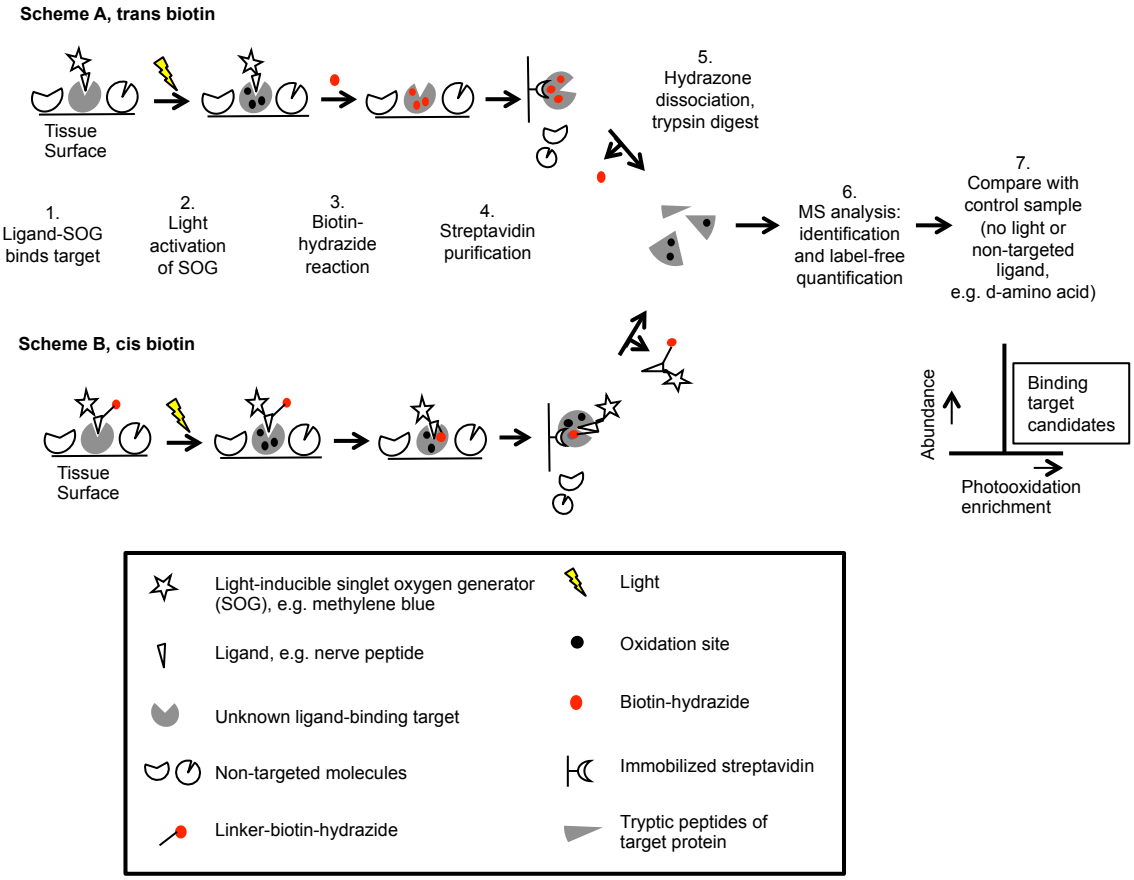

Figure 2.1. Schematic of ProxPhOx to identify ligand-proximal molecules. Scheme A: A ligand of interest is conjugated to a singlet oxygen-generating molecule (SOG), such as methylene blue, dibromofluorescein, or fluorescein. SOG-conjugated ligand is then applied to tissue or cells containing ligand binding activity. Upon excitation with the appropriate wavelength of light, singlet oxygen is produced, which reacts quickly with nearby molecules within a radius of 10-50 nm. Reaction of singlet oxygen with many molecules results in oxidation sites, including ketones and aldehydes. Biotin hydrazide is then applied to the sample, which reacts with oxidized residues. Biotinylated proteins are then streptavidin purified, the hydrazone bond is released, and proteins are trypsinized and analyzed by LC-MS/MS. Label-free quantification by protein spectral counts is used to compare relative protein amounts to a control sample using a no light or non-targeted ligand. Scheme B: Ligand is conjugated to SOG, biotin, and a hydrazide or an equivalent ketone-reactive group, e.g. pyridylhydrazine. Tissue is exposed to light and streptavidin purified as before. Lower labeling is expected to result, restricted to oxidized sites within the span of the length of the linker.

2.3. Methods

All experiments on mice were performed under protocols approved by the University of California San Diego Institutional Animal Care and Use Committee.

2.3.1. Peptide synthesis and fluorophore labeling

Peptides were synthesized in our laboratory on a Protein Technologies, Inc. peptide synthesizer using standard protocols for fluorenylmethoxycarbonyl (Fmoc) solid-phase synthesis on NovaSyn TGR resin. All NP41 peptides (acetyl-SHSNTQTLAKAPEHTGC-amide) were labeled on the C terminus cysteine by maleimide derivatives of methylene blue (AttoTec), dibromofluorescein (DBF), eosin (Life Technologies), or biotin (Sigma). FAM-NP41 was prepared as previously described.(Whitney, Crisp et al. 2011) Peptides were purified to >95% purity using C-18 reversed phase high-performance liquid chromatography (HPLC) with a 20–50% acetonitrile gradient in 0.05% trifluoroacetic acid and confirmed by mass spectrometry.

2.3.2. Ligand-Proximal Photooxidation on tissue sections for imaging

Facial nerve and surrounding muscle and fasciae was dissected from mice and frozen on dry ice embedded in Optimal Cutting Temperature (OCT). 10 μm-thick tissue sections were cut on a cryostat (Leica), placed, and dried on glass slides. Prior to the addition of peptide, unfixed tissues were pretreated with 50 μM nicotinic hydrazide in MES buffer, pH 5.5 for 30 minutes to block any pre-existing oxidized sites. NP41-fluorescein or d-amino acid NP41-fluorescein control at 375 μM was topically treated on tissues in half-strength Hank's Buffered Saline Solution (HBSS) for 20 minutes. Slides were then gently washed in a phosphate buffered saline (PBS) bath. Slides were exposed for 15 minutes to 480 nm excitation light (30 nm bandwidth, 0.07 W/cm^2) on a solar simulator, while control slides were kept covered in the dark. Streptavidin-Texas red was treated on slides for 1 hour, washed in PBS, and slides were imaged on a confocal

microscope (Zeiss) with 488 nm excitation and 520 nm emission (<1 sec exposure) to image peptide and 535 nm excitation and 565 emission to image Texas red.

2.3.3. Imaging of peptide binding on tissue sections

NP41 conjugated to methylene blue (MB), dibromofluorescein (DBF), or biotin were topically applied to frozen, unfixed mouse facial nerve sections (10 μm) at 375 μM in 0.5x HBSS for 20 minutes, then washed in PBS. For imaging biotin-NP41, sections were incubated with an avidin-conjugated peroxidase (ABC Reagent, Vector Labs) and stained for DAB precipitation. Slides were imaged with white light microscopy. Confocal microscopy was used to image MB-NP41 (640 nm excitation, 670 nm emission) and DBF-NP41 (488 nm excitation, 520 nm emission, Nikon).

2.3.4. Ligand-Proximal Photooxidation with NP41-MB on whole nerves and LC-MS/MS

Sciatic nerves were dissected from adult SKH1 mice (Charles River Laboratories) or wild type albino C57BL6 mice (Jackson Laboratories) and submerged in 50 μM methylene blue-peptide in PBS for 2 hours. After washing in PBS, nerves were exposed to 640 nm light for 10 seconds, 1 minute, 15 minutes, or kept in the dark as a control, while immersed in PBS containing 50 μM biotin hydrazide. To speed labeling, nerves were transferred to 50 mM MES buffer, pH 5.5 with 50 μM biotin hydrazide and reacted in the dark for 30 minutes and subsequently homogenized using a motorized tissue grinder in PBS. Tissue homogenates were solubilized in freshly prepared buffer 15mM Na_2HPO_4, pH7, 150mM NaCl, 1mM EDTA, 0.2mM AEBSF, 10 μg/ml aprotinin, 1% NP-40, 0.5% sodium deoxycholate, 1mM DTT.(Figeys, McBroom et al. 2001) 2.4 mL of

lysis buffer was added to 0.6 mL of homogenate. Solution was centrifuged 5 min 3000 rpm and decanted to Pierce Ultralink monomeric avidin agarose beads. The mixture was incubated on ice for 1 hr with mild stirring. Supernatant was removed and discarded, and beads were washed three times with 1 mL of fresh lysis binding buffer, 30 minutes each on ice.

The hydrazone bond between biotin and protein was hydrolyzed and biotin-bound streptavidin released with two additions of 200 μL 8 M urea tris buffer, pH 7, followed by 8 M urea 0.6% trifluoroacetic acid (TFA), pH 3, then 50 mM triethylamine, and each time transferring the eluted protein to the top of an Millipore Ultracon 0.5 mL concentrator tube. The Filter-Aided Sample Prep (FASP) method was used to remove detergent, and buffer exchange to 100 mM ammonium acetate prior to overnight trypsin digestion at 37°C.(Wisniewski, Zougman et al. 2009) The digest was acidified with 0.4% TFA, then C18 reverse-phase solid phase extraction was used to prepare samples of approximately 20 μL for LC-MS. (TopTip, Glygen Corp., Columbia MD) Two three hour LC-MS runs were done for each of the four samples. (Orbitrap XL ThermoFisher, San Jose CA) In each LC-MS run an 8 μL sample was injected.

The mass spec data was searched with Sequest (Bioworks version 3.3.1 software, ThermoFisher), using up to 3 modifications per peptide, i.e. +16 Da for methionine and tryptophan, and also +4 and +32 Da for tryptophan to detect kynurenine reverted from the protein-hydrazone linkage. Probability values were calculated by the software, and a filter of $p \leq 0.05$ was applied to the peptide-spectrum-matches for inclusion as a hit. Proteins with fewer than 4 hits were not included in the results shown in the final ratio plots.

Spectral counts for peptide-protein matches were tabulated using Matlab software. (Mathworks, Natick MA). The output from the Bioworks Search Results File (.srf) was exported as an excel comma separated value (.csv) spreadsheet. This spreadsheet data, for each LC-MS run, was imported into Matlab. Since the list of proteins varies between each LC-MS run, a Matlab script was written in-house to collate the listed number of spectral counts for each protein observed in each run. The Matlab script then wrote out the result as an Excel database, in which the number of hits for each protein is listed. This list is also tabulated to show the number of spectral counts for each LC-MS run and sample condition. In Excel it was straightforward to total the spectral count hits for each condition, light versus no-light, or L-peptide versus d-peptide control. Proteins with high ratio could be identified by sorting the spreadsheet list by total number of hits and then by ratio.

To check the peptide probability calculation, the data were searched against a reversed database and listed with the same $p \leq 0.05$ filter as above. The number of False Positive Hits were summed for all the proteins. This result was divided into the total number of hits for the search of the forward database, multiplied by 100, to give a false discovery rate at the peptide level of 4.5%. This was roughly in agreement with the filter that was set.

2.3.5. Ligand-Proximal Photoxidation with DBF-NP41-HB for imaging

Excised sciatic mouse nerves were treated with 50 μM DBF-NP41-HB for 1 hr, exposed to 480 nm light (30 nm bandwidth, 0.07 W/cm^2) on a solar simulator or no light

as a control, reacted in 50 mM MES buffer, pH 5.5, and frozen in OCT. Frozen tissues were cut into 10 μm sections on a cryostat (Leica), fixed in 4% paraformaldehyde, and stained with an avidin-conjugated peroxidase (ABC Reagent, Vector) and DAB. White light microscopy was used to visualize biotin deposition.

2.3.6. In vivo ProxPhOx with intramolecular pyridylhydrazine and biotin for mass spectrometry identification

SKH1 were tail vein injected with 450 nmoles DBF-NP41-HB or the D-amino-acid peptide. After 4 hours of washout, mice were anesthetized with an intraperitoneal (IP) injection of 100 μL of a 1:1 mixture of ketamine HCl (100mg/ml) and midazolam (5mg/ml) (KM), sciatic nerves were exposed and one side was photooxidized with 480 nm (30 nm bandwidth, 0.07 W/cm^2) light on a solar simulator for 15 minutes while the other was kept dark. Nerves were harvested from sacrificed animals and reacted in 50 mM MES buffer, pH 5.5. Tissue was processed as described above for LC-MS/MS analysis.

2.3.7. Immunohistochemistry

Histological imaging of NP41 in vivo binding was performed as previously described.(Whitney, Crisp et al. 2011) Healthy or degenerated facial nerves (6 weeks or 2.5 months post-transection) in surrounding muscle and tissue fasciae were dissected from uninjected mice and frozen in OCT (Sakura). 10 μm sections were cut on a cryostat (Leica), dried on glass slides, and fixed in 4% paraformaldehyde in PBS, blocked with 5% normal goat serum (Invitrogen), and stained with anti-laminin or anti-collagen antibodies and appropriate fluorescent secondary antibodies. Rabbit antisera to mouse

laminins α4, β2, and γ1 were kindly provided by T. Sasaki. Antisera to mouse laminin α5 was kindly provided by J. Miner. Polyclonal rabbit antibodies to collagen VI subunits α1 and α3 and rat monoclonal antibody to laminin α2 were purchased from Santa Cruz Biotech. AlexaFluor488 conjugated anti-rabbit polyclonal antibody and AlexaFluor488 conjugated anti-rat polyclonal antibodies were purchased from Invitrogen. Images were taken with Nikon confocal fluorescence microscope, 488 nm excitation, 520 nm emission. Serial sections of degenerated nerves were stained with hematoxylin and eosin and imaged with white light microscopy.

2.3.8. Phage binding ELISA

96-well plates were coated with purified recombinant human laminins-421, -211, and -521 (Biolamina), collagen VI (Abcam), or no protein as a control were each coated at 10 μg/mL in sodium bicarbonate (7.5%), pH 9.5, at 4°C overnight, then blocked with BSA. M13 phage expressing NP41 on pIII or a mixture of random 12-amino acid peptides (New England Biolabs) were treated for one hour in triplicate wells, washed in PBS, and detected by anti-M13-HRP and TMB 1-Step Ultra colorimetric substrate (ThermoFisher), and measured on a Tecan plate reader with 650 nm absorbance. Triplicate measurements were averaged and background subtracted from the no protein control, and scaled as a percentage of the maximum value in each experiment. Percentages were averaged across 4 independent experiments.

2.3.9. Imaging NP41 of healthy and degenerated nerve in vivo

Facial nerves were transected as previously described.(Hussain, Mastrodimos et al. 2015) Distal facial nerve branches were imaged 3 months after main branch

transection in 6 months old female SKH1 mice (left 2 panels) or a healthy facial nerve control. Mice were anesthetized with an intraperitoneal injection of ketamine (150 mg/kg) and xylazine (10 mg/kg). 20 nmols/g FAM-NP41 were injected through the tail vein, and facial nerves were exposed and imaged after 2.5 hour washout using a customized Olympus fluorescence dissecting microscope with white light reflectance and with fluorescence light with 450-490 nm excitation and 500-550 nm emission.

2.4. Results

Affinity chromatography was initially tested to determine the *in vivo* binding target of the previously identified nerve binding peptide NP41 using homogenized nerve tissue treated with immobilized NP41. No specific protein was selectively captured as determined by mass spectrometry analysis, with NP41 versus an all d-amino acid control. We speculated that this was possibly a result of the low affinity binding of NP41 or inefficient binding of NP41 to homogenized tissue and its protein target outside native context. Thus, we developed ProxPhOx to capture the NP41-receptor interaction in native tissue without physical disruption.

2.4.1. Imaging Ligand-Proximal Photooxidation (ProxPhOx)

To demonstrate that SOG photoactivation could induce biotin-hydrazide labeling proximal to NP41 binding, mouse peripheral nerve sections were preblocked with nicotinic hydrazine, incubated with 375 μM FAM-NP41 or its all d-amino acid enantiomer, washed with PBS, and illuminated with 480 nm light for 15 minutes or left in the dark. Oxidized sites were then labeled by reacting 50 μM biotin hydrazide in MES buffer, pH 5.5. Biotin was detected using streptavidin-Texas red. High perineurial biotin

staining, indicating localized oxidative damage, was detected only upon photooxidation with FAM-NP41, and correlated well with signal detected by direct visualization of NP41-fluorescein binding (Figure 2.2). Neither the all d-amino acid control nor non-light exposed tissues showed high perineurial fluorescence after biotin reaction and detection.

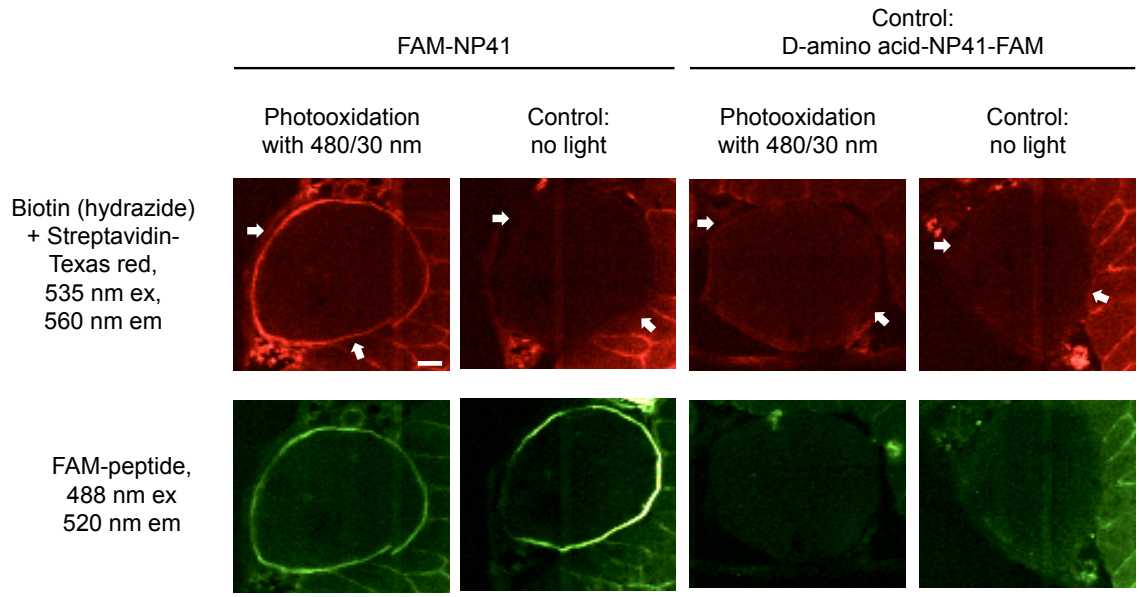

Figure 2.2. ProxPhOx can be used to specifically conjugate biotin to regions highlighted by NP41. Photooxidation of FAM-NP41-treated nerve tissue sections with 480 nm light induces biotin-hydrazide labeling (red, upper panels), of nerve tissue which is highest in the perineurium (white arrows). High perineurial labeling is absent from both the no light and all D-NP41 controls with and without light. High perineurial biotin labeling colocalizes with direct detection of peptide binding at the perineurium in the same section (green, lower panels), imaged following photooxidation exposure and biotin hydrazide conjugation. Higher peptide signal in the no light control compared to the photooxidized sample demonstrates photobleaching of the SOG at the perineurial peptide binding site after photooxidation, consistent with the production of singlet oxygen. Scale bar = 50 μm. Images are at matched gain within each color and representative of at least three independent samples. Scale bar = 50 μm.

2.4.2. Identification of NP41 binding targets by ProxPhOx using mass spectrometry

In order to identify NP41 binding partners using ProxPhOx, NP41-methylene blue (MB) was used (Figure 2.3 A), for efficient singlet oxygen production and deeper light penetration into tissue. Several different light exposure times were tested because excessive singlet oxygen exposure can generate compounding reactions and

crosslinks.(Davies 2003, Davies 2004) Whole dissected mouse sciatic nerves were incubated in 50 μM NP41-MB for 2 hours in the dark. Nerves were rinsed and transferred to PBS containing 50 μM biotin hydrazide and photooxidized with 640 nm light for 10 seconds, 1 min, or 15 minutes or not treated with light as a control. Nerves were transferred to MES buffer, pH 5.5 with 50 μM biotin hydrazide (BH) and incubated for 30 minutes at room temperature in the dark. Nerves were then homogenized and labeled proteins were affinity purified with immobilized streptavidin. After acid release and trypsinization, peptides were identified by LC-MS/MS and relatively quantified by spectral counting.(Liu, Sadygov et al. 2004, Bantscheff, Schirle et al. 2007)

A select group of proteins showed enrichment over the no light control spectral counts of different light-exposed samples were averaged (Figure 2.3), as well as in each individual exposure (Appendix Figure 2S.1). Those with abundant counts (>30) that showed the highest enrichment were laminin subunits α4 and β2 (0.76 and 0.72). These proteins were enriched after only 10 seconds of photooxidation (0.79 and 0.72). In addition, laminin subunits β1 (0.65), γ1 (0.57), and α2 (0.56), nidogen (0.64), and collagen VI α1, α2, and α3 (0.56, 0.57, and 0.55, respectively) were enriched, and values were greatest after 15 minutes of photooxidation. Other highly abundant peripheral-nerve specific proteins, such as neurofilament light chain (0.41) and myelin protein P0 (0.41) showed no enrichment under light-exposed conditions.

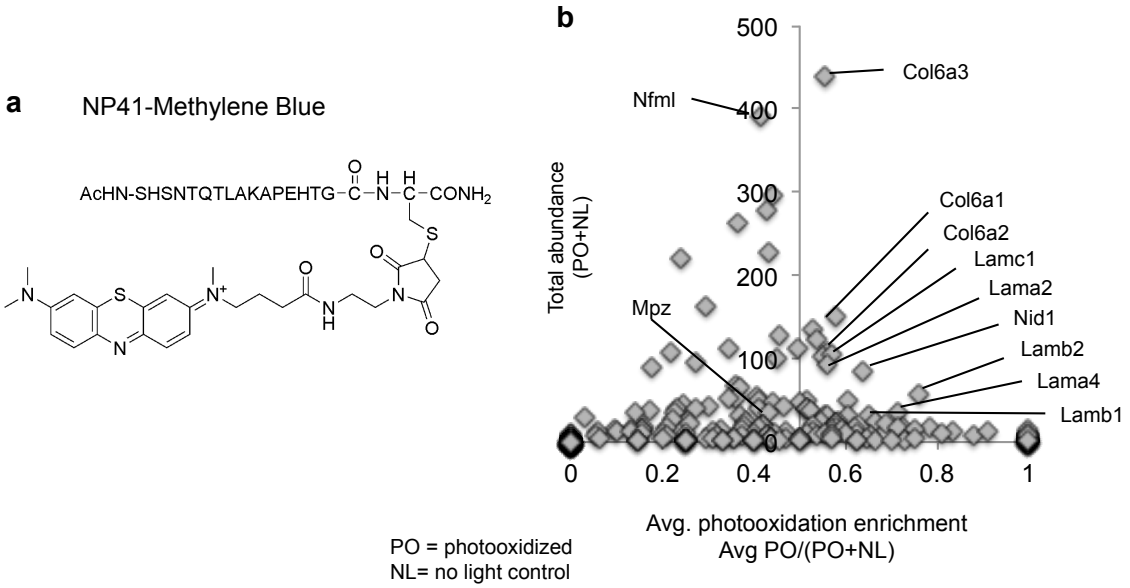

c

Abbreviation	Protein Name	Enrichment Avg. PO/(PO+NL)	Total abundance Avg. PO+NL
Lamb2	laminin subunit beta-2 precursor	0.76	58
Lama4	laminin subunit alpha-4 precursor	0.72	35
Lamb1	laminin subunit beta-1 isoform X1	0.65	32
Nid1	nidogen-1 precursor	0.64	86
Col6a1	collagen alpha-1(VI) chain precursor	0.58	151
Lamc1	laminin subunit gamma-1 precursor	0.57	105
Col6a2	collagen alpha-2(VI) chain precursor	0.56	109
Lama2	laminin subunit alpha-2 precursor	0.56	94
Col6a3	collagen alpha-3(VI) chain isoform 2 precursor	0.55	439
Nfml	neurofilament light polypeptide	0.41	391
Mpz	myelin protein P0 isoform X1	0.41	39

Figure 2.3. ProxPhOx using Methylene Blue (MB)-NP41 identifies binding candidates, laminin, collagen, and associated proteins. (a) Structure of MB-NP41. **(b)** Relative quantification of proteins by spectral counting in photooxidized (PO) sample versus no light (NL) control. Spectral counts for each protein were summed [abundance (PO+NL)] and the fraction of those that were identified in the PO sample [enrichment PO/(PO+NL)] are plotted on the y and x axes, respectively. Proteins that were enriched in the photooxidized compared to the no light control are shown on the right of the vertical axis at x=0.5. Enriched proteins with abundant spectral counts (y>30) include collagen-VI α subunits, laminin α, β, and γ subunits, and nidogen. Two abundant, nerve-specific proteins, neurofilament and myelin protein P0, were not enriched. Proteins which showed low total spectral counts (< 30) were considered likely non-specific background signal. **(c)** Table of values of proteins identified in graph, showing x and y values of the proteins identified in the graph.

2.4.3. Application of ProxPhOx in vivo with intramolecular biotin labeling

To confirm NP41's potential interaction with these proteins *in vivo* using intramolecular tagging with ProxPhOx, we used a slightly modified approach in which a SOG, biotin, and hydrazine were all directly conjugated to NP41 (Figure 2.1, Scheme B). Dibromofluorescein (DBF) was used as the singlet oxygen generator due to its efficient production of singlet oxygen and compatibility with *in vivo* NP41 targeting compared to other efficient SOGs, methylene blue and eosin (Appendix Figure 2S.2), and pyridylhydrazine was used for ketone conjugation (Figure 2.4 A).

First, to confirm that conjugation of biotin and pyridylhydrazine does not negatively affect NP41 binding or biotin labeling, whole nerves were incubated with 50 μM DBF-NP41-pyridyl-hydrazine-biotin (DBF-NP41-HB) *ex vivo,* illuminated with 480 nm light, frozen, sectioned and treated with streptavidin-horseradish peroxidase (HRP) and diaminobenzidine for imaging. Biotin labeling was significant at the perineurium of the photooxidized sample, consistent with the localization of other NP41 conjugates, and not in the no light control, (Figure 2.4 B, Figure 2.2 A, Figure 2S.2). To find potential *in vivo* binding partners, 450 nmol DBF-NP41-HB or the all-d-amino acid NP41 control version were injected into mice and allowed to circulate for 4 hours. Sciatic nerves were surgically uncovered and exposed to 480 nm light for 15 minutes or kept in the dark. Sciatic nerves were immediately dissected, treated in MES buffer, pH 5.5, and processed as before for mass spectrometry. Spectral counting analysis of the photooxidized sample versus the no light control, revealed enrichment of nidogens-1 and -2 (1 and 0.8), laminin subunits α4 (1), β2 (0.78), γ1 (0.88), α2 (0.83), β1 (0.67), heparan sulfate proteoglycan (Hspg, 0.78), and slight enrichment of collagen VI subunits α1 (0.67), α2 (0.61), α3 (0.61, Figure 2.4 C, D). Photooxidation of the d-amino acid control resulted in fewer

spectral counts and poor enrichment of the same proteins over the no-light control. A direct comparison of the spectral counts of the photooxidized DBF-NP41-HB sample to the photooxidized d-amino acid control confirmed high enrichment of the nidogen and laminin subunits named above and mild enrichment of collagen VI subunits (Appendix Table 2S.1). Though DBF-NP41-HB photooxidation showed enrichment of laminin subunit α5, its abundance was extremely low. As in the previous experiment, myelin protein P0 and neurofilament light peptide were abundant but not enriched (0.51 and 0.44). Other proteins with enrichment levels and abundance approaching the laminins, collagens, and nidogen were not highly enriched above the d-amino acid control peptide or showed low or no abundance in the previous ProxPhOx experiment (Appendix Table 2S.2).

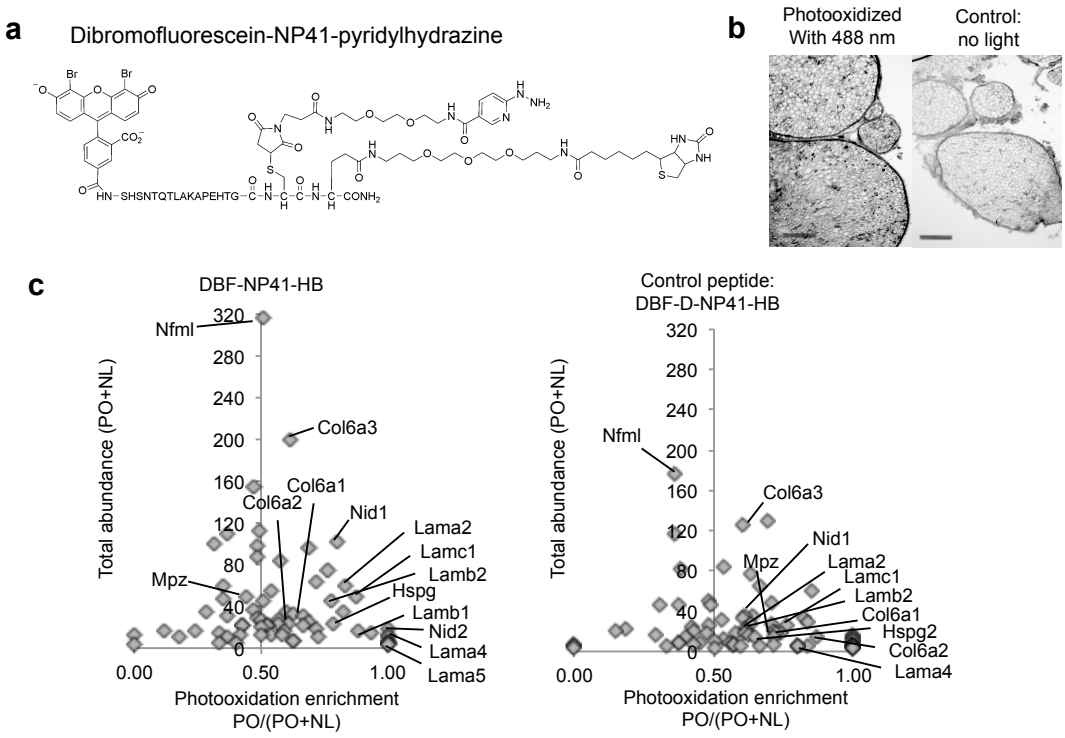

d

	DBF-NP41-HB Photooxidized vs. no light		Control peptide DBF-D-NP41-HB Photooxidized vs. no light	
Protein	Enrichment PO/(PO+NL)	Abundance NL+PO	Enrichment PO/(PO+NL)	Abundance NL+PO
nidogen-2	1	19	1	4
laminin subunit alpha-4	1	13	0.8	5
laminin subunit alpha-5	1	1		0
laminin subunit gamma-1	0.88	49	0.76	25
laminin subunit beta-1 isoform X1	0.88	17	1	3
laminin subunit alpha-2	0.83	60	0.61	23
nidogen-1	0.8	101	0.61	36
laminin subunit beta-2	0.78	45	0.62	21
basement membrane-specific heparan sulfate proteoglycan core protein isoform X1	0.78	23	0.64	14
collagen alpha-1(VI)	0.67	30	0.71	21
collagen alpha-3(VI)	0.61	200	0.6	126
collagen alpha-2(VI)	0.61	23	0.87	15
neurofilament light polypeptide	0.51	316	0.358	176
myelin protein P0	0.44	50	0.722	18

Figure 2.4. ProxPhOx in vivo with dibromofluorescein-NP41-pyridylhydrazine-biotin (DBF-NP41-HB) conjugate shows enrichment of laminin, collagen, and associated proteins. (**a**) Structure of DBF-NP41-HB conjugate. (**b**) Photooxidation-dependent biotin labeling with "cis"- conjugate shows predominantly perineurial localization (darkened areas), absent in the no light control. Images set to equal gain. Scale bar = 500 μm. (**c**) Relative quantification of spectral counts in PO sample versus NL control for each protein identified by mass spectrometry. *Left: in vivo* photooxidation of DBF-NP-HB shows high enrichment of basement membrane proteins, including laminin subunits and nidogens. Collagen VI subunits showed high abundance and low enrichment, and laminin α5 showed high enrichment but low abundance. Two abundant, nerve-specific proteins, neurofilament and myelin protein P0, were not enriched. *Right:* By comparison, *in vivo* photooxidation of a control conjugate with all d-amino acids showed low enrichment and low abundance of the same proteins. **(d)** Table of values of proteins identified in graph, showing x and y values of each identified protein.

Because laminins are heavily glycosylated, we also compared ProxPhOx with a previously described method that uses trifunctional chemoproteomic reagents (TRICEPS) for carbohydrate-directed crosslinking of ligand-glycoprotein receptor binding and subsequent receptor identification by mass spectrometry.(Timpl, Rohde et al. 1979, Frei, Jeon et al. 2012) In this approach, cis-glycol groups in carbohydrates are converted to aldehydes that are then crosslinked to NP41 hydrazine. NP41-fluorescein-biotin hydrazine (FAM-NP41-BH) or an all D-FAM-NP41-BH were synthesized (Appendix Figure 2S.3A) and injected into mice. Nerves were processed as previously described with modification for *in vivo* use, wherein nerves were excised prior to sodium metaperiodate application to oxidize glycans.(Frei, Moest et al. 2013) Imaging confirmed perineurial binding and hydrazine-mediated labeling (Appendix Figure 2S.3 C, D). Ion abundance quantification independently confirmed laminin γ1 and α4 as binding partners of NP41 *in vivo* (Appendix Figure 2S.4).

2.4.4. Confirmation of binding targets by colocalization and binding assays

In order to compare the histological localization of NP41 *in vitro* and *in vivo* with candidate binding targets, NP41 labeled with FAM or Cy5 was treated on mouse facial nerve sections or injected into mice, and nerves were dissected and imaged. While perineurial staining was the strongest both *in vitro* and *in vivo*, endoneurial basement membrane labeling was also visible *in vivo* (Figure 2.5A). For comparison, mouse facial nerve sections were treated with antibodies to mouse laminin α4, α5, β2, γ1 and collagen VI α1 and α3 and a fluorescent secondary antibody. Though laminin α5 did not show

abundant enrichment by ProxPhOx, it is known to form a complex with laminin subunits β2 and γ1 in nerves, making it a target candidate.(Patton, Miner et al. 1997) Laminins α4 and α5 showed mostly perineurial staining, while laminin α2 labeled only endoneurial basement membranes, and laminins β2 and γ1 and collagen VI highlighted a mixture of each (Figure 2.5 B). Nidogen and Hspg, identified as enriched by ProxPhOx, are ubiquitously expressed basement membranes proteins known to complex with most laminin isoforms, and may be photooxidized due to their proximity to the nerve-specific target or pulled down in complex with laminins.(Paulsson, Aumailley et al. 1987)

Laminins are trimers of α, β, and γ subunits, and laminin α4β2γ1 (laminin-421), laminin α5β2γ1 (laminin-521) and laminin α2β1γ1 (laminin-211) have been established as the isoforms expressed in peripheral nerve, and collagen VI is a trimer of α1-3 subunits.(von der Mark, Aumailley et al. 1984, Patton, Miner et al. 1997, Cho, Ko et al. 1998, Hill 2009, Chen, Cescon et al. 2014) Binding of NP41 to purified recombinant human laminins-421, -521, -211, and collagen VI was not detectable by surface plasmon resonance or peptide fluorescence detection possibly due to weak binding activity outside of the native context or lower affinity of the mouse-selected peptide to the human isoform. In order to test if NP41 could bind human nerve proteins in their native context, FAM-NP41 or d-amino acid control was treated on human nerve sections at 375 μM for 30 minutes. After a quick wash, NP41 showed low binding, only slightly higher than the control d-amino acid peptide (Appendix Figure 2S.5).

Despite low specific binding, we speculated that binding to human laminins may be detectable with higher avidity multivalent NP41-phage and in the context from which the sequence was selected.(Whitney, Crisp et al. 2011) NP41-expressing M13 phage or

phage expressing random peptides were treated on plates coated with human recombinant laminin-211, -421, -521, collagen VI, and a bovine serum albumin (BSA) control. Binding was detected using anti-M13-HRP antibody and chromogenic substrate. NP41-phage showed significantly greater binding than phage expressing non-targeted peptides to binding candidates laminins-421 and 211 ($p<0.01$, Student's t-test), and nearly significant binding to collagen VI ($p=0.07$, Figure 2.5 B), which showed lower enrichment by ProxPhOx (Figure 2.3 B and C, Figure 2.4 C and D). NP41 did not show significant binding to another non-targeted perineurial protein, laminin-521 ($p=0.61$). Though this protein shows similar perineurial localization (Figure 2.5 A), it was not consistently or abundantly enriched by ProxPhOx experiments using NP41 (Figure 3 C and D, 4 C and D).

Figure 2.5. NP41 colocalizes with laminins and collagens in nerve basement membranes and binds to purified laminins-421 and -211 and collagen VI. (**a**) FAM-NP41 treated on facial nerve sections showed typical bright perineurial staining with little endoneurial staining (left, scale bar = 50 μm), while systemically injected NP41, imaged in sciatic nerves in cross-section (middle) and longitudinally (right) shows both high perineurial staining and endoneurial basement membrane labeling with FAM-NP41 (middle) and Cy5-NP41 (right). Scale bar = 500 μm. (**b**) Immunofluorescence staining of laminins and collagens on mouse facial nerve tissue sections shows similar localization to NP41 binding. Laminin α4, α5, and collagen VIα1 show high perineurial specificity with low staining of endoneurial basement membranes, while laminin β2, laminin γ1, collagen VIα3, collagen VIα1 stain perineurial and endoneurial basement membrane staining, and laminin α2 shows only endoneurial basement membrane staining. Background staining of no antibody control was negligible. (**c**) ELISA showing NP41-expressing phage bind purified laminin-421 and -211 (n=4) significantly greater than phage expressing a library of random 12-amino acid peptides. Laminin-521 and collagen VI binding was not significantly greater than the control peptides but trended toward higher NP41 binding. * indicates p-value <0.05. Student's *t*-test, p-value = 0.0078 (Lam-421), 0.61 (Lam-521), 0.0069 (Lam-211), 0.071 (Col6). Error bars represent standard error of the mean.

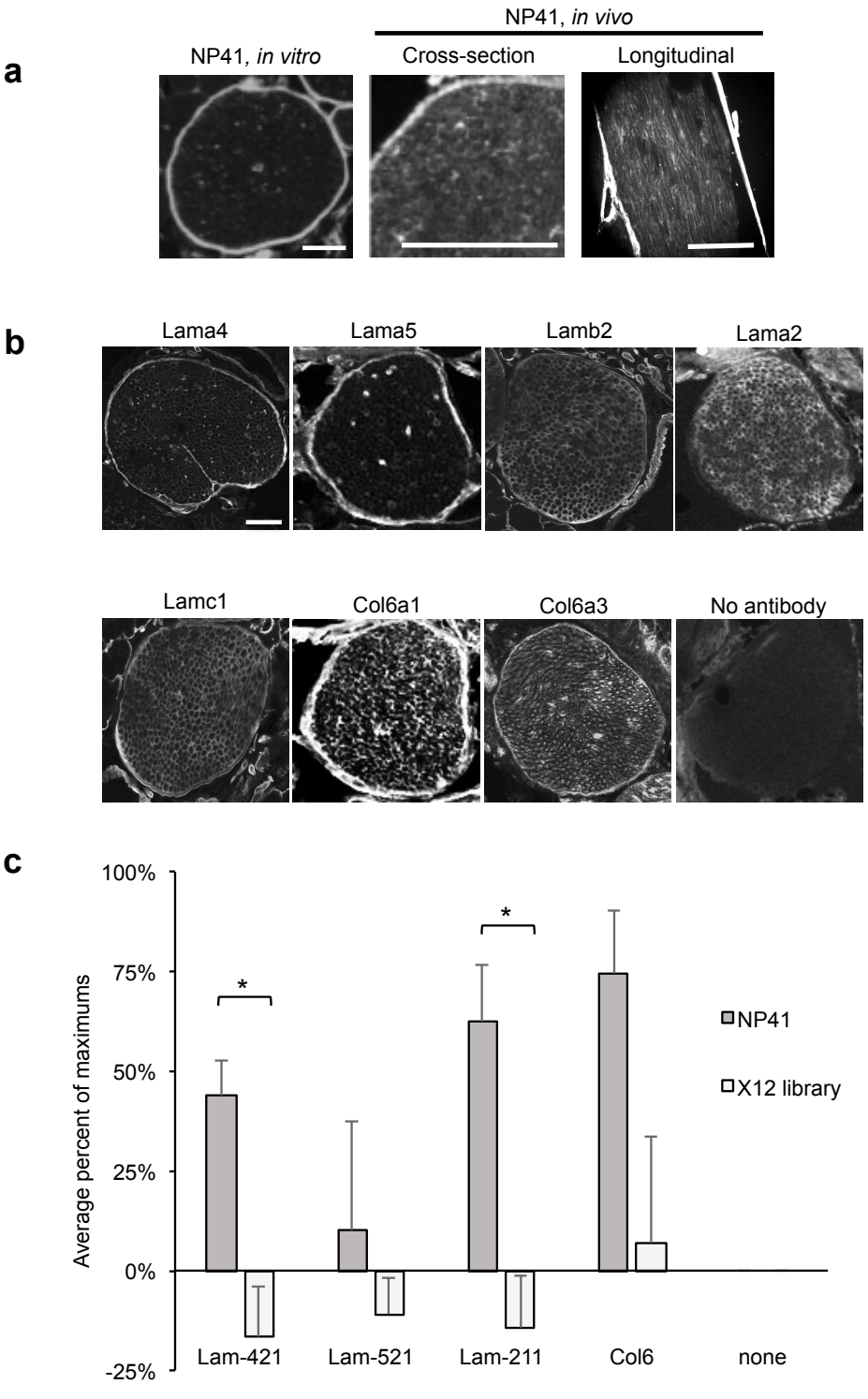
a
NP41, in vivo
NP41, in vitro
Cross-section
Longitudinal
b
Lama4
Lama5
Lamb2
Lama2
Lamc1
Col6a1
Col6a3
No antibody
c
100%
75%
50%
25%
0%
-25%
Average percent of maximums
*
*
NP41
X12 library
Lam-421
Lam-521
Lam-211
Col6
none

2.4.5. Confirmation of binding targets in nerve degeneration model

Following nerve injury and subsequent axonal degeneration, or Wallerian degeneration, the tubular space previously occupied by the axon within the nerve becomes highly cellularized, while many highly abundant components, such as myelin and neurofilament, are degraded, while structural proteins are maintained or upregulated (Salonen, Peltonen et al. 1987, Wallquist, Patarroyo et al. 2002, May and Mittag 2006, Hill 2009) Since NP41 showed evidence of binding to these targets, we tested NP41 localization and candidate protein expression in a degenerated nerve model.(Wu, Whitney et al. 2011, Hussain, Mastrodimos et al. 2015) NP41 was injected into mice in which the main branch of the facial nerve had been surgically transected three months prior and allowed to degenerate. Consistent with NP41 binding sites of laminin-421, laminin-211, and collagen VI, fluorescence imaging showed FAM-NP41 labeling of degenerated nerves *in vivo* though they were not detectable by white light reflectance imaging (Figure 2.6 A). To verify NP41 binding histologically, degenerated facial nerve at 6 weeks and 2.5 month post-transection was dissected within the surrounding muscle and fasciae from uninjected mice, sectioned, and stained with FAM-NP41 or hematoxylin and eosin (H&E), and various antibodies. In sections, NP41 staining showed consistent perineurial staining in highly cellular, demyelinated degenerated nerves (Figure 2.6 B). Immunostaining similarly revealed the retention of staining of laminins-421, -211, -521 and collagen VI which colocalized at the perineurium and at the basement membranes of the endoneurium (Figure 2.6 C).

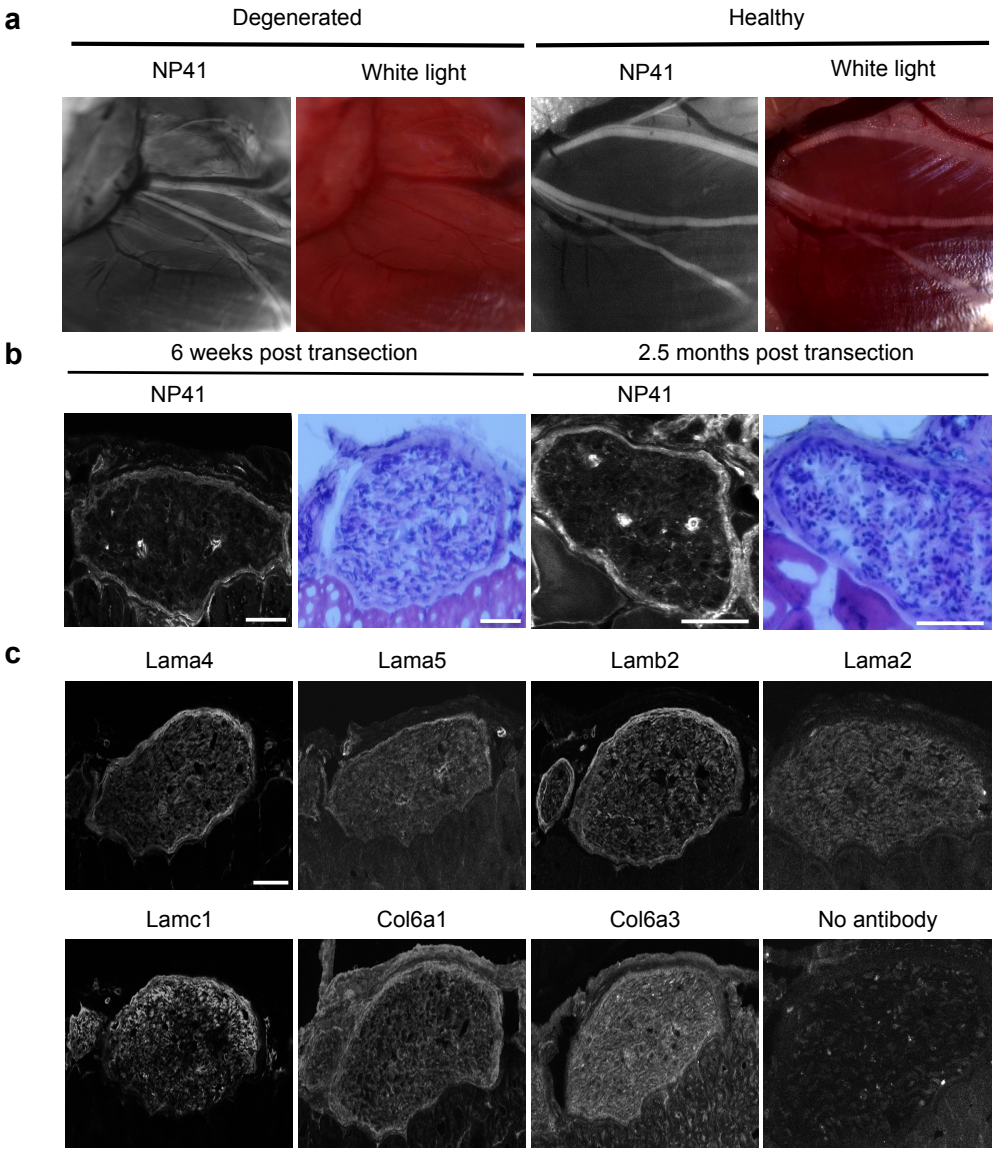

Figure 2.6. Nerve peptide highlights chronically degenerated nerve ghosts due to conserved collagen-laminin structure. (**a**) Degenerated facial nerve (left two panels) and healthy facial nerve (right two panels) in mice injected with FAM-NP41, imaged under fluorescence (first and third panels) and white light reflectance (second and fourth panels). (**b**) NP41 staining on sections of degenerated nerve, showing continued peptide binding in spite of extensive Wallerian degeneration of the endoneurium. Sections of degenerated facial nerve 6 weeks (left two panels) and 2.5 months post-transection (right two panels) treated topically with FAM-NP41 (first and third panels), or stained with hematoxylin and eosin (H&E, second, fourth, and fifth panels). H&E shows transected nerves are highly cellularized (dark blue punctae) with few myelinated sheaths (light pink round structures), indicative of extensive degeneration, while perineurial staining of NP41 is maintained. Scale bar = 500 μm (**c**) Immunostaining of laminin and collagen subunits show localization in degenerated nerve basement membranes similar to NP41. Immunostaining on serial sections of mouse facial nerve, 6 weeks post-transection, show continued perineurial and endoneurial basement membrane staining of laminin α4, laminin α5, laminin β2, laminin α2, laminin γ1, collagen VIα1, collagen VIα3. The gain for each image was set separately, and the no antibody control was set to the maximum gain used. Scale bar = 500 μm shown in the first panel is the same for all images.

2.5. Discussion

Fluorescent highlighting of peripheral nerves with molecules like NP41-FAM offers the potential to improve a myriad of surgical procedures by reducing morbidity caused by inadvertent nerve injury. However, optimization and characterization, including the identification of the binding target, will likely be required for clinical translation. Toward that goal ProxPhOx has been used here to identify laminin-421, 211 and collagen VI as likely binding targets of NP41-FAM.

ProxPhOx enables affinity tagging of photooxidized sites proximal to ligand using a photoactivatable SOG dye conjugated to ligand. Tagging can be done intermolecularly (trans) with exogenous biotin hydrazide or intramolecularly (cis) with biotin and hydrazide conjugated to ligand. Labeling potentially includes both direct ligand-binding target as well as closely interacting proteins with trans labeling casting a wider space, as it is not structurally constrained. In cis-labeling, hydrazine reaction is spatially limited by its tether length with ligand likely resulting in tagging of the closest reactive site, presumably within the direct binding target. In either format, ProxPhOx offers advantages over alternative approaches in that it can be used in case of fairly weak interactions and does not necessitate potentially disruptive pre-treatment of ligand bound tissue.

Similar to ProxPhOx (cis) tagging with even greater restrictions, most current crosslinking methods require a specific reactive group to exist in a ligand-accessible location on the target macromolecule. This limitation is eliminated with PhoxPhOx (trans) tagging. In addition, photocrosslinkers such as azides and diazirines are limited to UV wavelengths and can only be photolyzed once, ProxPhOx is compatible with a

myriad SOGs from UV to infared and can multiple photooxidation cycles limited only by bleaching.(Tanaka, Bond et al. 2008) Furthermore, ProxPhOx may be modifiable with alternatives such as using antibodies to pull down proteins containing methionine oxidation or N-formylkynurenine.(Suto, Ikeda et al. 2006, Ehrenshaft, Silva et al. 2009, Oien, Canello et al. 2009) Disadvantages include the limited knowledge of singlet oxygen generated hydrazide-reactive modifications on amino acids, glycans, and lipids, and potential loss of specificity due to singlet oxygen's diffusion range. ProxPhOx is a novel methodology that can be generally applied to identify ligand binding targets although it is not the first technology to use singlet oxygen to co-locate interacting proteins. Singlet oxygen triplet energy transfer (STET), was recently used to measure distances of proteins known to associate within complexes in live cells using genetically encoded miniSOG and fluorescent singlet oxygen detector on two putative interacting proteins.(To, Fadul et al. 2014)

We identified perineurial laminin-421 and endoneurial laminin-211 as binding targets of NP41, and high enrichment of laminin-421 at early time points using ProxPhOx suggests that it is likely the primary binding target. This is supported by its identification using TRICEPS glycoprotein capture, the prominent perineurial labeling of NP41 and laminin-421 in healthy and degenerated nerve, and the ability of NP41-phage to bind the purified protein *in vitro*. Having been selected by phage display for binding to whole nerves *ex vivo*, enriched peptides such as NP41 would logically target perineurial laminins and collagens, given these proteins' prominent exterior location and abundance and that large phage (100s-1000 nm long) are unlikely to penetrate the surface. For

clinical imaging agents, targeting extracellular matrix proteins is advantageous due to their accessibility from circulation and the reduced risk of adverse effects.

Collagens and laminins form extracellular matrix in the majority of tissues but are diverse in their composition of different subunit isoforms. Though laminin-421 has tissue selective expression, it is not neural-exclusive and is also expressed by some mesenchymal cells in other tissues, such as some blood vessels, which NP41 has also been found to label. (Patton, Miner et al. 1997, Thyboll, Kortesmaa et al. 2002, Ishikawa, Wondimu et al. 2014) Likewise, laminin-211, in addition to its endoneurial expression, is known to be localized in muscle basement membranes, so targeting it with fluorescent probes may limit the nerve-to-muscle contrast obtainable.

Future studies will address if molecules with higher affinity toward nerve-specific laminins can generate higher *in vivo* nerve contrast and human nerve compatibility, using phage-display selection or other methods. In addition, this study opens up the possibility for further developments of technologies using photooxidation to detect any ligand-protein or protein-protein interaction, such as with a genetically-encoded SOG.(Shu, Lev-Ram et al. 2011)

2.6. Acknowledgements

Chapter 2 is currently being submitted for publication of the material. Glasgow, H.L.; Whitney, M.A.; Gross, L.A.; Friedman, B.; Adams, S.R.; Crisp, J.L., Hussain, T.; Frei, A.P.; Wollscheid, B.; Nguyen, Q.T.; Tsien R.Y. The dissertation author was the primary author of this material.

The author would like to acknowledge:

Michael Whitney for collaboration on experimental design, performing TRICEPS experiments, and contributing to writing and editing of the manuscript, Larry Gross for performing mass spectrometry experiments and analysis, Beth Friedman for helping perform histological imaging experiments, Stephen Adams for design and synthesis of molecules, Jessica Crisp and Timon Hussain for performing animal experiments, Andreas Frei and Bernd Wollscheid (ETH Zurich) for performing TRICEPS experiments and mass spectrometry analysis, Quyen Nguyen for experimental design of degenerated nerve model, Roger Tsien for experimental design and editing the manuscript, John Ngo for providing helpful suggestions, Paul Steinbach for providing support, to Karel Novy for additional data analyses, and to members of the laboratory for discussions and comments.

2.7. Appendix

Supplementary Materials and Methods

Imaging NP41-SOGs in vivo:

Adult SKH1 mice (Charles River Laboratories) or wildtype albino C57BL6 mice (Jackson Laboratories) were used for all experiments and injections were done intravenously through the tail vein.
300 nmol dibromofluorescein-NP41 (DBF-NP41) was injected and imaged after 3 hours of washout. 150 nmol eosin-NP41 was injected and imaged 2 hours post-injection. 200 nmol of methylene blue-NP41 was injected and imaged 2.3 hours post injection. For imaging, mice were anesthetized with an intraperitoneal (IP) injection of 100uL of a 1:1 mixture of ketamine HCl (100mg/ml) and midazolam (5mg/ml) (KM), sciatic nerves were exposed and imaged with Zeiss Lumar.

Peptide synthesis and labeling:

5(6)-carboxy-4',5'-dibromofluorescein (DBF):

To a stirred suspension of 5(6)-FAM (376 mg, 1 mmol) in 80% aq. HOAc (5 ml) at room temperature, bromine (102 μL, 2 mmol) was added dropwise. The solid dissolves and after stirring overnight, the crude product is collected by filtration, washed with water, and dried *in vacuo* over P_2O_5. Yield (0.5 g). LC-MS revealed the desired product (56% by absorbance at 254 nm) with unreacted starting material (1%) and mono (5.5%), tri (15.6%) and tetrabrominated (21.7%) products, and was used without further purification. ES-MS($M+H^+$) 534.8, calc'd 534.9

5(6)-carboxy-4',5'-dibromofluorescein N-hydroxysuccinimide ester (DBF-NHS):

Crude 5(6)-carboxy-4',5'-dibromofluorescein (200 mg, 0.37 mmol) was dissolved in anhydrous THF (10 ml) under N_2 and N-hydroxysuccinimide (52 mg, 0.45 mmol) was added followed by diisopropylcarbodiimide (DIPC; 59 µl, 0.38 mmol). After 4h stirring at room temperature, LC-MS indicated an incomplete reaction so an additional 25 µL of DIPC was added. After overnight, the reaction mix was evaporated, dissolved in dry DMSO (1 mL), filtered and purified by prep HPLC eluting with a gradient of 10-90% acetonitrile-water-0.05% TFA in 20 mins. The collected fractions were pooled and immediately frozen and lyophilized to give a red solid. ES-MS($M+H^+$) 631.9, calc'd 632.9.

4',5'-dibromofluorescein-5(6)-carboxyamido-2''-ethylmaleimide:

5(6)-carboxy-4',5'-dibromofluorescein N-hydroxysuccinimide ester (12 mg, 19 µmol) and 2-aminoethylmaleimide trifluoroacetate (10 mg, 39 µmol) were dissolved in dry DMSO and 4-methylmorpholine (10 µL, 107 µmol) was added with mixing. After 30 min, HOAc (10 µL) was added and product was purified by HPLC eluting with a gradient of 10-90% acetonitrile-water-0.05% TFA in 20 mins. The collected fractions were pooled and lyophilized to give a red solid. ES-MS($M+H^+$) 656.9, calc'd 656.9.

Maleimide-peg2-pyridylhydrazine acetone hydrazone:

Succininimidyl 6-hydrazinonicotinate acetone hydrazone (ref US 6,800,728) (58 mg, 0.2 mmol) was dissolved in dry DMSO (200 µL) and acetone (5 µL), 2,2′-(ethylenedioxy)bis(ethylamine) (29 µM, 0.2 mmol), and 4-methylmorpholine (22 µL, 0.2 mmol) were added sequentially. After 30 mins at room temp, 3-maleimidopropanoic succinimidyl ester (58 mg, 0.22 mmol) was added and the reaction left overnight. HOAc (25 µL) was added and the product isolated by HPLC eluting with a gradient of X% acetonitrile-water-0.05% TFA in 20 min to give a colorless oil. Yield, 19.6 mg (21%). ES-MS($M+H^+$), 475.2, calc'd 475.2

DBF-L-NP41-Biotin-pyridylhydrazine:

NH2-SHSNTQTLAKAPEHTGCE(biotinyl-PEG)-CONH2 was synthesized by standard Fmoc chemistry on NovaSyn TGR resin using Fmoc-glu(biotinyl-PEG)-OH (Novabiochem). The washed and dried resin-bound peptide (160 mg, 25 µmol nominal) was suspended in dry DMF (1 mL) and DBF-NHS ester (15 mg, 24 µmol) was added with 4-methylmorpholine (50 µL, 0.45 mmol). After stirring overnight at room temperature, the product was collected by filtration, washed with DMF (3 x 5 mL), methanol (3 x 5 mL) and dried in vacuo. Following cleavage for 2 h with 2 ml of freshly-prepared cleavage cocktail (2.5% water, 2.5% thioanisole, 2.5% TIPS, 2.5% EDT 90% TFA), and removal of the resin by filtration, the peptide was precipitated with cold diethyl ether-hexane (1:1 v/v) and collected by centrifugation. The product was purified by prep reverse-phase HPLC using a gradient of acetonitrile-water with 0.05% TFA, to yield 11.1 mg L- and 11.8 mg D-peptides. ES-MS ($M+3H^+$), 952.6, calc'd 952.6 ($M+4H^+$), 714.8, calc'd 714.7

The peptide was dissolved in 50% ACN-water-0.1% TFA (0.5 mL, ~ 8 mM) and treated with maleimide-peg2-pyridylhydrazine acetone hydrazone (70 µL, 100 mM solution in dmso) and K.MOPS (100ul, 0.1M in water pH 7.2). After 1 hour at room temperature, acetic acid (100 µL) and acetone (50 µL) were added and kept overnight at 4C. The product was purified by prep HPLC to yield 11.5 mg. ES-MS ($M+3H^+$), 1110.7, calc'd 1110.4; ($M+4H^+$), 833.4, calc'd 833.1.

DBF-D-NP41-Biotin-pyridylhydrazine:

Synthesized from NH2-shsntqtlakapehtgcE(biotinyl-PEG)-CONH2 using the procedure for DBF-L-NP41-Biotin-pyridylhydrazine. ES-MS ($M+3H^+$), 1110.9, calc'd 1110.4; ($M+4H^+$), 833.4, calc'd 833.1

FAM-NP41-Biotin-Pyridylhydrazine:

NH2-SHSNTQTLAKAPEHTGK(FAM)CE(biotinyl-PEG)-CONH2 was synthesized by standard Fmoc chemistry on NovaSyn TGR resin using Fmoc-glu(biotinyl-PEG)-OH (Novabiochem) and Fmoc-lys(5,6-FAM)(Anaspec) . The washed and dried resin bound peptide (25 µmol nominal) was suspended in dry DMF (2 mL) and N-acetoxysuccinimde (100 mg, 0.64 mmol) was added with 4-methylmorpholine (100 µl, 0.91 mmol). The procedure from DBF-L-NP41-Biotin-pyridylhydrazine was then followed.

ES-MS ($M+3H^+$), 1114.7, calc'd 1114.7; ($M+4H^+$), 836.6, calc'd 836.3. Partial loss of acetone occurs to the free hydrazine, ES-MS ($M+3H^+$), 1101.2, calc'd 1101.3; ($M+4H^+$), 826.4, calc'd 826.3

TRICEPS Ligand-based receptor capturing:

Four NP41-labeled sciatic nerves were minced using a razor blade and tissue pieces were resuspended in 0.8 ml 50 mM ammonium bicarbonate (Sigma-Aldrich). Nerves were dissociated by the addition of 2% (wt/vol) RapiGest surfactant (Waters) and several rounds of indirect sonication (100% amplitude, 0.8 cycle, 60 s) in a VialTweeter (Hielscher). The resulting protein samples were reduced by adding 5 mM TCEP (Pierce) at 20°C for 30 min, and alkylated by adding 10 mM iodoacetamide (Fluka) in the dark at 20°C for 30 min. Trypsin (Sigma) was added to a 1:20 trypsin to protein ratio and protein digestion was carried out over night at 37°C. After digestion, peptide mixtures were heated to 96°C for 10 min to inactivate proteases and undigested particles were removed by centrifugation (13,000 g for 10 min). NP41-captured cell surface glycopeptides were bound to streptavidin by addition of 80 µl washed Streptavidin Plus UltraLink Resin (Pierce) and incubated for 2 h on a slow rotator at 4°C. Unbound peptides were kept and subjected to C18 purification and LC-MS/MS analysis as described later to serve as 'flow-through' protein loading control. Beads were washed extensively in Mobicols (Boca Scientific) connected to a Vac-Man Laboratory Vacuum Manifold (Promega) with a variety of buffers: 5 M NaCl, followed by 100mM NaCl, 100 mM glycerol, 50 mM Tris, 1% Triton-X 100, followed by 100 mM NaHCO3 pH 11, followed by 50 mM ammonium bicarbonate. Washed beads were incubated with 400 µL 50 mM ammonium bicarbonate containing 2 µL PNGase F (New England Biolabs) in a head-over-head shaker overnight at 37°C. Peptides were eluted by

spinning of the Mobicol and subsequent addition of another 500 µL of 50 mM ammonium bicarbonate. Combined eluates were acidified with 40 µL 10% formic acid and subjected to C18 purification using 3-30 µg UltraMicroSpin Columns (The Nest Group) according to the manufacturer's instructions.

LC-MS/MS analysis (TRICEPS):

Peptide samples were separated by reversed-phase chromatography on a high performance liquid chromatography column (75 µm inner diameter, New Objective) that was packed in-house with a 10 cm stationary phase (Magic C18AQ, 200 Å, 3 µm, Michrom Bioresources) and connected to a nano-flow EASY-nLC II Liquid Chromatograph (Thermo Scientific). The nLC system was coupled to an LTQ-Orbitrap XL mass spectrometer (Thermo Scientific) equipped with a nanoelectrospray ion source (Thermo Scientific). Peptides were loaded onto the column with 95% buffer A (98% water, 2% acetonitrile, 0.1% formic acid) and eluted with 300 nL/min over a 40 min linear gradient from 5% to 35% buffer B (2% water, 98% acetonitrile, 0.1% formic acid). After the gradient, the column was washed with 95% buffer B and re-equilibrated with buffer A. Mass spectra were acquired in a data-dependent manner, with an automatic switch between MS and MS/MS scans. High-resolution MS scans were acquired in the Orbitrap (60,000 FWHM, target value 106) to monitor peptide ions in the mass range of 350-1650 m/z, followed by collision-induced dissociation (CID) MS/MS scans in the ion trap (minimum signal threshold 150, target value 10'000, isolation width 2 m/z) of the five most intense precursor ions. To avoid multiple scans of dominant ions, the precursor ion masses of scanned ions were dynamically excluded from MS/MS analysis for 15 seconds. Singly charged ions and ions with unassigned charge states were excluded from MS/MS fragmentation.

MS data analysis and quantification (TRICEPS):

Raw data were converted to the open mzXML format with ReAdW (version 4.3.1). mzXML files were searched by the SEQUEST search engine against UniProtKB/Swiss-Prot protein database version 57.15 of *Mus musculus* concatenated with the sequences of common contaminants. Search parameters for the peptide identification included a precursor mass tolerance of 0.05 Da, a minimum of one tryptic terminus, and a maximum of two internal trypsin cleavage sites. Cysteine carbamidomethylation (+57.021 Da) was set as a static amino acid modification and methionine oxidation (+15.995 Da) and asparagine deamidation (+0.9840 Da) were set as differential modifications. The PeptideProphet and ProteinProphet tools of the Trans-Proteomic Pipeline (TPP version 4.5) were used for probability scoring of peptides and proteins, and identifications were filtered to a false discovery rate of ≤1%. For the analysis of NP41-captured glycopeptides, peptide features were filtered for the presence of the N[115]-X-S/T motif introduced by PNGaseF cleavage (wherein N[115] stands for a deamidated asparagine residue, X stands for any amino acid except proline, and S/T for serine or threonine, respectively). Peptides and proteins were quantified by label-free quantification using the Progenesis (Nonlinear Dynamics) software package.

Imaging NP41 binding to human nerve

Deidentified frozen, unfixed human sural nerve (post mortem) was purchased from Cambridge Biosource. Tissue was sectioned and NP41-FAM was treated as described in methods for mouse tissue

Supplementary Figures

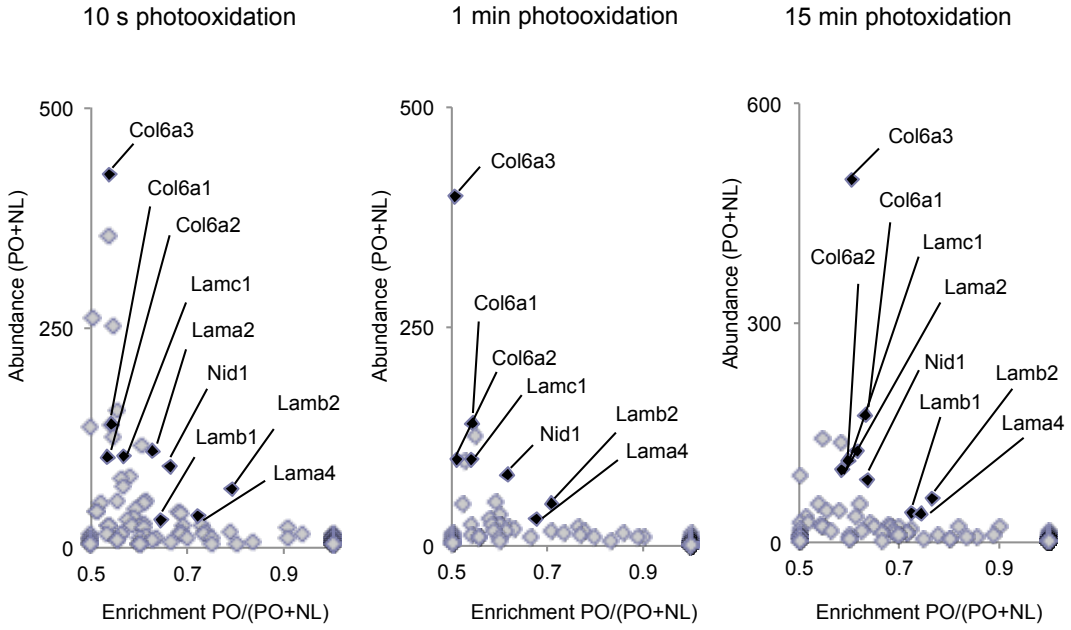

		10 s		1 min		15 min	
		Enrichment PO/ (PO+NL)	Abundance NL+PO	Enrichment PO/ (PO+NL)	Abundance NL+PO	Enrichment PO/ (PO+NL)	Abundance NL+PO
Lamb2	laminin subunit beta-2	0.79	67	0.71	48	0.77	60
Lama4	laminin subunit alpha-4	0.72	36	0.68	31	0.74	39
Nid-1	nidogen-1	0.66	92	0.62	81	0.64	85
Lamb1	laminin subunit beta-1	0.65	31	0.54	24	0.73	40
Lama2	laminin subunit alpha-2	0.63	110	0.43	72	0.59	99
Lamc1	laminin subunit gamma-1	0.57	104	0.54	98	0.6	112
Col6a3	collagen alpha-3(VI) chain	0.54	424	0.51	398	0.6	496
Col6a1	collagen alpha-1(VI) chain	0.54	140	0.54	140	0.63	174
Col6a2	collagen alpha-2(VI) chain	0.53	103	0.51	98	0.62	125

Figure 2S.1. ProxPhOx of MB-NP41 enriches laminin, collagen, and nidogen after various photooxidation exposures. Relative quantification of spectral counts for each protein identified by mass spectrometry in nerve samples photooxidized with methylene blue-NP41 with various light exposures (10 sec, 1 min, or 15 min) versus NL control. Proteins (individual points) identified as consistently enriched by light (x>0.5) and abundant (y>30) are highlighted in the graphs above and listed by number, and are identified by name and x and y values listed in the table below. Proteins showing photooxidation-induced enrichment in multiple samples include laminin subunits, nidogen, and collagen VI subunits.

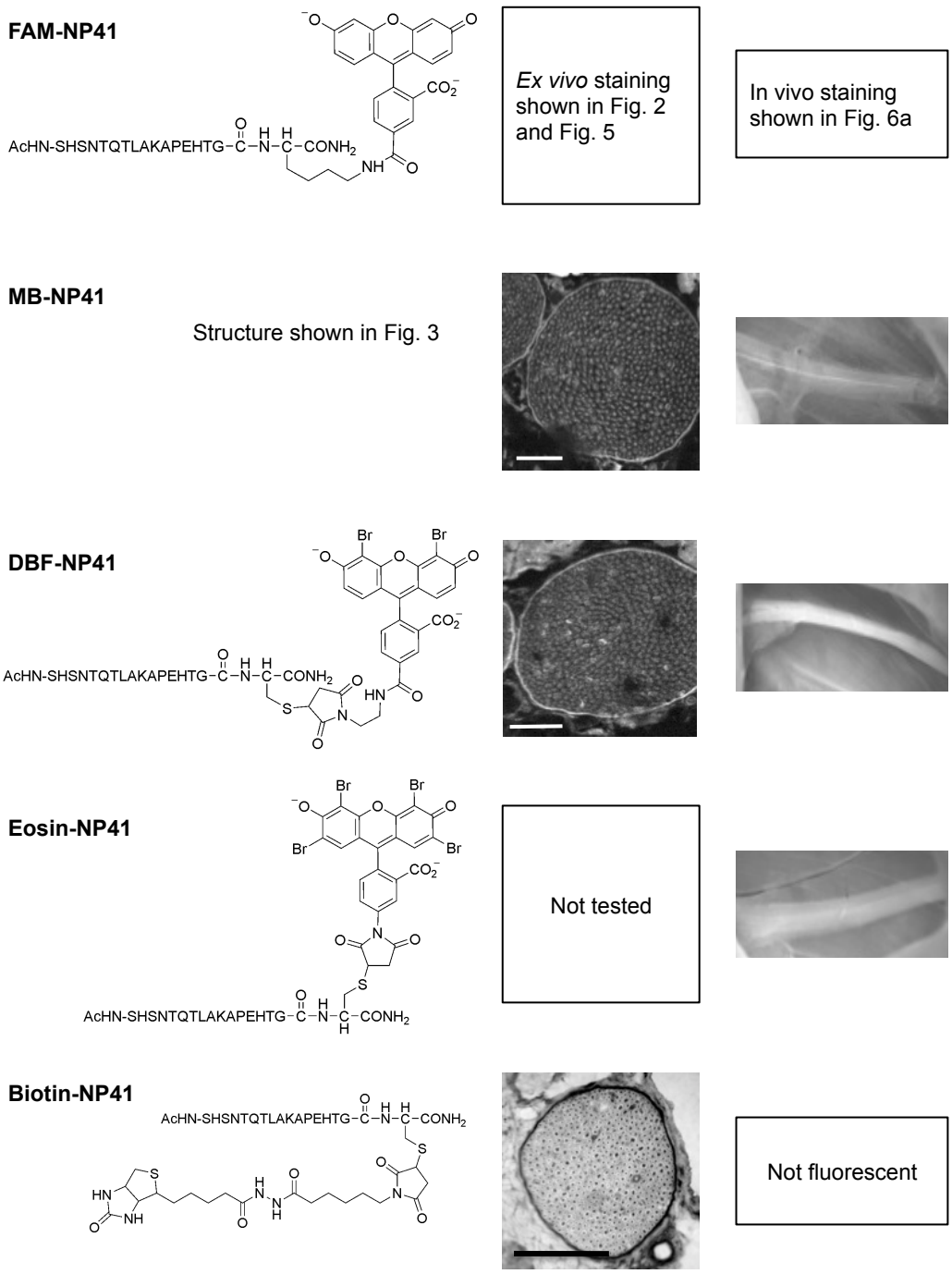

Figure 2S.2. NP41 conjugated to various SOGs and biotin shows consistent perineurial localization, while *in vivo* nerve-to-muscle contrast differs between conjugates. *Column 1:* NP41-conjugates and structures. *Column 2:* Methylene blue-NP41 and dibromofluorescein-NP41 treated on nerve sections and imaged by fluorescence show perineurial staining (highlighted areas). Biotin-NP41 treated on tissue sections and stained by streptavidin-HRP and DAB, shows strong perineurial signal (darkened areas). Scale bar = 500 μm. Gain levels set individually. Scale bar = 50 μm. *Column 3:* NP41-dyes, injected systemically into mice and imaged 2-4 hours post, show different sciatic nerve contrast *in vivo*. Methylene blue-NP41 showed low nerve fluorescence *in vivo* that was difficult to distinguish from the surrounding muscle. DBF-NP41 showed higher nerve fluorescence and contrast to muscle (n=2), and Eosin-NP41 showed distinguishable but low nerve to muscle fluorescence contrast (n=2).

Table 2S.1. ProxPhOx of DBF-NP41-HB in vivo enriches laminin subunits, laminin interacting proteins, and collagen VI over untargeted peptide control.
Direct comparison of spectral counts of a photooxidized DBF-NP41-HB conjugate compared to a photooxidized d-NP41 control conjugate, showing enrichment and total abundance of identified proteins. Laminin subunits and nidogen showed the highest target-specific enrichment with abundant spectral counts. Laminin α5 showed high enrichment but low spectral counts, and collagen subunits showed high spectral counts but low enrichment.

	DBF-NP41-HB photooxidized vs. D-NP41 photooxidized control	
Protein	Enrichment $NP41_{PO}$/($NP41_{PO}$+D-$NP41_{PO}$)	Abundance $NP41_{PO}$ +D-$NP41_{PO}$
laminin subunit alpha-5	1	1
nidogen-2	0.83	23
laminin subunit beta-1 isoform X1	0.83	18
nidogen-1	0.79	103
laminin subunit alpha-2	0.78	64
laminin subunit alpha-4	0.76	17
laminin subunit beta-2	0.73	48
laminin subunit gamma-1	0.69	62
basement membrane-specific heparan sulfate proteoglycan core protein isoform X1	0.67	27
collagen alpha-3(VI)	0.62	198
collagen alpha-1(VI)	0.57	35
collagen alpha-2(VI)	0.52	27

Table 2S.2. Relative quantification of other proteins slightly enriched in DBF-NP41-HB experiment not identified in MB-NP41 as enriched and abundant. Proteins showing moderate enrichment (>0.69) upon photooxidaton of DBF-NP41-HB compared to no light control had low enrichment in comparison to the photooxidized d-amino acid control, except for testis-specific ser/thr kinase and lumican. In the MB-NP41 photooxidation experiment, the former was not identified and the latter was unenriched.

	DBF-NP41-HB *in vivo*				MB-NP41 *ex vivo*	
	PO vs. NL		$NP41_{PO}$ vs. D-$NP41_{PO}$ control		L: PO vs. NL	
	Enrichment PO/(NL+PO)	Abundance NL+PO	Enrichment $NP41_{PO}$/($NP41_{PO}$+D-$NP41_{PO}$)	Abundance $NP41_{PO}$+D-$NP41_{PO}$	Enrichment PO/(NL+PO)	Abundance NL+PO
lumican precursor	0.93	15	0.7	20	0	3
collagen alpha-2(I)	0.82	34	0.62	45	0.73	15
testis-specific serine/ threonine-protein kinase 4 isoform X1	0.76	75	0.83	69	0	0
vimentin	0.72	64	0.66	70	0.56	129
collagen alpha-1(I)	0.69	97	0.66	101	0.54	22

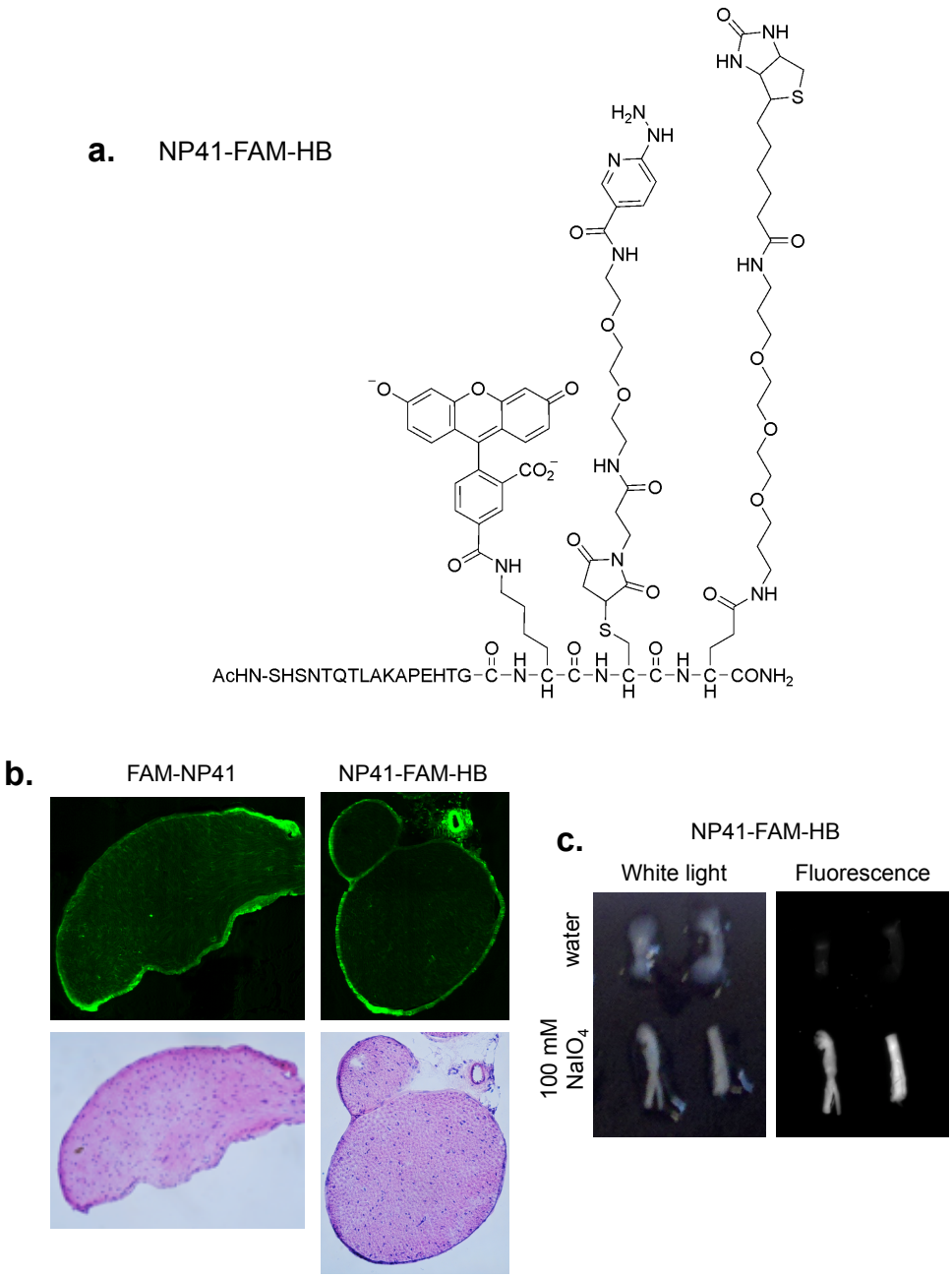

Figure 2S.3. Structure and imaging of FAM-NP41-HB for glycoprotein receptor capture crosslinking. (**a**) Structure of NP41-TRICEPS conjugate. Fluorescein allows for visualization of the peptide, hydrazine crosslinks the peptides to glycans after tissue is oxidized with sodium periodate. Biotin is used to isolate the peptide-target out of nerve homogenates. (**b**) FAM-NP41 and FAM-NP41-HB were injected into mice in parallel and sciatic nerves were dissected, frozen, and imaged to examine peptide localization. *Above*: FAM fluorescence. *Below*: H&E staining. (**c**) Periodate ($NaIO_4$) dependence on nerve cross-linking was tested by incubating sciatic nerves from mice injected with the TRICEPS-NP41 in either 100 mM $NaIO_4$ for 1 hour at 25°C or water and then washing the nerves overnight at 4°C prior to imaging fluorescein fluorescence.

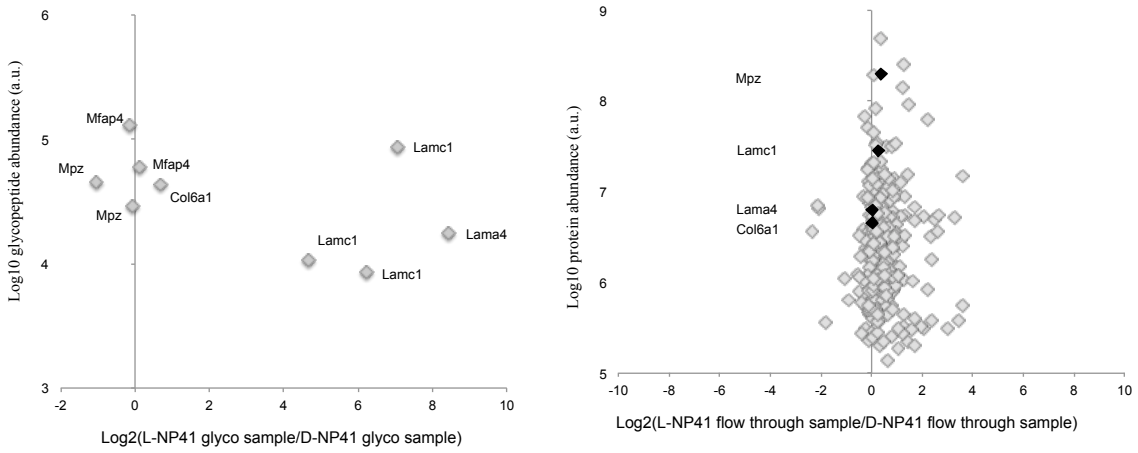

Figure 2S.4. Ligand-based glycoprotein receptor capture coupled to mass spectrometry identifies laminin proteins as NP41 binding partners. (**a**) TRICEPS glycoprotein receptor crosslinking with L-NP41 vs. control D-NP41. Samples shown in **b** were incubated with streptavidin beads for affinity purification of NP41-captured glycopeptides. Beads were washed extensively and N-glycopeptides were eluted through enzymatic cleavage with the endoglycosidase PNGase F. Shown are all identified peptides that contained the N_{115}-X-S/T motif (where 115 is the mass of the deamidated asparagine residue in formerly glycosylated peptides). Proteins identified with captured glycopeptides are highlighted in black in **b**. Glycopeptides specifically enriched in this L-NP41 vs. D-NP41 receptor capture experiment: Laminin γ1 or Lamc1 (TAN_{115}ETSAEAYNLLLR, RIPAIN_{115}R, IASAVQKN_{115}ATSTKADAER), Laminin α4 or Lama4 (HVTDMN_{115}STIHLLR). (**b**) Quantitative comparison of proteins identified in the samples generated by tryptic digest of whole sciatic nerves labeled with all L-amino acids-NP41 and all d-amino acids-NP41 control, respectively. Proteins identified and quantified with two or more independent peptides are shown (N=298). Signal intensities for individual peptides matching the same protein were summed up and unnormalized raw data are shown on the protein level. The ratio of protein abundances between the two samples is plotted against the higher abundance.

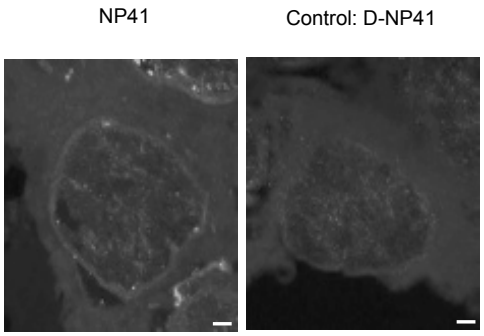

Figure 2S.5. NP41-FAM shows low specific staining in the perineurium of human nerve. NP41 shows low binding to sections of human sural nerve with slightly higher staining in perineurium than a d-amino acid control. Scale bar = 500 μm.

CHAPTER 3: Evolving Nerve-Binding Peptides Improves In Vivo Contrast and Human Nerve Targeting

3.1. Abstract

The use of fluorescent nerve-binding peptides has shown great promise for clinical utility in the reduction of peripheral nerve injury in the clinic; however, published sequence, NP-41 requires further characterization and optimization to increase nerve-to-non-nerve contrast for clinical development. NP-41-derivatized peptide NP-713 was selected by phage display and had 10% higher nerve-to-muscle contrast than NP-41 *in vivo* (2.83 vs. 2.56, $p<0.05$) and also had significantly higher perineurial affinity, with a K_d of 50 μM, compared to NP-41's K_d of 79 μM ($p<0.05$). NP-41 showed low binding to a sympathetic non-myelinated nerve *in vitro*, which correlated with low expression of perineurial binding target laminin-421. Increased endoneurial staining was seen in degenerated fibers, correlating with higher expression of target proteins collagen VI and previous reports of laminin expression. In human nerve cross-sections, NP-713 and a human nerve selected peptide HNP-301 showed higher binding than NP-41 at the perineurium. On sections of mouse and human nerve, NP-124 had the brightest nerve and non-nerve staining, producing comparable nerve-to-muscle contrast as NP-41 *in vivo*. ProxPhOx-mediated target capture of NP-713 and HNP-301 identified similar targets as NP-41 in mouse and human nerve, laminins-421, -211, and collagen VI. These peptides represent strong potential candidates for clinical application.

3.2. Introduction

Phage display technology has been widely used to display peptides, proteins, and antibodies, by genetically encoding sequences in fusion with bacteriophage coat proteins, rendering them solvent accessible. By linking a peptide or protein library to its encoding DNA within a self-replicating system, huge numbers of peptides can be screened simultaneously and over several rounds iteratively by amplifying phage between rounds in order to enrich and easily identify functional peptides that are rare within the original population (Smith and Petrenko 1997). Selection for binding to organs and whole tissues *in vivo* and *in vitro* has become a popular way of discovering new biomarkers (Pasqualini and Ruoslahti 1996).

However, affinity of first generation peptides is low, often with dissociation constants (K_d) around 1-100 μM, and is restricted by the diversity of the library screened (typically 10^7-10^9) due to the limitation of bacterial transformation. In the case of whole tissues, binding to complex target mixtures can result in lower specific affinity. Thus, further optimization toward specific molecules is often necessary for improved affinity. Commonly reported methods include evolution-like procedures by introducing some diversity in first generation-selected sequences and again selecting for target binding, often with more stringent conditions. Typically, techniques such as error-prone PCR are used to expand diversity, but they can create technical challenges in restricting the mutations to the desired locations in an intact plasmid or may create problematic cloning (Thie, Voedisch et al. 2009). As an alternative, one affinity-matured library used specifically mixed nucleotides to create a small proportion of varied amino acids at positions surrounding a binding motif found in the primary-selected sequences and

constrained the linear peptide into a circular one with disulfide-linked cysteines (Fleming, Sachdeva et al. 2005). Using this library and performing stringent selections resulted in a 100-fold improvement in K_d from 1-3 μM to 26 nM to the target protein. In the case of complex targets, molecular target identification and subsequent selections for binding to a single purified molecule may also improve specific affinity. We sought to optimize nerve peptides through similar but unique mechanisms, creating libraries with strategically randomized positions to encode residues with similar properties (polar, nonpolar, etc.).

Second, though *in vivo* nerve imaging experiments produce useful data on the potential of nerve peptides to function systemically, they have some disadvantages. Individual animals have highly variable fluorescent intensities and nerve contrast, making comparisons between different peptides difficult. The age of the animal and type of anesthesia used has also been found to affect nerve contrast (Crisp 2012). Furthermore, experiments are costly and laborious, requiring a large amount of peptide and injection of several animals. Lastly, results may not represent the efficacy of human tissue binding. Thus, animal experimentation is not the ideal method for high-throughput peptide screening and for determining the efficiency of clinical translation. An *ex vivo* screen for binding to thin unfixed sections of peripheral nerve tissue was developed in order to more efficiently screen binding candidates, ascertain the binding affinity, analyze binding to human tissue, and determine peptide binding locations histologically. The results contain clues about the possible molecular targets of nerve peptide that can be used to compliment experiments that identify molecular binding candidates, as demonstrated in the previous chapter. Application of peptides on human tissue demonstrates the translatability of peptides into clinical use.

3.3. Methods

3.3.1. Human nerve phage selection

Two M13 phage libraries with 7 and 12 random amino acid sequences expressed on the N-terminus of the gIII coat protein were used for selections (New England Biolabs). Selections were based on phage binding to freshly resected or frozen human nerves. Negative selections were performed by incubating the phage library with mouse muscle and fat tissue. For positive selection, phage libraries were incubated with whole human nerve, nerves were washed, homogenized, and plated for phage titering and re-amplification on *E. coli* strain ER2738. Amplified phage were purified and concentrated. After each round, sample plaques were chosen for sequence analysis. Once duplicate sequences were found, selection rounds were terminated.

3.3.2. Phage library design and construction

3.3.2.1. Oligo design

Inserts were amplified with forward primer HG85 5'-cgctgcggtacctttctattctcactct and reverse primer HG86 5'-aatgtgccaatgtgatacggccga with each of the following templates separately: for HNP-301-derivatized library: HG87 5'-cgctgcggtacctttctattctcactctngsgnstntcnscnsnccngggnsanggnsnccnacnnknnknnknnktcggcc gtatcacattggcacatt NP-41-derivatized library: HG88 5'-cgctgcggtacctttctattctcactctnacncccnsncccnsncgansncgcnsgnscnsnccnnknnknnknnktcggcc gtatcacattggcacatt in which n represents a, g, c, or t, s is c or g, and k is g or t.

3.3.2.2. High throughput cloning

96-well plates were used to batch amplify library inserts containing the above primers using Super Blue PCR Mix (Life Technologies) and 25 cycles of 92°C, 52°C, 72°C for 30 sec each. Amplified inserts were purified by gel electrophoresis in 2% agarose (mixed 1:1 with low-melt agarose) and extraction using Gel Extraction Kit (Zymo). Insert and M13KE DNA vector (New England Biosciences) were cut with restriction enzymes Acc65I and KpnI, purified, and ligated with Quick DNA Ligase (Life Technologies) at 20°C overnight. Ligated products were purified using 100k-cut off filter columns (Amicon), and electroporated into electrocompetent ER2738 cells in several batches. Cells were briefly recovered at 37°C in Luria Broth (LB), then plated on several large LB solid agar plates in 2.5% agar (top agar) and grown overnight.

3.3.2.3. Amplification and purification of phage

Phage were infected on ER2738 *E. coli*, mixed with molten LB agar at 60° C, and plated on solid LB agar plates. Plates were incubated at 37° C for 8 hours or overnight. To elute phage from top agar, phage buffer was added to cover agar surface and put at 4° C for 8 hr or overnight. Supernatant was removed from plates and heated to greater than 60° C to kill bacteria. Debris and bacteria were removed by centrifugation. Supernatants were transferred to centrifuge tubes containing 100 kD cutoff filters. Tubes were centrifuged and flowthrough discarded. Phage buffer or PBS was applied to the upper chamber over several cycles of centrifugation to purify phage. Concentrated phage were collected from upper chamber, centrifuged at high speed to remove any remaining debris and contaminants. Concentrations of phage were determined by titering for pfu on ER2738.

3.3.3. Phage selection for binding to nerve

To deplete non-specifically binding phage, purified phage libraries were first incubated with slightly smashed pieces of mouse skin and muscle for two hours. The supernatant was removed and added to a piece of mouse nerve and incubated at room temperature for two hours. The nerve was washed in PBS three times or five times at the third round and higher, then homogenized in phage buffer, and used to infect ER2738 bacteria to amplify the total selected phage population. Serial dilutions of the nerve homogenate were also plated with ER2738 to isolate individual phage plaques, which were subsequently sequenced at the pIII insert region. Selections for binding to whole human nerve were performed in parallel.

3.3.4. Assay of phage-peptide binding to whole tissue

Amplified, purified phage in phage buffer were incubated with freshly dissected pieces of mouse muscle or nerve tissue, normalized by weight. After one hour, tissues were washed, homogenized, and plated in serial dilutions with ER2738 *E. coli* in top agar for titering of plaque-forming units (pfu).

3.3.5. Peptide synthesis and fluorophore labeling

Peptides were synthesized on an Agilent Prelude peptide synthesizer by standard fluorenylmethoxycarbonyl (Fmoc) solid-phase synthesis with ε-(fluorescein-5(6)-carbonyl)-L-lysinamide, represented by K(FAM). Sequences include HNP-301: Ac-SHSSEFPRSWDMETN-K(FAM), NP-124: Ac-RLTNAPAYQAPA-K(FAM), and NP-713: Ac-NTHPHTTSRVPSQIARG-K(FAM), d-np-713: same as previous sequence using all d-amino acids.Ac- represents an acetyl. NP-41, NP-38, NP-43, and NP-44 were synthesized as previously described (Whitney, Crisp et al. 2011).

Peptides were purified to >95% purity using C-18 reversed phase high-performance liquid chromatography (HPLC) with a 20–50% acetonitrile gradient in 0.1% trifluoroacetic acid and confirmed by mass spectrometry.

3.3.6. *In vivo* imaging

Wild-type SKH (Charles River Laboratories) or albino C57BL6 (Jackson Laboratory) mice were injected through the tail vein with 150 nmol purified peptide diluted in water or PBS. Following a 2–4 h wash-out period, mice were anesthetized with ketamine and midazolam (80 mg/kg intraperitoneally), a skin incision was made over the dorsal surface of the hind legs and the sciatic nerves exposed bilaterally. Nerves were imaged using a Zeiss Lumar fluorescent dissecting microscope with 450–490 nm excitation and 500–550 nm emission.

3.3.7. Histology assays

3.3.7.1. Assay of peptide binding to tissue sections

Deidentified human sural nerve (removed post-mortem) was purchased from Cambridge Biosource and deidentified human recurrent laryngeal nerve (removed intraoperatively) and donated with patient consent. Dissected tissues (mouse and rat) or frozen nerve (human) were flash frozen in Optimal Cutting Temperature (OCT) on dry ice and methylbutane. 10 μm sections were cut on a cryostat (Leica) and dried on a glass slide. Peptides diluted in 0.5x HBSS (or water where noted) were treated on sections for 20-30 minutes and washed in PBS for at least 5 minutes, then coverslipped in PBS and imaged with a confocal microscope (Nikon) with 488 nm excitation, 520 nm emission.

3.3.7.2. Measurement of binding affinity of nerve peptides

The average fluorescence of the perineurium was measured using ImageJ software (National Institues of Health) to calculate the mean fluorescent intensity from 10 random 100-pixel^2 areas where perineurium was discerned, and these values were averaged. Three serial sections were analyzed for each peptide concentration, the average and standard deviation was used to plot a binding curve, fitted for nonlinear regression using least squares using Prism software (GraphPad).

3.3.7.3. Immunofluorescence

10 μm sections were fixed with 4% paraformaldehyde in PBS for 10 minutes, then rinsed in PBS, blocked with 10% normal goat serum (Life Technologies) for 1 hour, and incubated with antibody diluted in 5% normal goat serum for at least 1 hour, washed in PBS, then incubated with AlexaFluor488-labeled anti-rabbit secondary antibody (Life Technologies) for at least 30 minutes, washed, and coverslipped. Antibody to collagen VIα3, laminin α4 and laminin γ1 were purchased from Santa Cruz Biotech. Anti-laminin α5 was a kind gift from J. Miner. Slides were imaged on with a confocal microscope (Nikon) with 488 nm excitation, 520 nm emission.

3.4. Results

3.4.1. Selection of human nerve binding peptides using phage

The early part of this work was previously described but is repeated in part here to lay the groundwork for later results (Crisp 2012). In order to find human nerve-binding sequences, several rounds of phage display selection were performed by Dr. Michael Whitney and Rachel Levin using a random 7 or 12-amino acid library expressed on the N-terminus of the pIII protein of M13 filamentous phage. In brief, phage were treated on

small pieces of peripheral human nerve, which had been resected from surgeries and stored frozen. Negative selections for binding to mouse muscle and fat were performed prior to and alternating with positive selections. Three sequences were found enriched after the fifth round of selection, and selections were continued until a seventh round. *In vitro* assays showed preferential binding toward human nerve over mouse muscle or fat tissue (data not shown). Human nerve peptides (HNP)-301 (SHS-SEFPRSWDMETN), -303 (SHS-STMKTLSLG) , and -305 (SHSTMKTLSLG) were synthesized with an N-terminal SHS- added to the selected peptide sequence to enhance solubility and was conjugated to fluorescein. When injected into mice and imaged, HNP-301 showed the highest nerve-to-muscle contrast of the three peptides *in vivo* and was roughly equivalent to NP-41 (Crisp 2012). However, the peptide showed poor solubility in buffered solutions, and the same sequence was enriched in a published phage display selection for peptide binding to *M. bovis* antigens, showed positive binding to whole mycobacteria, and thus lacked exclusive specificity for nerve (Sun, Sun et al. 2009).

3.4.2. Evolution of nerve binding peptides using derivatized phage libraries

In order to increase the affinity and selectivity of the nerve peptides and optimize binding for human tissue, derivatized peptide libraries based on NP-41 and HNP-301 were created, introducing some diversity with semi-randomized amino acids and extending the binding site with random amino acids. To generate semi-randomized amino acids, one of more of the original nucleotide positions in each codon was replaced with a mixture of random nucleotides, either all four, encoded by N, or a mixture of two, C and

G, (called S), resulting in three or four other possible amino acids with somewhat similar characteristics (i.e. charge, nonpolar, etc.), plus the original (Figure 3.1). An extra four codons were added in order to potentially expand the binding site, using completely random amino acids encoded by the NNK codon, where K represents G and T, and is typically used in the third position in order to equalize the likelihood of encoding amino acids that have two or four different codons. The potential diversity encoded in these sequences was 6-8×10^7 unique peptides.

HNP-301:

SPTA **E**VADG **F**SYC **P**LHQR **R**LPHQ **S**PTA **W**RGCS **D**VAEG **M**TKR **E**VADG **T**SPA **N**YHQD X X X X

Codons:

NGS GNS TNT CNS CNS NCC NGG GNS ANG GNS NCC NAC NNK NNK NNK NNK

NP-41:

NYHQD **T**SPA **Q**LPHR **T**SPA **L**PHQR **A**SPT **K**MTR **A**SPT **P**LHQR **E**VADG **H**YQND **T**SPA X X X X

Codons:

NAC NCC CNS NCC CNS NCG ANS NCG CNS GNS CNS NCC NNK NNK NNK NNK

Figure 3.1. Design of Nerve Peptide Derivatized Phage Libraries. HNP-301 (shown above) and NP-41 (shown below) degenerate peptide libraries. Possible amino acids (single letter codes) for each position are shown in which the amino acid of the original sequence from which the library was derivatized is highlighted in bold and the other possible amino acid options are shown in parentheses. Nucleotide sequence encoding the library is shown (single letter code), in which N=A,G,C, or T; S=C or G; K=G or T. The calculated theoretical diversity of all possible peptide sequences is shown for each library, as well as the number of transformants actually obtained for each library after high-throughput cloning.

In order to generate a library that theoretically encodes a diversity of peptides at least as high as the possible number of unique peptide sequences (though multiplicity

dictates that it is extremely unlikely to encode every possible unique sequence), high-throughput cloning was performed via several large-batch PCR reactions, cloning into the M13KE wildtype phage vector, and large-scale electroporations into phage-competent *E. coli*, libraries were generated consisting of greater than 10^8 individual transformants.

Phage expressing HNP-301 and NP-41 derivative libraries were screened for binding to mouse and to human nerve in parallel. Negative selections were performed prior to each positive selection round to reduce non-specifically binding phage. First, phage libraries were incubated with pieces of mouse muscle and skin for two hours. Supernatant was then transferred to a piece of human or mouse nerve, mouse plasma was added, and the combination was incubated for one hour at room temperature. The nerve piece was removed and washed three times in phage buffer or five times, at the third round of selection and higher. Nerve was homogenized and used to infect *E. coli* to amplify the binding phage. In order to sample the diversity of the population after each round of selection a small aliquot of the nerve homogenate was serially diluted to isolate individual phage plaques and small sampling was sequenced. In selections for mouse nerve binding, three peptide sequences were found enriched in the phage population NTHPHTTSRVPSQIAR (NP-713), YTLPPANTQAHAMQGA, and GGF(W/Q)LAGVRGSHITQV (Figure 3.2). In a simultaneous selection for binding to human nerve, NP-713 was found once at round 4; however, only non-recombinant phage were found in subsequent rounds of selection (Figure 3.3) Other peptides containing a similar motif TTXXV(P) as NP-713 were identified at round 7 of the mouse nerve selection and round 4 of the human nerve selection.

Figure 3.2. Sequencing of phage selected with NP-41 and HNP-301-derivatized peptide libraries for binding to mouse nerve identifies enriched sequences. Phage expressing NP-41 or HNP-301 derivatives were negatively selected for binding to muscle and fat and positively selected for binding to excised mouse nerve. Peptides are listed by the round of selection in which they were identified. Subheadings “41” and “301” correspond to the derivatized peptide phage library from which they were identified. Peptides found in duplicate are highlighted in bold text. Asterisks represent the amber stop codon, which in the amber suppressor strain are translated into glutamine. X represents unknown amino acid due to poor sequencing data. q represents Q encoded by amber codon expressed in amber suppressor strain.

Round 1

301

GECHRTGVMGPHTVCR
GACRHAGGMVSHSqSV

41

DAPARATPQDLSLFSK
NTQFHANAPEPPMLGR
DARALTMSRELSLWVG

Round 2

41

DALPLPITPELTGKTM
DSHPLSKAPVHPERAG
HTLAPSRSPVQAqRTV
DTHARTKPRAQAPSMR
DAQALPKPHDRAGLTN
DARAPATSRDRPVGTW
HAHARSNAQGLPMTAG

301

SASHLAGVKAANGPAR
GDSLRAGVKESHQSWS
GGFRPAGDRGPDTAGG

Round 3

41

HAHSQATSQALARGAG
SYTLSHPMSHELSMPLR
SYSLSLSTAPERPFMGV
HARPHATAHVQSATqS
HSPSPANTRDRAMWSL
SYSPSHASSQGLAqGGP
DPPALSMSQELPRAVV

301

GAFHPTGERDPDSPVP
FFSPQARGTDTHAGSF
WDFPLTRGKVSYGqGV
SSFSQHPREMGTDMRRV
SVSPLSGDTVAYqRGV
SWDFPPAREKDPH*GFG

Round 4

41

DARALPTAHARAPMqT
DAHTPPISHGRSGVDK
DAPPRTTTRGPTGSEW
DPRSHPRPLERPVSSA
NSHAHAKPQARSVLLS
NSLAHPMTQVRTKLMA
YAQSLTTTRDRSILGH
YTHSLARSPERPKWWL
YTHTLSTSRDRTFqGQ
HALAQAKALGLSWqEG
HAHSLTKSPVP
HSLSLSLSTSQVRAWqGG

301

YEFHRAGEMAANHVLP
SGFRPAGGMEADRGGI
RDYPPPWVMGTNLKMG
WGSQRAGGTGAHSADS
WGSPQPWVMEANPTGQ
WESPLSEVKGSYHPNW
WEFPRSGGMGSNMGSW
GDFHLSGGRGSDFGRR
GGFLHAGAKCTNVqAV
GGSLPSWDTGTHqTGR
GGFQLAGVRGSHITqV
GVSQPTRDMVTDTGqI

Round 5

41

HPRSPATSLVHTqVQV
DSRAHASTPVLTRqNV
HSQTHSKTPVPSTWQR
HALPHPKARAP
DTHAHSSSRDQPHSWR
NAPSPPKSHVQAGRAG
DALAQSIAHGLPHRHF
DTLARTKARVQAWPqK
SYRALPKARAPALA
NTHPHTTSRVPSQIAR

301

GESQPARVKGPYEqAG
GAYPHSRETAPDNRqV
GASPPAGGKESDILLM
WEFPLPRGTASYTTqS
GVSLRAGDTGTHqRNV

Round 6

41

Y**TH**A**HT**NTPA**PS**RSGL
YSHSLSSSLGHPRGAV
YAHPQPRPQGLSTSGR
YTQPQATAPARSVPWM
HTLSHTITRGQSL
HSHTLTRPPGLAQTGL
HAQTQSSSQAHTPNXX
HAHARSTPHGHPPGXXXX
NALPRSNTLERAHKXG

301

WGFPLSGVRGPDLRQE
GEFPQSRGTGAYQXXX
GEFPPARGT
GDSRQSWARGPNIASG

Round 7

41

YTLPPANTQAHAMQGA
DSRTPTKAHGQSLLMA
HTQAQ**TT**PH**V**RAGGRV
XALAQAKALGLSWQEG
NTHPHTTSRVPSQIAR

301

NTHPHTTSRVPSQIAR
GGFWLAGVRGSHITQV
GESHQAREKDSHRRQA
GDFPHARVKGTDGITR
REFQPAWEMVAHQVSR
GVYPQPRDKAAHQDFG
WESPAWGKDADNSNS

Round 8

41

HSPSQAMALGPPRPQM
YPRSLASTPVRSSMQV
YTLPPANTQAHAMQGA
SDCQLTRATGANQRAC

301

GGFLQSRGMETNLRDL
GEYQRAWDKGTYRSML
GAHQLTRDKGPNQGHE
GGSPPTRGMVAYHQGV
GDYLRAGGMGSYREQV
SEYLPARVTGAHRYQS

Round 1
G G S P Q A W G R G A N A L V V
W G S P H A W V T E S H A G C I
D P R S L S M T P G Q T I E S G
Round 2
H T P A L T K T R G L A qG R V
Y A L P Q P K S L V R T **q** G H L
S D F Q P S R D R G S H T L W R
Round 3
G G F H Q S W V T G P Y A R T G
D T L S R P T S P D R S P H R V
N S L A H S K T P G L P R G
Round 4
H T R A P T M A Q A L T L G E R
G G Y H H S G G T G A D M R R A
D P L P R A I T R A L S V Y S A
G A F P Q A G A T G S N G F R G
S G F P P S G G M D S D F R G T
H S P A L P **T T** Q **V P** T L E R A
D S R S P S N P R G L A V E A V
D P L T H P I S R G R P G A T T
Round 5
D A L P Q S K P R G L P K V G V
G E Y L H S G D R A A H V D L L
N S L P Q T M T P A R T L D P S
N T H P H T T S R V P S q I A R
G G F L Q A R G M V A Y G A R I

Figure 3.3. Sequencing of phage selected with NP-41 and HNP-301-derivatized peptide libraries for binding to human nerve identifies a peptide also enriched in mouse nerve selection. Using mixed NP-41- and HNP-301- derivatized peptide phage libraries, phage were negatively selected for binding to muscle and fat and positively selected for binding to human nerve. Peptides are listed by the selection round in which they were identified. A peptide also identified in mouse selection is highlighted in bold text. q represents Q encoded by the amber stop codon, expressed in an amber-suppressor strain.

In order to test the binding specificity of the candidate peptides, an *ex vivo* assay for phage binding to mouse nerve or muscle tissue was performed in which phage expressing NTHPHTTSRVPSQIAR, YTLPPANTQAHAMQGA, and GGFWLAGVRGSHITQV were incubated with freshly excised muscle or nerve tissue, normalized by weight. Tissues were then washed three times with PBS and tissue-bound

phage were quantified from homogenates by titering plaque-forming units. Only phage encoding NP-713 showed 3.9-fold higher binding to nerve compared to muscle, while two other enriched phage showed nonspecifically high binding to both nerve and muscle (Figure 3.4 A). Compared to a non-recombinant phage, NP-713 phage showed 4.8-fold greater nerve selectivity.

To examine its *in vivo* binding selectivity and to compare it to the previously selected peptide NP-41, NP-713 was made synthetically attached to carboxyfluorescein (FAM), and purified. FAM-NP-41 or FAM-NP-713 were injected into mice (n=3 per peptide) and sciatic nerves were surgically exposed and imaged (488 nm excitation, 520 nm emission). One mouse injected with NP-713 did not recover from anesthesia, showed very high fluorescence in all tissues, and was excluded from analysis. NP-713 labeling resulted in high nerve labeling (Figure 3.4 B), and produced an average nerve-to-muscle contrast of 2.83, which was 10% higher than the average NP-41 fluorescence (Student's *t*-test p=0.042) (Figure 3.4 C).

A.

Phage titers			Ratio	
	Nerve	Muscle	Nerve/ Muscle	WT-normalized ratio
NTHHTTSRVPSQIR (NP-713)	1128	288	3.91	4.8
wildtype	108	132	0.81	1
YTLPPANTQAHAMQGA	3264	2784	1.17	1.4
GGFWLAGVRGSHITQV	976	1488	0.65	0.8

B.

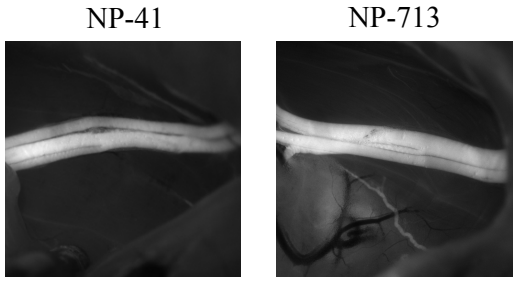

C.

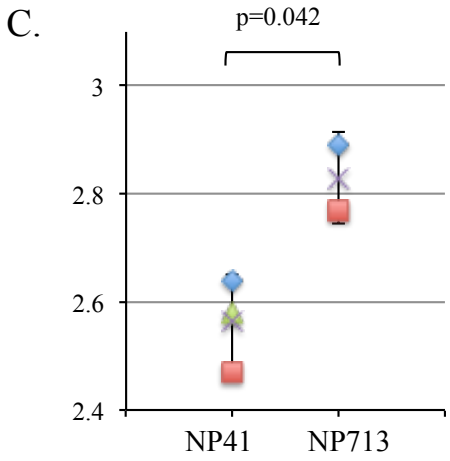

Figure 3.4. NP-713 identified by phage display shows nerve-specific binding and higher contrast than NP-41 in vivo. A. Phage binding assay to nerve and muscle tissue shows NP-713 binds specifically to nerve. Other sequences found more than once in phage selection showed higher binding to both nerve and muscle, suggesting non-specific enrichment. All showed higher binding that wildtype phage. **B.** The sequence of NP-713 was synthesized labeled with carboxyfluorescein. Peptides were injected into mice intravenously (150 nmol), and the sciatic nerve was exposed and imaged two hours post injection. Two representative images are shown. **C.** Average nerve to muscle fluorescence ratios for NP-41 labeled nerves (n=6) and NP-713 (n=4) shows slight but significantly higher contrast in NP-713 labeled nerves. p value<0.05, Student's *t*-test.

3.4.3. *Ex vivo* binding assay in histological sections shows selectivity and localization of various nerve peptides

In order to analyze the histological localization of nerve-selected peptides and screen in higher throughput fashion, a topical binding assay was developed using tissue sections. FAM-labeled nerve peptides were diluted to 0.375 mM in 0.5x HBSS and treated on unfixed section of frozen mouse facial nerve embedded in surrounding fascia and muscle for 20 minutes. After washing with PBS, slides were imaged by fluorescence microscopy (488nm excitation/520nm emission). NP-41 produced striking contrast, with high signal at the perineurium of the nerve, as well as some nearby blood vessels, endoneurial capillaries, and intersegmental areas of the muscle (Figure 3.5 A). NP-713 showed similar localization as NP-41 in the nerve, with higher perineurial signal and possibly lower blood vessel and muscle staining. HNP-301 showed more homogenous staining in nerve, but higher and more homogenous staining in muscle than NP-41. However, HNP-301 showed poor solubility in the buffer conditions used, therefore, staining patterns here may not be representative of true binding sites. NP-124 was previously selected by Dr. Michael Whitney for binding both to whole nerve and to myelin basic protein. When treated on tissue sections, NP-124 showed perineurial localization consistent with NP-41 and NP-713, but also showed high, homogenous staining in the endoneurium and surrounding muscle.

In order to compare peptide labeling on tissue sections with *in vivo* labeling, mice were injected with FAM-labeled peptides. In mice treated *in vivo* with NP-41 and NP-

713, staining was evident in some blood vessels but clearly absent in others (Figure 3.5 B), in agreement with the blood vessel staining seen in tissue sections.

HNP-301 *in vivo* treated nerves trended toward higher absolute fluorescence intensity than NP-41, but also higher muscle staining, producing an overall contrast that was not statistically different from NP-41 (Figure 3.5 C). NP-124 produced strikingly bright nerve fluorescence that was statistically higher than NP-41; however, the intensity of muscle staining was also higher, and again, the overall nerve-to-muscle contrast did not differ from NP-41 (Figure 3.5 D). These findings agreed with staining patterns seen in tissue sections.

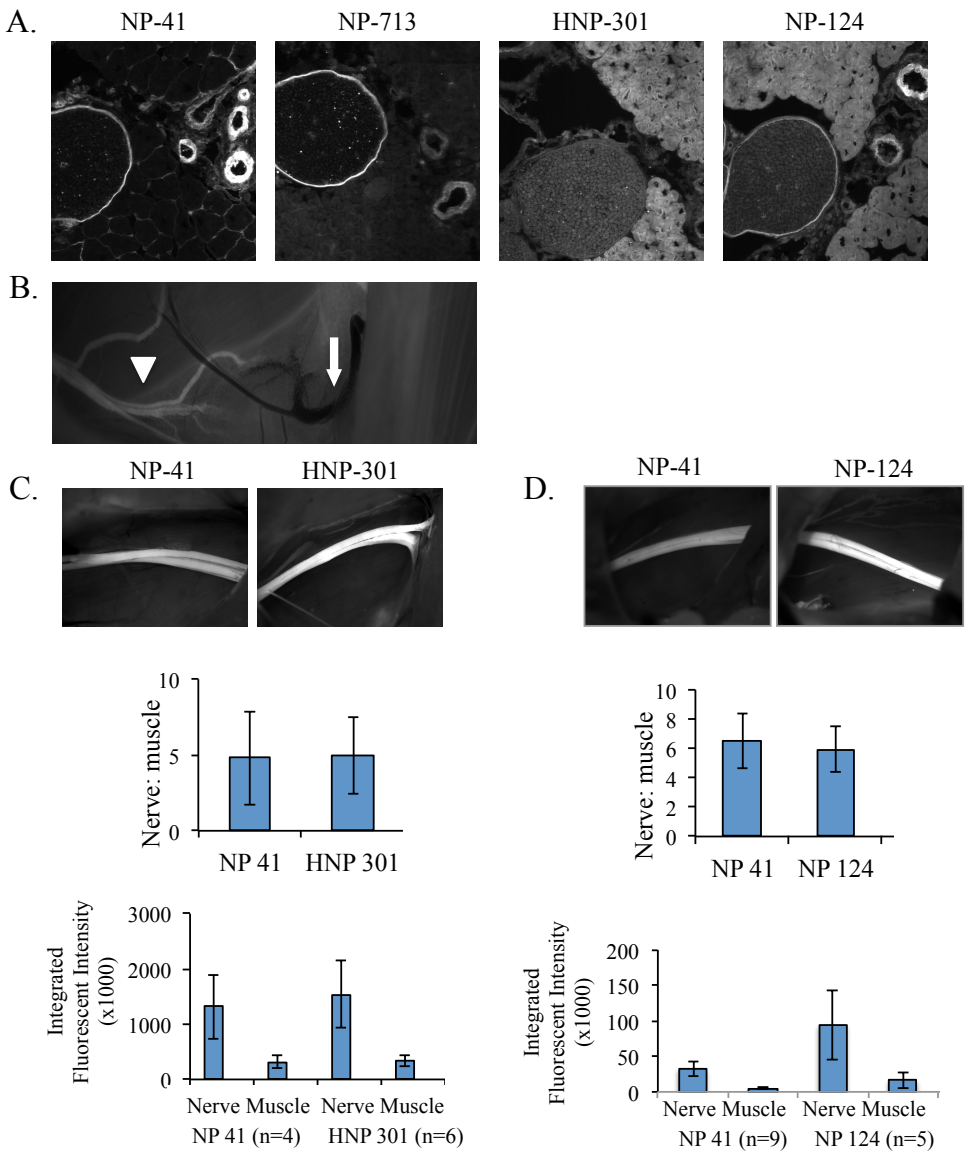

Figure 3.5. Nerve peptides have distinct localizations in nerve and muscle labeling in tissue sections that recapitulate in vivo staining. A. Nerve peptides applied to mouse facial nerve and surrounding tissue at 0.375 mM in 0.5x HBSS. NP-41, NP-713, and NP-124 show perineurial and blood vessel labeling. NP-124 and HNP-301 (which had low solubility) show high endoneurial staining and muscle labeling. **B.** Some blood vessels but not others labeled *in vivo* with NP-41 and -713. **C.** HNP-301 labeling *in vivo* shows slightly higher nerve and background fluorescence with overall contrast comparable to NP-41. *Top:* images of exposed sciatic nerves and surrounding muscle and skin 2-4 hr after intravenous injection of NP-41 or HNP-301. *Upper graph:* quantified average nerve-to-muscle contrast of individual sciatic nerves. *Lower graph:* average absolute integrated fluorescence intensity of individual sciatic nerves and surrounding muscle. Error bars represent standard deviation. **D.** NP-124 labeling *in vivo* shows high nerve fluorescence and high background with overall contrast comparable to NP-41. *Top:* images of exposed sciatic nerves and surrounding muscle and skin 2-4 hr after intravenous injection of NP-41 or NP-124. *Upper graph:* average nerve-to-muscle contrast of individual sciatic nerves. *Lower graph:* absolute integrated fluorescence intensity of individual sciatic nerves and surrounding muscle. Error bars

3.4.4. Determination of NP-41 and NP-713 binding affinity to nerve

Because NP-713 showed the strongest nerve to background staining in the topical assay and had higher *in vivo* staining than NP-41, the binding affinities of NP-41 and NP-713 toward nerve were investigated. Dilutions of each peptide were made between 0.4 mM and 40 nM in 0.5x HBSS in serial sections, and the average fluorescence of the perineurium was measured. NP-713 began to show signal above background at 400 nM, while NP-41 began to show signal at 1.56 μM (Figure 3.6). At 1.56 μM, NP-713 showed 3.6-fold higher fluorescence than NP-41. Binding curves generated from nonlinear regression analysis showed that NP-713 had a K_d of 50 μM and that NP-41 had a K_d of 79 μM.

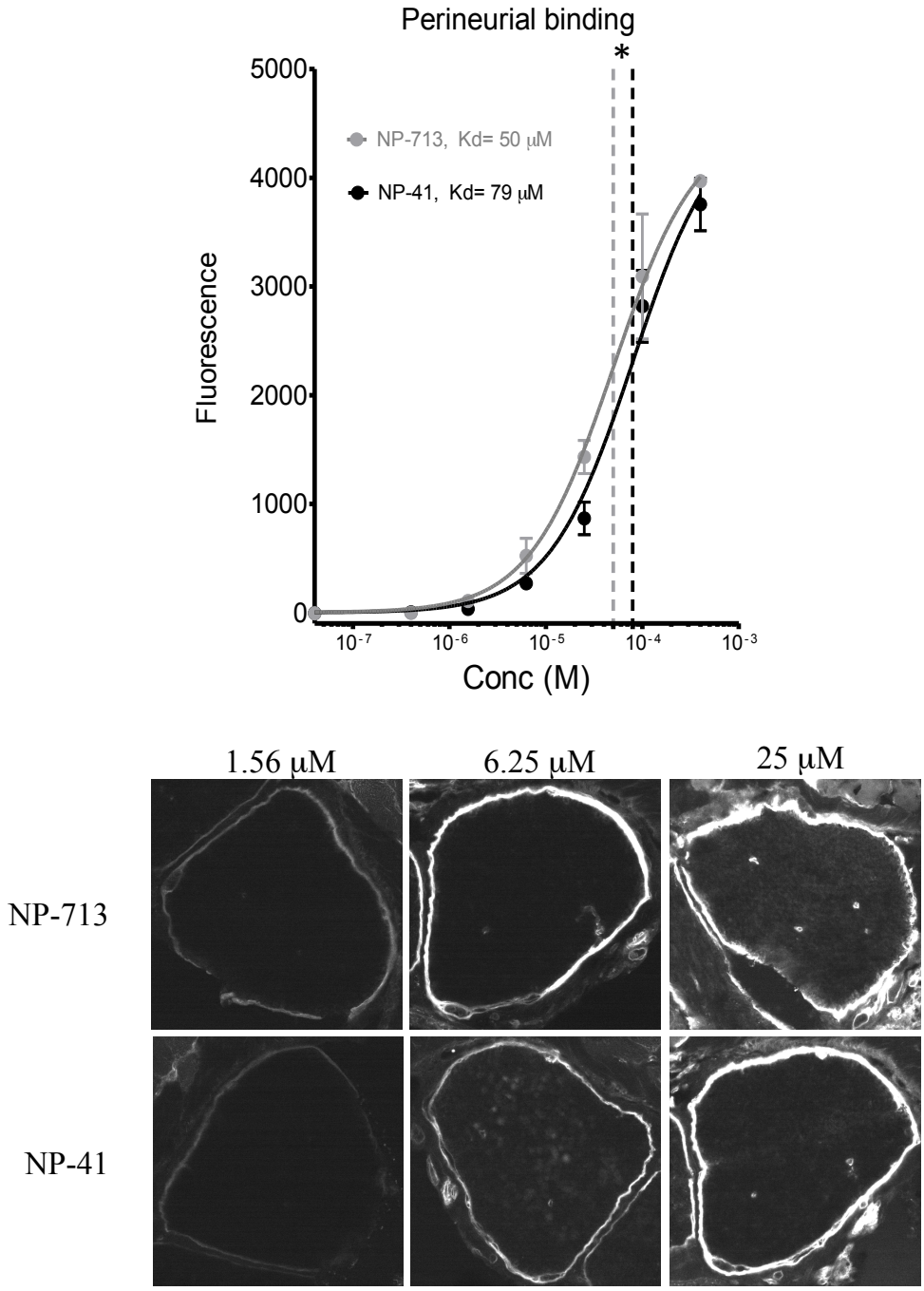

Figure 3.6. NP-713 has a 1.6-fold higher binding affinity to perineurium than NP-41. *Above:* Nonlinear regression curve fitted to average perineurial fluorescence at various peptide concentrations (Hill slope=1). NP-41 equation: y=4610*X/(0.00007939+X), NP-713 equation: y=4508*X/(0.00004992+X), R^2 >98% for both NP-41 and NP-713. *P=0.0152 that the K_d of NP-41 and NP-713, Extra sum of squares F-test. 10 μm sections of mouse facial nerve were covered with FAM-labeled peptide at 0.4 mM to 40 nM in 0.5x HBSS for 25 minutes. Slides were washed and coverslipped in PBS and imaged by confocal microscopy. Average perineurial fluorescence was calculated for each image (n=3) and background subtracted from a no peptide control. Images set to the same gain. *Below:* Representative images of perineurial fluorescence for a range of peptide concentrations showing increasing perineurial fluorescence with increasing concentrations of NP-41.

3.4.5. Application of NP-41 to other nerve types and surgical models

The preservation of prostate nerve during prostatectomies is one example of an important potential application of fluorescent nerve peptides. Because the nerve is especially small and buried, it is difficult to identify intraoperatively and frequently injured, leading to erectile dysfunction, incontinence, and other complications. In order to study the potential use of NP-41 in nerve sparing during prostatectomy surgeries, imaging was performed on male mice treated systemically with NP-41. Fluorescence contrast in the prostate nerve of mice was unreliable (data not shown). It was not clear whether these results were due to lower affinity of NP-41 to a different nerve type, as prostate nerve is an non-myelinated sympathetic nerve, the small size of the nerve producing low absolute fluorescence, or the lack of myelin and white appearance reducing the reflection of light. In order to discern if NP-41 did have affinity toward non-myelinated nerve, binding to tissue sections was performed.

The mouse prostate nerve is technically challenging to section when frozen due to the surrounding adipose, which easily disrupts tissue integrity and structure when cut. Therefore, to examine binding of NP-41 to another similarly non-myelinated nerve that is more easily handled, a sympathetic nerve from the trunk was dissected, frozen, sectioned, and FAM-labeled NP-41 or all d-amino acid NP-41 (d-np-41) were topically applied to slides, as before. NP-41 showed poor labeling of the sympathetic nerve, equal to that of the control peptide d-np-41, with no apparent perineurial staining (Figure 3.7 A).

The low affinity of NP-41 for non-myelinated nerve may be due to a thin perineurium, low expression of NP-41's binding targets, or different post-translational modification in myelinated versus non-myelinated nerve types. In order to ascertain the expression of likely binding partners and the existence of perineurium in non-myelinated nerve, immunostaining to subunits γ1, α5, and α4 was performed. Laminin-γ1 and α5 showed expression at the perineurial layer, while α4 showed no staining above the no antibody control (Figure 3.7 B). This suggests that laminin-421 may be absent in the perineurium of non-myelinated nerves and further supports evidence in Chapter 2 that laminin-421 is the dominant NP-41 binding target. Due to NP-41's affinity for other nerve proteins, such as laminin-211 and collagen VI, which may be expressed in non-myelinated nerves, some contrast may still be evident.

NP-41 staining was shown to also bind to degenerated nerves, supporting laminins and collagen as likely targets. In some tissue samples, nerve branches containing both a nerve bundle that was healthy and one that was degenerated, were observed side-by-side, as evident by light pink myelin staining in the endoneurium when sections were stained by hematoxylin & eosin (H&E). In these samples, NP-41 showed higher endoneurial labeling in the degenerated than the healthy branch. Because previous publications support an increased expression level of collagens and laminins during nerve regeneration, immunostaining of collagen VI was examined in these samples (Wallquist, Patarroyo et al. 2002, Hill 2009, Chen, Cescon et al. 2014). An antibody to collagen VIα3 showed higher immunostaining, as suspected, in the endoneurium of the degenerated nerve than the healthy nerve (Figure 3.7 C). This demonstrated that collagen

VI was upregulated, especially in the endoneurium, and lended further support to the likelihood that NP-41 does have affinity for this target.

Rats, being much larger animals than mice, make easier surgical models, especially because the nerves are much larger. In order to test the ability of NP-41 to bind rat nerves, NP-41 or all d-amino acid NP-41 control peptide, labeled with carboxyfluorescein or biotin, were topically applied to sections of rat facial nerve embedded in surrounding tissue. The latter was stained with streptavidin-horseradish peroxidase (HRP) and diaminobenzidine (DAB) precipitation. NP-41 showed sparse staining of the perineurium, slightly higher than the control peptide, though it maintained prominent blood vessel staining (Figure 3.8). This data suggests that NP-41 may not bind rat nerve as efficiently as mouse.

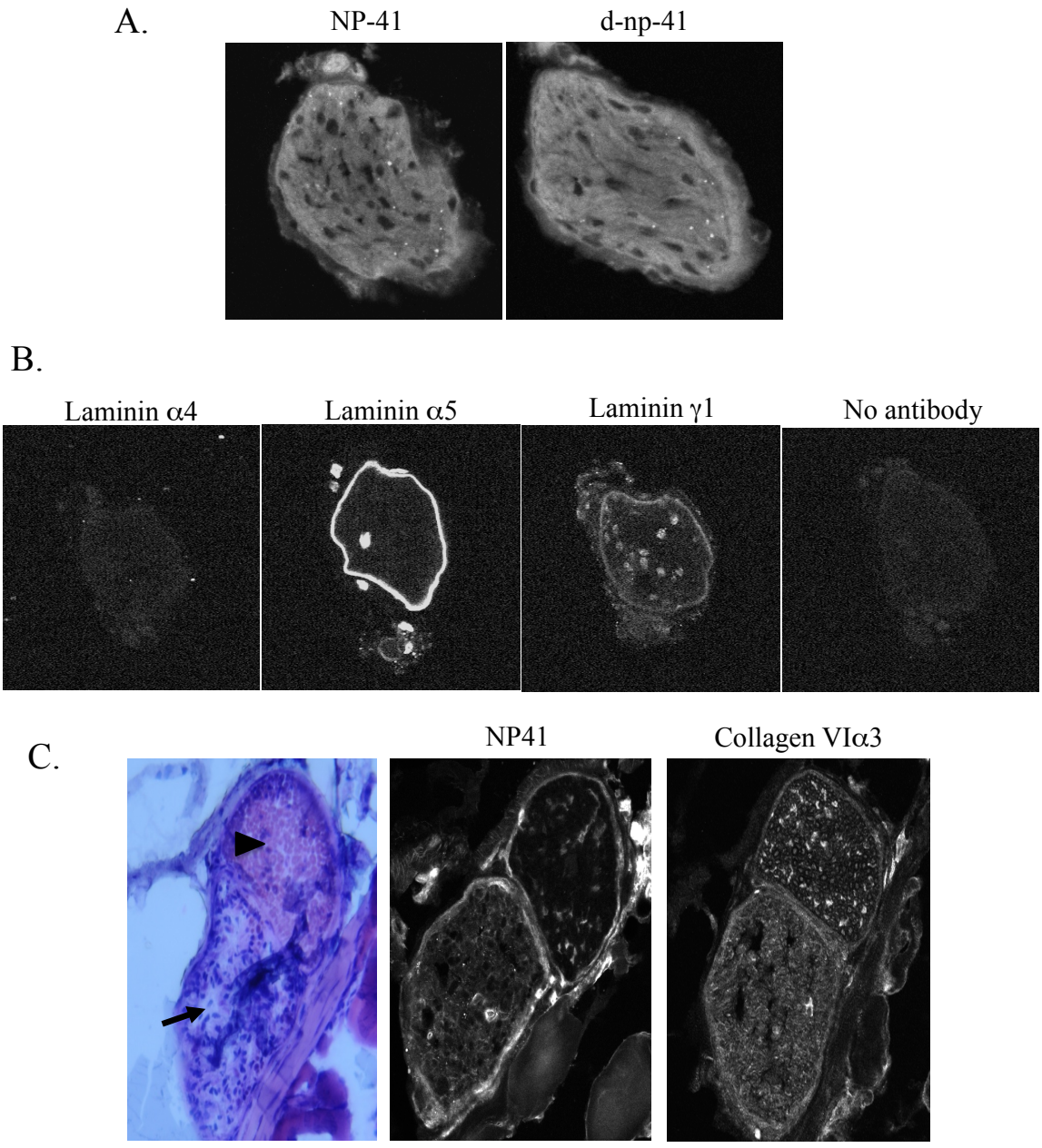

Figure 3.7. NP-41 shows low staining of non-myelinated nerves and increased endoneurial staining of degenerated nerves, which correlates with decreased and increases expression of candidate binding targets laminin-421 and collagen VI. A. NP-41 or all d-amino acid control was treated on unfixed frozen sections of non-myelinated autonomic mouse nerve from the trunk at 0.375 μM in 0.5x HBSS for 20-30 min. **B.** Immunostaining of non-myelinated nerve sections from the same tissue sample.shows absence of laminin α4 staining, and the presence of α5 and γ1 in the perineurium. **C.** H&E staining of side-by-side healthy (above) and degenerated (below) nerve branches, as evident by the presence of light pink endoneurial staining of myelin (arrowhead) in healthy nerve and the lack of myelin and high infiltrarion of dark blue-staining cells in the endoneurium (arrow). Nearby tissue sections stained with NP-41-FAM (middle) or an antibody to collagenVIα3 and a fluorescent secondary show higher endoneurial staining in the degenerated branch.

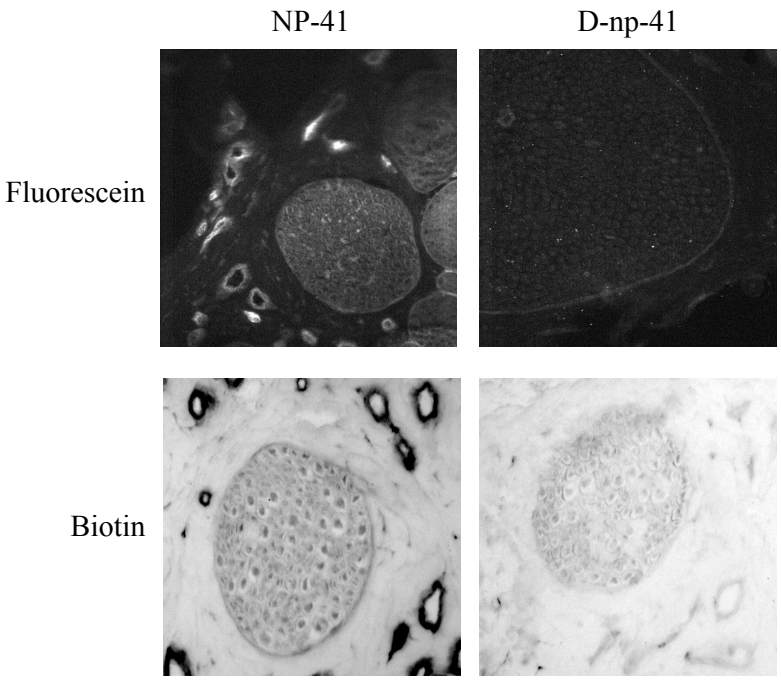

Figure 3.8. NP-41 shows low staining of rat facial nerves but retains high contrast in blood vessels. *Above:* NP-41-FAM and the all d-amino acid peptide control were treated on unfixed sections of rat facial nerve and imaged by confocal microscopy, as before. *Below:* NP-41-biotin or the all d-amino acid peptide control were treated on rat facial nerve sections, incubated with streptravidin-HRP conjugate, then treated with DAB and imaged for precipitation (darkened areas) by standard microscopy.

3.4.6. Binding target identification of NP-713 and HNP-301 using ProxPhOx

Because NP-713 showed perineurial staining in nerve cross-sections (Figure 3.5, Figure 3.6) and because NP-41, NP-713, and HN-301 peptides were selected in a similar fashion, for binding to whole nerve, we hypothesized that such peptides may bind the same targets as NP-41. In order to examine their potential binding partners, the ProxPhOx method detailed in Chapter 2 was applied. HNP-301 and NP-713 were labeled with dibromofluorescein (DBF) and applied to mouse nerve *ex vivo* at 50 μM in PBS. Nerves were rinsed in PBS, illuminated with 488 nm light or not illuminated as a control, and reacted with 50 μM biotin hydrazide in MES buffer, pH 5.5. Nerve homogenates were ground and incubated with streptavidin beads. After washing, strong acid treatment

and urea were used to release the proteins and hydrolyze the biotin-hydrazone bond. Proteins were trypsinized and filter purified. Peptides were analyzed by liquid chromotagraphy-tandem mass spectrometry (LC-MS/MS) and identified from a mouse protein database. Identified proteins were quantified as sums of the spectral counts of their peptides and photooxidized samples were compared to the non-illuminated control samples. These data demonstrated photooxidation-dependent enrichment of collagen VI, laminin-211, and laminin-421 subunits by both HNP-301 and NP-713 (Figure 3.9). Spectral count abundance in the HNP-301 sample was lower, and laminin subunits β-1 and α4 were not identified. This data supported the hypothesis that peptides selected in a similar manner are likely to bind to similar targets.

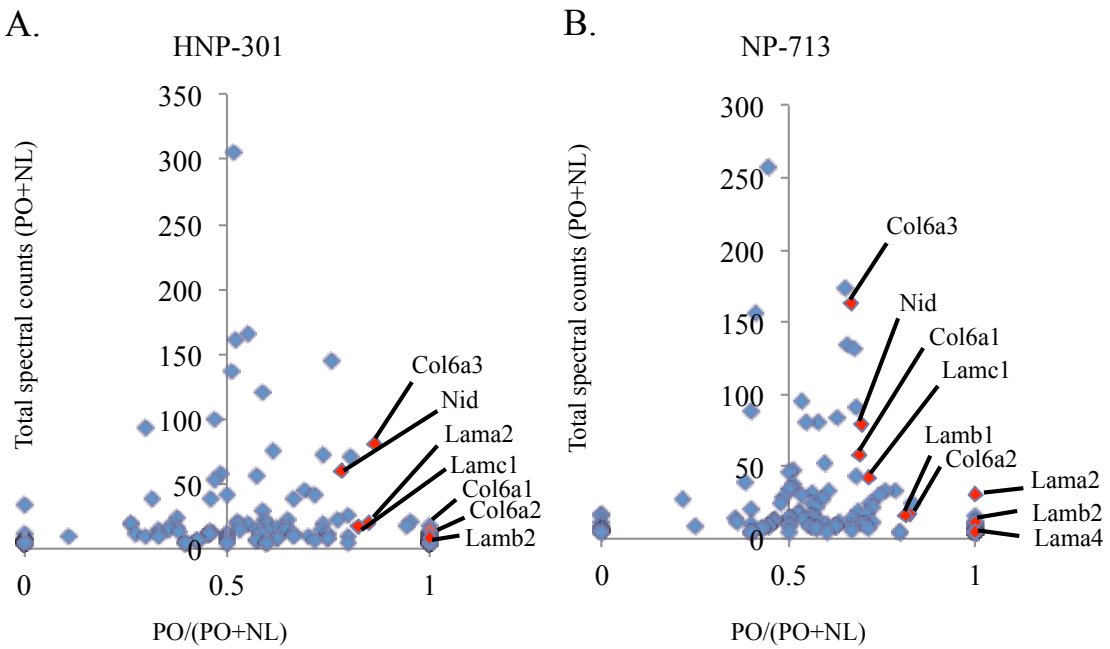

	HNP-301		NP-713	
Protein Name	**PO/ (PO+NL)**	**PO+NL**	**PO/ (PO+NL)**	**PO+NL**
collagen alpha-3(VI) chain isoform 2	0.86	81	0.668	163
nidogen-1	0.78	60	0.696	79
laminin subunit alpha-2	0.85	20	1	31
laminin subunit gamma-1	0.82	17	0.714	42
laminin subunit beta-1			0.812	16
collagen alpha-1(VI) chain	1	15	0.689	58
collagen alpha-2(VI) chain	1	12	0.823	17
laminin subunit beta-2	1	8	1	11
laminin subunit alpha-4			1	3

Figure 3.9. ProxPhOx of HNP-301 and NP-713 enriches laminins -211, -421 and collagen VI. A. DBF-NP-301 and **B.** NP-713 were photooxidized (PO) or not treated with light (NL) as a control. X-axis indicates fraction of phtotooxidation-induced enrichment. Vertical axis crossing at x=0.5 represents equal abundance of spectral counts in the PO and NL samples. Y-axis indicates total spectral count abundance. Abundant, enriched samples are highlighted in red and identified in graphs above, and x and y-values are listed with protein name in the table below.

In order to verify target-specific binding, ELISA was performed in which plates were coated with purified human recombinant laminins-421, -521, and -211, collagen VI, and BSA. Phage expressing NP-713 or a random 12 amino acid library (X12), normalized by titer, were incubated on coated plates, washed, and binding was detected

by incubation with streptavidin-HRP and colorimetric substrate. This assay demonstrated selective binding of NP-713 to laminins-211, laminin-421, and collagen VI above a control and lower or no specific binding to perineurial laminin-521 (Figure 3.10 A)

In order to investigate other potential non-nerve binding sites of the nerve peptides due to their laminin targeting, and because many laminin chains are expressed in the basement membrane of kidney, NP-41 and NP-713 were treated on mouse kidney sections (Virtanen, Laitinen et al. 1995). Consistent with published immunostaining of various laminin subunits, the peptides showed strong labeling of basement membranes throughout the kidney (Figure 3.10 B).

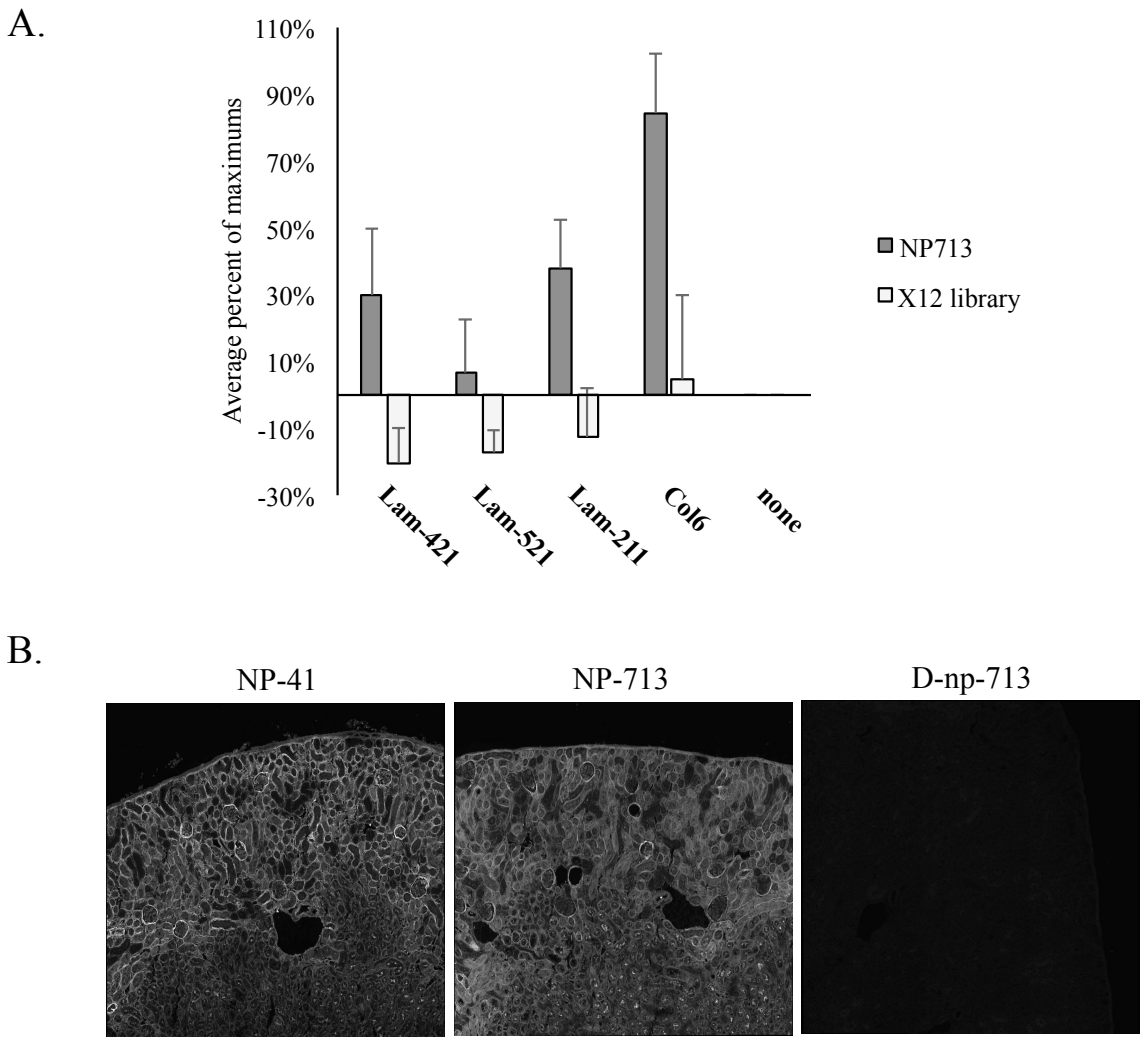

Figure 3.10. NP-713 specifically binds purified laminins-421, -211, and collagen VI. A. ELISA for binding of phage expressing NP-713 or control random peptides (X12 library) to plates coated with recombinant human isoforms of laminins-421, -521, and -211 and collagen VI. **B.** NP-41-FAM and NP-713-FAM peptides were treated on mouse kidney sections and imaged by confocal microscopy.

3.4.7. Application of nerve peptides to human nerves

In order to test how nerve peptides might perform in human patients, peptide binding was assayed on frozen human nerve specimens, both surgical and cadaveric. FAM-labeled NP-41, NP-713, HNP-301, NP-124, and all-d-amino-acid peptide control of NP-41 and NP-713 were treated on frozen unfixed sections of sural and recurrent laryngeal nerve at 0.375 mM in 0.5x HBSS for at least 20 minutes. NP-41 showed low

levels of perineurial staining, slightly higher than the control d-np-41 peptide (Figure 3.11 A and B). Blood vessels showed higher staining than nerve in all non-control treated samples. NP-124 consistently showed the highest overall staining, but was highly fluorescent in all three nerve areas of epineurium, perineurium, and endoneurium. HNP-301 and NP-713 both demonstrated high signal with perineurial specificity, greater than the control peptide d-np-713. Both the surgical sample of recurrent laryngeal nerve and cadaveric sample of sural nerve showed similar staining trends among the six peptides tested.

In order to further investigate the potential of other nerve peptides that were enriched in phage display selections, topical nerve staining was performed with three other FAM-labeled peptides and compared on mouse and human nerve samples. NP-38 (AHHNSWKAKHHS) was identified in a previous phage display selection for binding to mouse nerves *in vivo*, NP-43 (STARDLWPHGKE) is a control scrambled peptide using, and NP-44 (SVSVGMKPSPRP) was highly enriched across several nerve selections. None, however, generated significant nerve contrast *in vivo* (Whitney, Crisp et al. 2011) All FAM-peptides showed poor solubility in buffer and thus were treated on mouse and human nerve sections at 100 μM in water for at least 20 minutes. All showed non-nerve specific staining on both mouse and human nerve (Figure 3.12). This data further supports the use of the assay as a surrogate test of *in vivo* staining.

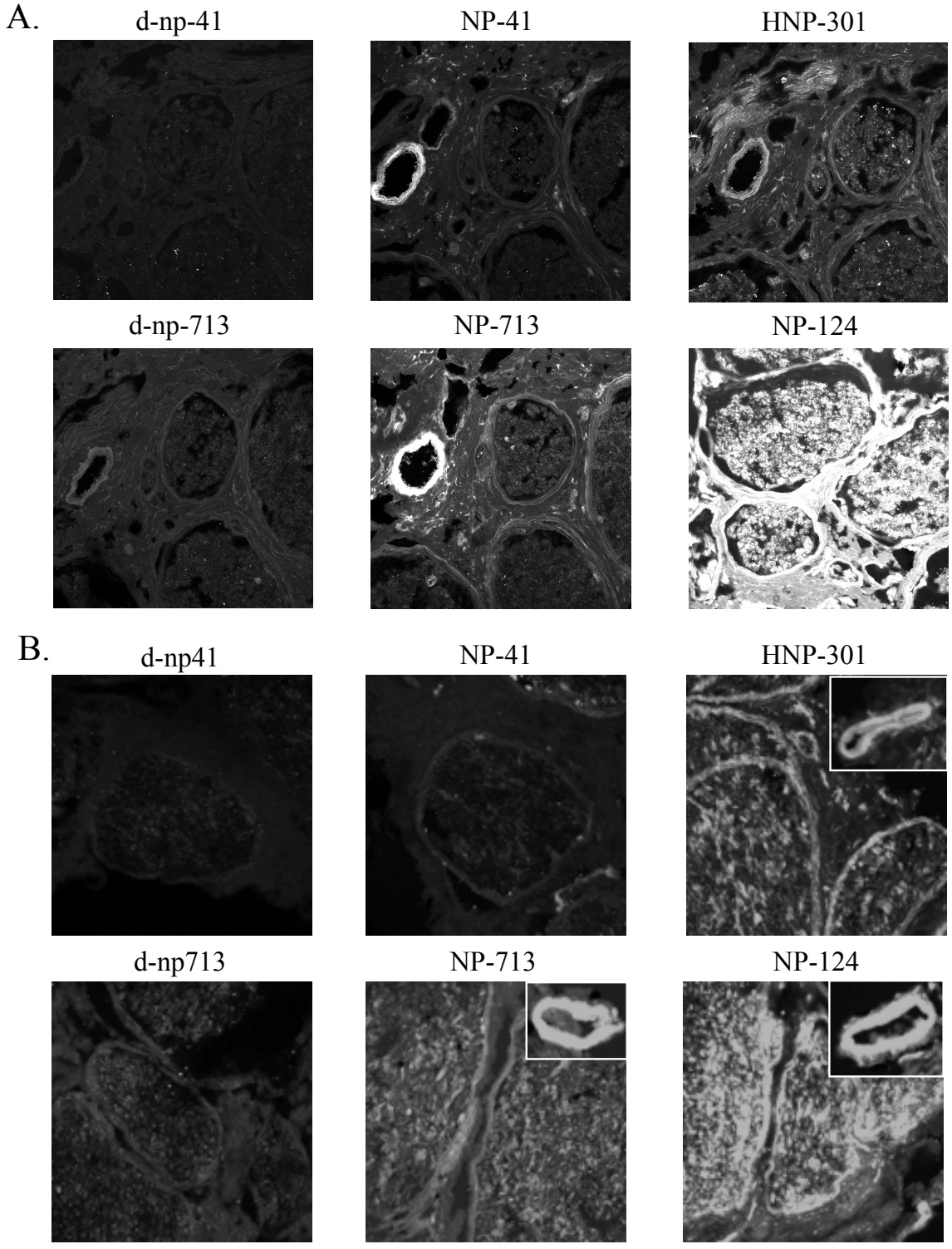

Figure 3.11. Nerve peptides show variable staining in human nerve sections, consistent across two nerve types. A. Human recurrent laryngeal nerve, surgical specimen. **B.** Human sural nerve, postmortem. Unfixed sections treated topically with carboxyfluorescein-labeled nerve peptides (0.375 mM for 20-30 minutes in 0.5x HBSS)

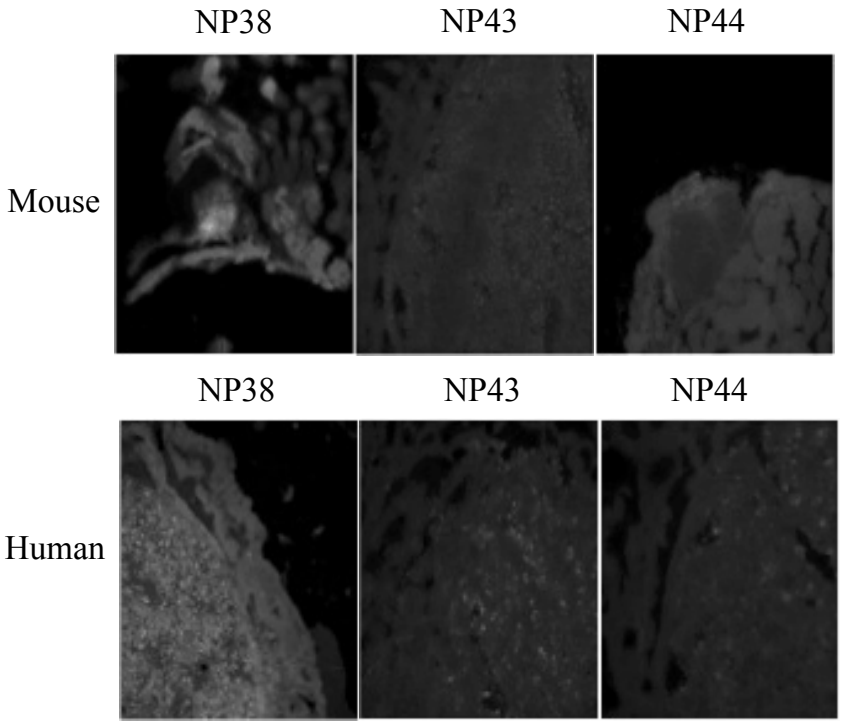

Figure 3.12. Other nerve peptides with poor *in vivo* contrast in mice show no nerve-specific staining in mouse and human nerve sections. Nerve peptides were treated on mouse facial nerve (above) or surgically-resected human recurrent laryngeal nerve (below) at 100 μM in water for at least 20 minutes.

In order to verify whether the same targets were expressed and bound by nerve peptide in human nerve as mouse nerve, ProxPhOx was performed, as before, using NP-713-DBF applied to human nerve. Nerve was photooxidized or not exposed to light as a control, reacted with biotin hydrazide, and processed for streptavidin enrichment and mass spectrometry identification as previously described in Chapter 2. Laminins α2, β2, and γ1 and collagen VI α1, 2, and 3 all showed light-induced enrichment (Figure 3.13 A). Spectral counts were relatively low in comparison to previous experiments, and laminin α4 did not show photooxidation-induced enrichment as in previous mouse nerve experiments (Figure 3.13 B). Immunostaining of human nerve samples confirmed the perineurial staining of laminin γ1, which at high magnification, could be seen likely

outlining perineurial fibroblasts, and correlated with the staining of NP-713 (Figure 3.13 C).

A.

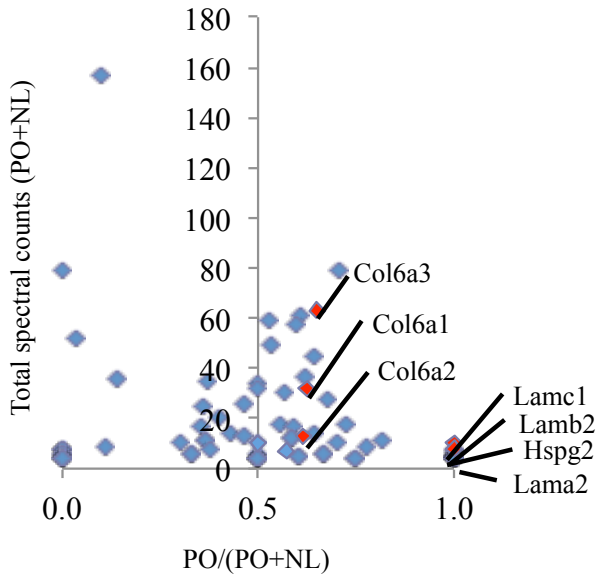

B.

	Human	
Protein Name	**PO/(PO+NL)**	**PO+NL**
collagen alpha-3(VI) chain	0.651	63
collagen alpha-1(VI) chain	0.625	32
collagen alpha-2(VI) chain	0.615	13
laminin subunit gamma-1	1	10
laminin subunit beta-2	1	8
basement membrane-specific heparin sulfate proteoglycan core protein	1	8
laminin subunit alpha-2	1	5
laminin subunit alpha-4	0	2

C.

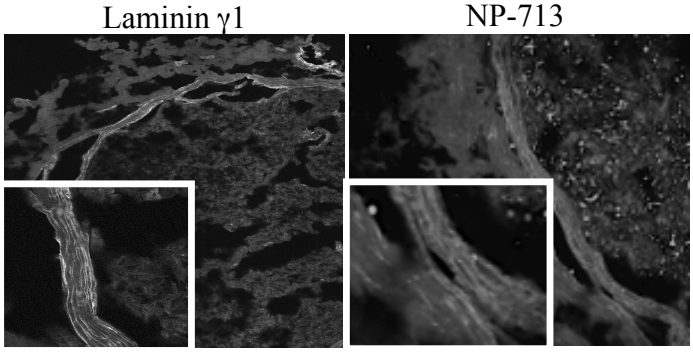

Figure 3.13. ProxPhOx of DBF-NP-713 on human nerve shows light-induced enrichment of laminins and collagens. A. Graph of spectral counts, showing fraction of enrichment (PO/PO+NL, PO=spectral counts in photooxidized sample, NL=spectral counts in no light sample) on x-axis and total spectral counts (PO+NL) on y-axis. **B.** Table of values plotted in graph above for proteins of interest. Calculated fraction of enrichment (PO/PO+NL) and total spectral counts (PO+NL). **C.** Surgical sample of human nerve, fixed and stained with anti-laminin γ1 antibody (left). Surgical sample of recurrent laryngeal nerve unfixed and topically applied NP-713 (0.375 mM in 0.5x HBSS) *Box insets*: high magnification image of outlined perineurial cells.

3.5. Discussion

To optimize HNP-301 and NP-41 by affinity maturation, derivatized peptide-phage libraries were created and selected for binding to both mouse and human nerve, resulting in the selection of an improved sequence, NP-713, with 10% higher *in vivo* nerve contrast and a 58% higher K_d of 50 μM. Like NP-41, NP-713 targets the perineurium via binding to laminins-421, -211, and collagen VI.

Histological staining reveals hints about the possible binding partners by showing peptide localization in greater detail and enables co-localization studies with immunofluorescence of binding candidates, an great asset for molecules screened in a functional, target-blind way. Importantly, this assay also allows for assessment of binding to human tissue, essential information for developing peptides for future clinical use. NP-713 and HNP-301 showed higher staining than NP-41 in human nerve samples, while NP-124 showed the brightest overall staining, which is likely to produce high non-nerve staining in human nerve as well, based on its staining in mouse muscle tissue both *ex vivo* and *in vivo*.

NP-41's low staining of an non-myelinated autonomic nerve from the trunk correlated with low expression of laminin α4 in the perineurium, while positive staining for laminin α5 and γ1 subunits was present, suggesting laminin-521 may be a desirable target for labeling both nerve types. However, further confirmation of these laminin expression and nerve peptide binding studies and a more global analysis of several other non-myelinated nerves will be first needed to support these preliminary findings.

These data indicate that peptide binding targets differ somewhat between species, and the optimization of nerve peptides specifically for binding to human tissue will likely

be necessary for clinical application. Interestingly, strong blood vessel staining was high across species for peptides NP-41, -713, -124, and -301, even when nerve staining was low. This suggests that blood vessels have especially high expression of the binding target.

Perineurial staining of several nerve peptides and ProxPhOx identification of laminins-421, -211, and collagen VI as potential binding targets of HNP-301 and NP-713 in addition to NP-41 suggest that selection for binding to whole nerve likely leads to peptide binding of the same target(s), and that the binding target may be differ somewhat in mice and human nerves.

Future possible improvements to screening peptides for nerve binding include utilizing the topical assay of binding to tissue sections to directly examine phage-peptide binding, thus obviating the time-consuming necessity of synthesizing and purifying many peptides, and enabling faster and higher throughput screening of large sets of molecules, or even potentially as a method for phage display selections of specific tissue binding (Arap, Kolonin et al. 2002).

Muscle is typically a major source background fluorescence that results in overall lower nerve contrast in spite of high nerve fluorescence signal. However, some muscle fluorescence may be masked due to the shorter wavelength of fluorescein which penetrates thicker tissues such as muscle poorly. Furthermore, the red coloring of muscle likely contributes to some fluorescence quenching from fluorescein, while the naturally whiter color of nerve better reflects light, enhancing this effect. Supporting this hypothesis, NP-41 targeting with farther red fluorescent dyes, the light from which is capable of deeper tissue penetration and has lower level of autofluorescence, showed

lower levels of contrast (Crisp 2012). Future attempts to improve the pepetide will involve reducing binding to off-target tissues such as muscle so that farther red fluorophores may be used in order to better visualize nerves that are more deeply buried.

3.6. Acknowledgements

The dissertation author would like to thank:

Dr. Mike Whitney for training in phage display selection techniques and for collaboration and help with peptide purification. Qing Xiong, and Cintia Vazquez for synthesis and labeling of peptides. Rachel Levin for phage display selection of the HNP300-series of peptides. Dr. Jessica Crisp for performing animal experiments. Dr. Beth Friedman for training me in animal dissection techniques and histological sectioning and for assistance in the development of the histological section assay. Dr. Quyen Nguyen for providing human nerve samples. Dr. Timon Hussain and Melina Mastrodimos for making degenerated nerve animals.

CHAPTER 4: Characterization and Development of Enzyme-Selective ACPPs

4.1. Abstract

Activatable cell-penetrating peptides (ACPPs) are promising molecular-targeted agents that detect proteolytic activity and attach to nearby tissue. An ACPP designed for activation by cancer-associated matrix metalloproteinases (MMPs) -2 and -9 with the sequence E_9-PLGmeCAG-R_9 has been shown to mediate delivery of drugs and dyes in tumor models. Here, we have characterized, in detail, the enzyme selectivity and kinetics of its cleavage on a full panel of MMPs and other enzymes. PLGmeCAG showed broad cleavability by many MMPs but was most sensitive to MMP-2, MMP-13, and MMP-20 activity at 20 nM, followed by MT1-MMP and MMP-9 among others. Two substrates designed to be selective for MMP-2 (SLAYYTA) or MT1-MMP (RPAHLRDSG) were not highly MMP-selective, and another substrate selected by phage display for tumor cleavage (RLQLKL), did not show complete cleavage by any MMP tested. In order to increase the specific localization of the ACPP, and reduce off-target activation, selections for novel substrates with high selectivity for a single metastasis-associate enzyme, were performed; however no new sequences have been generated. Future work will continue to pursue this goal.

4.2. Introduction

The progression of cancer to metastatic disease, in which vital organs are overtaken by cancer cells, is the main cause of death in cancer patients. Currently used therapeutics do not effectively combat metastases. Abraxane and Doxil, for example, are two clinically approved nanoparticles used to treat different types of cancer. Both are molecularly untargeted and rely on the phenomenon of enhanced permeability and retention (EPR). These nanoparticles are not likely to work efficiently, however, in small tumors less than 100 mm^3 in size or microscopic clusters of cancer cells at metastatic sites, where EPR does not occur (Adiseshaiah, Hall et al. 2010). Thus, for new nanoparticle therapies and diagnostics to be effective at these sites, active targeting that is specific to diseased single cells within a large healthy population and internalizing into the cell are crucial.

Much of the current research on molecularly targeted cancer therapeutics and imaging modalities uses animal models of primary tumors. In the clinic, however, primary tumors are often effectively treated with surgical resection when diagnosed in early stages of progression. Patient death is more typically the result of distant metastases, which often occur in large numbers, dispersed throughout critical organs or other inoperable locations. As a result, much research based on treating primary tumors fails to accurately predict true outcomes of therapeutics in patients (Francia, Cruz-Munoz et al. 2011). Though improving detection and treatment of the primary tumor will likely prevent some metastasis, patients whose cancers have already spread are not likely to benefit. For instance, metastatic disease is present in over 80% of lung cancer patients at the time of diagnosis (2011, Schroeder, Heller et al. 2012) Some data suggests that

metastasis may occur in the early stages of cancer. Thus, even with the advent of earlier diagnosis and treatment, metastatic disease may remain problematic (Husemann, Geigl et al. 2008).

In order to target agents specifically to invasive cancerous cells, our lab has developed a peptide-based probe for the detection of cancer-associated proteases, termed activatable cell-penetrating peptides (ACPPs) (Jiang, Olson et al. 2004). Cell penetrating peptides (CPPs) are a class of short membrane-adherent and cell-internalizing sequences rich in positively charged residues, originally found in domains of Antennapedia and HIV Tat protein, and also includes oligoarginine, the most efficient known CPP (Derossi, Joliot et al. 1994, Fawell, Seery et al. 1994, Wender, Mitchell et al. 2000). In order to target the CPP to specific cells, ACPPs consist of a polycationic Arg_9 (r9) CPP linked by a protease substrate to a negatively charged Glu_9 (e9) masking domain (Figure 4.1). Upon protease cleavage of the substrate, the e9 domain is released, and r9 is unmasked for cell-internalization and delivery of imaging agents or therapeutic payloads (Jiang, Olson et al. 2004).

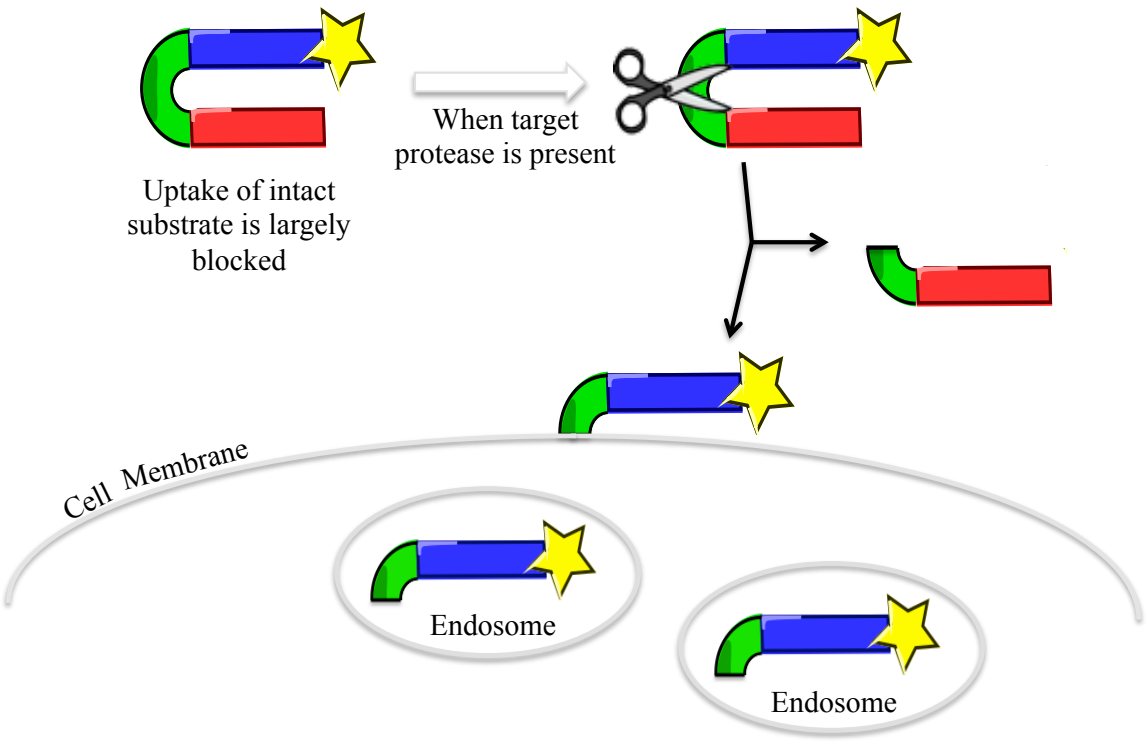

Figure 4.1. Schematic of activatable cell-penetrating peptides (ACPPs). A cargo (yellow star) is targeted by a cell-penetrating peptide r_9 (blue bar) is linked to masking domain e_9 (red bar) via a cleavable substrate (green connector). Upon cleavage of the substrate by a targeted protease, the masking domain is released from the CPP-cargo, which adheres to and is taken up by proximal cells.

A great deal of research has shown that many proteases, including matrix metalloproteases, serine proteases, and cysteine proteases, are highly upregulated during the progression of cancer to invasive and metastatic stages (Lee, Fridman et al. 2004). Degradation of the extracellular matrix permits extravasation of cancer cells to the lymph or circulatory system and intravasation at new sites. It also may allow for neoangiogenesis and release growth factors, promoting cancer growth (Deryugina and Quigley 2006).

Matrix metalloproteases (MMPs) are a family of extracellular proteases that function in a variety of normal biological processes and are additionally involved in multiple pathogenic processes, including cancer (Egeblad and Werb 2002, Fingleton

2006). MMPs are able to degrade many types of extracellular matrix (ECM) proteins, and their activity is naturally regulated through many mechanisms, including at the protein level by tissue inhibitors of metalloproteinases (TIMPs) (Visse and Nagase 2003). Studies have shown MMPs to have both pro- and anti-tumorigenic effects. Retrospective analyses have shown increased expression of MMP-1, -2, -3, -7, -9, -13, -14 in primary tumors or secondary metastases are positively correlated with worsened disease and poor outcomes (Deryugina and Quigley 2006, Hauff, Raju et al. 2014). While pro-tumorigenic effects of many MMPs have been widely supported by *in vitro* studies, reduced expression of some MMPs, such as MMP-8 and MMP-3 have been associated with worse outcomes in human cancer and an increase in tumorigenic or metastatic effects in animal studies (Agarwal, Goodison et al. 2003, Balbin, Fueyo et al. 2003, McCawley, Crawford et al. 2004). Failure of MMP inhibitors in clinical trials for the treatment of cancers suggest a complex role of MMPs in cancer, requiring more detailed study. Because of their complex regulation at many levels and poorly understood roles, understanding the activity of specific MMPs in normal and pathological tissues beyond simple expression studies is necessary. Thus, imaging probes with selective response to the activity of specific MMPs will likely reveal greater biological insight into these enzyme's functions and potentially enable new diagnostic or therapeutic platforms for cancer.

Membrane type 1 metalloprotease (MT1-MMP), also known as MMP-14, is a transmembrane enzyme whose expression correlates with negative outcomes in several cancers (Maatta, Soini et al. 2000, Uchibori, Nishida et al. 2006, Hauff, Raju et al. 2014, Li, Cai et al. 2015). By degrading fibrillar collagens and other proteins in the ECM, active enzyme enables tumor growth, tissue remodeling, metastasis, and angiogenesis.

MT1-MMP activity is present at the leading edge of the cell at membrane protrusions known as llamelopodia in normal cells and invadopodia in cancer cells (Artym, Zhang et al. 2006). MT1-MMP represents great potential for targeted delivery of imaging agents and therapeutics because of its known involvement in metastasis (Itoh and Seiki 2006). MT-MMPs are especially suitable for ACPP targeting as they are bound to the surface of their cells of origin, rather than secreted and capable of diffusion away from the target cells (Friedl and Wolf 2008). Thus, identifying ACPPs with good substrates and that are selective for MT1-MMP has the potential to effectively target metastasis.

4.3. Methods

4.3.1. Peptide synthesis

Peptides were synthesized using standard solid phase Fmoc syntheses. These include the following ACPPs: ac-e_9-O-PLGmeCAG-r_9-c-nh_2, ac-e_9-O-PLGLAG-r_9-c-nh_2, ac-e_9-RPAHLRDSG-r_9-c-nh_2, ac-e_9-O-SLAYYTA-r_9-c-nh_2, ac-e_9-O-RLQacLKL-r_9-c-nh_2, ac-e_9-O-nLTPRSFL-r_9-c-nh_2, ac-e_9-*x*-YGRAA-r_9-c-nh_2. Selected ACPPs for MT1-MMP cleavage include: ac-e_9-O-NFQGAV-R-r_8-k(FAM)-nh_2, ac-e_9-O-SRHRQS-R-r_8-k(FAM)-nh_2, ac-e_9-O-LEQLWR-R-r_8-k(FAM)-nh_2, ac-e_9-O-QLWKRW-Rr_8-k(FAM)-nh_2, ac-e_9-O-QLWLNRK-R-r_8-k(FAM)-nh_2, ac-e_9-O-RMWERG-R-r_8-k(FAM)-nh_2. For the FRET peptide: nh2-e_9-C(SS-*t*Bu)o-PLGC(Me)AG-r_9c-ac. The ac- represents an acetyl group ($CONH_2$), the meC represents S-methylcysteine, nL represent noroleurcine. Lower case letters represent d-amino acids and uppercase letters represent L-amino acids. The O represents 5-amino-3-oxapentanoyl, *x* represents 6-aminohexanoyl, both spacers. FAM represents the 5(6)-carboxyfluorescein-lysinamide fluorescent dye.

4.3.2. Peptide labeling

For single-Cy5-labeled ACPPs: purified cys-containing peptides were labeled with maleimide-Cy5 (GE Healthcare) in N-methylmorphiline overnight at 25°C. For the FRET PLGmeCAG probe, peptide was reacted with Cy5 Maleimide (GE Healthcare) and subsequently treated with triethylphosphine to deprotect *tert*-BuSH group and then purified using high-performance liquid chromatography (HPLC; Note: This extra cysteine allows to covalently link solubilizing agent.) The purified compound was then reacted with SPDP-peg12-peg2-peg2-cyclo[RADfK]. After completion of the reaction, Cy7mono NHS ester (Cy7-NHS, GE Health Sciences) was added (Savariar, Felsen et al. 2013).

Final compounds were purified C-18 reverse-phase HPLC. Collected fractions were pooled, vacuum dried, and resuspended in water. Identity was confirmed by mass spectrometry.

4.3.3. Gel-based enzyme cleavage assay

Peptides were diluted to 5μM in cleavage buffer (20 mM Tris, 150 mM NaCl, 2 mM $CaCl_2$, pH 7.5). The catalytic domain of various MMPs (Sigma, Calbiochem, Enzo) was added to the dilute peptide at a final concentration of 50 nM. Reactions were transferred to a 37°C incubator. At the indicated time point, 10 μL aliquots were removed from the reaction wells, immediately mixed in a 1:1 ratio with 2X tricine sample buffer (Life Technologies) and heated at 95°C for 5-10 minutes. Samples were then loaded on 10-20% tricine gradient gels (Life Technologies) and run for 100 min at 100 mV. Gels

where removed from their casings and imaged on a Maestro Imager using an excitation filter of 620/22nm and an emission filter of 670/20nm.

4.3.4. FRET-based enzyme cleavage assay

Peptide substrates were diluted to 1 μM (2x final concentration) in cleavage buffer (20 mM Tris,150 mM NaCl, 2 mM $CaCl_2$, pH 7.5) containing 1% BSA and stored on ice. Enzymes were diluted to 40 nM (2x final concentration) in cleavage buffer with 1% BSA on ice. Peptides were aliquoted in a 96-well plate. Prior to mixing, baseline fluorescence was measured in a plate reader (Tecan, Infinite M1000Pro) preheated to 37°C. The plate was removed and placed on ice, enzyme was quickly added and mixed in wells, and the plate was reinserted and a time course of fluorescence measurement with 630 nm excitation and 680 nm (Cy5) and 780 nm (Cy7) emission, 12 nm bandwidth, was initiated with measurements every 15 min over 210 min with continuous 37°C incubation and periodic shaking. Gain was set to 80. Reactions were performed in triplicate wells. Signals in both fluorescent channels were averaged and the ratio of the Cy5 to Cy7 signal was plotted over time.

4.3.5. Phage subcloning

PCR amplification by 25 cycles of 52°C annealing and standard reaction conditions were used. The product was subcloned by restriction digest with SacI and SpeI enzymes into pComb3H vector (Barbas, Kang et al. 1991).

4.3.5.1. H_6-E_9-X_N-R_9-pIII phage libraries

Phage expressing the insert EL-HHHHHHLEEEEEEEEEX$_N$ RRRRRRRRR-TS were constructed with forward primer HG 66 5’ -atccttgagctccatcaccaccatcaccatctcgag,

HG67 5’ - tacgtaactagtcctacgtcgtctccgacgcctccg using oligo templates for the X7 substrate HG84 tccatcaccaccatcaccatctcgaggaagaggaagaagaggaggaagagnnknnknnknnknnknnkagacggaggcgtcggagacgac, for the X6 substrate HG68 tccatcaccaccatcaccatctcgaggaagaggaagaagaggaggaagagnnknnknnknnknnknnkagacggaggcgtcggagacgac, for the X5 substrate HG69 5'-tccatcaccaccatcaccatctcgaggaagaggaagaagaggaggaagagnnknnknnknnknnkagacggaggcgtcggagacgac, or for the X4 substrate HG70 5'-tccatcaccaccatcaccatctcgaggaagaggaagaagaggaggaagagnnknnknnknnkagacggaggcgtcggagacgac.

4.3.5.2. His-PLG-phage

Phage expressing the insert EL-HHHHHHLEEEEEEEEEGGPLGLAGRRRRRRRRR-TS was subcloned into the pComb3H vector with SacI and SpeI restriction enzymes by Dr. Michael Whitney.

4.3.5.3. Myc-PLG-phage

Phage expressing the insert EL-EQKLISEEDLGGGEEEEEEEEEGGPLGLAGRRRRRRRRRGGGG-TS were constructed with forward primer HG102 5'-tagtagagctcgaacagaaactgattagcgaagaagatctgggaggtggcgaggaa and reverse primer HG104 5'- aacttactagtgccgcctccacccctacgtcgtctccgacgcctccgtctgcctgcgag using the oligo template HG103 5'-

gaagaagatctgggaggtggcgaggaagaggaagaagaggaagaggaaggaggtccacttggactcgcaggcagacggaggcgt.

4.3.6. Phage display selections

4.3.6.1. MT1-MMP-selective ACPPs via Ni^{2+} affinity

H_6-E_9-X_N-R_9-pIII phage libraries were pooled for equal representation of each unique phage (roughly 154 each) and $2x10^{11}$ phage were combined in 2 mL phage buffer and first negatively selected for cleavage by kidney and liver extracts (2% weight to volume homogenized in PBS) from MMP-knockout mice 2/9 knockout mice at 37°C for 2.5 hrs. 5-10 μL Ni^{2+}-NTA beads were incubated with the mixture for 2.5 hr at 37°C. Beads were washed 3 times with PBS or phage buffer. As a second negative selection, a mixture of MMP-1, 3, 7, 8, 9, 10, 11, 12, 13, 19, 20, MT2-MMP, MT3-MMP, MT4-MMP, MT5-MMP (Sigma, Calbiochem, Enzo) at 12 nM (19 nM at round 3) in cleavage or phage buffer were added and rotated at 37°C for 3 hours 20 min. Beads were washed 3 times with PBS or phage buffer. Cleavage buffer and 50 nM MT1-MMP were added to beads and rotated at 37°C for 2 hr. Supernatant of cleaved phage was reserved and beads were rinsed once with PBS or phage buffer and combined with the supernatant. Phage were amplified and the process was repeated iteratively using $3x10^9$ phage in round 2.

4.3.6.2. MT1-MMP fast-cleaving ACPPs via Ni^{2+} affinity

H_6-E_9-X_N-R_9-pIII phage libraries were pooled for equal representation of each unique phage. Phage were incubated with 20 μL magnetic nickel beads and rotated at 37°C for at least 30 minutes, and supernatant was removed. 1 mL phage buffer was added, vortexed, and supernatant was removed. 500 μL cleavage buffer containing 1%

BSA was added containing MT1-MMP at 100 nM and the mixture was rotated at 37°C for 15 minutes. Phage collected from the supernatant were then amplified, and phage were reapplied to the selection for subsequent rounds with decreasing concentration of enzyme and incubation time: 50 nM for 7.5 min (round 2), 25 nM for 3.75 min (round 3), and 12.5 nM enzyme for 1.87 min (round 4).

4.3.6.3. MT1-MMP cleavable ACPPs via cell affinity

H_6-E_9-X_7-R_9-pIII -phage library ($3.2x10^{10}$ phage) in 1 mL phage buffer was treated with 50 μM MT1-MMP enzyme at 37°C in phage buffer for 2 hr and stored at 4°C overnight. Cleaved phage were added to 3.5 - $6x10^7$ Jurkat cells in 1 mL RPMI, incubated at 37°C for 40 min. Cells were pelleted, supernatant was removed, and cells were rinsed in 45-50 mL HBSS with mild agitation. Cell pellet was resuspended in phage extraction buffer with 0.05% Tween and cOmplete protease inhibitor cocktail (Roche) and lysed by sonication at 25% amplitude for 10 seconds. Half of the total lysates, or all lysates at round 1 of selection, were treated on ER2738 *E. coli* to amplify total phage and were plated at dilutions of 1 μL and 0.01 μL to isolate single colony forming units. 10 individual colonies per round were chosen at random and phage pIII was sequenced.

4.3.7. Phage assay for enzyme cleavage

100 μL Myc-E_9-PLGLAG-R_9-pIII (Myc-PLG-phage) and H_6-E_9-PLGLAG-R_9-pIII phage (His-PLG-phage) were cleaved with 50 nM MMP-2 at 37°C for 2 hr and stored at 4°C. $1.8x10^7$ Jurkat cells were pelleted and resuspended in 2 mL HBSS. 1 mL cells were added to 75 μL His-PLG-phage +/- MMP-2, and incubated at 37°C for 2.25 hr. Cells were gently washed with 1 mL HBSS. 100 μL phage buffer was added, cells were

vortexed and sonicated at 10% amplitude for 10 sec, and 10 µL was titered for colony-forming units. 100 µL Myc-PLG-phage were each added to 2 tubes each containing 15 µL anti-myc agarose with 400 µL cleavage buffer and rotated at room temperature for 4 hr at 25 °C and 4°C overnight. Agarose was pelleted and supernatant removed, then rinsed with 1 mL phage buffer. Cleavage buffer was added to 200 µL, and 6.6 µL MMP-2 was added to one tube, and both were rotated at 37 °C for 2 hours. Beads were pelleted and supernatant was removed and titered.

4.4. Results

4.4.1. Analysis of ACPP enzyme selectivity and kinetics by gel assay

Previous work from our lab showed that an ACPP with the substrate PLGmeCAG could be cleaved by MMPs-2 and -9; however, detailed characterization of the sensitivity, speed, and completion of complete cleavage kinetics of the peptide over time by targeted MMPs and its selectivity against all other MMPs was unknown. Furthermore, peptide cleavage and tumor uptake was sometimes evident in PLGmeCAG ACPP injected mouse tumor models, in which MMP-2 and MMP-9 were genetically knocked out or pharmacologically inhibited with MMP-inhibitors prinomastat or GM6001 (data not shown). We speculated this non-MMP-2/-9 signal was possibly due to the existence of other tumor-expressed enzymes or possibly compensatory up-regulation of other enzymes upon MMP-knockout or inhibition that cleave PLGmeCAG. Thus, identification of other tumor-expressing enzymes that could generate signal was desirable. Furthermore, to explore potentially more selective MMP substrates, an ACPP with the

reportedly MMP-2 selective substrate SLAYYTA the MT1-MMP selective sequence RPAHLRDSG, were made and tested (Ouyang, Huang et al. 2010).

In order to test the MMP selectivity of ACPPs bearing MMP-cleavable substrates PLGmeCAG, PLGLAG, RPAHLRDSG, and SLAYYTA labeled with Cy5 were treated at a concentration of 5 μM with various MMPs at a concentration of 50 nM or no enzyme as a control at 37°C for 2.5 hours and reaction was stopped by mixture with SDS tricine buffer. Peptide cleavage was analyzed by gel electrophoresis, in which cleavage was detected by the presence of a fluorescent band migrating lower than the peptide treated without enzyme. PLGmeCAG and PLGLAG showed complete or nearly complete cleavage by MMPs-2, 9, 13, and 20 and partial cleavage by MMPs-1 (minor), 3, 7, 8 (minor), 10, MT1-MMP, MT2-MMP, and MT5-MMP (Figure 4.2). RPAHLRDSG was completely or nearly completely cleaved by MMP-2, 7, 13, 20 and MT1-, MT2-, MT5-MMP, partially cleaved by MT3-MMP, and minimally cleaved by all other MMPs tested. The substrate SLAYYTA showed complete cleavage by MMP-2, MT2-MMP, and MMP-20 and partial cleavage by MMP-3 and -19 and MT1, MT4, MT5-MMP.

Other ACPPs, which were developed for or found to be cleaved by other enzymes, were tested in parallel. An elastase-cleavable ACPP selected by phage display for tumor cleavage and *in vivo* uptake, RLQLKacL was only partially cleaved by MMPs-3 and 20 (Figure 4.3) (Whitney, Crisp et al. 2011). None of the MMPs tested cleaved thrombin substrate NleTPRSFL or the substrate xYGRAAA, which was selected by phage display for thrombin cleavage and found to also be cut by urokinase-type plasminogen activator (uPa) by Dr. Michael Whitney and Shannon Muir (Whitney, Savariar et al. 2013).

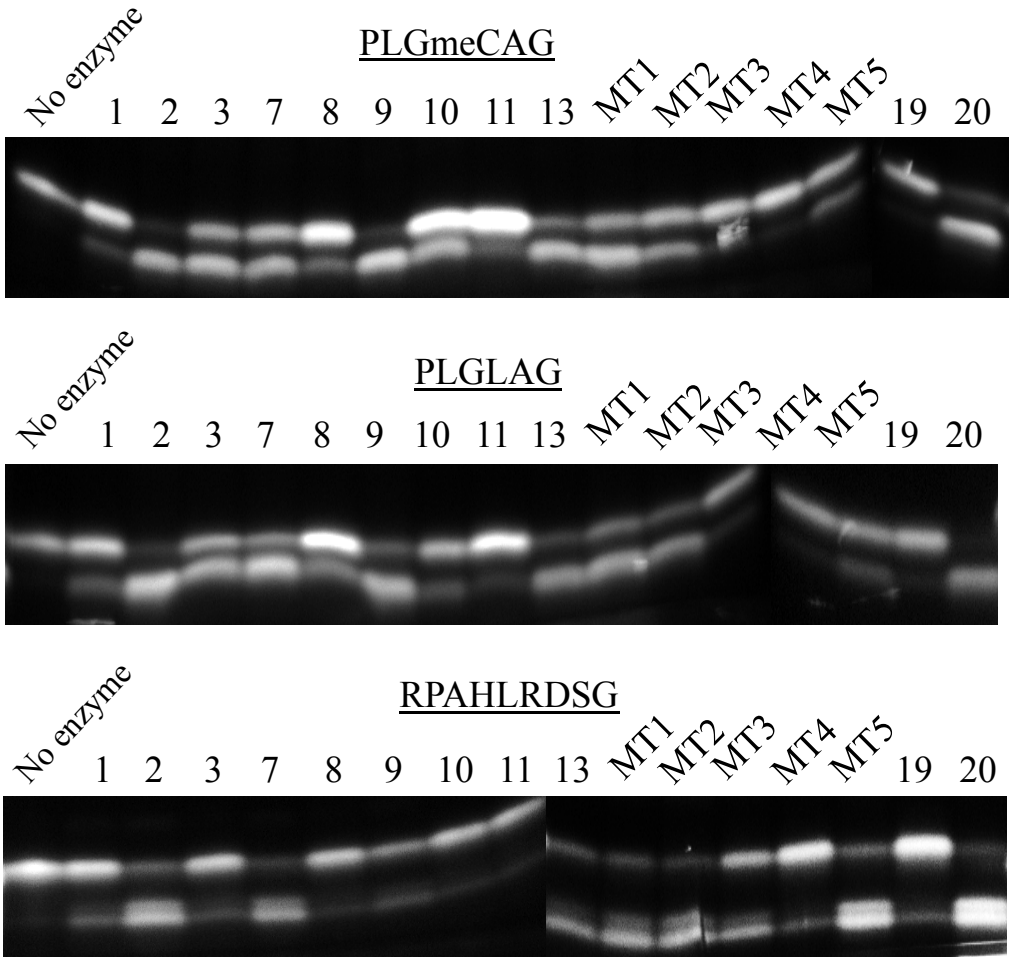

Figure 4.2. Three MMP-cleavable ACPP substrates show little MMP enzyme selectivity. Substrates shown are flanked by an N-terminal Cy5-e_9 and C-terminal r_9. 5 μM substrate was cleaved with 50 nM enzyme. PLGmeCAG is cleaved by MMP-2,3,7,8,9,10,13,MT1,MT2,MT5,MMP-20. PLGLAG is cleaved by MMP-2,3,7,8,9,10,13,MT1,MT2,MT5,MMP-20. PW-ACPP is cleaved by MMP-2, MMP-7, MMP-9, MMP-13, MT1, MT2, MT3, MT4,MT5, MMP-20

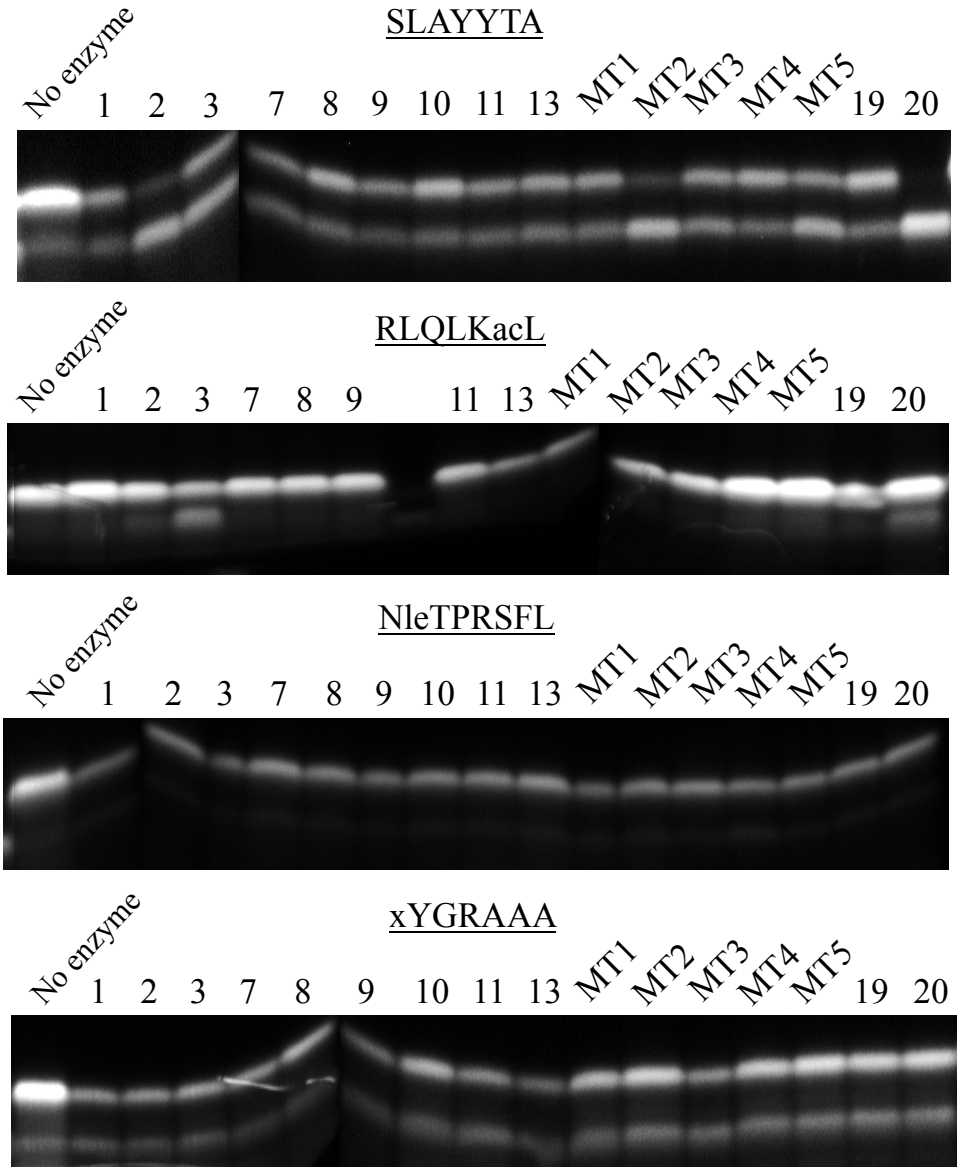

Figure 4.3. ACPP substrates SLAYYTA and RLQLKLacL are cleaved by only 3 MMPs and NleTPRSFL and xYGRAAA are cleaved by no MMPs tested. SLAYYTA is cleaved by MMP-2, MT2-MMP, and MMP-20. RLQLKacL is cleaved by MMP-2, 3, 20. Nle-TPRSFL and xYGRAAA are not cleaved by any MMPs. SLAYYTA and xYGRAAA peptides show slight degradation or impurity in the absence of enzyme (lower band, no enzyme well). RLQLKacL was cleaved by MMP-10.

In order to assay the sensitivity of PLGLAG and RPAHLRDSG to MMPs-2, -9, MT1-MMP, a time course of peptide cleavage was performed, similarly as before with the reaction being stopped at various time points between 0 and 4 hours. Cleavage of both

RPAHSLRDSG and PLGLAG was detectable with all 3 enzymes by 15 minutes post. Cleavage was incomplete after 4 hours for RPAHSLRDSG and showed no preferential activity by any of the 3 enzymes (Figure 4.4). PLGLAG was completely cleaved by MMP-2 by 30 minutes post, by MT1-MMP by 1 hour post, and by MMP-9 by 2.5 hours post.

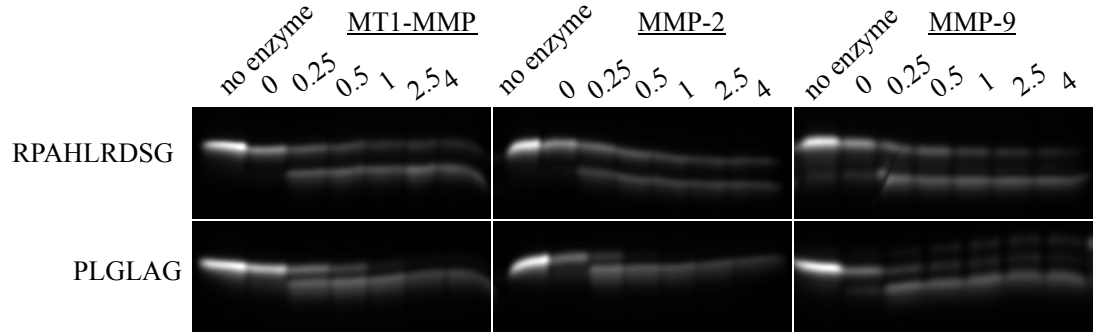

Figure 4.4. Time course of ACPP substrate cleavage shows RPAHLRDSG and PLGAG are quickly cleaved by MT1-MMP, MMP-2, and MMP-9. 5 μM peptide was treated with 50 nM enzyme at 37°C for up to 4 hours. PLGLAG was cleaved most quickly by MMP-2, followed by MT1-MMP, and MMP-9. RPAHLRDSG showed similar cleavage rates with all 3 enzymes.

4.4.2. FRET dequenching assay for high throughput enzyme selectivity and kinetic analysis of ACPPs

In order to efficiently generate more quantitative information on the selectivity and cleavage kinetics of different ACPPs, a fluorescence resonance energy transfer (FRET)-based assay was generated. FRET involves the energy transfer of fluorescence excitation of a donor fluorophore, when directly excited, to an acceptor fluorophore with a longer wavelength, causing the latter to fluorescence, rather than the former fluorophore. FRET peptides enable cleavage measurement in solution by fluorescence quantification of both donor and acceptor, both due to fluorescence dequenching of the

donor fluorophore upon dissociation of the acceptor fluorophore, and the concomitant loss of fluorescence by the acceptor fluorophore.

A FRET ACPP with the substrate PLGmeCAG peptide was recently shown to label tumors and metastases in mouse models (Savariar, Felsen et al. 2013). In this reporter, Cy5 is conjugated to the r_9 end of the ACPP and serves as the donor fluorophore, and Cy7 is conjugated to the e_9 end of the ACPP and serves as the acceptor. In order to assay its selectivity for various enzymes, the 500 nM of the ACPP was cleaved at with 20 μM enzyme in Tris-buffer containing 1% BSA. The addition of BSA was found in preliminary assays to be critical for FRET peptides solubility and stability in solution (data not shown). Cy5 and Cy7 fluorescence were measured by excitation of the Cy5 channel and collecting fluorescence emission signal in the Cy7 channel. This assay showed PLGmeCAG can be cleaved by several MMPs. MMPs-2, -13, and -20 cleaved the substrate the fastest, followed by MT1-MMP, MMP-3, MMP-9, MMP-12, MT2-MMP, and slight activity by MMP-7 (Figure 4.5). Other MMPs assayed, as well as other enzymes, such as plasmin, thrombin, factor Xa, trypsin, cathepsin H, cathepsin L, and granzyme A did not cleave the substrate. Thus, the substrate was found to be selective for MMPs and have very high sensitivity toward MMP-2, MMP-13, and MMP-20.

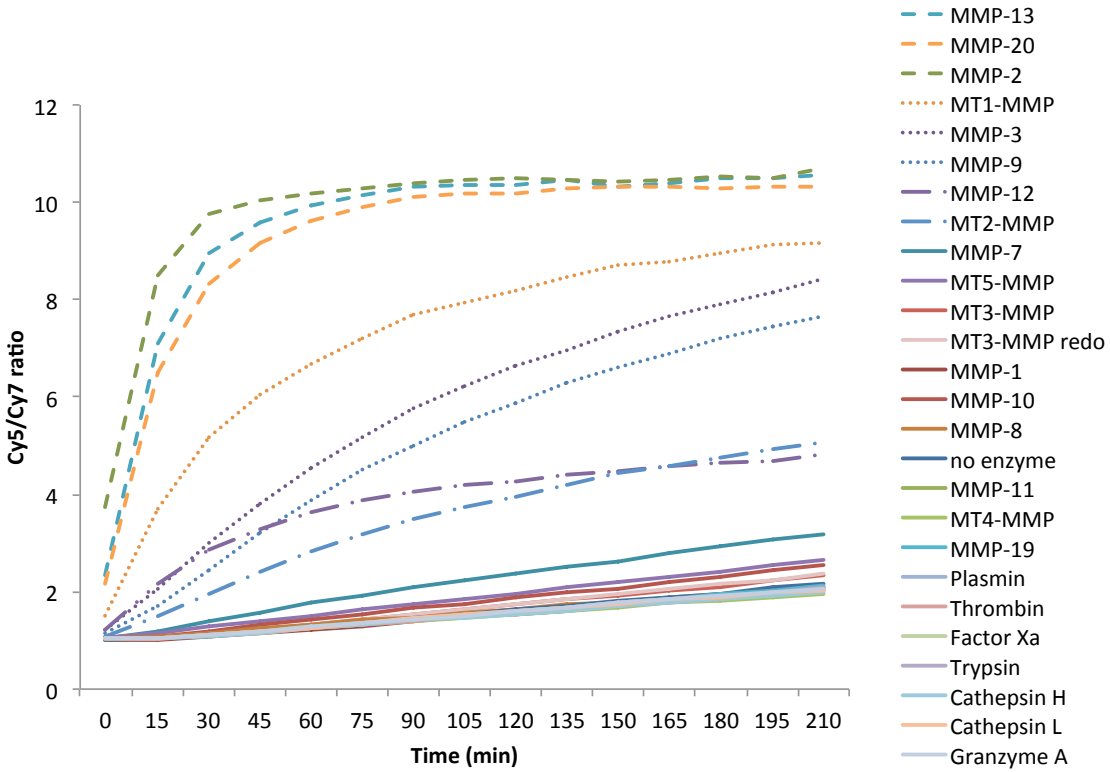

Figure 4.5. FRET assay of MMP-selectivity of PLGmeCAG substrate. 20nM enzyme and 500 nM substrates were incubated at 37°C in cleavage buffer with 1% BSA. MMPs 13, 20, and 2 showed the greatest increase in FRET signal, while MT1-MMP, MMP-3, MMP-9, MMP-12, MT2-MMP, also showed some cleavage. Cy5 channel was used for excitation, and both Cy5 and Cy7 were used for emission. Mean of triplicate measurements was plotted.

4.4.3. Phage display selection of MT1-MMP selective ACPPs

Next, in order to develop ACPP substrates that are more selective for and sensitive to active MT1-MMP, a phage display peptide selection was developed by encoding a peptide library in which ACPPs with a variable substrate sequence were displayed in fusion with coat protein pIII on M13. The N-terminus of the peptide encoded a hexahistidine (His_6) tag to affinity purify phage bearing the ACPP insert using nickel beads and to isolate cleaved phage via their dissociation (Figure 4.6). This mechanism was previously used to select tumor-cleavable ACPPs, wherein a 6-amino acid substrate library with $5x10^6$ diversity was generated, representing approximately 8% of the

theoretical peptide diversity (Whitney, Crisp et al. 2010). In order to encode a greater diversity of ACPP substrates, new phage libraries was constructed with 4, 5, 6, and 7 amino acid substrates. The sequence was encoded within a pIII phagemid vector, in which recombinant phage express peptide in 0-4 copies of pIII, along with wildtype pIII due to superinfection of phagemid-bearing *E. coli* with helper phage (Barbas, Kang et al. 1991, Sidhu 2001). Each library was separately generated, encoding 10^8 to 10^9 transformants, which exceeded the theoretical peptide diversity by upwards of 2-2000-fold (Figure 4.6).

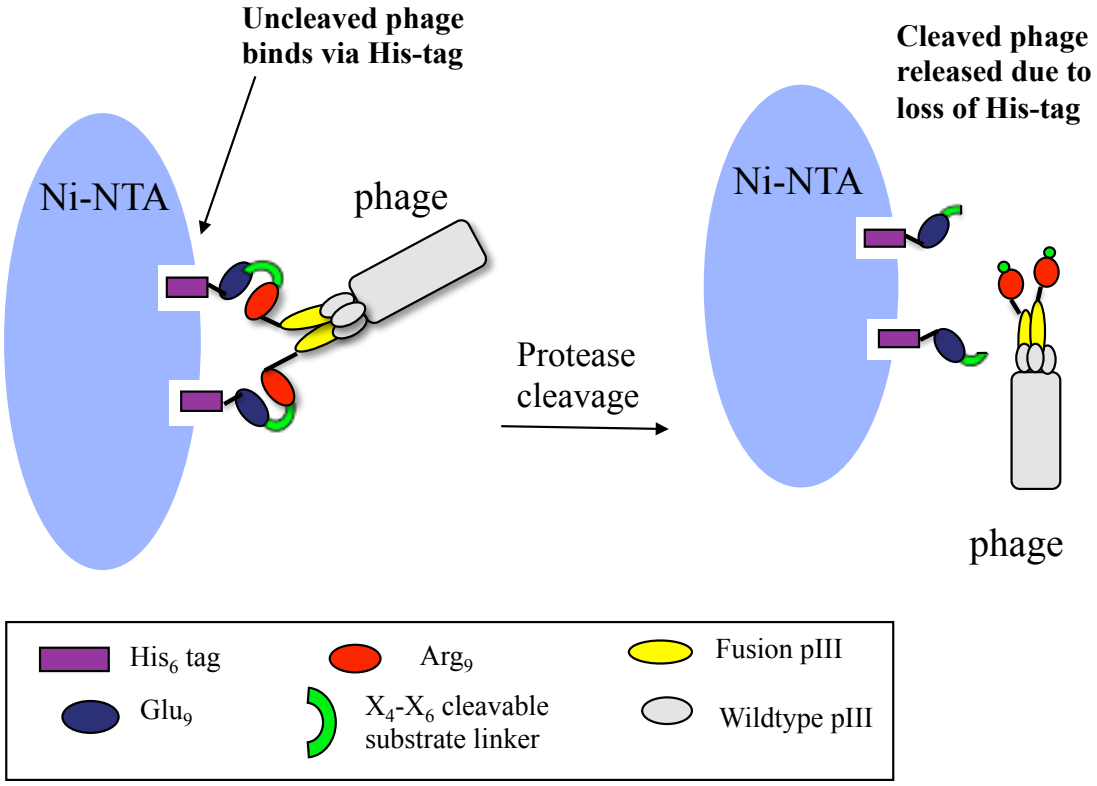

Figure 4.6. Schematic of phage display selection for enzyme-selective ACPPs. For negative selection against cleavage with non-target enzymes, nickel resin-bound phage are treated with enzymes and uncleaved phage remaining on the resin are retained, while immobilized phage are discarded. Next a positive selection is performed in which bound phage are treated with the target enzyme(s) and cleaved phage which dissociate from the resin are collected, amplified, analyzed, and reapplied to the selection.

His_6-E_9-X_n-R_9-pIII

	Possible diversity	Actual obtained (individual transformants)
X_4 :	$1.6*10^5$	$4.1*10^8$ = 2600 x possible diversity covered
X_5 :	$3.2*10^6$	$2.8*10^8$ = 87.5 x possible diversity covered
X_6 :	$6.4*10^7$	$2.7*10^8$ = 4.2 x possible diversity covered
X_7 :	$1.3*10^9$	$3.1*10^9$ = 2.3 x possible diversity covered

Figure 4.7. Design and construction of a variable-substrate ACPP-phage library. A phage library was constructed bearing the peptide sequence His_6-E_9-X_n-R_9-pIII, where X represents any amino acid and is encoded by the nucleotide sequence nnk, where n represents a mixture of all 4 nucleotides and k represents g or t, and is used rather than n in order to equalize the likelihood of encoding amino acids that have two or four different codons.

The four phage libraries were pooled based on theoretical peptide diversity and phage titer, so that each sequence was roughly equally represented in the starting library. In order to reduce nonspecific enzymatic cleavage, negative selections first performed with liver and kidney extracts because cleavage and retention of many ACPPs by non-targeted enzymes in these organs has been a common problem with past molecules. Phage treated with the extracts at 37°C and uncleaved bead-bound phage were allowed to adhere to Ni^{2+} agarose. Next, a secondary negative selection with a pool of other non-target MMPs, excluding MT1-MMP, were added to beads at 12 nM and incubated at 37°C for 3 hours and retaining bound phage again. For positive selection, the agarose-bound phage were treated with MT1-MMP at 50 μM for 2 hours and cleaved phage supernatant released from the agarose was recovered. Phage were amplified and selections were repeated over 5 rounds, and sequencing of a sampling of individual phage was performed at each round. As might be suspected, given their higher diversity and thus composition of the library, most selected sequences had 6 or 7 variable residues (Figure 4.7). The sequences NFQGAV and SRHRQS were identified twice at round 5 of

selection, and peptides with similar sequences LEQLWR, QLWKRW, QLWLNRK were also identified.

r1B selection
11 – ALLRFLY
10 – SRRSME
9 – IRNYSQ
8 – RqRCVS
7 – PCXMRKV
5 – VGVKVS
4 – SGRGKAA
3 – VAGDSD
2 – SVQLGA
1 – KGEISK

r2B selection
25 – FRLGNN
24 – LRRRSSE
23 - qPKLRV
22 – TPLMTK
20 – YGRDVq
19 – VDqHLW
18 – TLCSGKE
17 – TMVNGN
16 – IRTqSSQ
15 - qVQQYG
14 – AEFWMPL
13 – CVGVqGY
12 – RVWPRW
11 – VYPCVK
10 – AqFQRSP
9 – GVKGDM
8 – GSKRRV
7 – SPSGGN
6 – RRAEqW
5 – RNq
4 – NPGPLPD
3 – GMDqVVQ
2 – FVRNKM
1 – LDLESH
(1 parent vector)

r3B selection
7 – ARGLKq
17 – ARRKLDT
23 – AqSCRqT
20 – EVCRTLK
28 – GqSCSSH
27 – GRAKRM
10 – GWCGDV
26 – LRRQDL
30 – LRMPNR
22 – LGGPRHE
24 – NRVGRTN
29 - qNQSLN
25 - qNSRVSP
8 – QGSRQWA
16 – RYLqGA
6 – RRMGQVD
14 – RRYRPIV
5 – RTqLVGR
4 – RqPECA
11 – SqVVCqW
18 – SLqHSVS
13 – VPQTSSS
2 – VRENGRM
3 – WHRGGRL
9 – YCFGVGG
(3 parent vector, one frameshift)

r4b selection
12 – CTFqARG
6 – GSDDRAG
4 – GqGDVT
16 – GSGVSTR
11 – IMRWQT
15 – LVTqHI
3 – KRqDRTW
7 – MAVRPV
6 - qRHKDF
1 - qWWSRDY
10 – SCECARQ
(4 frameshift, one junk)

r5b selection
57b – ATqWGRT
87B – ARGPRqD
29b – CAqVSHT
10 – CVRRYq
37b – DGDRqQ
33b – DNQGLG
102B – DRNDqF
14b – ESqSVG
54b – FqHACYG
1b – GDNSRW
82B – GIHqR
38b – GqVGCNM
72b – GSVTGQ
78B – HAGVS
53b – IMRWQT
8 – IESSGR
16b – KASNSW
14 – KNPRKT
13 – KARVTM
69b – LEqLWR
17 – LVqCCRH
81B – MAGIqG
103B – MMMREH
61b – NqRDWI
76b – NFqGAV
86B – NFqGAV
77b – PAVTMq
2 – PSTTLGG
50b - qASKKM
4b - qCGRFRS
19 - qEVHqHW
41b - qFRMPWL
10b - qHSGLQ
65b - qHRTGTA
71b - qLWKRW
92b - qLWLNRK
24b - qRGAGAM
5b - qRYRqK
36b - qTQKSP

3 - qVEVAS
60b – QAqPLAR
89B – RqWAVVC
42b – RGSSS
75b – RLVSASq
30b – RRGNMS
93B – RRRPGq
101B – RSVqG
11b – RYRNRR
1 – SCGRAEQ
48b – SETRERL
3b – SESFqN
34b – SNTPGC
19b – SNIANMR
14b – SqSVG
64b – SRHRqS
59b – SRHRqS
66b – TARPAWT
63b – TMRVAA
26b – TPGNAq
20b – TVVHDT
68b – VGqqCAG
44b – VGSLIRq
47b – VTIqYS
17b – WDLVqS
100b – YSREVS
18 – YqMGGKS

Figure 4.8. Two ACPP substrate sequences found enriched in the 5th round of phage display selection for MT1-MMP-selective cleavage. Negative selection against cleavage by a liver/kidney extract and a non-target MMP-mixture cleavage was performed for 3 hours each, followed by positive selection for MT1-MMP cleavage and isolation of cleaved phage released from nickel beads. For each clone listed, sequences are cleavage sites between H_6-E_9 and R_9. q=Q encoded by amber stop codon, expressed in amber suppressor *E. coli* strain. Sequences highlighted in red were found more than once, and sequences highlighted in blue contained similar sequences to other peptides.

4.4.4. Phage display selection of fast cleaving MT1-MMP ACPP substrates

A separate phage selection was also performed for rapid cleavage by MT1-MMP, in order to specifically search for ACPP substrates that were especially sensitive to that enzyme. The pooled phage library was incubated with Ni^{2+} beads, and beads were washed to remove unbound phage. Cleavage buffer containing 1% BSA was added to beads with 100 nM MT1-MMP and allowed to cleave for 15 minutes, following which, supernatant of cleaved phage was collected and reamplified. The selection was repeated and made more stringent at each round by reducing in half both the concentration of enzyme and the time of incubation. DNA was isolated from at least 10 individual phage clones and sequenced at each round of selection to analyze the diversity of selected pools. After 4 rounds of selection, one phage sequence bearing the ACPP substrate RMWERG was found to be enriched (Figure 4.9).

R1C	55 – CVRCVH	43 – TEVEWqE	16 – LVAVPHD
10 – GTRAWPG	28 – CLAVPG	20 – VAEYTT	39 – LWARPEL
9 – KQWADSL	34 – CSVEPGF	51 – VCAqLPM	63 – MDLKQS
8 – ASWqMDV	37 – DGTAKQD	50 – VWTGDD	10 – MQRKVY
7 – LPRPRD	14 – EAAIMT	9 – YYMTLQ	60 – NSKRKA
6 – VNSKLW	44 – EFHTKGT		24 – NEGSPE
5 – ERqGWT	47 – GLNDWG	R4C	52 – PRRGRWQ
4 – YLPVFRq	27 – GVPGYVG	7 – AGTHTEM	57 – PRGRPGD
3 – MNGGRK	2 – GGPVXGq	38 – AVVqVG	43 – PPSEFFq
2 – IQWKRRL	1 – GRTELE	20 – CqKRLVY	60 - qHQVIR
1 – GRVSGD	8 – GLYKVD	9 – DGSVGV	51 - qqLAKER
	56 – LCqRDE	3 – DARTDS	49 – QLFSGGC
R2C	16 – LCqFVRq	54 – EVTNGE	33 – RGVETT
8b – SGqRRIK	39 – LGFWGGR	28 – ETRGRY	32 – RLNGLLR
7b - qCEGCRV	12 – LqVWSLR	58 – FLLEGSN	62 – RNLqAT
5b – CGSVPAK	15 – LRGKEA	37 – FELTTYG	59 – RSFDLRW
4b – EXRWEL	17 – NESNG	19 – FGRPqFQ	36 – RVSLXE
3b – WVRTGKL	53 – PCVYNXC	27 – FGGYEVq	42 – RMWERG
2b – IWLHSLL	49 – PDKGCC	50 – FVDREq	12 – RMWERG
1b – CAMSKq	45 – PACRKLS	47 – GAPXTGG	29 – RRAMRLC
5 – TVSKAY	31 – QGYRMW	68 – GRYKCG	2 – SGGWqNE
3 – LETEKA	13 - qQWEGAW	22 – GGEYSE	71 – SKRqSTQ
1 – ERLDLS	38 - qNPTHE	67 – GDHSGD	70 – SFTqRRH
	35 – RCGDRAE	56 – GSGDIE	45 – SQSVVA
R3C	33 – RMAGG	64 – GVEMGE	21 – SLYWHV
26 – AEVLAQK	21 – RKRINq	55 – HNRKSG	48 – TVLGGSQ
54 – AGVTRQ	10 – RHATGW	35 – IVTXGCK	14 - VKKDES
48 – ANEEAG	6 – RIRKKK	5 – KKHPNW	17 – WRRREQV
3 – ARSCDVA	4 – RWWQSET	18 – KRERRVT	13 – WFSTqVq
46 – ASqAGAL	43 – SAERDMQ	31 – KAMTEqP	1 – WRRAW
52 – CqWICES	18 – SEqRGLG	8 – LPWqLAR	

Figure 4.9. Sequences selected for MT1-MMP fast-cleaving ACPPs. For each clone listed, peptide substrate between H_6-E_9 and R_9 is shown. q=Q encoded by amber stop codon, expressed in amber suppressor *E. coli* strain. R1C was selected with 100nM enzyme with 15 min cleavage, and 10 phage clones were sequenced, all of which were contained the ACPP and insert sequence. R2C was selected with 50 nM enzyme for 7.5 min cleavage, and 15 phage were sequenced of which 4 contained a non-recombinant sequence. R3C was incubated with 25 nM enzyme for 3.75 min, and 55 clones were sequenced of which 12 contained a non-recombinant sequence. R4C was performed with 12.5 nM enzyme for 1.8 min, and 71 colony forming units were sequenced of which 16 were non-recombinant. Non-recombinant sequences not shown contained a frameshift mutation, a non-interpretable sequence, or encoded the parent vector insert.

In order to assay the cleavage kinetics of sequences enriched in each selections, the 5 peptides were synthesized with a fluorescent dye as acetyl-e_9-O-X_n-R-r_8-FAM, where O represents the spacer 5-amino-3-oxapentanoy in order lend flexibility to the sequence and separate it from the d-amino acid masking domain, and one arginine of the CPP was synthesized in L-form in order to maximize the potential of the natural-amino acid peptide substrate to be recognized and cleaved by the cognate enzyme. Peptides at 5 μM were incubated with 50 nM MT1-MMP at 37°C for 2 hours, then analyzed for cleavage by gel electrophoresis. A minor lower band was detected in all samples and was more prominent for substrates NFQGAV and SRHRQS (Figure 4.10 A). For these peptides, selectivity was tested by treatment with 50 nM MMP-2 and MMP-9 or no enzyme as a negative control at 37°C for 2 hours, and PLGmeCAG ACPP was tested in parallel as a positive control. Minor lower bands were found in all conditions for substrates NFQGAV and SRHRQS, while for the positive control substrate PLGmeCAG, only an upper fluorescent band was found in the absence of enzyme, while lower bands, indicating cleavage were found upon MMP-2 and MMP-9 treatment (Figure 4.10 B). Thus, the apparent cleavage of the selected substrates by MT1-MMP was likely due to peptide impurity, rather than cleavage.

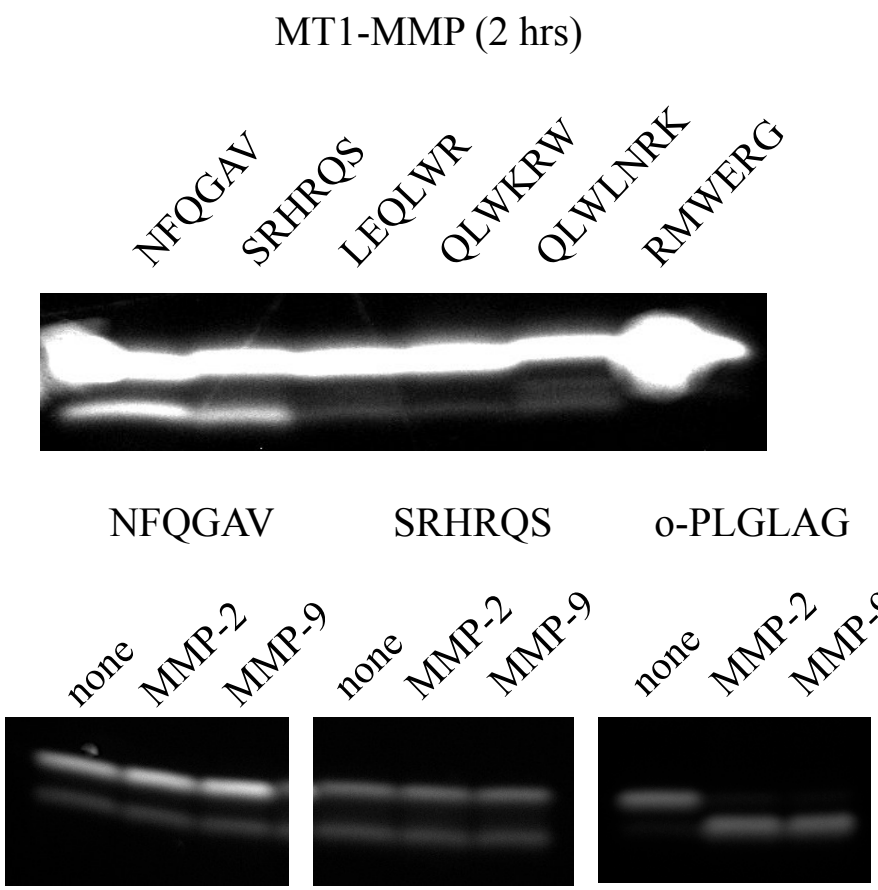

Figure 4.10. Cleavage profiles of MT1-MMP phage-selected substrates do not show robust cleavage as peptides. Sequences shown are cleavage sites between E9 and R9. Cleavage of ACPP substrates by MT1-MMP showed only small cut bands (lower band) for NFQAV and SRHRQS, but these were impurities, as detected by the presence of both upper and lower bands in control-treated wells ("none"). Substrates NFQGAV and SRHRQS were also not cleaved by MMPs -2 and -9, while positive control o-PLGLAG shows complete MMP-2 and MMP-9 cleavage as a positive control. 5 μM substrate cleaved with 50 nM enzyme in cleavage buffer for 2 hr at 37 °C. Gel was imaged with Maestro FAM filters.

To analyze the efficiency of phage peptide selection, experiments were performed testing the cleavability of phage expressing H_6E_9-PLGLAG-r_9-pIII with purified MMP-2 via nickel agarose dissociation; however, these experiments showed unreliable phage enrichment over a no enzyme control (data not shown). Thus, we speculated that assay optimization based around a known MMP substrate could improve the efficiency of selection.

As an alternate mechanism of selection, ACPP cleavage should be detectable by an increase in affinity to cells due to unmasking of the CPP (Figure 4.11). To evaluate the efficiency of selection, H_6-E_9-PLGLAG-R_9-pIII were incubated with 50 nM MMP-2 or no enzyme as a control at 37°C for 2 hours, then added to concentrated Jurkat cells (~10^7 in 1 mL HBSS) and incubated for 2.25 hours at 37°C. Cells were pelleted, rinsed 1x with HBSS, and cells were resuspended in phage buffer and sonicated. Phage titers showed 3-fold higher recovery of MMP-cleaved phage than uncleaved phage (Table 4.1). Using the Jurkat assay to select MT1-MMP cleavable ACPP-phage would enable its compatibility with previously constructed ACPP phage libraries.

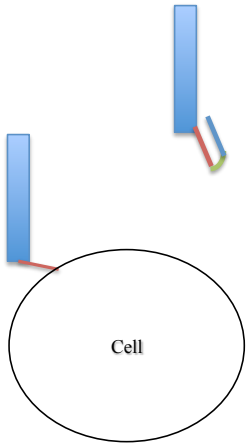

Figure 4.11. Schematic of alternate phage selection mechanisms for MT1-MMP-cleavable ACPPs. In a cell assay for phage cleavage, uncleaved ACPP-phage is non-adherent due to the masked r_9 domain, and attaches to cells after cleavage due to release of the masking e_9 domain.

Table 4.1. Assay for ACPP-phage cleavage by cell adherence shows 3.1-fold enrichment of cleaved over uncleaved phage. H_6-E_9-PLGLAG-R_9-pIII phage incubated with MMP-2 and Jurkat cells (Jurkat assay) showed a 3-fold increase in phage recovery upon peptide cleavage. Phage were titered for colony-forming units.

+MMP2	No enzyme	Fold-enrichment
267,000	84,000	3.1

Next, the Jurkat assay was applied as a phage selection mechanism to find MT1-MMP cleavable ACPPs using the previously described X_7 ACPP pIII phage library, due

to its high diversity. In the first selection round, 3.2×10^{10} cfu of the X_7 substrate ACPP phage library were treated with 20 nM MT1-MMP for 2 hr at 37°C, then incubated with $3\text{-}6 \times 10^7$ Jurkat cells in 1mL media at 37°C for 40 minutes. Supernatant was removed from pelleted cells, and cells were washed with HBSS. Cells were lysed, and phage were amplified and titered. Roughly 10^6 cfu (X_7 library) were recovered after the first round of selection. The selection was repeated iteratively for 5 rounds using roughly 10^9 cfu of phage per round. A sampling of phage clones were sequenced at each round, and the variable peptide region of each is shown in Figure 4.12. At round 1, no non-recombinant phage were found. After round 2, 2 of 10 phage clones were non-recombinant and 2 other generated no signal. 2 of 10 sequences were non-recombinant at round 3. 15 of 35 sequences were non-recombinant in round 4, and 8 of 10 sequences were non-recombinant at round 5. Unfortunately, after 5 round of selection the percentage of non-recombinant sequences, especially those that could not be aligned with surrounding vector sequences, overtook the population becoming 80% of the total population, and no trends were identified. The increasing recovery of non-recombinant phage suggested that the phage selection mechanism was not powerful enough to overcome the replication advantage of phage not expressing peptide.

R1	R2	R3	R4	R5
FGSDAAT	LGLQGET	SAGWqSS	AWMCALS	GIAGRQG
DCGMGVL	DGAAGRT	IVSSMGT	qRLGAFR	QSSVRQG
ATMSLSA	LRMWKDK	qYASEWA	RRLQLY	
RSXSWVD	RWFRESA	RGVDEKC	AAGQVRR	
CqAIGCA	TNSRFRD	SNLIPTK	HqCNESL	
	SAqVFLS	YSITCqC	ASELEGG	
		STRRGLE	RRYPEqC	
		KCGqQEP	LLSSLGS	
			SEAKVqR	
			GVSRAVA	
			RWREEQG	
			DPSSERL	
			RqPPRCR	
			RqRRGLN	
			KIqPGER	
			GLqSLRw	
			SQqLTRq	
			WQQQqHG	

Figure 4.12. ACPP substrate sequences selected by phage display for cleavage by MT1-MMP using cell affinity method. Sequences listed are cleavage sites between H_6-E_9 and R_9. q=Q encoded by amber stop codon, expressed in amber suppressor *E. coli* strain. Phage expressing H_6-E_9-X_7-R_9-pIII were treated with purified MT1-MMP and cleaved phage were isolated by Jurkat affinity. 5-35 individual phagemid colony-forming units per round were chosen at random, DNA was collected, and phage pIII was sequenced. Sequences not shown were frameshifted, uninterpretable, or did not contain an ACPP insert.

4.5. Discussion

ACPPs represent promising probes for targeting nearly any disease via active protease expression, enabling better biological understanding, and a potential means to improve their detection and treatment. Critical to their success is the ability to sensitively and specifically detect activity by target enzymes. Here, we have demonstrated the efficacy of gel and plate reader assays to measure the selectivity and cleavage kinetics of known substrates and used them to characterize the total MMP-selectivity of several important substrates, which have been shown to label tumors in cancer models and

inflammation in asthma models (Jiang, Olson et al. 2004, Olson, Aguilera et al. 2009, Felsen, Savariar et al. 2014).

Of the 4 ACPP substrates designed to be MMP-cleavable that were profiled for cleavage by nearly every MMP, SLAYYTA appeared the most MMP-selective, with preferential activity by MMP-2. Interestingly, the substrate RLQLKacL, which was selected for cleavage by tumor tissue, was not efficiently cleaved by most MMPs suggesting that in certain tumor types or models, MMPs may not be the dominant class of proteases.

A FRET-based assay showed the cleavage kinetics of the ACPP substrate PLGmeCAG with the large panel of MMPs and several non-MMP enzymes, and showed it had the highest sensitivity to MMPs-2, -13, and -20. In theory, cleavage of FRET substrates should result in a loss of emission of the fluorescent acceptor, Cy7; however, the emission channels showed a large dequenching of Cy5 and with a gradual increase in Cy7, suggesting that at least *in vitro* a dequenching mechansim may be more predominant. This difference in molecular mechanism of signal generation does not affect the ability of the assay to efficiently and accurately generate cleavage kinetics data.

Desirable advancements to the current ACPP technologies include targeting metastatic cancer cells *in vivo.* A published MT1-MMP-selective substrate RPAHLRDSG assayed in the context of an ACPP for cleavage by many MMPs did not show high MT1-MMP selectivity (Ouyang, Huang et al. 2010). Thus we aimed to create new highly selective and efficient ACPPs for cleavage by this clinically-important enzyme. Phage display selections were pursued for ACPP substrates of MT1-MMP with enzyme selective cleavage or fast cleavage rates. Unfortunately, enriched sequences

made synthetically did not show cleavage. Growth bias of non-recombinant phage, coupled with the low throughput of Sanger sequencing, was a primary obstacle toward the selection of new sequences. The faster reproduction of non-recombinant phage during *E. coli* infection and propagation, allowing them to out-compete recombinant phage, in spite of functional selections is a common issue with many phage selections.

The lack of success in discovering functional sequences may be indicative of low efficiency of phage expression of ACPPs. It has been established that phage expressing several positively charged residues have lower efficiency of expression due to interference of pIII's proper membrane insertion (Peters, Schatz et al. 1994).

Because each of the selection mechansims for phage cleavage work using opposite mechanisms - loss of adherence to nickel beads vs. gain of adherence to cells upon cleavage - it is possible that the combination of the two mechanisms could generate a more powerful selection mechanism in which negative selections could be incorporated with lower likelihood of non-recombinant phage recovery.

4.6. Acknowledgements

The dissertation author would like to thank:

Dr. Michael Whitney for collaboration in experimental design and preliminary assay optimization experiments and for labeling and purifying peptides. Dr. Elamprakash Savariar and Qing Xiong for synthesizing, labeling, and purifying peptides.

CHAPTER 5: Quantitative Endosome Escape Assay Using Cytoplasmic Enzymatic Modification

5.1. Abstract

One of the major limitations of drug targeting, after reaching the target site, is delivering non cell-permeable, cytoplasmically active molecules intracellularly. Various agents have been reported to assist in crossing the plasma membrane or endosomal membrane, but none has proven robust *in vivo*. Current methods to assess cytoplasmic delivery are limited in ability to quantitate efficiency and have not been widely translated into screening platforms for new agents. A reporter was developed to measure delivery using a small peptide substrate modifiable by cytoplasmic biotinylation or phosphorylation. Phosphorylation of the substrate RRRSLG by PKA was most compatible with the cell-penetrating peptide polyarginine, and detectable with a phospho-specific antibody. Phosphorylation was demonstrated to occur intracellularly when the reporter-CPP was treated on cells at high, known cell-penetrating concentrations and not at lower concentrations when peptide is localized in endosomes. Detection of pre-phosphorylated and kinase-inhibited controls demonstrated a wide and tunable detection range, at least as low as 2 μM cell-treated peptide. Chloroquine and methyl-beta cyclodextrin did not trigger efficient endosome escape of 2 μM phosphorylatable CPP, consistent with lack of *in vivo* efficacy. This assay has promise for screening different compound libraries for endosome escape and improving our understanding of intracellular delivery.

5.2. Introduction

Nanocarriers represent a vast improvement over current small molecule therapeutics because of their potential to concentrate drug action on desired tissue sites and reduce off-target effects systemically. They would be especially useful for cancer treatment, in which the maximum tolerable toxicity typically determines the level of dosing. However, the translation of nanoparticles to clinical therapeutics faces a variety of barriers, especially in efficient drug delivery. Nanoparticles are designed to carry large amounts of cargo and shield them from inhospitable extracellular environments and activity at non-targeted sites. Nanoparticles such as magnetic beads, liposomes, dendrimers, and quantum dots range in size from 1 to 1000 nanometers. However, this size impediment restricts the molecules from freely diffusing through cell membranes, as many small molecule drugs and dyes do. Their large size prevents accessibility to intracellular targets in the case of therapeutic drugs, and it limits their intracellular accumulation, which is often necessary for imaging. As a result, they must be specially engineered with devices for intracellular delivery.

Cell penetrating peptides, described in Chapter 6, represent a promising mechanism of intracellular delivery. The intracellular route of uptake of CPPs, whether through endocytic uptake into vesicles or direct membrane translocation into the cytosol, has been disputed based on discrepant findings about the temperature dependence and rate of uptake (Vives, Brodin et al. 1997, Polyakov, Sharma et al. 2000) A reevaluation of these publications, however, demonstrated that evidence of direct membrane translocation was likely an artifact of cell permeabilization in the experimental protocol, rather than the true mechanism of uptake in living cells (Richard, Melikov et al. 2003).

Subsequent studies suggest that the main routes of CPP uptake likely include different types of endocytosis and nonspecific macropinocytosis (Fittipaldi, Ferrari et al. 2003, Wadia, Stan et al. 2004). They typically remain trapped in these compartments, though at concentrations in the micromolar range, many CPPs have been found to reach the cytosol (Potocky, Menon et al. 2003).

Since the discovery of the membrane-associative behavior of these class of peptides, a variety of large payloads have been conjugated to them as a means for intracellular delivery, for instance, nanoparticles such as magnetic beads (Josephson, Tung et al. 1999), liposomes of ~ 200 nm in diameter (Torchilin, Rammohan et al. 2001), and quantum dots (Ruan, Agrawal et al. 2007). Although CPPs alone are able to traverse biological membranes at high concentrations, when conjugated to large cargo, they become trapped in endosomal compartments (Ruan, Agrawal et al. 2007). However, in order to be effective carriers of drug or imaging payloads, nanoparticles must escape the endosome, enabling them to elude export from the cell, avoid degradation upon vesicle acidification, reach cytosolic or nuclear targets, and accumulate to effective concentrations. Nanoparticles therefore require development of a mechanism for cytosolic delivery.

In previous studies, endosomal escape of different cargo has been somewhat enhanced by the conjugation of peptides. Some of these peptides have been isolated from the coat proteins of endocytosed viruses, and others have been designed based on proposed escape mechanisms (Plank, Oberhauser et al. 1994, Wadia, Stan et al. 2004, Lundberg, El-Andaloussi et al. 2007). The best-studied published sequences that report endosome escape include INF7 (an improved version of HA2):

GLFEAIEGFIENGWEGMIDGWYG (Plank, Oberhauser et al. 1994), EB1: LIRLWSHLIHIWFQNRRLKWKKK (Lundberg, El-Andaloussi et al. 2007), GALA: WEAALAEALAEALAEAHLAEALAEAALEAAA (Li, Nicol et al. 2004), and LAH4-L1: KKALLAHALHLLALLALHLAHALKKA (Mason, Leborgne et al. 2007). Though these peptides have been shown to moderately improve delivery of CPP-linked nucleic acids and proteins, the assays used, such as DNA translation, are designed to indirectly detect and amplify small changes, while the majority of cargo molecules remain entrapped or become exported (Kaplan, Wadia et al. 2005). Furthermore, in the application to pharmaceutical delivery, endosomal entrapment, especially of large molecules, remains the rate-limiting factor (El-Sayed, Futaki et al. 2009).

One major obstacle in the development of improved endosomolytic peptides for payload delivery is the lack of an easy and direct quantitative assay that can gauge efficiency by measuring the percentage of peptide-cargo delivered to the cytoplasm. Most current assays used to test endosomolytic function measure the ability of peptides or other agents to transfect conjugated nucleic acids, elicit a biological response using a bioactive protein, or disrupt liposomes, each of which introduce confounding factors, such as peptide charge disruption, complex dissociation, cytoplasmic diffusion, nuclear uptake, or a nonlinear readout (Tseng, Liu et al. 2002, Moore, Sheppard et al. 2008). Membrane disruption assays fail in their inability to replicate the intracellular and endosomal environments, and each of these assays can yield vastly different, sometimes contradictory results (Tseng, Liu et al. 2002). Furthermore, these assays do not directly quantify the fraction of cargo molecules that reach the cytoplasm or nucleus. None of them can be used for high-throughput selection of efficient endosomolysis.

Assays developed to quantify cytoplasmic localization of CPPs have not generally been used to test other peptides, molecules, or methods for endosomolytic function, nor coupled to screens to find molecules that enhance endosomal lysis. One assay that was developed to directly quantify cytoplasmic concentrations of Tat peptide used a microanalytic system of capillary electrophoresis coupled with mass spectrometry to quantify cytoplasmic phosphorylation of releasable kinase substrates in single cells (Soughayer, Wang et al. 2004). However, such difficult detection methods and small scale limit its application to screening compounds. It has hence only been used to test a few new CPPs in one published report (Aussedat, Sagan et al. 2006). We took a similar, but unique approach to develop a cell-based system to assay the efficiency of test endosomolytic peptides or other agents, which can also be adapted to identify novel peptides through functional screening.

In order to generate an assay to quantitate the efficiency of endosome escape, a scheme was developed in which escaping peptide could be measured by cytoplasmic enzyme modification, such as cytoplasmic biotinylation or phosphorylation by an endogenous kinase (Figure 5.1). A peptide substrate for the enzyme is linked to a cell-delivering molecule, which may induce uptake into vesicles or direct cytoplasmic delivery, such as a CPP. Alternatively, the CPP may be tethered to one end of the probe via a releasable linker. The reporter may be linked to a cargo, such as an imaging agent or drug. If the cell-uptake domain is insufficient to deliver the conjugate across either the endosome or plasma membrane, an agent, such as a peptide or small molecule, to induce endosome escape is directly conjugated or treated exogenously. If the reporter reaches the cytoplasm, the peptide substrate becomes enzymatically modified with a small molecule,

such as a biotin or a phosphate, by the cognate cytoplasmic enzyme, biotin ligase or a kinase. Biotinylation may be assayed in cells exogenously expressing *E. coli* biotin ligase because it is more efficient and the substrate can be encoded in a smaller sequence than mammalian endogenous biotin ligase (Beckett, Kovaleva et al. 1999, de Boer, Rodriguez et al. 2003). Thus, following cell lysis, the amount of conjugate that reaches the cytoplasm and becomes modified can be quantified using streptavidin or a phospho-specific antibody, linked to horseradish peroxidase (HRP). This method enables the assay to be employed as a high-throughput screen for endosomolytic function and also creates a handle by which to separate and retain functional molecules from mixed libraries, which will be discussed in the subsequent chapter.

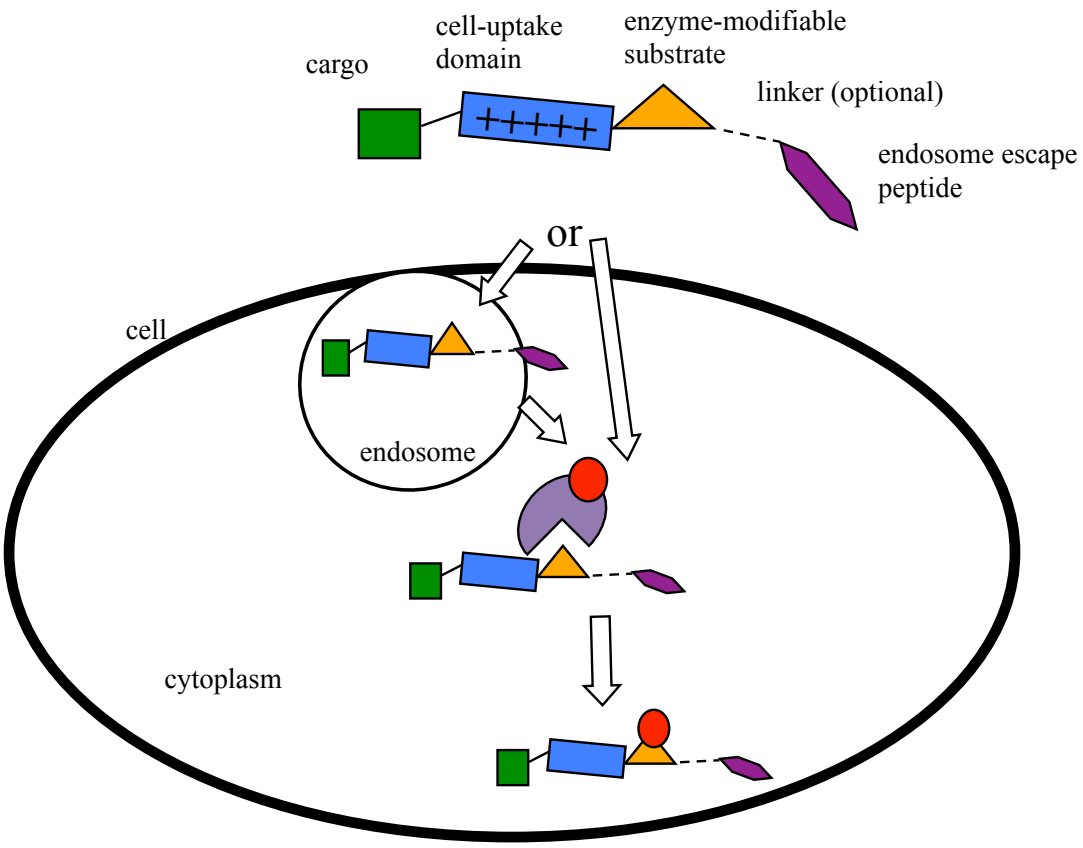

Figure 5.1. Endosome escape assay by cytoplasmic enzyme modification. A cargo (green) such as a drug, dye, or other reporter is linked to a molecule that induces uptake into endosomes, such as cell-penetrating peptide (CPP) which is positively charged (blue bar), alongside an enzyme-modifiable substrate (orange triangle). If the CPP induces endocytic uptake into cells, then another potential endosome-escaping peptide (dark purple) is directly conjugated or an unconjugated drug would be co-treated with reporter. If the conjugate or drug acting on the conjugate induces its translocation across either the endosomal membrane or plasma membrane, an enzyme expressed in the cytoplasm of the cell (light purple) modifies the substrate peptide with a small molecule (red circle), enabling quantification of the amount of peptide that escapes.

5.3. Methods

5.3.1. Peptide synthesis

Peptides were synthesized using an automatic peptide synthesizer (PTI Prelude) using standard protocols for fluorenylmethoxy-carbonyl (Fmoc) solid-phase synthesis. Peptides were purified using reverse phase high performance liquid chromatography, HPLC, vacuum dried and dissolved in water or DMSO. The biotinylatable reporter

sequence was c-GLNDIFEAQKIEWHES-$CONH_2$ (cys-AP). The phosphorylatable reporter was FAM-rrrrrrRRRSLGc, and the unphosphorylatable control was FAM-rrrrrrRRRALGc-$CONH_2$. D-amino acids are represented by lower case type, and $CONH_2$ represents a C-terminal amine.

5.3.2. Peptide labeling

Purified cys-AP was dissolved in Na-MOPS and reacted with excess carboxyfluorescein-maleimide in DMSO, using sonication to solubilize at room temperature overnight. Labeled peptide (M.W. 2502) was purified by HPLC eluting with a gradient of 10-90% acetonitrile-water-0.05% TFA in 25 minutes. Collected fractions were pooled, lyophilized, and dissolved in water.

Purified FAM-rrrrrrRRRSLGc and FAM-rrrrrrRRRALGc (M.W. 2126) were dissolved in dry DMF at 1.4mM and 5-fold excess biotin maleimide (3.1mg in 1mL reaction) was added with 10uL 4-methylmorphiline, gassed with nitrogen, sonicated to dissolve, and reacted in dark at 25°C O/N. Labeled peptides were purified by HPLC eluting with a gradient of 10-90% acetonitrile-water-0.05% TFA in 25 minutes. Collected fractions were pooled, lyophilized, and dissolved in water.

5.3.3. Peptide biotinylation

10 μM FAM-AP was incubated with 1 μL purified BirA enzyme in buffers containing ATP and free biotin provided by the manufacturer (Avidity) in a final volume of 10 μL at 37°C overnight.

5.3.4. Peptide phosphorylation

300 μM FAM- r_6R_3SLGc-biotin was reacted in 1x PKA buffer (NEB) with 1mM ATP, and 12 μL PKA enzyme in 200uL total volume at 37°C overnight.

5.3.5. Enzyme Linked Affinity Assay

5.3.5.1. Detection of peptide biotinylation

Biotinylated and unbiotinylated FAM-AP were serially diluted from 2 μM - 2 nM in sodium bicarbonate buffer, pH 9.4 in a 96-well plate and incubated at 4°C for 4 hr. Wells were rinsed 3x with water, blocked with 2% bovine serum albumin (BSA) in PBS, for 1 hr at 25°C, and rinsed. Wells were incubated with streptavidin-HRP (Life Technologies) diluted 1:1000 or anti-fluorescein antibody (Sigma) diluted 1:50 in blocking buffer at 4°C overnight, and washed with water and blocking buffer. Secondary anti-mouse-HRP, diluted 1:2000 in blocking buffer was subsequently incubated on anti-fluorescein-treated wells, and the others were maintained in blocking buffer, for 2.5 hr at 25°C, then washed 3x with water. Fluorogenic peroxidase substrate Quanta Blu (Thermo Pierce) was added to wells and fluorescence was measured at 325nm excitation, 420nm emission on a plate reader (Safire, Tecan).

5.3.5.2. Detection of peptide phosphorylation

Cell lysates containing FAM-r_6R_3SLGc-biotin, or control peptide FAM-r_6R_3ALG-c-biotin were treated on preblocked streptavidin-coated plates (Life Technologies) at 4°C overnight. Cells were pretreated with 10 μM forskolin or H-89 for 3 hr and subsequently cotreated with peptide in serum-free media. Cells were treated with 200 μL lysis buffer containing protease and phosphatase inhibitor cocktails at 37°C for 5-10 min and pipetted vigorously. 150 μL of lysate was transferred to a streptavidin-coated

plate for phosphorylation detection and 50 μL of lysate was plated on a streptavidin plate for total peptide detection; plates were kept at 4°C overnight. Plates were rinsed 4x with 100 μL/well PBS 1% BSA 0.05% Tween. Rabbit antibody to RXXS* (Cell Signaling 110B7E) was treated at 1:500 in wash buffer for 2 hr at 25°C, washed 3x, and treated with anti-rabbit-HRP, diluted approximately 1:12,000-25,000 in wash buffer for 2 hr at 25°C. Mouse antibody to fluorescein (Sigma) was treated at 1:2,000 in wash buffer for 2 hr at 25°C, washed 3x, and treated with anti-mouse-HRP diluted 1:5,0000 in wash buffer for 2 hr at 25°C. Plates were developed with TMB 1-Step Ultra (Life Technologies) and measured on a plate reader (Tecan) at 650 nm absorbance.

5.3.6. Confocal imaging

HeLa cells (ATCC) were plated at 15,000 cells/well on glass-bottom 96-well plates and grown overnight in DMEM media (CellGrow) containing 10% fetal bovine serum (FBS). Cells were rinsed with serum-free imaging buffer, containing phenol red-free DMEM with HEPES and GlutaMAX (Gibco), and peptide was treated on cells for 40 minutes in serum-free imaging buffer. Cells were rinsed and imaged with imaging buffer containing 10% FBS and 20 μg/ml Calcein Blue AM ester (Life Technologies), a cell viability marker. Cells were imaged on a Zeiss 5 Live line scanning confocal microscope using a 40X water objective. FAM was visualized with a 488nm excitation laser and a 505nm longpass emission filter and Calcein Blue was imaged with a 405nm excitation laser and 415-450nm emission filter.

5.3.7. Cell viability assay

HeLa cells were plated at 15,000 cells/well in a 96-well plate and grown overnight in DMEM media with 10% FBS. Cells were rinsed with serum-free buffer, treated with up to 50 μM peptide in serum-free DMEM for 30 minutes. Cells were rinsed and serum-containing media was replaced with CellTiter96 reagent (Promega), and incubated for 2-3 hours at 37°C. 490 nm absorbance was measured on a plate reader (Tecan).

5.4. Results

5.4.1. Validation of biotinylation assay for endosome escape

To assay the detection potential for endosome escape to be measured by biotinylation, BirA acceptor peptide (AP) sequence GLNDIFEAQKIEHWES was synthesized with an N-terminal carboxyfluorescein (Beckett, Kovaleva et al. 1999). Purified peptide was biotinylated *in vitro* with purified BirA enzyme, biotin, and ATP Liquid chromatography-mass spectrometry (LC-MS) was used to verify complete peptide biotinylation. Unbiotinylated and biotinylated peptide were distinguished by elution roughly 1 minute apart of the UV chromatogram traces, corresponding to presence of both peptide at 211-219 nm and carboxyfluorescein fluorescence at 430-450 nm (Figure 5.2 and 5.3). Unbiotinylated peptide had a theoretical mass of 2502 Da and biotinylated 2746 Da, and each peak contained ions with correct mass-to-charge (m/z) ratios (1252 and 1365 Da, respectively). No unbiotinylated peptide was detected in the biotinylated sample, as determined by the absence of a 1252 Da mass peak at 18.4-18.7 minutes.

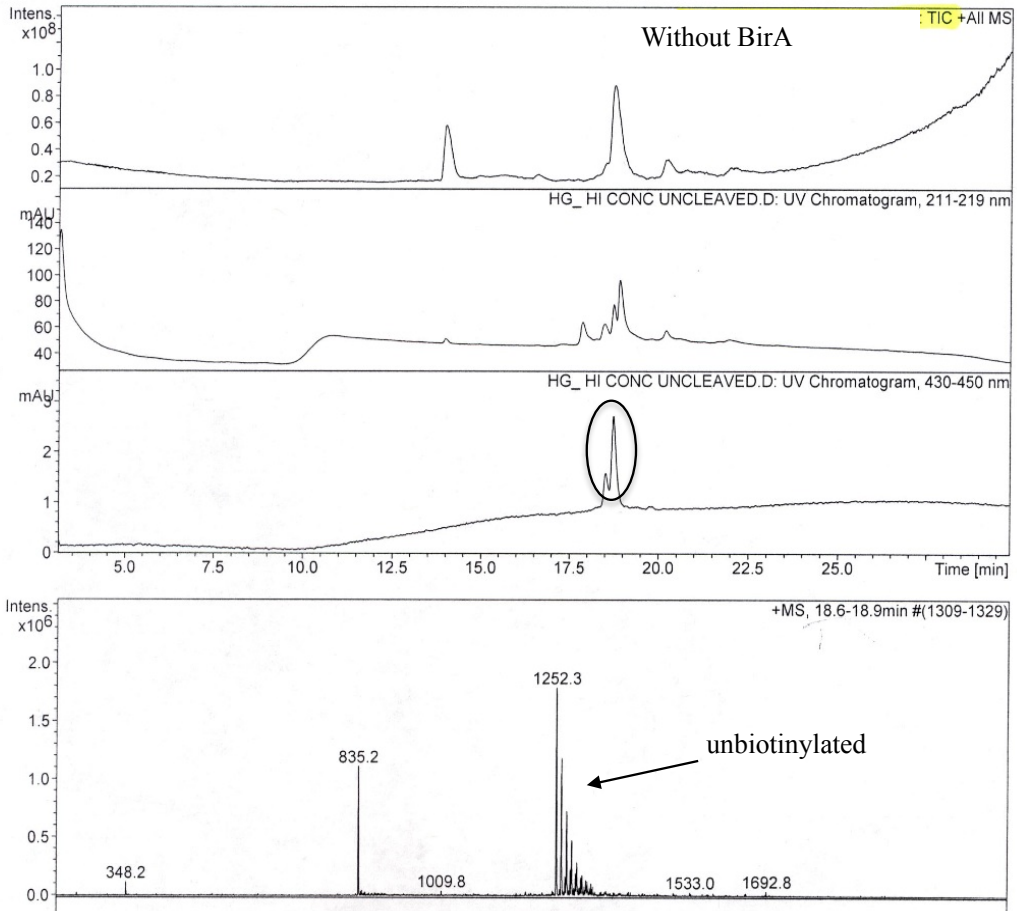

Figure 5.2. LC-MS trace of unmodified FAM-labeled biotin acceptor peptide. Upper trace shows the liquid chromotagraphy trace of all mass peaks, middle trace shows the UV chromatogram of all peptides and proteins, using the 211-219 nm absorbance with a peak between 18 and 19 minutes, third trace shows the UV chromatogram of FAM absorbance, 430-450 nm, which shows a matching peak. Bottom two mass spectra show the mass peaks at the FAM-fluorescent peak eluting at 18.6-18.9 min, predominately a mass of 1252.3, which is the correct mass/charge (m/z) for the unbiotinylated peptide.

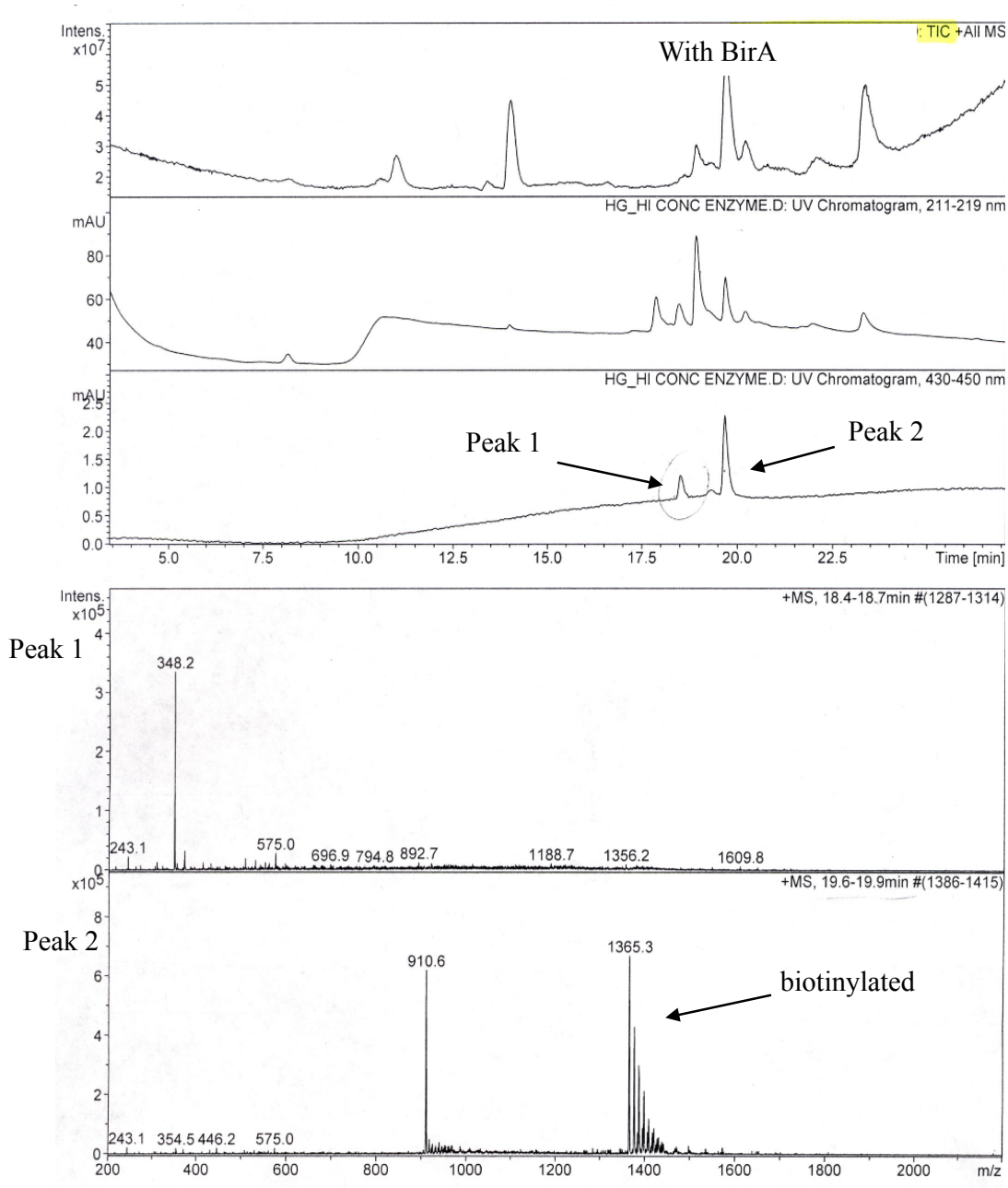

Figure 5.3. LC-MS trace of biotinylated FAM-labeled biotin acceptor peptide. Upper trace shows the UV chromatogram, middle trace shows the UV chromatogram of all peptides and proteins, using the 211-219 nm absorbance, third trace shows the UV chromatogram of all molecules with FAM absorbance, 430-450 nm. The upper ion mass spectra show the mass peaks at the FAM-fluorescent peak eluting at 18.4-18.7 min, that is notably absent of the unbiotinylated mass peak (1252), while the lower ion mass spectra shows the mass of the FAM peak at 19.6-19.9 min, containing ions of 1365 Da, which is the correct mass/charge (m/z) for the biotinylated peptide.

To measure the detection range by an enzyme-linked affinity assay, biotinylated and unbiotinylated peptide between 0.002 and 2 μM were coated in a 96-well plate, incubated with streptavidin-HRP, and a fluorescent peroxide substrate for detection. Signal was linear within the peptide detection range probed (Figure 5.4 A). To verify equal total peptide was plated and because direct fluorescence measurements of carboxyfluorescein showed low signal, wells were treated with anti-fluorescein antibody quantification was performed similarly on uncoated plates and showed high signal that increased 5-fold within the peptide range tested, suggesting that it was near signal saturation (Figure 5.4 B). Thus, less antibody or no stacking may improve the linearity of the signal for peptide in this range, while lower levels of peptide recovery may be more effectively detected with these conditions.

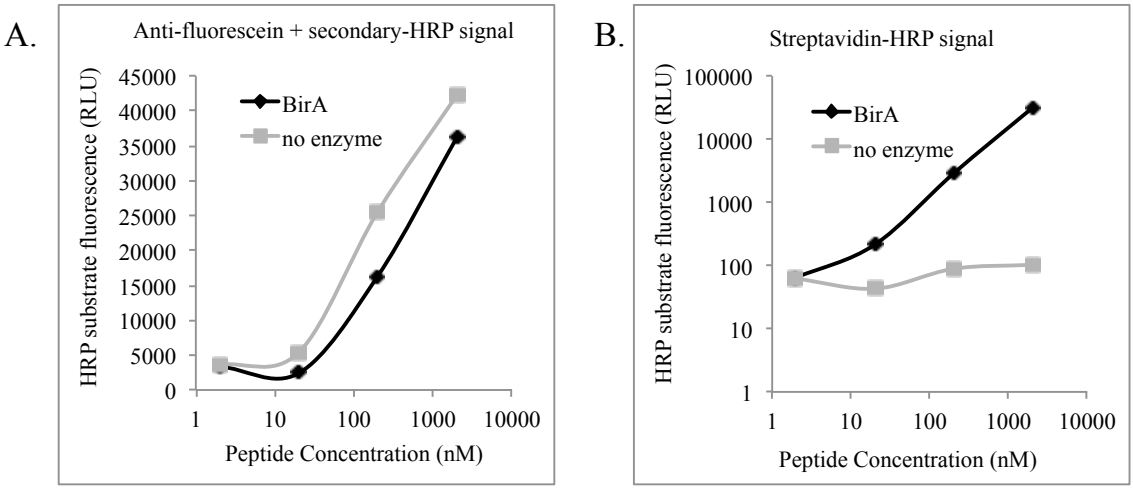

Figure 5.4. Preliminary testing of peptide biotinylation with purified BirA shows limits of biotinylation detection in low nM range. 10 μM acceptor peptide was reacted with purified BirA and free biotin at 37°C overnight. Serial dilution of reaction mixture plated in bicarbonate buffer, pH 9.4. **A.** Biotinylation detected by incubation with streptavidin-HRP. **B.** Total peptide detected by incubation with anti-fluorescein and HRP-conjugated secondary. Raw data for each was background subtracted for no peptide and no primary antibody controls.

Preliminary experiments to evaluate peptide detection when mixed with cell lysates showed low signal, likely due to saturation of the plate binding surface

preferentially by larger cellular proteins (data not shown). Thus, adding an additional peptide-capture component for specific post-lysis recovery was desirable. A new molecule was made adding a second fluorescent dye, Cy5 added for this reason, as well as the cell-penetrating peptide r9, in order to test intracellular biotinylation. The FAM-r_9-AP-c-Cy5 peptide was treated on cells but found to precipitate even under weak buffer conditions (data not shown). Though the peptide was soluble in water, cells were not were not viable under these conditions. Thus, although this approach has the potential to detect endosome escape even down to low nanomolar concentrations, it was not pursued due to its incompatibility with the r9 peptide.

5.4.2. Phosphorylatable reporter detects cytoplasmic localization

As an alternate approach, peptide phosphorylation was developed as a means of detecting cytoplasmic peptide. A new reporter was designed that would minimally encode both the CPP and the phosphorylatable substrate of an endogenous kinase that was also amenable to detection with existing phospho-specific antibodies, in tandem with a fluorophore for detection and a purification handle for peptide recovery on either end (Figure 5.5A). To fit these criteria, the sequence FAM(K)-r6R3SLGc-(mal.)biotin was designed (Figure 5.5B). The first six arginines of the CPP were preserved in their typical d-amino acid form to avoid degradation, while the last three were synthesized in L-form amino acids to function as part of the phosphorylatable sequence RRRSLG, in which the serine is modified by protein kinase A and recognized by a phospho-specific antibody selective for RXX(S*/T*). FAM was added for visualization and total peptide quantitation and biotin was added for efficient peptide recovery and assay plating post-cell lysis.

A.

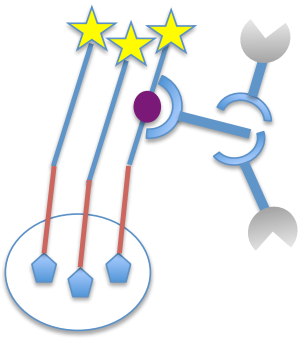

B. FAM-rrrrrrRRRSLG-c-(mal)-biotin

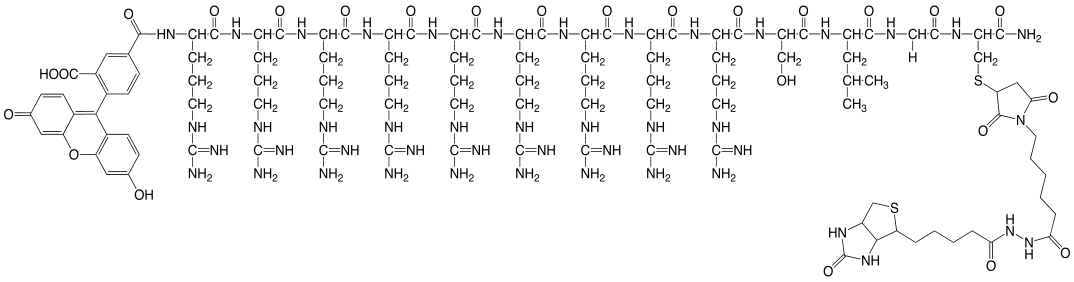

Figure 5.5. Schematic and chemical structure of a phosphorylatable endosome escape reporter, FAM-rrrrrrRRRSLGc-biotin. A. A CPP and/or endosome escaping peptide (red bar) is conjugated to a substrate peptide (blue bar) of a cytoplasmic enzyme. A modification-specific antibody (blue) linked directly or via a secondary antibody contains HRP (grey) for ELISA detection. A fluorescent dye (yellow star) is conjugated to one end of the peptide to facilitate intracellular imaging and subsequent quantification of total peptide. A coated plate specifically captures a small tag on the peptide (blue pentagon) from the total cell lysate. **B.** Fluorescein is used to quantitate total recovered peptide or to image live cells. The CPP r9 (r6R3) escapes from endosomes at high concentrations. The first six arginines are in d form, and the latter three are in L form to overlap with the phosphorylation domain using natural amino acids for enzyme recognition. RRRSLG is a substrate of Protein Kinase A (PKA) substrate, in which the serine is phosphorylated when exposed to PKA enzyme, ATP, and phosphate. Biotin, conjugated via maleimide and a linker, is attached in order to recover peptide specifically post cell lysis using a streptavidin-coated plate.

In order to test whether the reporter was phosphorylated at mid-μM concentrations where endosome escape or direct plasma membrane translocation of CPPs is known to occur, cells were pretreated for 3 hours with 25 μM forskolin to activate PKA and negative control wells were treated with 10 μM PKA inhibitor H-89. The phosphorylatable CPP reporter peptide FAM-r_6R_3SLG-c-biotin was added at 0.4 - 50 μM on cells in serum-free media with forskolin or H-89. As a positive control, pre-

phosphorylated peptide was treated on cells in the presence of H-89. In addition, a second negative control was included, an unphosphorylatable peptide, with a serine to alanine mutation co-treated on cells with forskolin. After 30 minutes, cells were washed with HBSS and lysed in the presence of phosphatase and protease inhibitors, and lysates were plated on immobilized streptavidin. Phosphorylated peptide was detected by ELISA with phospho-specific antibody. Pre-phosphorylated control peptide showed a detection range of peptide phosphorylation that was distinguishable from the negative control as low as 2 μM peptide (Figure 5.6). Phosphorylation of the reporter peptide FAM(K)-r6R3SLGc-(mal.)biotin occurred at 30 and 50 μM. Phosphorylation was not evident above the level of the negative controls at lower concentrations. Of the two negative controls, phosphorylatable peptide co-treated with H-89 showed higher background signal, possibly due to insufficient kinase inhibition or inhibitor wash-off or of some non-phosphorylation specific binding of the antibody to the serine-containing peptide.

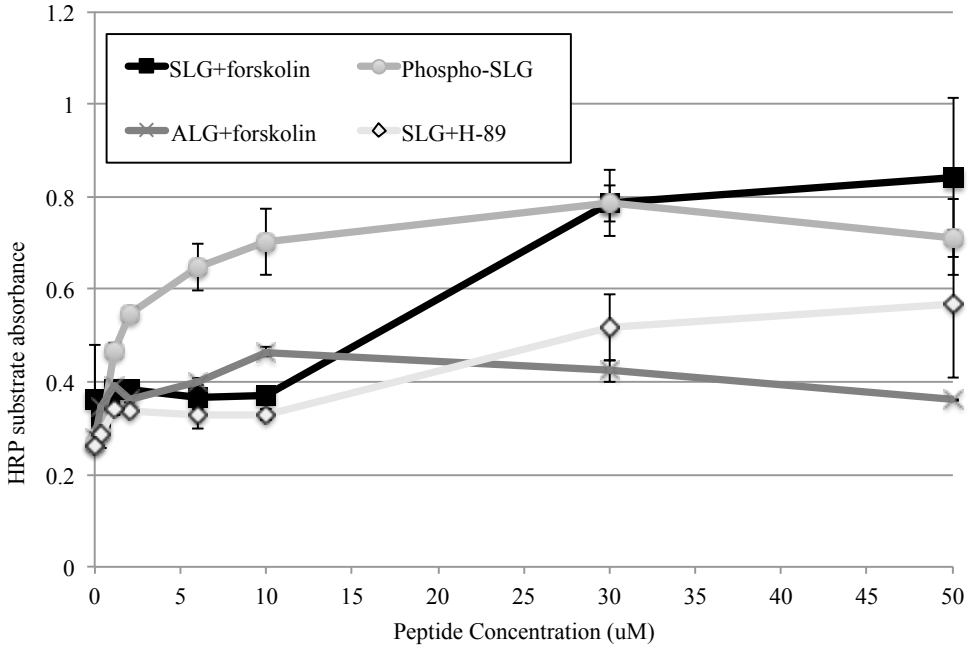

Figure 5.6. Phosphorylatable endosome escape reporter peptide can be used to measure the proportion of cytoplasmic peptide at in the low μM range of concentrations. FAM-r_6R_3SLG-c-biotin and forskolin-treated was treated on cells, and lysates were incubated on streptavidin-coated plates and probed with phospho-specific antibody, diluted 1:1000, and secondary HRP-anti-rabbit, diluted 1:3000. Plate reader was used to measure 650 nm absorbance of TMB 1-step Ultra and after >10 min 370 nm absorbance. Mean signal of 3 independent biological replicates and standard deviation (error bars) are shown.

To measure cell cytotoxicity, the reporter peptide was treated on cells in serum-free media and cell viability was assayed with a colorimetric indicator of metabolism. Cell viability was largely unaffected at low peptide concentrations but was reduced down to 50% after treatment with 30 and 50 μM peptide (Figure 5.7). This supported that cytoplasmic translocation and reduction of cell viability occur at high treatment concentrations.

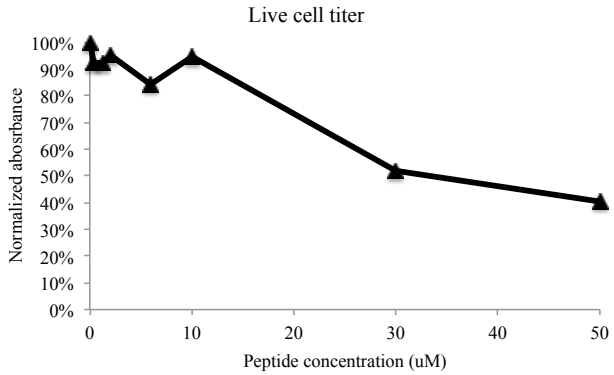

Figure 5.7. Peptide has some toxicity at mid μM concentrations. HeLas were plated at 15,000 cells per well and allowed to settle overnight. Cells were treated with up to 50 μM peptide for 30 minutes, and cell titer was assayed with an MTS colorimetric indicator by standard protocol. Signal was normalized as percentage to negative control wells containing no cells and positive control wells containing cells with no treatment.

Next, in order to assay the effects of agents previously reported to elicit or block cytoplasmic delivery, the phosphorylation assay was repeated and, additionally, the reporter peptide was co-treated with chloroquine at 10, 50, and 150 μM or 5% serum. Again, phosphorylation was evident in the pre-phosphorylated control peptide sample and the experimental sample, above the level of the two unphosphorylated controls between 20 and 50 μM, but was poorly differentiated at lower peptide concentrations (Figure 5.8 A). No significant increase in phosphorylation was apparent with increasing chloroquine treatment, and there was a decrease in signal at high peptide co-treated with 150 μM chloroquine (Figure 5.8 B). When reporter peptide was co-treated between 10-50 μM with 5% serum, phosphorylation signal was much lower.

Assaying total signal by anti-fluorescein ELISA, substrate developed quickly relative to the anti-phospho detection and signal was similar or increasing up to 10 μM, and decreased at higher peptide treatment concentrations (Figure 5.8 C). These observations and results suggest that total peptide signal was likely saturated. However,

in wells co-treated with 10-50 μM and 150 μM chloroquine, and in all wells co-treated with 5% serum, lower peptide recovery was evident (Figure 5.8 D). The former result was consistent with observations of cell rounding and detachment, indicating toxicity (data not shown).

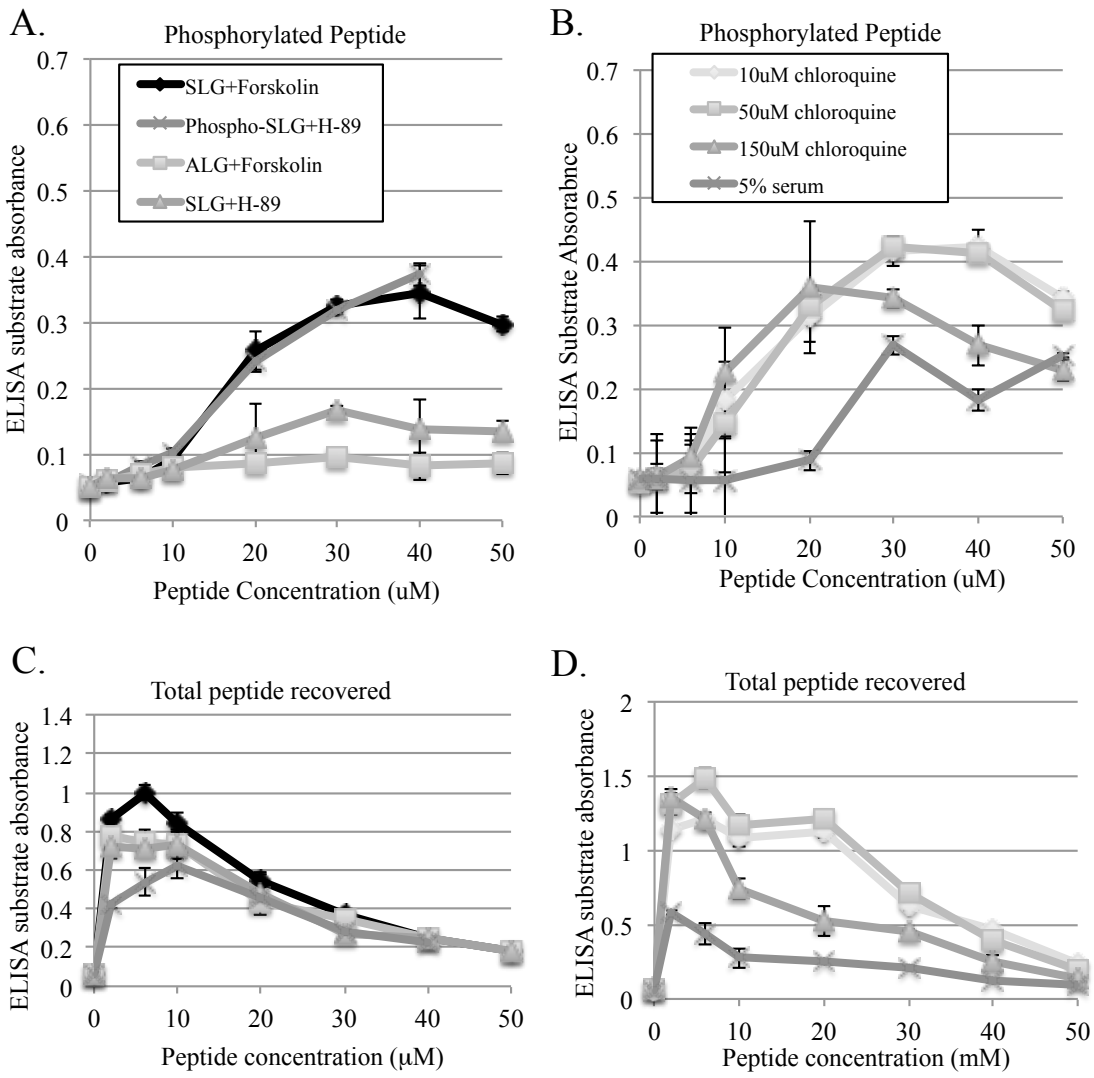

Figure 5.8. Increasing chloroquine shows no clear enhancement of endosome escape; addition of serum shows reduced phosphorylation and peptide recovery. Peptide captured on streptavidin plate phosphorylated peptide detected with phospho-specific antibody (anti-RXXS*) diluted 1:500 (in **A** and **B**) and total peptide detected with anti-fluorescein antibody dilute 1:2,000 (in **C** and **D**), and appropriate HRP labeled secondary and colorimetric substrate. **A.** and **C.** Phosphorylatable reporter (SLG+Forskolin) without additional agents shows comparable phosphorylation to positive control (Phospho-SLG+H-89) between 20 and 50 μM and significant phosphorylation not evident in negative controls (SLG+H-89 and ALG+Forskolin). **B.** and **D.** Phosphorylatable reporter (SLG+Forskolin) treated with 10, 50, or 150 μM chloroquine shows comparable phosphorylation to untreated control and higher phosphorylation that reporter co-treated with 5% serum. Measurements from triplicate samples were averaged and the mean and standard deviation (error bars) were plotted.

Because the anti-fluorescein ELISA signal seemed to be saturated, peptide quantification was assayed by direct fluorescence measurement. Reporter peptide was

treated on cells for 30 minutes, cells were washed, and fluorescence was measured. Cells were then lysed and fluorescence was again measured, and finally, cell lysates were incubated on a streptavidin-coated plate, and an ELISA with anti-fluorescein antibody was performed as before. Fluorescence of peptide in whole cells and in cell lysates increased approximately linearly with treated peptide concentration, while at lower concentrations of peptide, signal was better separated in lysates than in cells (Figure 5.9 A and B). ELISA using anti-fluorescein and a secondary antibody again showed a peak of high signal at the lowest peptide treatment concentration, and decreasing signal at higher concentrations (Figure 5.9 C). This data supported the hypothesis that peptide treatment concentrations at mid-μM are more accurately quantified by fluorescence; however, low or sub-μM peptide concentrations may be better assayed by ELISA.

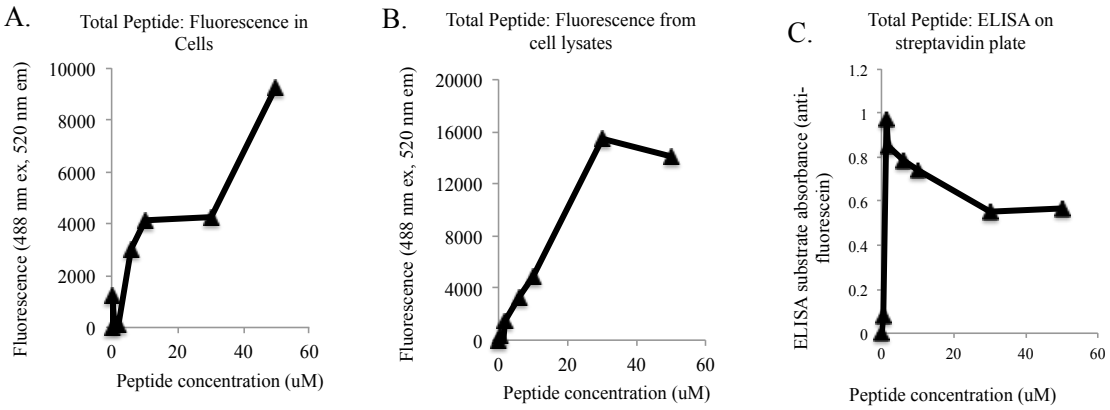

Figure 5.9. Total peptide signal appears more linear at mid-μM concentrations when assayed by direct fluorescence but may be better detected at lower concentrations by ELISA. A. Fluorescence of peptide was measured after treatment on cells. Cells were rinsed and measured at 488 nm excitation, 520 nm emission in buffer. **B.** Peptide fluorescence was measured following cell lysis. **C.** Cell lysates were incubated on a streptavidin-coated plate and peptide was detected by incubation with an anti-fluorescein antibody and HRP-labeled secondary.

To examine endosome escape at lower reporter peptide concentrations, ELISA was carried out similarly for higher signal development. Phosphorylation signal between the positive and negative controls at 1, 5, 10, and 20 μM, showed a dynamic range of 7,

9.8, 2.4, and 1.2-fold respectively with minimal variability in signal (Figure 5.10). The reporter peptide showed little or no phosphorylation above the inhibited control at 1 and 5 μM, and high phosphorylation similar to the positive control at 10 μM. Increasing signal of the negative control at 10 and 20 μM peptide, suggests that kinase inhibition was likely incomplete.

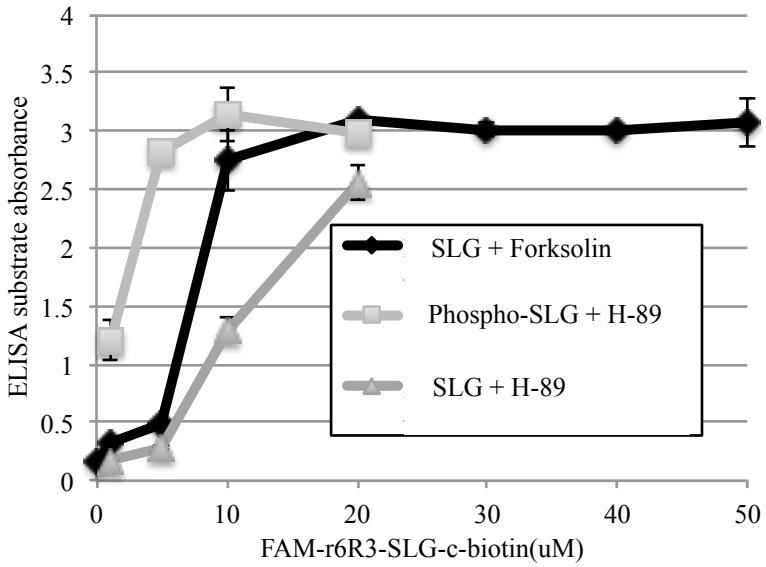

Figure 5.10. Phosphorylatable endosome escape reporter peptide can be used to measure the proportion of cytoplasmic peptide at in the low μM range of concentrations. FAM-peptide was treated on cells and ELISA was optimized for detection of low levels of phosphorylation signal. Positive and negative control peptides phospho-SLG+H-89 and SLG+H-89 were treated on cells up to 20 μM and reporter, SLG+Forskolin, was tested up to 50 μM.

To confirm that endosome escape of the reporter took place at 10 μM and higher concentrations and was not striking at lower concentrations, localization was assayed by confocal microscopy after peptide treatment on cells. Fluorescence was punctate in cells treated with 2 μM peptide and diffuse or nuclear when treated 10, 30, and 50 μM peptide (Figure 5.11). These results supported that high endosome escape occurred at 10 μM but not at 2 μM reporter.

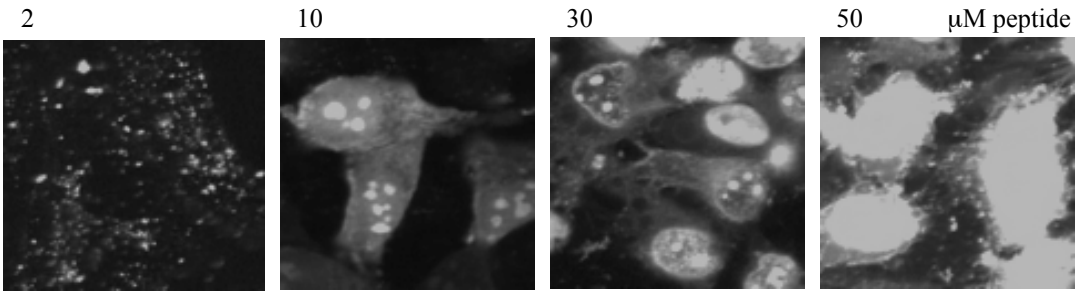

Figure 5.11. FAM-r6R3SLG-c-biotin shows concentration-dependent endosome escape. HeLa cells plated on glass bottom dishes, treated with FAM-r6R3SLG-c-biotin for 30-40 minutes in serum free media, washed with media with 10% serum 3x and imaged on confocal microscope within 1hr of washing.

To further examine chloroquine effects at lower peptide concentrations, peptide was treated at 2 μM for 30 min with chloroquine at a range of concentrations. Phosphorylation signal was scaled to the signal of the pre-phosphorylated positive control in order to roughly estimate percent of peptide phosphorylation and signal from samples treated peptide and inhibitor (H-89) was used as background signal for subtraction. Evidence of slight peptide phosphorylation (~5%) above the level of the PKA-inhibited control, was evident in non-treated wells. Peptide phosphorylation trended upward slightly from 1-66 μM chloroquine, though noise was high with standard deviations varying between 5-7% (Figure 5.12 A). Total peptide remained the same across all concentrations (Figure 5.12 B). Given the high amount of variability in ELISA detection and the lack of a large upward trend across increasing chloroquine concentrations, the experiment was repeated similarly to examine reproducibility of possible slight effects. Peptide phosphorylation was again slightly higher in untreated wells (~5%) and at the lower chloroquine concentrations, increasing roughly 1% at 4.7 and 9.3 μM chloroquine, but phosphorylation signal appeared lower with 18.7 μM chloroquine and progressed downward (Figure 5.12 C). Total peptide remained the same (Figure 5.12 D). Between

the two experiments, the apparent divergence in slight upward and downward trends suggests that the signal may fall within experimental noise and suggest thats chloroquine did not induce high levels of endosome escape.

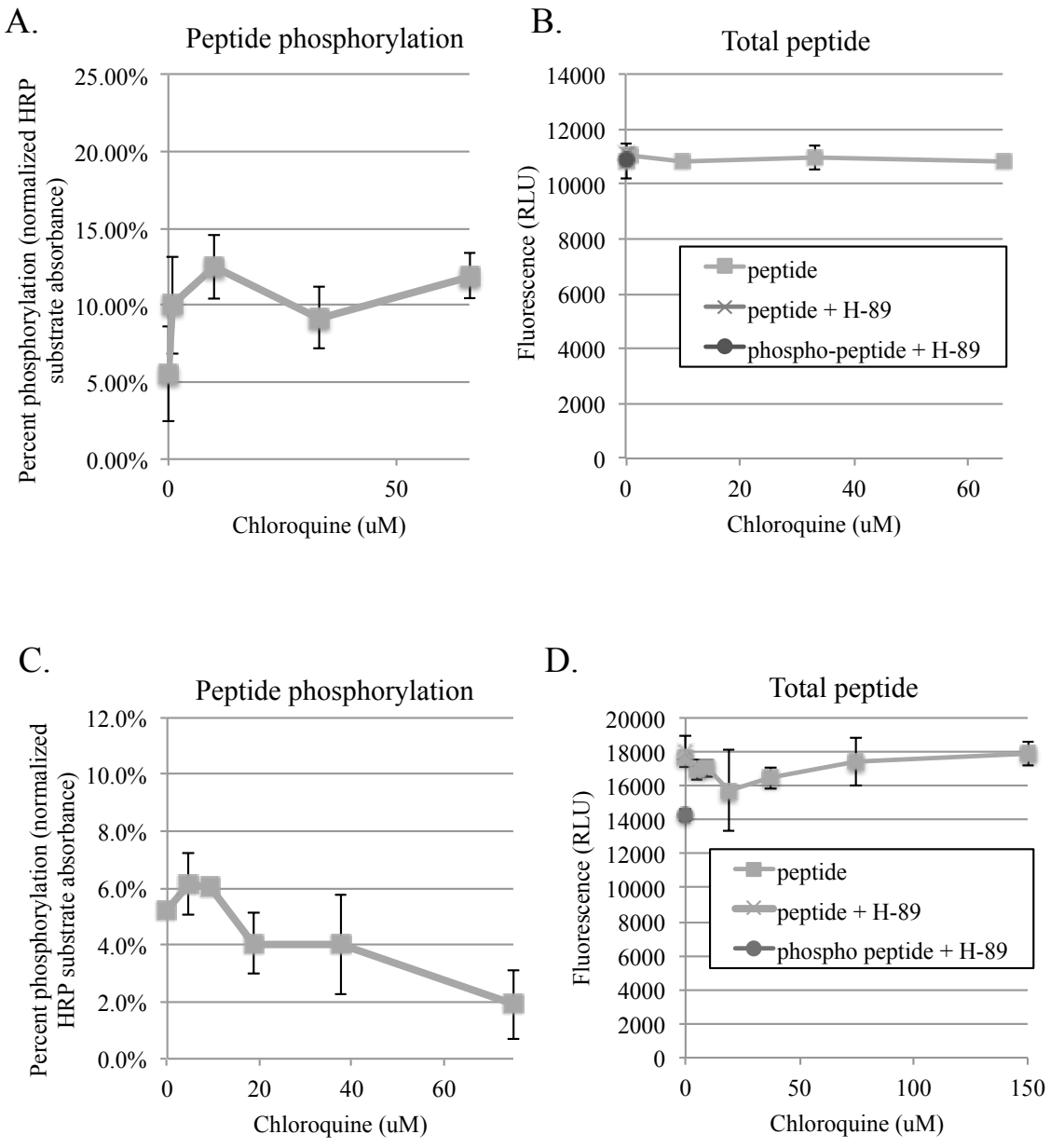

Figure 5.12. Chloroquine treatment shows minimal effects on peptide endosome escape by phosphorylation assay. Peptide and drug treated on HeLa cells for 30 min in serum free media, cells washed in media with serum, then lysed in the presence of phosphatase and protease inhibitor cocktails. Signal was background subtracted against an H-89 inhibited control, and divided by a pre-phosphorylated control.

In order to verify the lack of large endosome escape effects, peptide was co-treated with up to 150 μM chloroquine and cells were imaged by confocal microscopy. Fluorescence remained punctate across all tested concentrations (Figure 5.13). These findings supported the lack of large scale induction of endosome escape but do not necessarily preclude the possibility of low levels of escape, such as those observed in assays on the delivery of nucleic acid or protein reporters, which have the ability to demonstrate high signal upon delivery of few molecules.

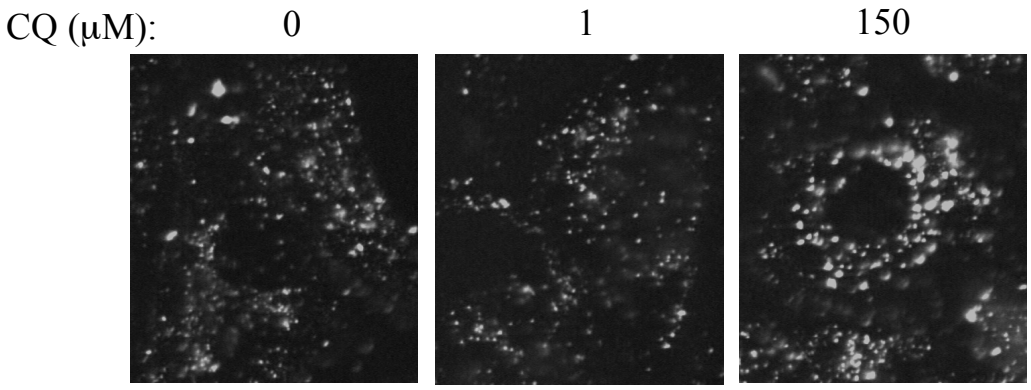

Figure 5.13. Chloroquine treatment shows minimal effects on peptide localization by confocal microscopy. Peptide and drug treated on HeLa cells for 30 min in serum free media, cells washed in media with serum, then imaged by confocal microscopy.

Another agent published to induce endosome escape of CPPs, methyl-beta-cyclodextrin (MβCD), a detergent-like molecule, was tested for its ability to induce peptide endosome escape using the phosphorylation assay (Appelbaum, LaRochelle et al. 2012). The reporter peptide was treated at 2 μM on cells and co-treated with 1-5 mM MβCD. Again, slight phosphorylation (~5%) was evident in the non-inhibited control. Phosphorylation signal increased at low concentrations (300 and 600 μM) but then dropped off to similar levels of no drug treatment and lower at higher concentrations (Figure 5.14 A). Total peptide also showed a slight increase at these concentrations

(Figure 5.14 B). Due to the detergent-like nature of the agent, it is possible that MβCD could assist in the delivery of peptide by solubilizing it; however, it is likely that such high concentrations of detergent reduce cell viability or alter membranes, which could reduce the intracellular concentration of ATP and could affect the ability of PKA to phosphorylate peptide.

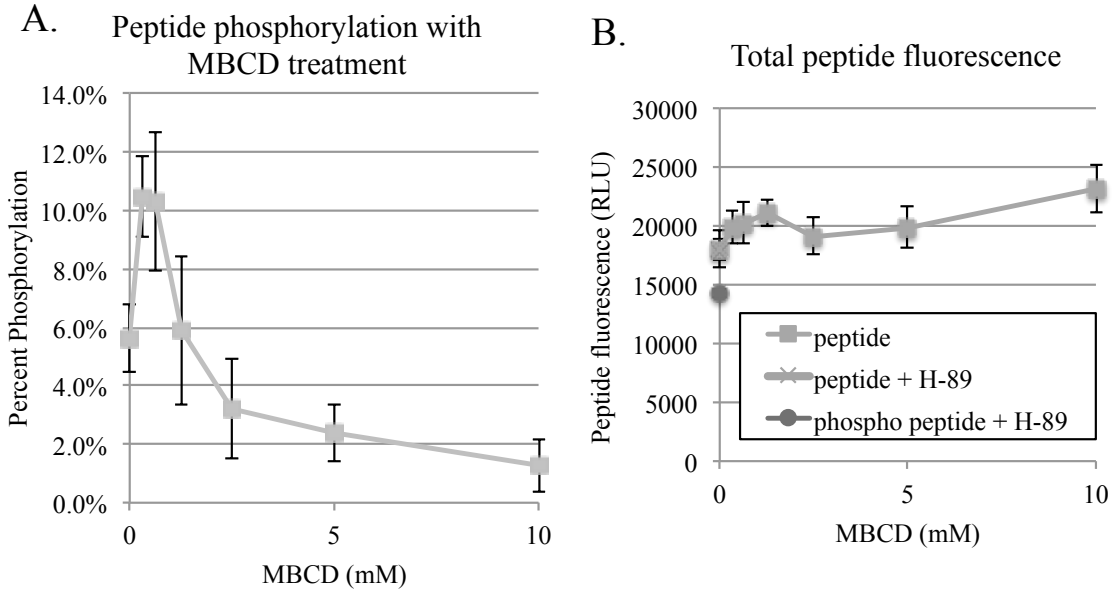

Figure 5.14. MβCD treatment shows possible slight effects on peptide endosome escape by phosphorylation assay. 2 μM FAM-r_6R_3SLG-c-biotin was treated on cells with 0-10 mM MβCD for 30 minutes. Cell lysates were collected and transferred to a streptavidin-coated plate. **A.** Phosphorylation was measured in a streptavidin-coated plated by ELISA with phospo-specific antibody. **B.** Total peptide was assayed by measuring fluorescence (488 nm excitation/ 520 nm emission). The mean of triplicate measurements was plotted. Error bars represent the standard deviation.

5.5. Discussion

To assay cargo transport across membranes and select efficient endosomolytic peptides, enzymatic modification was used as a readout for cytosolic localization of cargo in the cell, through biotinylation of an acceptor peptide and phosphorylation of a kinase substrate attached to the cargo. As a method for detection, enzymatically marked cargo

attached to functional endosomolytic peptides were detected by enzyme-linked affinity assays with streptavidin or an antibody to the phosphorylated substrate, directly or indirectly linked to horseradish peroxidase (HRP).

In preliminary experiments, a biotinylation reporter peptide was highly sensitive; however, the reporter was insoluble when coupled to poly-arginine. However, a small phosphorylatable peptide substrate was highly compatible with the CPP, along with fluorescein and biotin on each end of the peptide to enable detection and recovery from cells, post-lysis.

Treatment of a polyarginine-based phosphorylatable reporter resulted in significant cytoplasmic localization at 10 μM and higher concentrations and very low or no endosome escape at up to 5 μM peptide as determined by both confocal microscopy and ELISA for detection of reporter phosphorylation. Co-treating peptide with serum reduced endosome escape, likely by reducing uptake. The phosphorylation assay demonstrated that neither chloroquine nor MβCD triggered high levels of endosome escape of the reporter peptide when added at 2 μM.

Total peptide recovery was best quantified by measuring fluorescence from cell lysates when peptide was treated at 1 and 50 μM. In whole cells, fluorescence quantification at lower non-cytoplasmic peptide concentrations may result in lower measurements, due to high peptide concentration within small endosomes, where low endosomal pH or stacking effects could reduce carboxyfluorescein fluorescence.

To investigate this assay's detection range, controls of mixed phosphorylated and non-phosphorylated peptide in various amounts would be useful. Efforts to reduce the amount of extracellular, membrane-adherent peptide, which could skew the calculations

of percent peptide phosphorylation and relative endosome escape, such as whole cell trypsinization would also be beneficial. Ultimately, the assay is likely useful for application to panels of putative endosome escape agents and validated through confocal microscopy.

5.6. Acknowledgements

The dissertation author would like to thank:

Dr. Michael Whitney for collaboration in experimental design. Dr. Stephen Adams and Qing Xiong for synthesizing and purifying peptides. Paul Steinbach and Dr. Jessica Crisp for their assistance with imaging experiments.

CHAPTER 6: Phage Display Selection of Endosome Escaping Peptides

6.1. Abstract

Though targeted delivery of non-cell permeable therapeutics with cytoplasmic or nuclear targets has promise for the treatment of many diseases, the development of agents capable of delivering them across cell membranes is critical. A phage display selection of peptides capable of delivering large cargo across membranes was developed wherein biotinylation or phosphorylation of a displayed peptide substrate by cytoplasmic enzymes tags functional, endosome-escaping peptide-phage. Phage expressing a biotin acceptor peptide (AP) were validated to be efficiently biotinylated in cells expressing biotin ligase. Low throughput of screening was rate-limiting to selection. Subsequent optimizations were made including the creation of a new dual pIII/pVIII display platform, wherein phage have combined landscape libraries of short sequences in high-copy (~2700) on pVIII and AP is expressed in 5 copies on pIII, or alternatively a short phosphorylatable enzyme substrate is expressed in high-copy on pVIII and longer library peptide sequences are expressed in 5 copies on pIII. Lastly, the original phagemid pIII biotinylatable-library fusion in up to 4 copies was also optimized. All were validated to be cytoplasmically modifiable and recoverable, showing that these approaches have potential to find new endosome escaping sequences.

6.2. Introduction

Previous peptide screens for endosome escape, in which peptides were made synthetically and tested individually, have typically biased their diversity around a given mechanism in an attempt to enrich for functional peptide and deplete insoluble peptides (Rathinakumar and Wimley 2008). However, the mechanisms of peptide escape are still poorly understood and limiting a library to one mechanism means excluding many potentially functional peptides, within an already limited screening capacity. Additionally, the efficiency of peptide delivery and the route of uptake have been shown to depend on the type of cargo used (Foerg and Merkle 2008). In contrast, an unbiased phage selection would be impartial to the means of escape and would isolate the most efficient peptides from much larger libraries, provided that they function while anchored to large phage cargo, as befitting their application to the delivery of nanoparticles, many of which are similar in size.

The assay described in the previous chapter was applied as a mechanism of peptide selection using phage display, wherein phage expressing a library of peptide sequences and an enzyme substrate fused to the N-terminus of pIII are constructed. Selection is performed by treatment on mammalian cells, and if the expressed peptide enables the phage to reach the cytoplasm, either through endosome escape or through direct transduction across the plasma membrane, it becomes modified by an enzyme localized there, such as phosphorylation by an endogenous protein kinase or biotinylation by exogenously expressed *E. coli* biotin ligase (BirA). Recovery of functional phage is then possible by affinity purification of the modified phage using affinity purification (such as streptavidin or phospho-specific antibodies), and a few of these phage are

sequenced to sample the diversity and the majority infected on *E. coli* for the next cycle of selection (Figure 6.1).

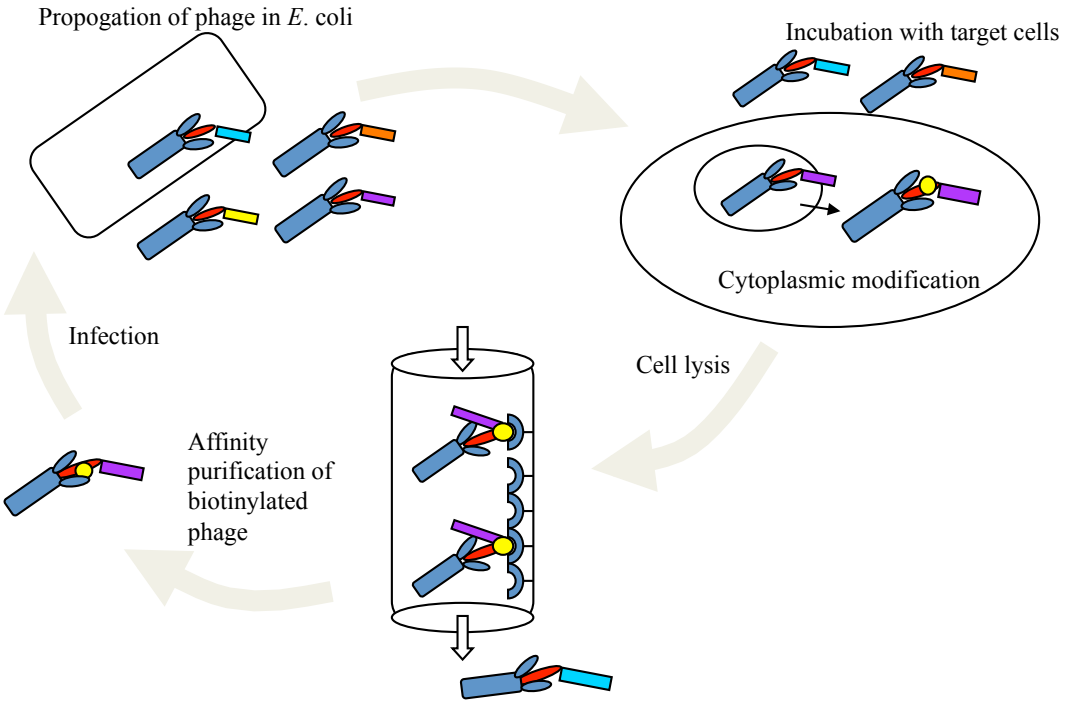

Figure 6.1. Schematic of phage display selection for endosome escaping peptides. Phage displaying peptide library and peptide enzyme substrate are propogated in *E.* coli. Phage interact with or are endocytosed by mammalian cells expressing modifying enzyme in the cytoplasm, e.g. PKA or BirA. Endosomolytic phage become modified in the cytoplasm with a small molecule, such as phosphate or biotin. All cell-associated phage (endosomal, surface, and cytoplasmic) are recovered by cell lysis. Cytoplasmic modified phage are isolated by affinity putification for the small molecule modification, such as biotin or phosphate, while unmodified phage are removed. *E. coli* are infected with the purified phage for amplification in the next selection round.

6.3. Methods

6.3.1. Buffers

Phage extraction buffer (20 mM Tris, pH 7.5, 100 mM NaCl, 6mM $MgSO_4$), top agar (3.75g Luria Broth powder, 1 g Agar, 150 mL water autoclaved and shaken during cooling for even suspension), Cytomix electoporation buffer: 120 mM KCl, 0.15 mM CaCl2, 10 mM K2HPO4, pH 7.6, 25 mM HEPES, pH 7.6 2 mM EGTA, pH 7.6, 5 mM MgCl2.

6.3.2. Phage cloning

6.3.2.1. Amplification, purification, and ligation

All phage-displayed peptide inserts were constructed by PCR amplified in Platinum Blue PCR Supermix (Life Technologies) at 90°C for min, then 25 cycles of 90°C for 30 sec, 52°C for 30 sec, 72°C for 30 sec. For 0-4 copy pIII display, M13 phagemid vector pComb3H (C.F. Barbas, III) and inserts were digested with SacI-HF and SpeI restriction enzymes in NEBuffer4 (NEB) for 4-6 hrs at 37°C. For all 5-copy pIII display, M13KE vector and inserts were digested with Acc65I and EagI (NEB). For all >2000 pVIII display, M13KE 8-3 vector (described below) and inserts were digested with KpnI and BspHI. Digested insert and vector were purified by standard gel electrophoresis procedures. T4 DNA ligase (Life Technologies) was used to circularize the plasmid. *E. coli* strain ER2738 was electroporated with the ligated DNA.

6.3.2.2. pComb insert phospho-pIII, AP-pIII, and HA2-phospho-pIII

M13 phagemid pComb vector was used to subclone DNA inserts containing sequences encoding adenovirus HA2 and the Protein Kinase A (PKA) substrate EL-GLFGAIAGFIENGWEGMID-GG-RRSSDT-TS (phospho-phage). An insert with the BirA acceptor peptide GLNDIFEAQKIEWHES (AP-phage) was constructed on the N-terminus of pIII subsequent to the signal sequence cleavage site SHS.

6.3.2.3. Library pComb 3H X_{12}-AP-pIII

Inserts encoding X_{12}-GSS-GLNDIFEAQKIEWHES and X_{20}-GSS-GLNDIFEAQKIEWHES were made by PCR amplification with primers HG28 5'-

gtgtcgtcatctaggagagctc and HG29 5'-tcatgatcagactgcctcgag with template HG30 or HG31, transformed by electroporation into SS320, TG1, and ER2738 cells (Lucigen).

6.3.2.4. M13KE AP-pIII

A DNA insert encoding SHSHGG-GLNDIFEAQKIEWHES-GGGSAET was made by PCR amplification of primers HG38 5'-tttagtggtacctttctattctcactcccatggaggtctaaatgac, HG39 5'-tcccatggaggtctaaatgacatctttgaagcccagaaaattgaatggcatgaaagtggt, and template HG40 5'-catgtttcggccgatccgccaccactttcaatgccattcaatt. The product was subcloned into the pIII cloning site of the M13KE vector.

6.3.2.5. M13KE 8-3 dual pVIII/pIII display vector

To create PstI and BamHI sites in pVIII, HG41 5'-aacttcctcatgaaaaagtctttagtcc was PCR amplified with HG42 5'-cgcttttgcgggatcctcaccctctgcagcgaaagacagc using M13KE vector as a template, producing a 106bp product. To create a cloneable segment with KpnI restriction site, HG48 5'-gctgtctttcgctgcagagggtgaggatcccgcaaaagcg was amplified with HG43 5'-agaaaggtaccactaaaggaattgc using M13KE as a template to produce a 264 bp fragment. The two resulting pieces were purified by gel electrophoresis, combined, and amplified as templates with oligos HG41 and HG43 to create a large insert that was cut with PstI and KpnI and ligated into similarly cut M13KE, and transformed into bacteria. Plasmid was purified from clone cultures bearing the correct sequence. In order to delete another PstI site in the vector, a point mutation was created by PCR amplifying the previously vector with primers HG46 5'-cctgtaggtcctcg and HG47 5'-aattcgaggacctacaggcatg. The product was annealed and ligated into M13KE cut

with SphI and EcoRI restriction enzymes and transformed into bacteria, from which plasmid was purified. Sequencing primers HG51 5'-cgacaggtttcccgactggaaagc and HG52 (5'-gaagatcgcactccagccagctttc were used to confirm the sequence of the resulting 8-3 vector.

6.3.2.6. M13KE 8-3 AP-TEV-pIII

Insert encoding GLNDIFEAQKIEWHES-GG-ENLYFQ (AP-TEV) within the cloning site of pIII of M13KE phage backbone was constructed by PCR using the forward primer HG79 5': gcactgggtacctttctattctctcactccggtctaaatgacatcatctttgaagc, template primer HG80 5': cggtctaaatgacatctttgaagcccagaaaattgaatggcatgaaagtggtggcgagaa and reverse primer HG81 5': attctcggccgatccctggaagtacaaattctcgccaccactttcatgccat.

6.3.2.7. M13KE 8-3 phospho-pVIII

M13 phage vector M13KE 8-3 was used to clone a MAPK substrate into pVIII, MLSFAAEGE**S**PAKAA..., using 3 PCR reactions, first with primers HG43 with HG71: 5'-ttcgctgcagagggtgag**ag**tcccgcaaaagcggccttt amplified with the 8-3 vector, a second reaction with primers HG42 and HG72: 5'-aaaggccgcttttgcggga**ct**ctcaccctctgcagcgaa amplified with the 8-3 vector, each of which were purified by gel electrophoresis, then combined in a third PCR reaction to amplify the overlapping PCR products.

6.3.2.8. Library pComb 3H X_{12}-AP-His_6-pIII

The insert EL-GXXXXXXXXXXXX-G-GLNDIFEAQKIEWHES-GSS-HHHHHH-TS was made via PCR amplification was performed with the following primers: HG92 5'-ccgcacttgagtatccttgagctcggcnnknnknnknnknnknnknnknnknnknnknnknnkggaggtctgaacgac

atcttcgaggctcagaagatcgagtggcatgagtccggctcgagccatcaccatcatcaccacactagtctacga, HG93 5'-ccgcacttgagtatccttgagctcggc, and HG94 5'- tcgtagactagtgtggtgatgatggtgatggc.

6.3.3. Phage phosphorylation with purified kinase

6.3.3.1. pComb phospho-pIII phage

Approximately 3.2×10^9 cfu of pComb-HA2-PKA phage were phosphorylated with 1 μg of catalytic PKA (Calbiochem) or no enzyme as a control in PKA buffer (NEB) with 0.5 mM ATP in 40 μL at 25°C overnight. For immunoprecipitation, 1 μL antibody to RXXS* (CellSignal #9624) was added to 10 μL of phosphorylated or control phage and 40 μL phage buffer and allowed to bind at 4°C overnight. 20 μL Pansorbin was rinsed with PBS and allowed to bind on ice for 3-4 hr. Beads were washed 4x in 1mL PBS and resuspended in 400 μL phage buffer and 1 μL was titered. For Western blot detection, 15 μL of phosphorylated or control-treated phage were boiled in SDS-Tricine gel loading buffer and loaded on a 20% Tricine gel (Life Technologies) alongside a prestained standard at 100 V. Gel was transferred to a nitrocellulose membrane at 25 V for 2 hr, blocked for 40 min with TBS 0.05% Tween containing 5% nonfat dry milk. Membrane was probed with anti-RXXS* (CellSignal 110B7E), where S* represents phosphorylated serine, diluted 1:1000 in blocking buffer at 4°C overnight, washed, then HRP-anti-rabbit, diluted 1:5000 in blocking buffer for 2 hr at 25°C. Chemilluminescent substrate SuperSignal West Pico was applied and film was developed by standard protocols.

6.3.3.2. Purified MAPK phosphorylation and purification of M13KE phospho-pVIII phage

Purified MAPK phosphorylatable-pVIII displaying phage, at ~430 pM, were treated with 1 µL purified MAPK enzyme or water in PKA enzyme buffer and 500 µM ATP at 37°C overnight. 1.5 x 10^9 phage were incubated with 10 µL anti-phospho antibody (CellSignal #34B2) in Tris-buffered saline (TBS) with 0.05% Tween and 0.1% BSA, rotating at 4°C overnight. 20 µL Protein A beads were added and rotated at 25°C for >2 hr. Beads were pelleted, washed 3x with buffer, and flowthrough was saved. 200 µL buffer was added, and both flowthrough and recovered bead solutions were titered for plaque-forming units (pfu). For elution, beads were immersed in IgG elution buffer at pH 2.5 (Life Technologies), and neutralized with 1M Tris buffer, pH 9.

6.3.4. Phage biotinylation with purified BirA

Phage were biotinylated *in vitro* with purified BirA enzyme (Aviditiy) at 37°C overnight, in buffer containing 4 mM ATP, 4 mM MgOAc, 20 µM biotin, 0.02 M Bicine, 10 mM Tris. Biotinylated phage were affinity purified with magnetic streptavidin beads (Solulink).

6.3.4.1. pComb AP-pIII phage

7x10^7 cfu pComb AP-pIII phage (substrate concentration approximately 2-10 pM) were biotinylated *in vitro* with 1 µL BirA or no enzyme at 37°C > 24 hr. Phage were filtered in a 10 kD MWCO Microcon, and washed 2x with PBS to remove free biotin. Volume was normalized to approximately 200 µL. 100 µL filtered biotinylated phage were incubated with 20 µL magnetic streptavidin beads (Solulink) in PBS with BSA, rotated for 1.5-2 hr, and beads were washed in 1 mL buffer for 1 hr while rotating at

25°C twice, then washed 3x and resuspended in 30 μL phage buffer and 10 μL of the mixture was titered for colony-forming units (cfu).

6.3.4.2. M13KE AP-TEV-pIII phage

10^{10} pfu M13KE AP-TEV-pIII phage were incubated with 2 μL BirA or water as a control in a 30 μL reaction at 37°C overnight (Avidity). 70 μL phage extraction buffer was added to each reaction. 20 μL was incubated with 20 μL of streptavidin beads (SoluLink) in PBS 2.5% BSA 0.05% Tween-20 and rotated at 4°C overnight. Streptavidin beads were washed in the same buffer 3 times. Half of the beads were resuspended in 100 μL TEV buffer (50 mM Tris HCl, pH 8, 0.5 mM EDTA) to which 1 μL TEV protease was added and incubated at 25°C for 4 hours.

6.3.5. Synthetic labeling of phage

6.3.5.1. Fluorescently- labeled phage

For rhodamine-phage ~1 nM M13 pComb phage were reacted with 100 μM NHS-rhodamine (Life Technologies) in water. Phage were filter purified in a Amicon YM-100 (Millipore) with 5 changes of 4-5 mL PBS and finally into Cytomix, normalized to 400-500 μL. Protein concentration (280 nm absorbance) was determined to be ~1mg/mL, and dye concentration (555 nm absorbance) was determined to be 1 μM. For Cy5-phage,

6.3.5.2. r9-phage

M13 pComb phage (~4.2 nM) were labeled with 1μL of 5 nM-25 μM r_9-NHS ester (stored in DMSO) made by Dr. Stephen Adams, or no peptide as a control. Reaction was incubated at 25°C for 30 min, then filtered in a 100 kD Amicon (Millipore) with PBS.

6.3.5.3. AP-cys-mal-NHS-pComb AP-pIII

pComb AP-pIII phage (200 μL at ~1nM) were reacted to NHS-maleimide (20 μL at ~1μM) with 24 μL Bicine, pH 8.3 at 4°C for >2hr. 20 μL cys-AP was added and reacted at 4°C for >2 hr. Phage were filter purified in a 100K Amicon column with PBS and Cytomix, then normalized to 1 mL volume.

6.3.6. Generation of HeLa-BirA expressing cell line

HeLa cells (ATCC) were transfected with BirA pcDNA 3' (A. Ting) with Fugene (Roche) following manufacturer's protocol, and selection for stable cell lines was performed with geneticin for 2 weeks. >60 clones were picked and cultured individually, maintained with drug. Standard Western blot procedures were performed with chicken anti-BirA antibody (from A. Ting) was used to detect transfected cells.

6.3.7. CFP-AP cytoplasmic biotinylation

HeLa BirA or untransfected control cells were grown to confluency in T162-cm^2 flasks. Cells were trypsinized and resuspended to a concentration of 10^7 cells/mL in Cytomix. 2 and 10 μg pcDNA3' containing CFP-AP DNA (from A. Ting) were electroporated into 1mL of cells in 4mm electroporation cuvettes (BioRad) with 350 Volts, 1075 μF. Cells were recovered in complete media at 37°C overnight. 48 hours post-transfection, cells were incubated in complete media containing 10 μM biotin for 5-6 hours, lysed by sonication, and soluble lysates were run on a 10-20% Tricine gel, and detected by standard Western blot procedures, using streptavidin-HRP (Life Technologies), diluted 1:5000 bound for 1 hr at 25°C. CFP-AP was imaged on cells, >48 hr post transfection on an epifluorescent microscope with a 560 nm cube filter.

6.3.8. Detection of phage cytoplasmic biotinylation by electroporation

6.3.8.1. Whole phage titering

2×10^{10} of excess-AP reacted or unreacted AP-phage were electroporated with 7.5 - 8×10^{6} HeLa-BirA cells or HeLa cells as a control. Cells were recovered in DMEM complete media with 10 μM biotin at 37°C overnight. Cells were washed, normalized by cell count, and lysed. Phage were streptavidin purified from cell lysates and titered directly from streptavidin beads for cfu on *E. coli*.

6.3.8.2. Imaging

10^{10} rhodamine-phage were sterilized by heating to 60°C for 15 min. Approximately 10^{6} cells were trypsinized from near-confluent plates, gently pelleted, and resuspended in Cytomix. Phage were added to cells and the mixture was aliquoted in 4-mm electroporation cuvettes and electroporated with 350 Volts, 1075 μF (Bio-Rad Gene Pulser Xcell) and recovered for 6 hrs at 37°C with 1.5 mL culture medium on 6-cm glass bottom dishes. Cells were gently washed 2x with HBSS and imaged with 560 nm cube filter on an epifluorescent microscope.

6.3.9. Cell uptake of r_9-labeled phage and imaging

A 6-well plate of HeLas grown to confluency was wash with PBS and r_9-labeled phage were treated in 500 μL DMEM with 10% FBS for 3 hr. Cells were washed in 2 mL PBS and trypsinized with 300 μL ATV for 5 min at 37°C and neutralized with 300 μL DMEM. Cells were pelleted at lysed in 50 μL M-PER (Thermo). Insoluble matter was pelleted at 4°C 14kg for 10 min, and supernatant was titered.

6.3.10. Phage library selections for endosome escape

6.3.10.1. pComb3H X_{12}-AP-pIII and X_{20}-AP-pIII libraries

Four separate selections were performed using the two libraries created. One set was precleared with streptavidin beads to remove any phage biotinylated in E. coli, and one set was not precleared to avoid loss of potential functional phage. 1 large flask of nearly confluent cells in 15 mL media were treated with 10^{10}-10^{11} library phage in total, and phage in 1-2 mL were added daily over 2 or 3 days, with 2x dose on days 2 and 3. To collect lysates, cells were sonicated in streptavidin binding buffer with protease inhibitor. Lysates were incubated with streptavidin beads for at least 2-3 hours at 4°C, rocking, unbound phage was removed, and beginning at selection round 3, streptavidin beads were additionally washed. Half of streptavidin-bound phage were reamplified by *E. coli* infection.

6.3.10.2. pComb3H X_{12}-AP-His6-pIII library

10^9 phage were added to HeLa BirAs in 15mL media with serum (10 μM biotin) at the following time points prior to lysis: 24 hrs, 8 hrs, 4 hrs, 2 hrs, 1 hr, 30 min, 15 min. Cells were washed, trypsinized, pelleted, and lysed. Lysate was cleared and incubated with streptavidin beads at 4°C overnight. Beads were washed 4 times with buffer containing 1% BSA and 0.5% Tween. Streptavidin-bound phage were amplified and titered on *E. coli* ER2738.

6.3.11. Cotreatment of phage and r_9

HeLa cells were plated the day before in a 6-well plate ($2x10^5$ cells/well) and grown overnight. Cells were rinsed with 1mL PBS. 1mL DMEM no serum was added to

each well and 10 μL r9 to a final concentration of 1-50 μM was added to cells and allowed to adhere for 5 minutes at 25°C. 10 μL M13KE AP-pIII phage ($1.2x10^7$ pfu) were added and the cells were incubated for 1.25 hr at 37°C. Cells were rinsed twice with 1mL PBS. Surface-adherent phage were removed with 0.5 mL ATV for 5 min at 37°C, then 1 mL DMEM with 10% FBS was added to each well. Cells were pelleted at 90 g for 5 min and supernatant was aspirated. Cells were resuspended in 100 uL phage extraction buffer and lysed by sonication at 10% amplitude for 10 sec. Nonsoluble material was pelleted by centrifugation at 13,000rpm at 4°C for 10 minutes. 50 μL of lysate was titered for plaque-forming units (pfu) on *E. coli* in top agar.

6.4. Results

6.4.1. Evaluation of PKA phosphorylation as mechanism of endosome escape selection

To analyze whether phage expressing a PKA substrate could be phosphorylated and purified by phospho-specific antibodies, M13 phage were constructed with a N-terminal fusion to pIII of the sequence RRSSDT in the pComb phagemid, which is expresses recombinant fusion peptides in up to 5 copies along with wildtype pIII (Barbas, Kang et al. 1991). 10^9 cfu purified phage were phosphorylated with the purified catalytic subunit of PKA or no enzyme as a control, 0.5 mM ATP, and phosphate-containing buffer. A Western blot probed with a phospho-specific antibody to the sequence RXXS* where serine is phosphorylated and an antibody to pIII protein showed that in the presence of enzyme, bands the same size as those of pIII were detected (Figure 6.2 A). Next, a whole phage pulldown assay was performed where phage were incubated with a

phospho-specific antibody at 4°C overnight, then incubated with Pansorbin beads for several hours, which were then wash 4 times with PBS. About 60% more phage were recovered in the phosphorylated sample than the unphosphorylated sample (Figure 6.2 B). When the experiment was repeated twice more, the effect was not highly reproducible (data not shown). It is possible that the phosphorylation reagents were not stable or that PKA substrate is not effectively displayed that is amenable for whole phage pull-down, or that optimized binding or washing conditions could improve recovery.

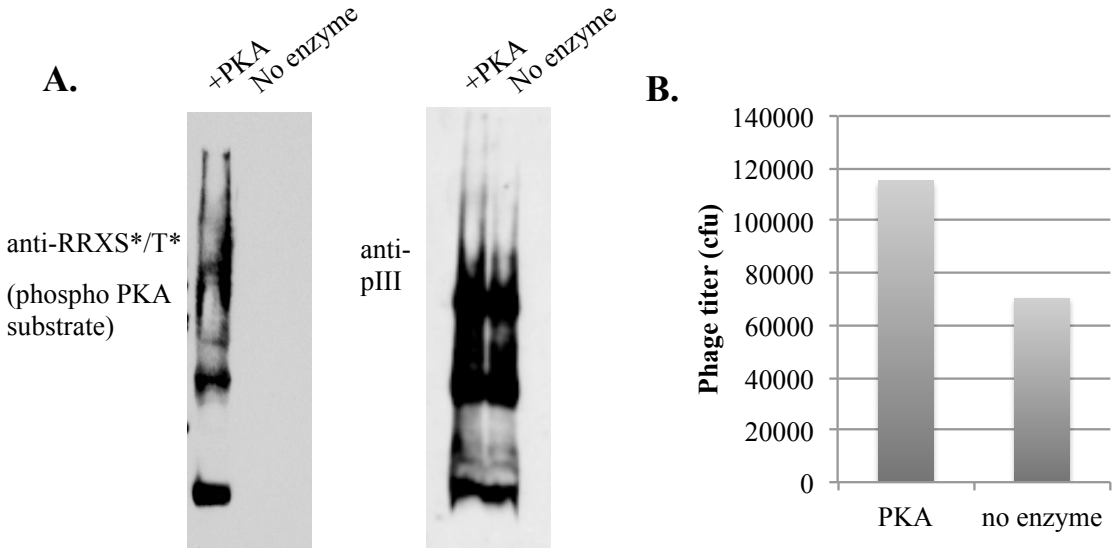

Figure 6.2. Phospho-reporter phage are phosphorylated by PKA but purification of whole phosphorylated phage requires optimization. Phage expressing RRSSDT-pIII were treated with purified catalytic PKA (+PKA) or no enzyme as a control (-PKA), ATP, and phosphate. A. Western blot of denatured phage detecting phosphorylation (left) or phage protein pIII (right) B. Affinity purification of phosphorylated phage, using anti-RXXS* antibody bound to agarose beads, and phage titered by addition of E.coli to beads and plating.

6.4.2. Biotinylation shows promise as mechanism for endosome escape phage selection

Biotinylation and streptavidin purification of phage expressing the BirA acceptor peptide (AP) was also examined as a means to detect cytoplasmic localization. M13

phage were made expressing the AP sequence GLNDIFEAQKIEWHES fused to pIII. 10^7 purified phage were treated with BirA enzyme or no enzyme as a control in buffer containing ATP and biotin. Whole phage were incubated with streptavidin beads and washed 5 times, and phage were titered directly from the streptavidin beads. While no phage were recovered from the untreated sample, greater than 10^4 phage were recovered from the BirA-treated sample (Figure 6.3). These results suggested the potential for a strong phage selection mechanism; however, the efficiency of phage recovery relative to the starting material was non-optimal.

Next, in order to create a BirA-expressing cell line that would facilitate cytoplasmic biotinylation, HeLa cells were transfected with BirA pcDNA3 and transformed cells were selected with geneticin and clonal populations were cultured. A clone found to express high levels of BirA by Western blot was selected and used for all subsequent assays (Figure 6.4 A). In order to examine if BirA was functional within the cytoplasm, HeLa BirA cells or an untransfected control were transformed with cyan fluorescent protein (CFP) tagged with acceptor peptide. Biotinylation of CFP-AP was evident by Western blot, and cytoplasmic expression was apparent by fluorescence microscopy (Figure 6.4 B and C).

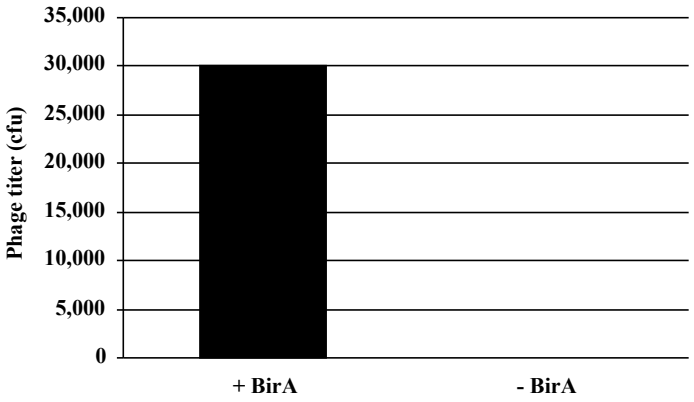

Figure 6.3. Enzymatic biotinylation and streptavidin purification of phage results in 10^4-fold enrichment over background. Phage made expressing GLNDIFEAQKIEWHES-pIII (AP); 10^7 phage treated with purified BirA and free biotin O/N, streptavidin purified with 5 washes in buffer. Phage titered by addition of *E.coli* to streptavidin beads.

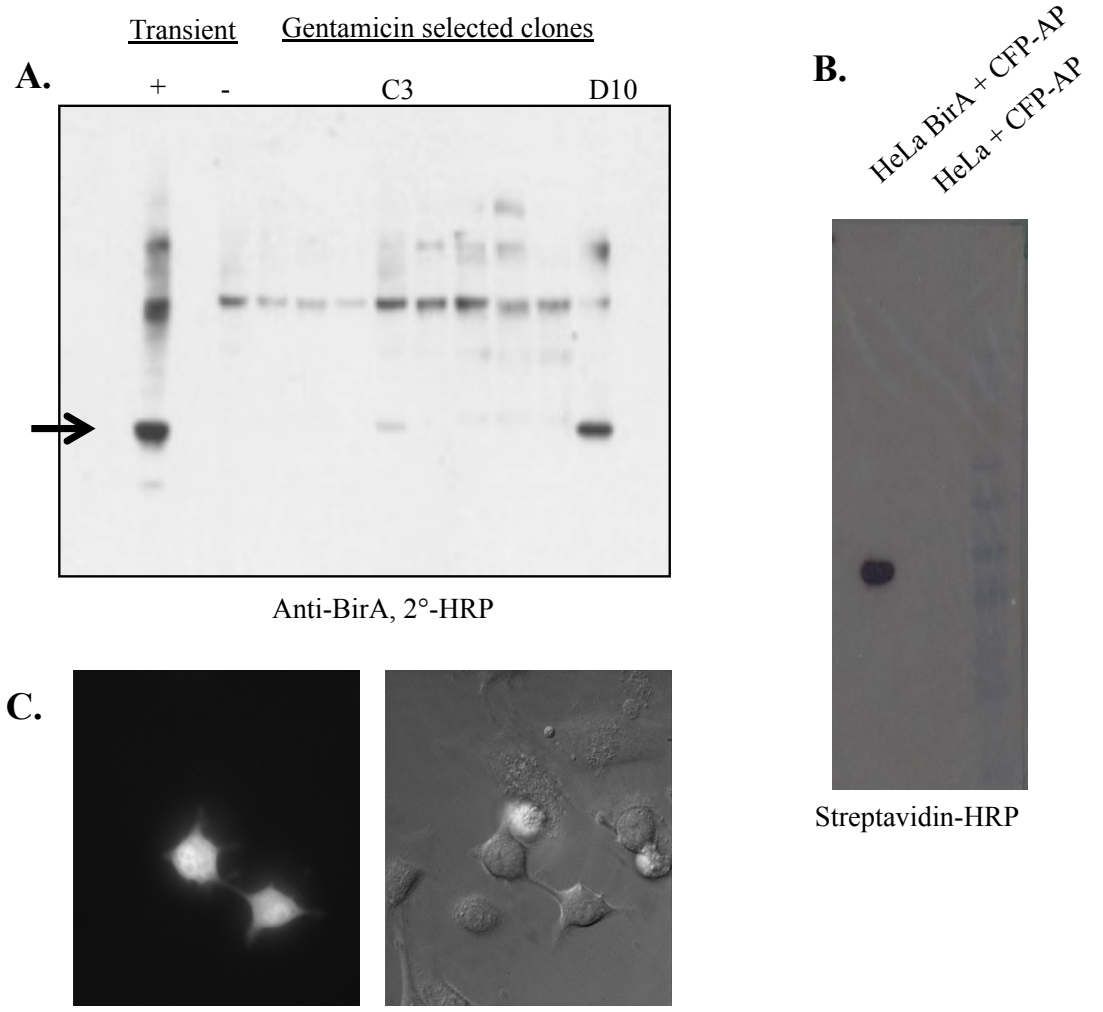

Figure 6.4. Generation of a stable HeLa-BirA expressing cell line, which biotinylates acceptor peptide upon overexpression in the cytoplasm. **A.** Western blot for BirA expression in transient and stably-transfected HeLa cells. *Left two lanes*: control cell lysates from cells that were transiently transfected with BirA (+) or no DNA as a control (-) 48 hours prior to lysis. *Right lanes*: Geneticin-selected clones. Clones C3 and D10 were positive for BirA expression. Arrow indicates BirA band at ~36kD. **B.** Overexpressed CFP-AP is biotinylated in Hela BirA-expressing cells. pcDNA encoding CFP-AP (~29 kD) was transiently transfected into a stably expressing HeLa BirA cell line or a control untransfected control. Cell lysates were separated by SDS-PAGE and probed for biotinylation by streptavidin-HRP. **C.** HeLa BirA cells transiently transfected with CFP-AP were imaged by fluorescence microscopy at 560nm (left) and white light (right).

Next, in order to test whether phage biotinylation could facilitate their isolation from the cytoplasm of cells for selection, and if chemical conjugation of extra acceptor peptide would increase the efficiency of phage recovery, phage expressing AP-pIII either

additionally conjugated to AP or unreacted were electroporated into HeLa-BirA cells or HeLa cells as a control. Cells were recovered in DMEM complete media with 10 μM biotin at 37°C overnight. Phage were streptavidin purified from cell lysates and titered directly from streptavidin beads on *E. coli*. Cell lysate titers showed approximately 4-fold higher recovery of phage expressing pIII-AP and an additional 2-fold higher recovery of phage conjugated to extra AP (Figure 6.5 A).

To confirm that electroporated phage were cytoplasmically localized, phage were labeled with rhodamine-NHS ester, purified, electroporated into cells. Cells were allowed to settle for 5-6 hr and imaged by fluorescence microscopy. Localization appeared diffuse in the cytoplasm of adherent cells, and few punctae were also observed (Figure 6.5 B). These results supported the hypothesis that phage electroporation induced cytoplasmic localization, where biotinylation of AP by BirA would occur. The punctae observed may have been endocytosed phage, internalized from the extracellular media during the cell recovery period following electrophoresis.

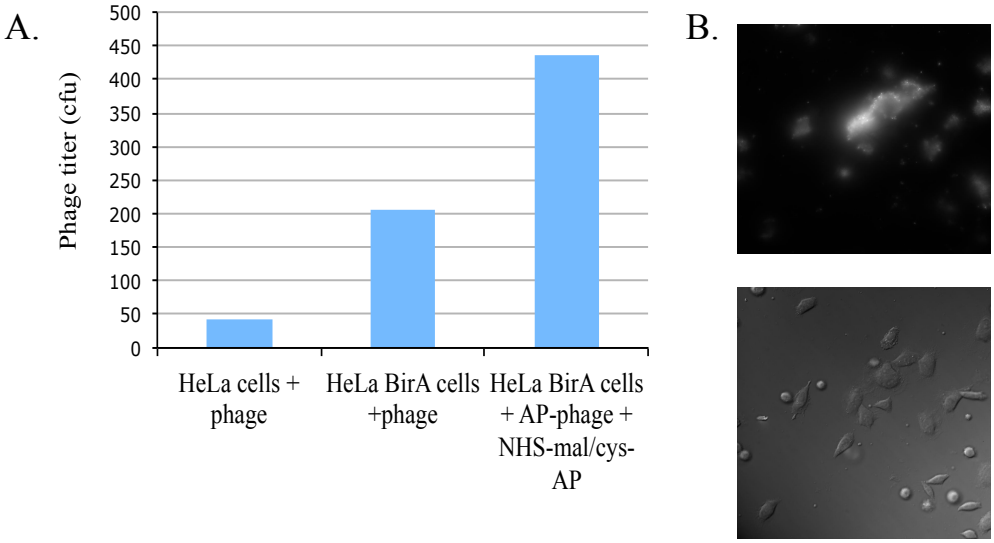

Figure 6.5. Electroporated phage are biotinylated in cells and appear mostly cytoplasmic by fluorescence. A. AP-pIII phage electroporated into HeLa BirA or HeLa cells and recovered by streptavidin purification of lysates and titering. More phage were recovered from HeLa-BirA cells than the control and additional AP_reaction facilitated higher recovery. **B.** 10^{10} rhodamine-labeled phage electroporated into cells, recovered for 6 hrs in 1.5 mL culture medium and imaged on 6-cm glass bottom dishes.

6.4.3. CPP labeling of phage causes precipitation

Next, a delivery method for inducing phage uptake was sought in order for phage to reach endosomal compartments for screening. Cell-penetrating peptides, such as R_9 or Tat could not be genetically encoded because peptides containing several positively charged residues fused to pIII are known to interfere with proper membrane insertion and secretion in *E. coli* (Peters, Schatz et al. 1994). As an alternative to genetic encoding, phage were labeled with various amounts of synthetic r_9. Phage were mixed with 1-10^5 molar equivalents of r_9-NHS ester. Precipitation was immediately visible upon labeling and difficult to solubilize during purification. Phage were treated on cells in serum free media, and cell lysates were collected to quantify phage uptake. Equal levels of phage

were recovered across all r_9 reaction concentrations, except 500 μM, which resulted in 600-fold higher increase in phage (Figure 6.6 A). Though this represented a vast improvement in phage uptake, the potential effects of such significant r_9 labeling on cell viability and intracellular localization were suspected to be prohibitive to the endosome escape selection. To verify the endocytosis of phage were reacted with Cy5-NHS ester, purified, and treated on cells. Phage appeared to be localized in intracellular endosomes (Figure 6.6 B), which was verified by punctate confocal imaging under high magnification. These results suggested that phage could be endocytosed by cells without labeling and observations of precipitation suggest that r_9 conjugation could obstruct uptake by reducing solubility.

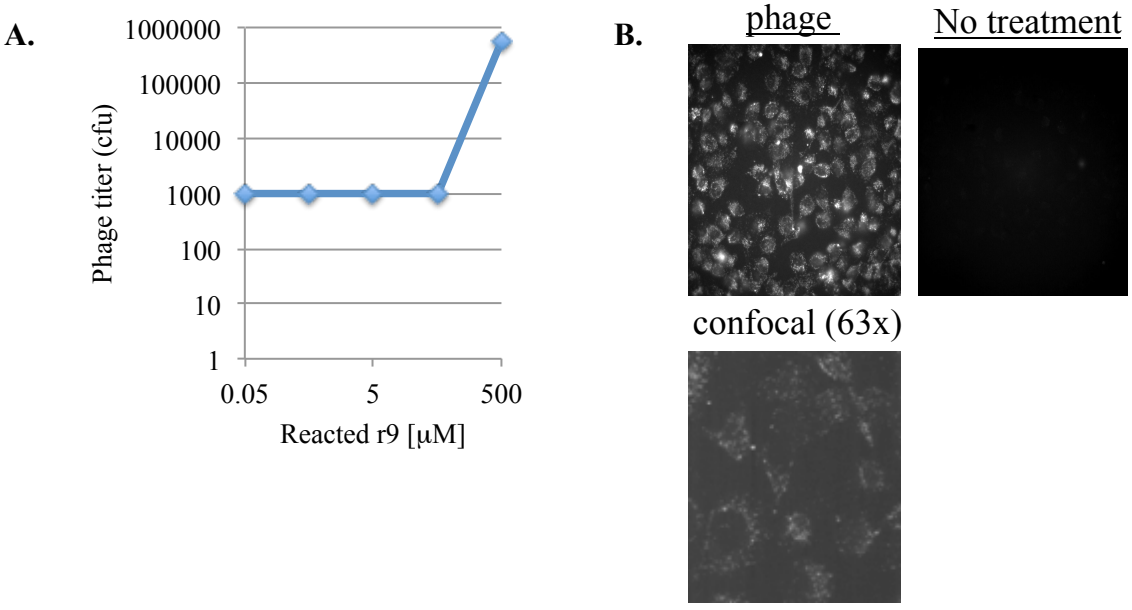

Figure 6.6. Conjugation of phage to r_9 peptide induces precipitation and does not enhance cell uptake except at ultra-high concentrations. A. 10^{11} phage reacted with 5 nM-0.5 μM r9-NHS (1-10^5 molar equivalents) in 10% pH 8.3 buffer on ice, filter purified, treated 6 well dish of cells for 3 hours in 6-well dish at 37°C. Titers of 50uL cell lysate shown. **B.** Phage labeled with Cy5 were treated on cells and imaged by epifluorescence and confocal microscopy.

6.4.4. Endosome Escape Selection of X_{12}-AP and X_{20}-AP peptide libraries

In order to perform the endosome escape selection, phage libraries were generated using pComb3H vector to encode N-terminal 12 and 20-amino acid peptides separated by a short amino acid linker to AP, fused to pIII (Figure 6.7). The potential diversities of $>10^{15}$ and 10^{26} of the libraries were restricted by the practicalities of cloning and bacterial transformation, and libraries of $>10^{7}$ individual transformants were generated. Separate selections were undertaken in parallel, using each library, which in one set was precleared with streptavidin beads to remove any phage that were prebiotinylated in *E. coli* or had affinity for streptavidin. Phage were treated on cells for 2-3 days with additional phage added daily to maximize the number of phage screened, or endocytosed into a cell, while daily replenishment was meant to replace any phage that may be degraded. Cells were lysed and treated on streptavidin beads. Unbound phage were removed and bound phage were reamplified. 10^{10} - 10^{11} phage (equaling 10^{3}-10^{4} copies of each unique phage sequence), were treated on cells. After cell lysis, roughly 10^{6} phage were recovered, and after gentle streptavidin purification, 10^{3}-10^{4} phage were recovered and reamplified for the subsequent round (Table 6.1). Sequences were used to analyze the peptide libraries pre and post-selections. Interestingly, sequencing after round 1 of selection showed a CPP-like peptide, SRRRERVRDK, bearing an insert containing 6 positively charged residues (Figure 6.8). Since pIII insertion restricts expression of highly positively charged sequences, it is highly unlikely to find such a sequence at random.

However, many other phage bore non-coding sequences or early stop codons. Fewer peptide-coding sequences were found in the X_{20} library than the X_{12} library, where more frameshifted mutants or non-recombinant parent phage vector sequences were found abundantly, even after the first and second rounds of selection. Phagemid encoding non-translatable sequences express all 5 copies of pIII in wildtype form because of their co-transfection with non-recombinant helper phage. Such non-recombinant phage have a growth bias for replication in *E. coli*, and can become enriched in phage selections inadvertently if the selection is not stringent enough.

X_{12}-AP library

N-term. - X_{12} - G S S - G L N D I F E A Q K I E W H E - pIII - C-term.

Theoretical diversity = $4 * 10^{15}$

Library diversity generated (adjusted for noncoding sequences) = **$1.7 * 10^7$**

X_{20}-AP library

N-term. - X_{20} - G S S - G L N D I F E A Q K I E W H E - pIII - C-term.

Theoretical diversity = $1 * 10^{26}$

Library diversity generated (adjusted for noncoding sequences) = **$2.4 * 10^7$**

Figure 6.7. M13 random 12 and 20 amino acid libraries fused to AP generated with $>10^7$ diversity. Oligomers were constructed using a mixture of random nucleotides at the variable positions (X). High throughput cloning was performed using large batch PCR amplification of oligos, gel purification, restriction digest of insert and pComb3H vector DNA, and ligation. Electrocompetent *E. coli* were transformed

Table 6.1. Titers of treated, recovered, and reamplified phage during round 1 of selection for endosome escape.

	X20	X12	X20, SA precleared	X12, SA precleared
Total phage treated (appx, calculated based on titer in 15ml)	5×10^{11}	4×10^{10}	4×10^{11}	3×10^{10}
Total phage internalized	3×10^{6}	10^{6}	10^{6} -10^{7}	10^{6}
Total phage reamplified for next round	3×10^{4}	10^{3}	10^{4}	3×10^{3}

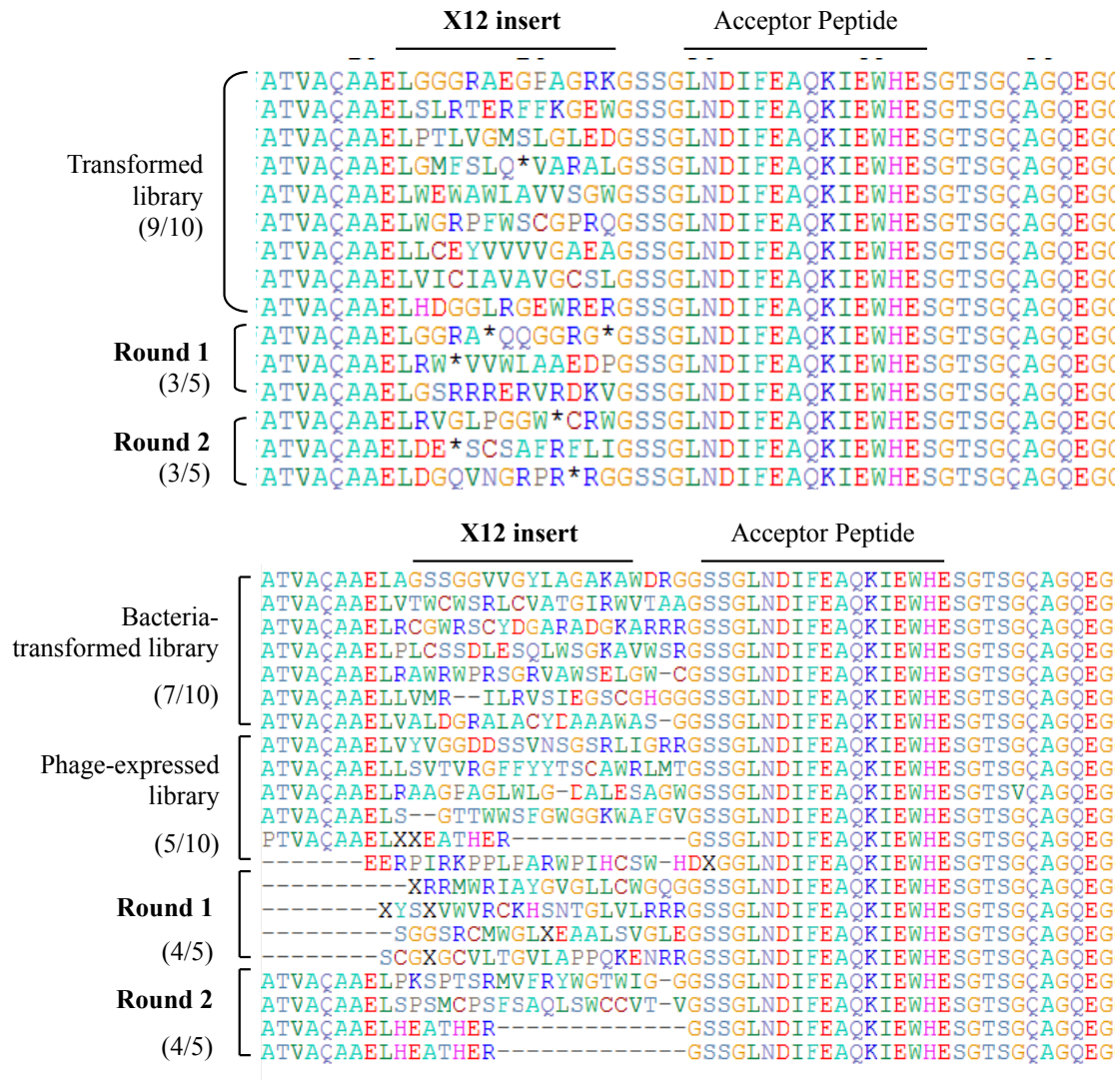

Figure 6.8. Sequences of libraries and endosome escape selected phage reveal high proportion of non-recombinant phage. Sequences of phagemid pIII containing the library insert and acceptor peptide which were transformed (plasmid) and expressed (phagemid) libraries and phage clones after 2 round of selection for endosome escape. The fraction of clones which had a sequence that could be aligned with the upstream and downstream phage sequences are shown in parentheses. * represents stop codons, which when expressed in the amber supressor *E. coli* strain, tag codons are translated as Q.

6.4.5. Testing alternate phage constructs to optimize endosome escape selection

Based on the apparent inefficiencies of the first phage selection attempts, alternate phage expression platforms and enzymatic selection mechanisms were tested, illustrated in Figure 6.9. Alternate platforms (i)-(iii) utilize wildtype phage display, instead of the

phagemid expression system (iv), the former of which encodes the complete phage genome and requires no superinfection by helper phage, ensuring efficient expression on all 5 copies of pIII or all 2,700 copies of pVIII of the inserted peptide. Thus, any non-coding inserts within a library will result in non-viable phage, and only the phage in which no recombinant DNA is inserted can form non-recombinant phage. The population of these phage is low, typically <0.01% of transformants.

However, wildtype phage suffer from the limitation of poor expression of inserts greater than 30 amino acids on pIII and 6-8 amino acids on pVIII without disrupting viability. Secondly, phage bound tightly to a substrate on all 5 copies of pIII, which is used for bacterial membrane attachment and insertion, cannot infect *E. coli*. Because the biotin-streptavidin bond is extremely strong, with a dissociation constant on the order of 10^{-14} M, elution could pose a problem. However, the biotin-streptavidin bond has been found to dissociate in some conditions, including treatment in 6M urea and in water at high temperature, >70°C. (Holmberg, Blomstergren et al. 2005). We speculated that the latter would allow dissociation of biotinylated phage from streptavidin beads without destroying phage viability as would protein denaturants. Preliminary experiments showed no loss of phage viability after 5 minute incubation in 80 or 90°C water (data not shown).

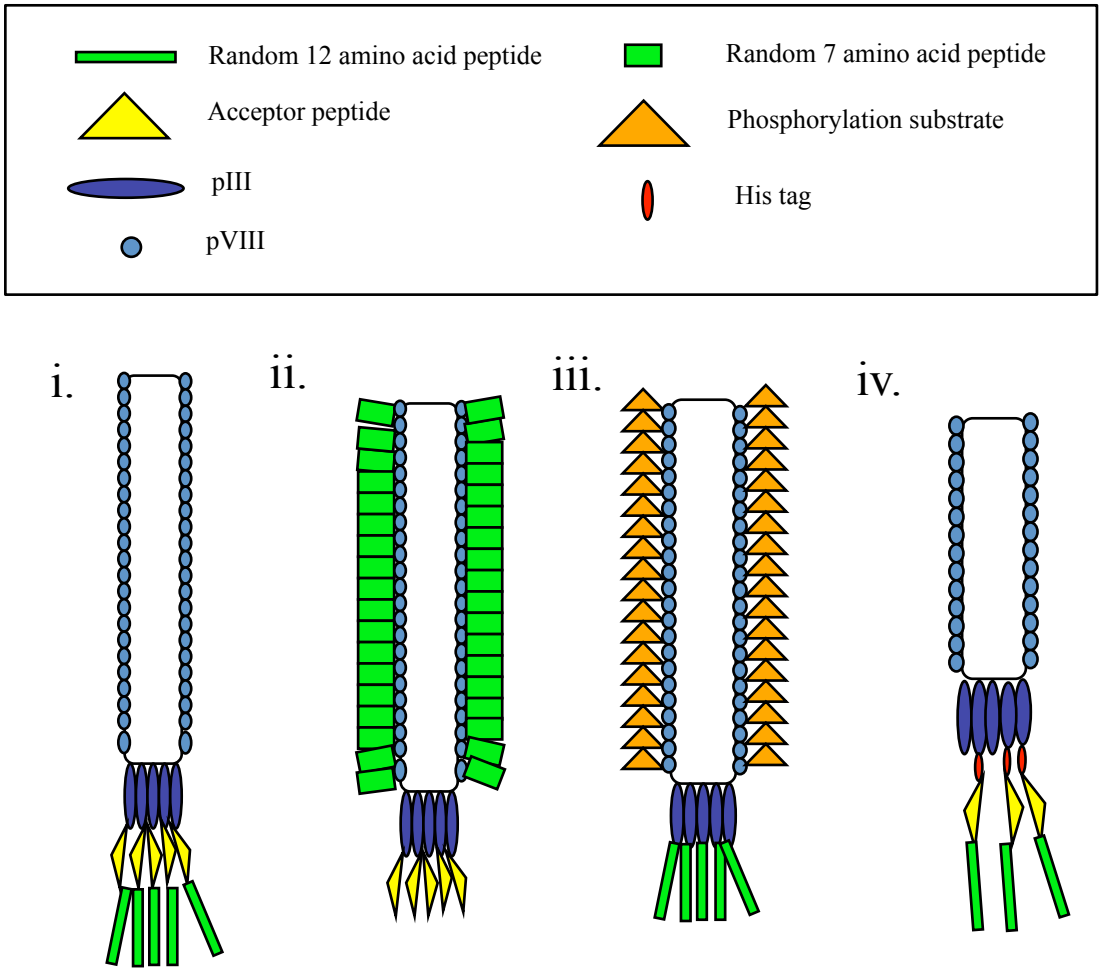

Figure 6.9. Schematic of alternate phage constructs for endosome escape., **i.** Biotinylatable phage expressing 5-copy pIII fusion of 12 amino acid library and AP. **ii.** Biotinylatable phage expressing high-copy (~2700) pVIII fusion of a shorter 7-amino acid library and AP-pIII fusion. **iii.** Phosphorylatable phage expressing phospho substrate-pVIII fusion and 12-amino acid library on pIII. **iv.** Phagemid expressing 12 amino acid library, AP, and His purification tag fusion in 0-4 copies.

First, wildtype phage vector M13KE was constructed to express AP on the N-terminus of pIII. In order to test whether the phage could be efficiently cytoplasmically biotinylated, phage were electroporated into HeLa BirA cells or untransfected HeLa cells as a control. After recovery, cell were lysed and biotinylated phage were purified with streptavidin beads. Phage-bound to streptavidin beads were incubated in 80°C water for 5 minutes. 7.8-fold more phage were recovered from BirA-expressing cells than non-expressing cells (Figure 6.9).

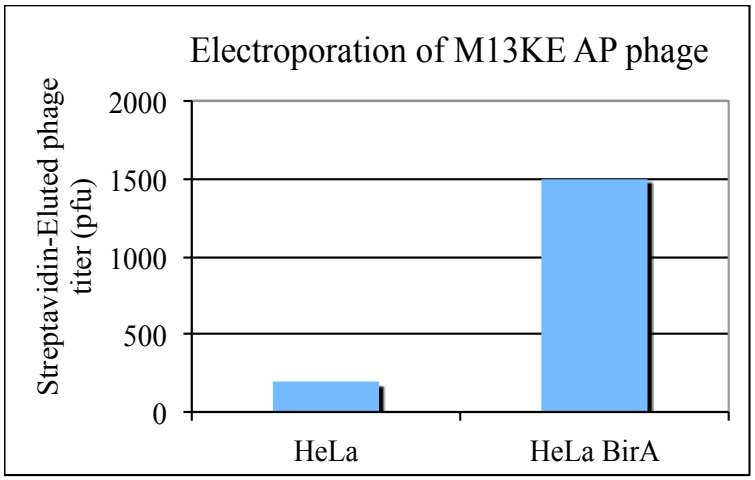

Figure 6.10. Electroporation of M13KE AP AP-pIII phage are cytoplasmically biotinylated in the cytoplasm of cells. M13KE pIII-AP phage (10^7 pfu/μL) electroporated into cells and streptavidin purified. Phage eluted from streptavidin with 80°C water for 5 minutes and titered for plaque forming units (pfu).

A phage library was created to display X_{12}-AP pIII M13KE and $>10^7$ transformants were generated. However, around 50% of sequences of the primary library contained no DNA insert (data not shown). The extensive length of the insert was close to 30 amino acids in length, and peptides of this length are known to affect the efficiency of expression (Smith and Petrenko 1997, Sidhu 2001). The library was not expected to be efficient for endosome escape selection due to the high percentage of non-recombinant sequences.

Thus, we sought to separate the enzymatic substrate sequence from the library sequence, displaying each on separate phage proteins. The ubiquitous phage coat protein pVIII has been established as an alternate phage display platform, displaying in several thousand copies to create a landscape library (Smith and Petrenko 1997). Dramatically increasing the valency of the library peptide by encoding it on pVIII may increase the odds of finding even weakly functional sequences by mass interaction of the long filamentous phage with the endosomal membrane. Alternatively, a longer peptide

expressed focally on one end of the phage but in 5 copies could potentially work in a more pore-forming manner, while ultra high copy of the enzyme substrate would increase the odds of enzyme modification and purification, if either is inefficient.

Thus, a wildtype phage vector for double pIII and pVIII display was constructed using the M13KE vector, which already contains cloning sites at pIII, to additionally insert cloning restriction sites PstI and BamHI at the N-terminus of pVIII and mutating a PstI site at another location in the vector (Petrenko, Smith et al. 1996)

First, in order to ensure efficient dissociate biotinylated phage from streptavidin, a short Tobacco Etch Virus (TEV) protease cleavable sequence was inserted C-terminal to the acceptor peptide on pIII. M13KE vector was used to insert DNA encoding AP-GG-ENLYFQG at the N-terminus of pIII, and phage were expressed in *E. coli*. To test their potential efficiency of biotinylation, streptavidin purification, and recovery, roughly 10^9 phage were biotinylated with purified BirA or no enzyme as a control and incubated at 37°C overnight, and the reaction was bound to streptavidin beads overnight at 4°C in PBS with 2.5% BSA and 0.05% Tween. Beads were washed 3 times with buffer and treated with TEV protease in TEV cleavage buffer for 4 hours at 25°C, and phage were quantified. Biotinylated phage were recovered 250-fold greater than control-treated phage and approximately 5×10^7 phage were recovered, at a relatively high percentage of starting material (Figure 6.11).

AP TEV cleavage site

MKKLLFAIPLVVPFYSHS**GLNDIFEAQKIEWHES**GG**ENLYFQ**GSAETVESCLAKSH

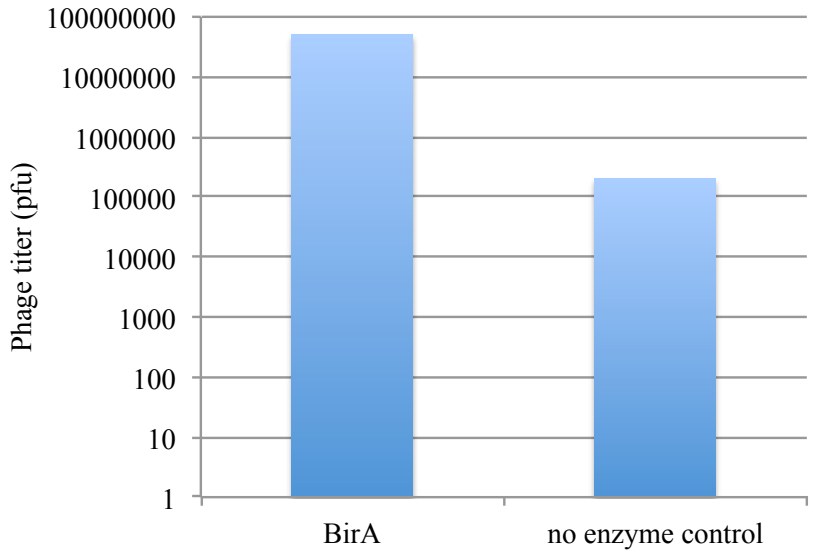

Figure 6.11. TEV protease efficiently frees biotinylated M13 p3-AP phage from streptavidin. Sequence of M13KE vector containing AP-TEV-pIII fusion (above). AP-TEV-pIII M13KE was biotinylated with purified BirA, ourified with streptavidin, and cleaved from beads with TEV protease. Beads slurry was titered on *E. coli* for pfu..

Because we could also speculate that longer peptide sequences could more efficiently cross a lipid bilayer, we also tested the potential efficacy of using pVIII-to display the enzyme substrate. We attempted to insert AP into pVIII; however, bacterial transformation yielded no recombinant phage (data not shown). This could be expected because pVIII is known to tolerate only short sequences, so the extensive length of the AP sequence likely renders phage nonviable. Phosphorylation substrates being typically only around 5 amino acids were thus the ideal choice and although purification of phosphorylated phage was unsuccessful originally in the context of the pIII phagemid, we speculated that the exceptionally high copy display on pVIII would render it more efficient. A MAP kinase (MAPK) substrate was ideal because the phage pVIII closely mimicked a possible substrate sequence and thus only three additional residues were

inserted to yield the sequence FAAEGES*PAKAAF, where S* represents the phosphorylatable serine. ~10^9 purified MAPK phospho-pVIII phage were incubated with MAPK enzyme or no enzyme as a control, 500 μM ATP, and phosphate-containing kinase buffer at 37°C overnight. Phage were then treated with an appropriate phospho-specific antibody in TBS with 0.1% BSA and 0.05% Tween at 4°C overnight, and 20 μL Protein A beads were added and rotated for at least 2 hr, which were then washed 3x and the bead slurry was titered by direct *E. coli* infection as well as the flowthrough. Surprisingly, although 10^3-fold fewer MAPK-treated phage than the control were recovered in the antibody flowthrough of MAPK-treated phage, no phage were recovered from directly titering the beads (Figure 6.12 A). These results suggested that phosphorylation of phage or binding to antibody-bound phage reduced the infectivity of phage. Phosphorylation of phage was clearly efficient; however, phage would need to be dissociated for infection. First, a competitive elution was tested, where roughly 5×10^5 phage previously treated with MAPK or no enzyme were immunoprecipitated with antibody and beads as before and after beads were washed, they were incubated with 10 μM free phosphorylated MAPK peptide substrate for 4 hours in order to attempt to compete for binding to the beads. The eluted supernatant was separated from the beads, and each were titered as well as the flowthough. Titers showed a dramatic reduction in phage titer in the bead flowthrough, but again, no MAPK-treated phage were recovered from either the beads or the eluant (Figure 6.12 B).

A low pH elution was next tested to see if antibody dissociation coupled with binding competition could facilitate improved capture. Again phage were phosphorylated with MAPK or no enzyme as a control, and was treated with 1 μL phospho-specific

antibody, rotated at 25°C for 2 hr, and then Protein A beads were bound, and washed 3x with buffer and beads were immersed in antibody dissociation buffer at pH 2.5 for 15 minutes, then neutralized in 100 mM Tris, pH 7.5 and the beads slurry was titered. Nearly 10-fold more phage were recovered in the MAP-kinase elution sample than in the control (Figure 6.12 C) Notably, bead flowthrough titers in this experiment were only slightly lower in the MAPK-treated samples than the control, perhaps due to the shorter antibody incubation period.

Though each phage expression and selection platform may be useful for isolating different types of mechanistic functionalities of an endosome escaping peptide sequence, a comparative assessment was performed to analyze the intracellular enzymatic modification efficiency and recovery of each of the 3 phage types, phosphorylatable phage in ~2700 copies, biotinylatable phage in 5 copies, and biotinylatable phagemid in <5 copies.

M13KE phage expressing AP-TEV-pIII were electroporated into HeLa BirA expressing cells or HeLa cells as a control. Cells were recovered for 4-5 hours at 37°C co-treated with 10 μM biotin. Cell lysates were incubated with streptavidin beads, and the beads were washed. Bound phage were cleaved from beads using TEV protease and titered for pfu. Of the roughly 100,000 pfu that were present in the cell lysates, about 0.25% were captured and recovered by streptavidin elution, 2.6-fold higher than the percentage of phage recovered in the control lysates (Figure 6.13 A)

M13KE 8-3 phage expressing MAPK-phospho-pVIII were electroporated in HeLa cells or treated on cells to which no current was applied as a control. Cells were recovered 4-5 hours at 37°C and co-treated with 50 ng/mL EGF 1 hr before lysis to

activate MAPK. Lysates were incubated with phospho-specific antibody bound to Protein A agarose, beads were washed, and phage were eluted with low pH and excess phosphorylated peptide. In this experiment, of the 10,000 pfu that were collected in cell lysates, less than 0.02% of them were recovered by phospho-affinity purification and elution, while no phage were recovered in the control sample after purification (Figure 6.13 B).

A third sample of HeLa BirA cells or untransfected cells as a control were electroporated with pComb AP-pIII phage as in panel A except phage were directly titered while bound to streptavidin beads. Of the 100,000 cfu collected in cell lysates in this experiment, roughly 2% were recovered from purification and 5.9-fold more phage were recovered than the control treated sample (Figure 6.13 C).

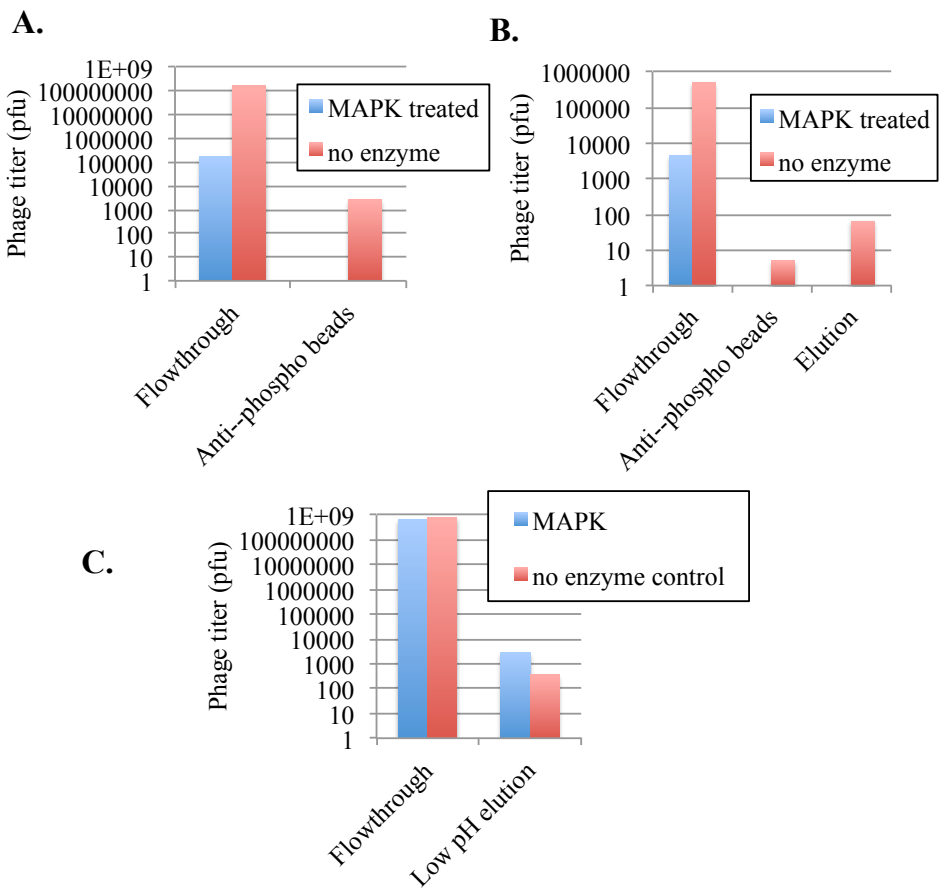

Figure 6.12. MAPK phospho-pVIII phage are efficiently phosphorylated and captured but phage require elution for recovery. A. Few phosphorylated phage recovered in flowthrough but none were recovered bound to beads. $>10^8$ phage (treated +/- MAPK) were incubated with antibody overnight. Beads were washed and bound phage were titered. **B.** Competitive elution failed to dissociate antibody-bound phage. $>10^5$ phage (treated +/- MAPK) were incubated with phospho-specific antibody overnight. Beads were washed and incubated with 10 uM free peptide (phosphorylated, purified) for 4 hrs. Eluant was removed from beads and both were titered. **C.** Low pH elution enable recovery of phosphorylated phage. $>10^8$ phage (treated +/- MAPK) were incubated with antibody for 2 hours. Beads were washed, and elution was performed in low pH buffer for 10 min, then neutralized, and the supernatant was titered.

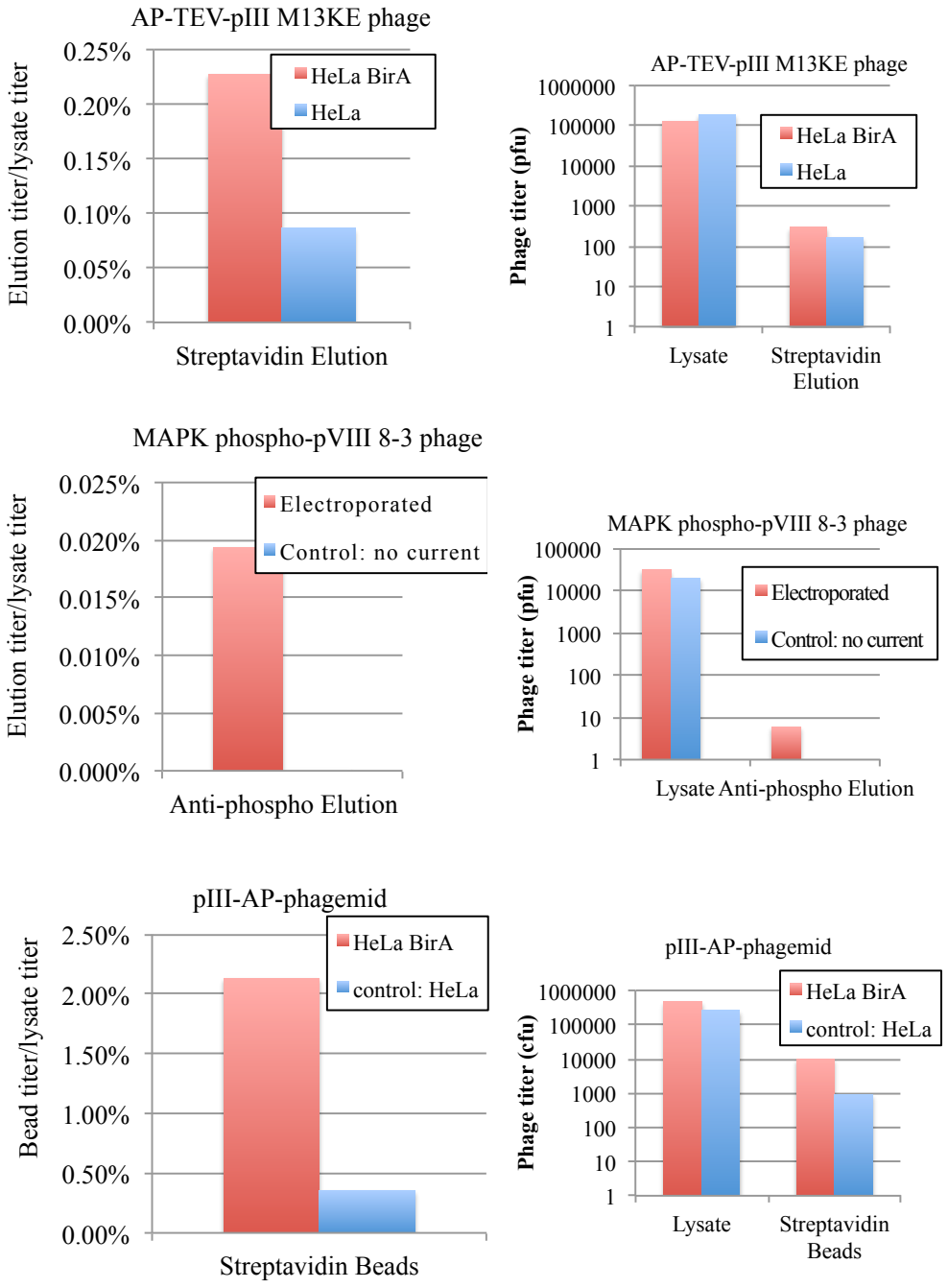

Figure 6.13. Cytoplasmic phageemid biotinylation yields higher phage recovery than phage biotinylation or phosphorylation. A. Fraction of M13KE AP-TEV-pIII phage in cell lysates recovered from streptavidin in HeLa BirA cells or control untransfected cells (left). Total phage titer of cell lysates and streptavidin elution (right). **B.** Fraction of MAPK-phospho-pVIII 8-3 phage in cell lysates of electroporated or non-electroporated cells that were recovered after binding to and elution from phospho-specific antibody bound beads (left). **C.** Fraction of pComb AP-pIII phage in cell lysates recovered from streptavidin in HeLa BirA cells or control untransfected cells (left). Total phage titer of cell lysates and streptavidin elution (right).

6.4.6. Design, construction, and selection for endosome escape of pComb-X12-AP-His6-pIII library

Of the three phage platforms, phagemid AP-pIII resulted the highest percentage recovery of infective particles, perhaps due to the lack of elution requirement. Thus, in order to maximize the efficiency of the selection, a phagemid library encoding was created bearing a histidine tag in order to purify coding phage, placed C-terminal to the X_{12} library and AP (Figure 6.14 A). The library was cloned into the pComb3H vector bearing a myc tag in order to also negatively select non-recombinant phage containing no insert, generating 10^8 bacterial transformants, of which roughly half were calculated to contain a coding sequence, as determined by sequencing of 10 clones (Figure 6.14 B).

The library was treated on nickel beads to purify coding phage, and the flowthrough and beads were directly titered to estimate the efficiency of recovery. Unfortunately, the percentage of recovery was low and because of the risk of losing rare functional phage from the naive library, it was not used for coding phage enrichment prior to the first round of selection. Thus, selection was pursued under more stringent conditions so as to reduce bias of noncoding phage. 10^9 phage added to HeLa BirAs in 15 mL media with serum and 10 μM biotin at each time point: t minus 24hrs, 8hrs, 4 hrs, 2 hrs, 1 hr, 30 min, 15 min, and the final concentration of phage was $3x10^8$ phage/mL. Cells were washed, trypsinized, pelleted, and lysed. Lysate was cleared and streptavidin beads incubated at 4°C overnight. Streptavidin beads were washed 4 times with buffer containing 1% BSA and 0.5% Tween. Streptavidin beads were treated on *E. coli.* This procedure resulted in lysate titers of 10^4 phage of which only 2 phage were recovered

after streptavidin purification (Figure 6.16). Sequencing showed that neither encoded recombinant peptide.

A. X_{12}-AP-His_6-pComb3H library

MKKTAIAIAVALAGFATVAQAAELGXXXXXXXXXXXXGGLNDIFEAQKIE
HESGSSHHHHHHTSGQAGQEGGGSEGGGSEGGGSEGGGSGGGSGSGDFD
YEKMANANKGAMTEN

Total possible diversity = $4 * 10^{15}$
Total transformants generated = $1.26 * 10^8$, with ~1.1% parent vector background
Total peptide diversity (adjusted for non-coding sequences) = $6.4*10^7$

B.

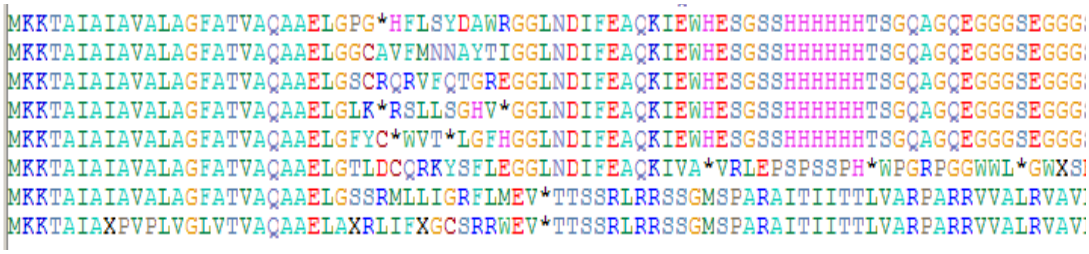

Figure 6.14. Design of pComb X_{12}-AP-His_6-pIII made from a pComb-myc vector, constructed with total peptide diversity of ~6.4×10^7. A. Phage library design, encoding 12 random amino acids, AP, and a His tag for purification on the C-terminus of M13KE. Library diversity determined by calculations from serial dilutions of transformation solution, plated for cfu. Actual peptide diversity was calculated from the percent of clones that had correct recombinant inserts determined by sequencing and represents ~0.0000016% of theoretical peptide diversity of 12 random amino acids. ~1.1% parent vector background determined by transformation of a control ligation reaction without library insert. **B.** Sequences from 10 random clones of the primary transformed library. Of 10 sequenced clones, 5 contained correct recombinant sequences, 3 showed a C-terminal frameshift, and sequencing for 2 clones could not be determined. Actual peptide diversity determined to be roughly 50% of the $1.26 * 10^8$ clones transformed, or $6.4*10^7$.

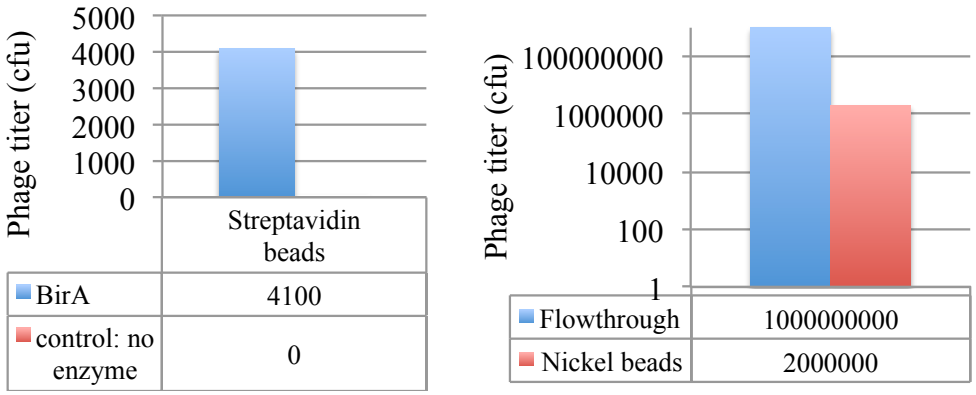

Figure 6.15. Biotinylated pComb-X_{12}-AP-H_6-pIII phage library can be purified but nickel purification of recombinant phage reduces population 500-fold. A. X_{12}-AP-H_6 phage was biotinylated *in vitro* with purified enzyme and streptavidin purified. Phage were titered directly from streptavidin beads for colony-forming units (CFU). **B**. Nickel beads were incubated with phage library and washed.

<u>Titers</u>
Total phage in cell lysates 10^4
Streptavidin purified phage 2

<u>Sequencing</u>
MKKTAIAIAVALAGFATVAQAAELGYYSVR*FLCVLLEV*TTSSRLRRSSGM
MKKTAIAIAVALAGFATVAQAAELGLYLLMVLLLRLVEV*TTSSRLRRSSGM

Figure 6.16. Endosome Escape Phage Selection with pComb-X12-AP-His6-pIII. Few got in, none got out. Of 10^4 phage that were recovered from the cell lysates, 2 were subsequently purified under stringent washing conditions and each bore frameshifted sequences that align with the N-terminal vector sequence to "AELG", but not to the C-terminal AP after 12 amino acids.

One major bottleneck to phage screening was inefficient endocytosis of phage from the cell media. Titering data showed that roughly 0.1% of phage applied to the selection were recovered in whole cell lysates, suggesting few phage may have actually reached the endosome. Thus, other methods for enhancing uptake were pursued. High density cell cultures using Cytodex beads and roller bottles were attempted, however, optimal conditions for cell growth in minimal media were not found (data not shown). Though covalent conjugation of r_9 was initially abandoned due to phage precipitation, co-treatment of cells with unconjugated r_9 was a plausible solution to induce phage uptake

without inducing precipitation prior to treatment. To test whether unreactive r_9 might improve cell uptake without causing precipitation, 1-50 μM r9 was added to cells in serum-free DMEM for 5 min, followed by ~10^7 pfu/mL M13KE AP-pIII phage, and incubated for 1.25 hr at 37°C. Cells were rinsed twice with PBS and surface-adherent phage were removed with ATV and neutralized with DMEM 10% FBS. Cells were pelleted and lysed, and soluble lysate was titered. Phage precipitation upon co-treatment with free r9 was not visible, and titers showed increasing recovery of phage from cell lysates, with increasing r9 peptide, up to nearly 5-fold (Figure 6.17). Thus free r9 appears to be a useful method of phage delivery, though it requires cell treatment in serum-free media which will likely restrict the total amount of time phage can be treated on cells to a few hours. Unconjugated r9 co-treated with phage is not believed to result in endosome escape of large molecules, though experimental confirmation will be required for future use.

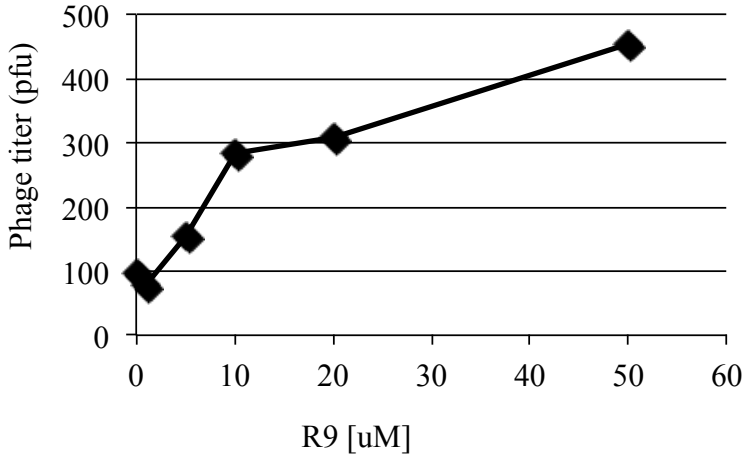

Figure 6.17. Cotreatment of phage with free r9 improves recovery of phage from cell lysates. Free r_9 up to 50 μM was treated on HeLa cells in media without serum and phage were added for 1.25 hr, and 50 μL of cell lysates were titered on *E. coli* for plaque forming units (pfu).

6.5. Discussion

Endosomal entrapment remains a major hurdle in the advancement of many targeted therapeutic agents with intracellular targets and poor membrane permeability. Finding new molecules to enhance their delivery requires the development of novel methodology. The peptide selection mechanism described and validated in this chapter representing a promising advancement toward that end.

Selection for endosome escape proved a daunting task, requiring many points for optimization. Lack of novel sequence discovery could be attributed to the limited diversity of peptides (10^7-10^8), which is restricted by the efficiency of bacterial transformation, and to the low levels of phage endocytosis, limiting the number of peptides that could be screened.

Future possible improvements include library selections using alternate phage platforms such as dual pVIII/pIII display described and validated here, wherein a short library peptide may be expressed on the entire phage coat in ~2800 copies by fusion with pVIII, while the 5 copies of pIII express the biotin AP for capture. Alternatively, pIII could be made to express longer library sequences for more focal or concerted action at one end of the phage, while pVIII expresses a short phosphorylatable peptide for capture. One limitation with this approach was the need to efficiently elute captured phage from beads after affinity purification. In comparison, because phagemid pIII express a mixture of wildtype and recombinant sequences, they are able infect *E. coli* directly from streptavidin beads. However, biotinylated, streptavidin purified phage were found to be efficiently removed from beads via TEV protease cleavage of an encoded substrate. Potential future improvements to utilizing the dual-display approach and

phosphorylatable pVIII-mediated capture include using phosphatases to selectively dissociate phosphorylated phage from the antibody-bound beads and thus facilitate greater and more specific recovery and comparing various purification tags and their display site for efficient enrichment of coding phage.

Furthermore, because peptide diversity is limited, it is often more advantageous to use a peptide library that is enriched for the desired function. Viruses are an ideal source for an endosome escape selectable library because they have undergone eons of selection for efficient host cell infection, traversing cell membranes to deliver their genomes, often with the large viral capsids intact, into the cytoplasm. Future work could derive peptide libraries from the DNA of non-enveloped or naked viruses. The mechanism of endosome escape for enveloped viruses, in contrast, may involve lipid fusion between virus and host and therefore may be less effective at delivering non-enveloped phage and non-lipid nanoparticles. One advantage of using viral genomes versus other intracellular pathogens is their compact genomes, which carry few genes and are enriched in protein-coding sequences (Hughes, Westover et al. 2001). The molecular mechanisms of virus entry are poorly understood. Therefore, this assay and selection may prove additionally valuable to the field of virology by providing simplified peptides and a new tool with which to study those events.

Finally, other peptide display methods may prove advantageous in this selection method. Filamentous M13 phage can be up to 1 μm long, and this extensive size may prove a major impediment to efficient endosome escape. Other smaller phage, such as T7, may thus be more useful, as may be different selection platforms such as mRNA display, composed simply of peptides and nucleic acids linked by puromycin.

6.6. Acknowledgements

The dissertation author would like to thank:

Dr. Michael Whitney for collaboration in experimental design, Paul Steinbach and Dr. Jessica Crisp for assistance and training in confocal microscopy, Qing Xiong for peptide synthesis, and Dr. Stephen Adams for training in chemical conjugation techniques. Dr. Alice Ting (MIT) and laboratory members for providing BirA plasmid and helpful discussion.

CHAPTER 7: Conclusions

A main goal of the work presented here was to characterize and improve nerve-highlighting peptides in order to enable their translation to the clinic. To improve nerve contrast, we identified binding targets, increased affinity and specificity, and demonstrated potential translation from animal models into humans. To enhance nerve contrast, increasing the molecule-specific affinity of first-generation peptides, such as nerve highlighting peptide (NP-41), was necessary. The once-problematic identification of NP-41's binding targets was made possible by the development of a novel mass spectrometry-based technology, ProxPhOx, which enhances the identification of weakly interacting molecules, by covalently tagging molecules within close proximity to the bound ligand of interest. The validation of ProxPhOx showed that a light-activated singlet oxygen generator (SOG) conjugated to the ligand creates localized oxidation sites on surrounding molecules allowing the subsequent tagging of those sites with biotin hydrazide. This technology was used to identify the physical interaction of NP-41 with extracellular matrix proteins laminin-421, -211 and collagen VI. In addition NP-41 labeling was shown to co-localize with laminins and collagens in nerve tissue and interact with purified proteins in an *in vitro* binding assay. Knowledge of the binding targets will allow for target-specific affinity optimization. Interestingly, the targeting of these proteins that are abundant in connective tissue allows the use of NP-41 probe to highlight degenerated nerve "ghosts" which are highly cellularized and demyelinated with intact

connective tissue and are almost invisible to the naked eye several months post-transection.

Selection of a new nerve binding peptide, NP-713, from an NP-41-derivatized library resulted in higher nerve contrast and perineurial binding affinity. Characterization of peptide binding to human nerve revealed that NP-713 and human nerve-selected HNP-301 had higher labeling than NP-41. An additional nerve binding peptide NP-124 had the overall highest nerve uptake but least was the least selective for binding to mouse and human nerve, indicating it may bind a less specific protein target. ProxPhOx showed that NP-41 and HNP-301 also target laminins-421, -211, and collagen VI.

A second broad goal of this work was to improve disease-specific targeting via ACPPs with more selective enzyme activity. Detailed characterization of the selectivity a group of ACPP substrates designed to target MMPs-2, -9, or MT1-MMP for nearly every MMP was performed. These cleavage profiles demonstrated high enzyme sensitivity to specific MMPs but relatively poor enzyme selectivity to specific MMPs indicating selectivity and target tissue specific uptake could likely be improved through optimization. Progress toward the generation of novel substrates with ultra high specificity and sensitivity toward single enzymes was initiated and will continue in future work.

The third goal was to improve intracellular drug delivery after reaching the target disease site, specifically for drugs that lack the ability to cross cellular membranes but require intracellular access for drug action. A cytoplasmic delivery assay was shown to quantify efficiency based on the intracellular modification of a short peptide sequence, and demonstrated that two agents, chloroquine and methyl beta cyclodextrin, previously

reported to induce endosome escape of some molecules were not highly efficient. This assay coupled to molecular library screening should enable the identification of new more robust “endobusting” molecules that can work within the context of any targeting agent or cargo. Towards this goal, a phage display selection was tested and validated and although no new peptide sequences capable of delivering nanoparticle-sized phage across cell membranes was identified, the approach has been procedurally validated, and subsequent optimized display systems show a great deal of promise for efficiently discovering novel sequences in future selections.

The research presented here demonstrates advancements made toward target-specific optimization of nerve-binding peptides and ACPPs and their clinical application. These molecular probes could someday enable surgeons to easily see nerves during operation which would reduce patient morbidities and improve clinical outcomes for a wide variety of surgically invasive procedures.

REFERENCES:

(2011). SEER Cancer Statistics Review, 1975-2008. N. A. M. Howlader N., Krapcho M., Neyman N., Aminou R., Waldron W., Altekruse S.F., Kosary C.L., Ruhl J., Tatalovich Z., Cho H., Mariotto A., Eisner M.P., Lewis D.R., Chen H.S., Feuer E.J., Cronin K.A., Edwards B.K., National Cancer Institute, Bethesda, MD.

Adiseshaiah, P. P., J. B. Hall and S. E. McNeil (2010). "Nanomaterial standards for efficacy and toxicity assessment." Wiley Interdiscip Rev Nanomed Nanobiotechnol **2**(1): 99-112.

Agarwal, D., S. Goodison, B. Nicholson, D. Tarin and V. Urquidi (2003). "Expression of matrix metalloproteinase 8 (MMP-8) and tyrosinase-related protein-1 (TYRP-1) correlates with the absence of metastasis in an isogenic human breast cancer model." Differentiation **71**(2): 114-125.

Appelbaum, J. S., J. R. LaRochelle, B. A. Smith, D. M. Balkin, J. M. Holub and A. Schepartz (2012). "Arginine topology controls escape of minimally cationic proteins from early endosomes to the cytoplasm." Chem Biol **19**(7): 819-830.

Arap, W., M. G. Kolonin, M. Trepel, J. Lahdenranta, M. Cardo-Vila, R. J. Giordano, P. J. Mintz, P. U. Ardelt, V. J. Yao, C. I. Vidal, L. Chen, A. Flamm, H. Valtanen, L. M. Weavind, M. E. Hicks, R. E. Pollock, G. H. Botz, C. D. Bucana, E. Koivunen, D. Cahill, P. Troncoso, K. A. Baggerly, R. D. Pentz, K. A. Do, C. J. Logothetis and R. Pasqualini (2002). "Steps toward mapping the human vasculature by phage display." Nat Med **8**(2): 121-127.

Artym, V. V., Y. Zhang, F. Seillier-Moiseiwitsch, K. M. Yamada and S. C. Mueller (2006). "Dynamic interactions of cortactin and membrane type 1 matrix metalloproteinase at invadopodia: defining the stages of invadopodia formation and function." Cancer Res **66**(6): 3034-3043.

Aussedat, B., S. Sagan, G. Chassaing, G. Bolbach and F. Burlina (2006). "Quantification of the efficiency of cargo delivery by peptidic and pseudo-peptidic Trojan carriers using MALDI-TOF mass spectrometry." Biochim Biophys Acta **1758**(3): 375-383.

Balbin, M., A. Fueyo, A. M. Tester, A. M. Pendas, A. S. Pitiot, A. Astudillo, C. M. Overall, S. D. Shapiro and C. Lopez-Otin (2003). "Loss of collagenase-2 confers increased skin tumor susceptibility to male mice." Nat Genet **35**(3): 252-257.

Bantscheff, M., M. Schirle, G. Sweetman, J. Rick and B. Kuster (2007). "Quantitative mass spectrometry in proteomics: a critical review." Anal Bioanal Chem **389**(4): 1017-1031.

Barbas, C. F., 3rd, A. S. Kang, R. A. Lerner and S. J. Benkovic (1991). "Assembly of combinatorial antibody libraries on phage surfaces: the gene III site." Proc Natl Acad Sci U S A **88**(18): 7978-7982.

Beckett, D., E. Kovaleva and P. J. Schatz (1999). "A minimal peptide substrate in biotin holoenzyme synthetase-catalyzed biotinylation." Protein Sci **8**(4): 921-929.

Bremerich, J., D. Bilecen and P. Reimer (2007). "MR angiography with blood pool contrast agents." Eur Radiol **17**(12): 3017-3024.

Brown, K. C. (2000). "New approaches for cell-specific targeting: identification of cell-selective peptides from combinatorial libraries." Curr Opin Chem Biol **4**(1): 16-21.

Chen, P., M. Cescon, A. Megighian and P. Bonaldo (2014). "Collagen VI regulates peripheral nerve myelination and function." FASEB J **28**(3): 1145-1156.

Chitchian, S., T. P. Weldon, M. A. Fiddy and N. M. Fried (2010). "Combined image-processing algorithms for improved optical coherence tomography of prostate nerves." J Biomed Opt **15**(4): 046014.

Cho, S. I., J. Ko, B. L. Patton, J. R. Sanes and A. Y. Chiu (1998). "Motor neurons and Schwann cells distinguish between synaptic and extrasynaptic isoforms of laminin." J Neurobiol **37**(3): 339-358.

Cortez-Retamozo, V., M. Lauwereys, G. Hassanzadeh Gh, M. Gobert, K. Conrath, S. Muyldermans, P. De Baetselier and H. Revets (2002). "Efficient tumor targeting by single-domain antibody fragments of camels." Int J Cancer **98**(3): 456-462.

Cotero, V. E., T. Siclovan, R. Zhang, R. L. Carter, A. Bajaj, N. E. LaPlante, E. Kim, D. Gray, V. P. Staudinger, S. Yazdanfar and C. A. Tan Hehir (2012). "Intraoperative fluorescence imaging of peripheral and central nerves through a myelin-selective contrast agent." Mol Imaging Biol **14**(6): 708-717.

Crisp, J. L. (2012). Molecular Targeting with Peptide Based Probes for the Imaging and Treatment of Cancer. Ph.D., University of California, San Diego.

Davies, M. J. (2003). "Singlet oxygen-mediated damage to proteins and its consequences." Biochem Biophys Res Commun **305**(3): 761-770.

Davies, M. J. (2004). "Reactive species formed on proteins exposed to singlet oxygen." Photochem Photobiol Sci **3**(1): 17-25.

Davis, W. E., J. L. Rea and J. Templer (1979). "Recurrent laryngeal nerve localization using a microlaryngeal electrode." Otolaryngol Head Neck Surg (1979) **87**(3): 330-333.

de Boer, E., P. Rodriguez, E. Bonte, J. Krijgsveld, E. Katsantoni, A. Heck, F. Grosveld and J. Strouboulis (2003). "Efficient biotinylation and single-step purification of tagged

transcription factors in mammalian cells and transgenic mice." Proc Natl Acad Sci U S A **100**(13): 7480-7485.

Derossi, D., A. H. Joliot, G. Chassaing and A. Prochiantz (1994). "The third helix of the Antennapedia homeodomain translocates through biological membranes." J Biol Chem **269**(14): 10444-10450.

Deryugina, E. I. and J. P. Quigley (2006). "Matrix metalloproteinases and tumor metastasis." Cancer Metastasis Rev **25**(1): 9-34.

Egeblad, M. and Z. Werb (2002). "New functions for the matrix metalloproteinases in cancer progression." Nat Rev Cancer **2**(3): 161-174.

Ehrenshaft, M., S. O. Silva, I. Perdivara, P. Bilski, R. H. Sik, C. F. Chignell, K. B. Tomer and R. P. Mason (2009). "Immunological detection of N-formylkynurenine in oxidized proteins." Free Radic Biol Med **46**(9): 1260-1266.

El-Sayed, A., S. Futaki and H. Harashima (2009). "Delivery of macromolecules using arginine-rich cell-penetrating peptides: ways to overcome endosomal entrapment." AAPS J **11**(1): 13-22.

Fawell, S., J. Seery, Y. Daikh, C. Moore, L. L. Chen, B. Pepinsky and J. Barsoum (1994). "Tat-mediated delivery of heterologous proteins into cells." Proc Natl Acad Sci U S A **91**(2): 664-668.

Felsen, C. N., E. N. Savariar, M. Whitney and R. Y. Tsien (2014). "Detection and monitoring of localized matrix metalloproteinase upregulation in a murine model of asthma." Am J Physiol Lung Cell Mol Physiol **306**(8): L764-774.

Figeys, D., L. D. McBroom and M. F. Moran (2001). "Mass spectrometry for the study of protein-protein interactions." Methods **24**(3): 230-239.

Fingleton, B. (2006). "Matrix metalloproteinases: roles in cancer and metastasis." Front Biosci **11**: 479-491.

Fittipaldi, A., A. Ferrari, M. Zoppe, C. Arcangeli, V. Pellegrini, F. Beltram and M. Giacca (2003). "Cell membrane lipid rafts mediate caveolar endocytosis of HIV-1 Tat fusion proteins." J Biol Chem **278**(36): 34141-34149.

Fleming, T. J., M. Sachdeva, M. Delic, J. Beltzer, C. R. Wescott, M. Devlin, R. C. Lander, A. E. Nixon, V. Roschke, D. M. Hilbert and D. J. Sexton (2005). "Discovery of high-affinity peptide binders to BLyS by phage display." J Mol Recognit **18**(1): 94-102.

Foerg, C. and H. P. Merkle (2008). "On the biomedical promise of cell penetrating peptides: limits versus prospects." J Pharm Sci **97**(1): 144-162.

Francia, G., W. Cruz-Munoz, S. Man, P. Xu and R. S. Kerbel (2011). "Mouse models of advanced spontaneous metastasis for experimental therapeutics." Nat Rev Cancer **11**(2): 135-141.

Frei, A. P., O. Y. Jeon, S. Kilcher, H. Moest, L. M. Henning, C. Jost, A. Pluckthun, J. Mercer, R. Aebersold, E. M. Carreira and B. Wollscheid (2012). "Direct identification of ligand-receptor interactions on living cells and tissues." Nat Biotechnol **30**(10): 997-1001.

Frei, A. P., H. Moest, K. Novy and B. Wollscheid (2013). "Ligand-based receptor identification on living cells and tissues using TRICEPS." Nat Protoc **8**(7): 1321-1336.

Friedl, P. and K. Wolf (2008). "Tube travel: the role of proteases in individual and collective cancer cell invasion." Cancer Res **68**(18): 7247-7249.

Gantz, B. J. (1985). "Intraoperative facial nerve monitoring." Am J Otol **Suppl**: 58-61.

Gibbs-Strauss, S. L., K. A. Nasr, K. M. Fish, O. Khullar, Y. Ashitate, T. M. Siclovan, B. F. Johnson, N. E. Barnhardt, C. A. Tan Hehir and J. V. Frangioni (2011). "Nerve-highlighting fluorescent contrast agents for image-guided surgery." Mol Imaging **10**(2): 91-101.

Hadjipanayis, C. G., H. Jiang, D. W. Roberts and L. Yang (2011). "Current and future clinical applications for optical imaging of cancer: from intraoperative surgical guidance to cancer screening." Semin Oncol **38**(1): 109-118.

Hauff, S. J., S. C. Raju, R. K. Orosco, A. M. Gross, J. A. Diaz-Perez, E. Savariar, N. Nashi, J. Hasselman, M. Whitney, J. N. Myers, S. M. Lippman, R. Y. Tsien, T. Ideker and Q. T. Nguyen (2014). "Matrix-metalloproteinases in head and neck carcinoma-cancer genome atlas analysis and fluorescence imaging in mice." Otolaryngol Head Neck Surg **151**(4): 612-618.

Hellebust, A. and R. Richards-Kortum (2012). "Advances in molecular imaging: targeted optical contrast agents for cancer diagnostics." Nanomedicine (Lond) **7**(3): 429-445.

Hensley, K. (2009). "Detection of protein carbonyls by means of biotin hydrazide-streptavidin affinity methods." Methods Mol Biol **536**: 457-462.

Hill, R. (2009). "Extracellular matrix remodelling in human diabetic neuropathy." J Anat **214**(2): 219-225.

Holmberg, A., A. Blomstergren, O. Nord, M. Lukacs, J. Lundeberg and M. Uhlen (2005). "The biotin-streptavidin interaction can be reversibly broken using water at elevated temperatures." Electrophoresis **26**(3): 501-510.

Hong, H., S. Goel, Y. Zhang and W. Cai (2011). "Molecular imaging with nucleic acid aptamers." Curr Med Chem **18**(27): 4195-4205.

Hughes, A. L., K. Westover, J. da Silva, D. H. O'Connor and D. I. Watkins (2001). "Simultaneous positive and purifying selection on overlapping reading frames of the tat and vpr genes of simian immunodeficiency virus." J Virol **75**(17): 7966-7972.

Husemann, Y., J. B. Geigl, F. Schubert, P. Musiani, M. Meyer, E. Burghart, G. Forni, R. Eils, T. Fehm, G. Riethmuller and C. A. Klein (2008). "Systemic spread is an early step in breast cancer." Cancer Cell **13**(1): 58-68.

Hussain, T., M. B. Mastrodimos, S. C. Raju, H. L. Glasgow, M. Whitney, B. Friedman, J. D. Moore, D. Kleinfeld, P. Steinbach, K. Messer, M. Pu, R. Y. Tsien and Q. T. Nguyen (2015). "Fluorescently Labeled Peptide Increases Identification of Degenerated Facial Nerve Branches during Surgery and Improves Functional Outcome." PLoS One **10**(3): e0119600.

Ishikawa, T., Z. Wondimu, Y. Oikawa, G. Gentilcore, R. Kiessling, S. Egyhazi Brage, J. Hansson and M. Patarroyo (2014). "Laminins 411 and 421 differentially promote tumor cell migration via alpha6beta1 integrin and MCAM (CD146)." Matrix Biol **38**: 69-83.

Itoh, Y. and M. Seiki (2006). "MT1-MMP: a potent modifier of pericellular microenvironment." J Cell Physiol **206**(1): 1-8.

Jiang, T., E. S. Olson, Q. T. Nguyen, M. Roy, P. A. Jennings and R. Y. Tsien (2004). "Tumor imaging by means of proteolytic activation of cell-penetrating peptides." Proc Natl Acad Sci U S A **101**(51): 17867-17872.

Josephson, L., C. H. Tung, A. Moore and R. Weissleder (1999). "High-efficiency intracellular magnetic labeling with novel superparamagnetic-Tat peptide conjugates." Bioconjug Chem **10**(2): 186-191.

Kalia, J. and R. T. Raines (2008). "Hydrolytic stability of hydrazones and oximes." Angew Chem Int Ed Engl **47**(39): 7523-7526.

Kaplan, I. M., J. S. Wadia and S. F. Dowdy (2005). "Cationic TAT peptide transduction domain enters cells by macropinocytosis." J Control Release **102**(1): 247-253.

Ke, S., X. Wen, M. Gurfinkel, C. Charnsangavej, S. Wallace, E. M. Sevick-Muraca and C. Li (2003). "Near-infrared optical imaging of epidermal growth factor receptor in breast cancer xenografts." Cancer Res **63**(22): 7870-7875.

Kim, J., M. E. Rodriguez, M. Guo, M. E. Kenney, N. L. Oleinick and V. E. Anderson (2008). "Oxidative modification of cytochrome c by singlet oxygen." Free Radic Biol Med **44**(9): 1700-1711.

Kobbert, C., R. Apps, I. Bechmann, J. L. Lanciego, J. Mey and S. Thanos (2000). "Current concepts in neuroanatomical tracing." Prog Neurobiol **62**(4): 327-351.

Kubler, H. R., T. Y. Tseng, L. Sun, J. Vieweg, M. J. Harris and P. Dahm (2007). "Impact of nerve sparing technique on patient self-assessed outcomes after radical perineal prostatectomy." J Urol **178**(2): 488-492; discussion 492.

Lee, M., R. Fridman and S. Mobashery (2004). "Extracellular proteases as targets for treatment of cancer metastases." Chem Soc Rev **33**(7): 401-409.

Lee, S., J. Xie and X. Chen (2010). "Peptide-based probes for targeted molecular imaging." Biochemistry **49**(7): 1364-1376.

Li, W., F. Nicol and F. C. Szoka, Jr. (2004). "GALA: a designed synthetic pH-responsive amphipathic peptide with applications in drug and gene delivery." Adv Drug Deliv Rev **56**(7): 967-985.

Li, Y., G. Cai, S. Yuan, Y. Jun, N. Li, L. Wang, F. Chen, R. Ling and J. Yun (2015). "The overexpression membrane type 1 matrix metalloproteinase is associated with the progression and prognosis in breast cancer." Am J Transl Res **7**(1): 120-127.

Liu, H., R. G. Sadygov and J. R. Yates, 3rd (2004). "A model for random sampling and estimation of relative protein abundance in shotgun proteomics." Anal Chem **76**(14): 4193-4201.

Luker, G. D. and K. E. Luker (2008). "Optical imaging: current applications and future directions." J Nucl Med **49**(1): 1-4.

Lundberg, P., S. El-Andaloussi, T. Sutlu, H. Johansson and U. Langel (2007). "Delivery of short interfering RNA using endosomolytic cell-penetrating peptides." FASEB J **21**(11): 2664-2671.

Maatta, M., Y. Soini, A. Liakka and H. Autio-Harmainen (2000). "Differential expression of matrix metalloproteinase (MMP)-2, MMP-9, and membrane type 1-MMP in hepatocellular and pancreatic adenocarcinoma: implications for tumor progression and clinical prognosis." Clin Cancer Res **6**(7): 2726-2734.

Maeda, H., J. Wu, T. Sawa, Y. Matsumura and K. Hori (2000). "Tumor vascular permeability and the EPR effect in macromolecular therapeutics: a review." J Control Release **65**(1-2): 271-284.

Marangos, N., R. B. Illing, J. Kruger and R. Laszig (2001). "In vivo visualization of the cochlear nerve and nuclei with fluorescent axonal tracers." Hear Res **162**(1-2): 48-52.

Mason, A. J., C. Leborgne, G. Moulay, A. Martinez, O. Danos, B. Bechinger and A. Kichler (2007). "Optimising histidine rich peptides for efficient DNA delivery in the presence of serum." J Control Release **118**(1): 95-104.

May, C. A. and T. Mittag (2006). "Optic nerve degeneration in the DBA/2NNia mouse: is the lamina cribrosa important in the development of glaucomatous optic neuropathy?" Acta Neuropathol **111**(2): 158-167.

McCawley, L. J., H. C. Crawford, L. E. King, Jr., J. Mudgett and L. M. Matrisian (2004). "A protective role for matrix metalloproteinase-3 in squamous cell carcinoma." Cancer Res **64**(19): 6965-6972.

Moan, J. and K. Berg (1991). "The photodegradation of porphyrins in cells can be used to estimate the lifetime of singlet oxygen." Photochem Photobiol **53**(4): 549-553.

Moore, N. M., C. L. Sheppard, T. R. Barbour and S. E. Sakiyama-Elbert (2008). "The effect of endosomal escape peptides on in vitro gene delivery of polyethylene glycol-based vehicles." J Gene Med **10**(10): 1134-1149.

Nilsson, R., P. B. Merkel and D. R. Kearns (1972). "Unambiguous evidence for the participation of singlet oxygen (1) in photodynamic oxidation of amino acids." Photochem Photobiol **16**(2): 117-124.

Nolte-Ernsting, C., G. Adam, A. Bucker, S. Berges, A. Bjornerud and R. W. Gunther (1998). "Abdominal MR angiography performed using blood pool contrast agents: comparison of a new superparamagnetic iron oxide nanoparticle and a linear gadolinium polymer." AJR Am J Roentgenol **171**(1): 107-113.

O'Malley, M. R., J. E. Wittkopf, J. L. Cutler, R. F. Labadie, T. A. Hackett and D. S. Haynes (2006). "Fluorescent retrograde axonal tracing of the facial nerve." Laryngoscope **116**(10): 1792-1797.

Oien, D. B., T. Canello, R. Gabizon, M. Gasset, B. L. Lundquist, J. M. Burns and J. Moskovitz (2009). "Detection of oxidized methionine in selected proteins, cellular extracts and blood serums by novel anti-methionine sulfoxide antibodies." Arch Biochem Biophys **485**(1): 35-40.

Olson, E. S., T. A. Aguilera, T. Jiang, L. G. Ellies, Q. T. Nguyen, E. H. Wong, L. A. Gross and R. Y. Tsien (2009). "In vivo characterization of activatable cell penetrating peptides for targeting protease activity in cancer." Integr Biol (Camb) **1**(5-6): 382-393.

Ouyang, M., H. Huang, N. C. Shaner, A. G. Remacle, S. A. Shiryaev, A. Y. Strongin, R. Y. Tsien and Y. Wang (2010). "Simultaneous visualization of protumorigenic Src and MT1-MMP activities with fluorescence resonance energy transfer." Cancer Res **70**(6): 2204-2212.

Park, M. H., H. Hyun, Y. Ashitate, H. Wada, G. Park, J. H. Lee, C. Njiojob, M. Henary, J. V. Frangioni and H. S. Choi (2014). "Prototype nerve-specific near-infrared fluorophores." Theranostics **4**(8): 823-833.

Pasqualini, R. and E. Ruoslahti (1996). "Organ targeting in vivo using phage display peptide libraries." Nature **380**(6572): 364-366.

Patton, B. L., J. H. Miner, A. Y. Chiu and J. R. Sanes (1997). "Distribution and function of laminins in the neuromuscular system of developing, adult, and mutant mice." J Cell Biol **139**(6): 1507-1521.

Paulsson, M., M. Aumailley, R. Deutzmann, R. Timpl, K. Beck and J. Engel (1987). "Laminin-nidogen complex. Extraction with chelating agents and structural characterization." Eur J Biochem **166**(1): 11-19.

Peters, E. A., P. J. Schatz, S. S. Johnson and W. J. Dower (1994). "Membrane insertion defects caused by positive charges in the early mature region of protein pIII of filamentous phage fd can be corrected by prlA suppressors." J Bacteriol **176**(14): 4296-4305.

Petrenko, V. A., G. P. Smith, X. Gong and T. Quinn (1996). "A library of organic landscapes on filamentous phage." Protein Eng **9**(9): 797-801.

Plank, C., B. Oberhauser, K. Mechtler, C. Koch and E. Wagner (1994). "The influence of endosome-disruptive peptides on gene transfer using synthetic virus-like gene transfer systems." J Biol Chem **269**(17): 12918-12924.

Poduslo, J. F., M. Ramakrishnan, S. S. Holasek, M. Ramirez-Alvarado, K. K. Kandimalla, E. J. Gilles, G. L. Curran and T. M. Wengenack (2007). "In vivo targeting of antibody fragments to the nervous system for Alzheimer's disease immunotherapy and molecular imaging of amyloid plaques." J Neurochem **102**(2): 420-433.

Polyakov, V., V. Sharma, J. L. Dahlheimer, C. M. Pica, G. D. Luker and D. Piwnica-Worms (2000). "Novel Tat-peptide chelates for direct transduction of technetium-99m and rhenium into human cells for imaging and radiotherapy." Bioconjug Chem **11**(6): 762-771.

Potocky, T. B., A. K. Menon and S. H. Gellman (2003). "Cytoplasmic and nuclear delivery of a TAT-derived peptide and a beta-peptide after endocytic uptake into HeLa cells." J Biol Chem **278**(50): 50188-50194.

Rajotte, D. and E. Ruoslahti (1999). "Membrane dipeptidase is the receptor for a lung-targeting peptide identified by in vivo phage display." J Biol Chem **274**(17): 11593-11598.

Rathinakumar, R. and W. C. Wimley (2008). "Biomolecular engineering by combinatorial design and high-throughput screening: small, soluble peptides that permeabilize membranes." J Am Chem Soc **130**(30): 9849-9858.

Richard, J. P., K. Melikov, E. Vives, C. Ramos, B. Verbeure, M. J. Gait, L. V. Chernomordik and B. Lebleu (2003). "Cell-penetrating peptides. A reevaluation of the mechanism of cellular uptake." J Biol Chem **278**(1): 585-590.

Richmond, F. J., R. Gladdy, J. L. Creasy, S. Kitamura, E. Smits and D. B. Thomson (1994). "Efficacy of seven retrograde tracers, compared in multiple-labelling studies of feline motoneurones." J Neurosci Methods **53**(1): 35-46.

Ruan, G., A. Agrawal, A. I. Marcus and S. Nie (2007). "Imaging and tracking of tat peptide-conjugated quantum dots in living cells: new insights into nanoparticle uptake, intracellular transport, and vesicle shedding." J Am Chem Soc **129**(47): 14759-14766.

Salonen, V., J. Peltonen, M. Roytta and I. Virtanen (1987). "Laminin in traumatized peripheral nerve: basement membrane changes during degeneration and regeneration." J Neurocytol **16**(5): 713-720.

Savariar, E. N., C. N. Felsen, N. Nashi, T. Jiang, L. G. Ellies, P. Steinbach, R. Y. Tsien and Q. T. Nguyen (2013). "Real-time in vivo molecular detection of primary tumors and metastases with ratiometric activatable cell-penetrating peptides." Cancer Res **73**(2): 855-864.

Schroeder, A., D. A. Heller, M. M. Winslow, J. E. Dahlman, G. W. Pratt, R. Langer, T. Jacks and D. G. Anderson (2012). "Treating metastatic cancer with nanotechnology." Nat Rev Cancer **12**(1): 39-50.

Sheth, R. A., L. Josephson and U. Mahmood (2009). "Evaluation and clinically relevant applications of a fluorescent imaging analog to fluorodeoxyglucose positron emission tomography." J Biomed Opt **14**(6): 064014.

Shu, X., V. Lev-Ram, T. J. Deerinck, Y. Qi, E. B. Ramko, M. W. Davidson, Y. Jin, M. H. Ellisman and R. Y. Tsien (2011). "A genetically encoded tag for correlated light and electron microscopy of intact cells, tissues, and organisms." PLoS Biol **9**(4): e1001041.

Sidhu, S. S. (2001). "Engineering M13 for phage display." Biomol Eng **18**(2): 57-63.

Silvester, J. A., G. S. Timmins and M. J. Davies (1998). "Protein hydroperoxides and carbonyl groups generated by porphyrin-induced photo-oxidation of bovine serum albumin." Arch Biochem Biophys **350**(2): 249-258.

Sinz, A. (2010). "Investigation of protein-protein interactions in living cells by chemical crosslinking and mass spectrometry." Anal Bioanal Chem **397**(8): 3433-3440.

Smith, G. P. and V. A. Petrenko (1997). "Phage Display." Chem Rev **97**(2): 391-410.

Soughayer, J. S., Y. Wang, H. Li, S. H. Cheung, F. M. Rossi, E. J. Stanbridge, C. E. Sims and N. L. Allbritton (2004). "Characterization of TAT-mediated transport of detachable kinase substrates." Biochemistry **43**(26): 8528-8540.

Sun, W., C. Sun, H. Zhao, H. Lin, Q. Han, J. Wang, H. Ma, B. Chen, Z. Xiao and J. Dai (2009). "Improvement of sciatic nerve regeneration using laminin-binding human NGF-beta." PLoS One **4**(7): e6180.

Suto, D., Y. Ikeda, J. Fujii and Y. Ohba (2006). "Structural analysis of amino acids, oxidized by reactive oxygen species and an antibody against N-formylkynurenine." Journal of Clinical Biochemistry and Nutrition **38**(2): 107-111.

Tanaka, Y., M. R. Bond and J. J. Kohler (2008). "Photocrosslinkers illuminate interactions in living cells." Mol Biosyst **4**(6): 473-480.

Thie, H., B. Voedisch, S. Dubel, M. Hust and T. Schirrmann (2009). "Affinity maturation by phage display." Methods Mol Biol **525**: 309-322, xv.

Thyboll, J., J. Kortesmaa, R. Cao, R. Soininen, L. Wang, A. Iivanainen, L. Sorokin, M. Risling, Y. Cao and K. Tryggvason (2002). "Deletion of the laminin alpha4 chain leads to impaired microvessel maturation." Mol Cell Biol **22**(4): 1194-1202.

Timpl, R., H. Rohde, P. G. Robey, S. I. Rennard, J. M. Foidart and G. R. Martin (1979). "Laminin--a glycoprotein from basement membranes." J Biol Chem **254**(19): 9933-9937.

To, T. L., M. J. Fadul and X. Shu (2014). "Singlet oxygen triplet energy transfer-based imaging technology for mapping protein-protein proximity in intact cells." Nat Commun **5**: 4072.

Torchilin, V. P., R. Rammohan, V. Weissig and T. S. Levchenko (2001). "TAT peptide on the surface of liposomes affords their efficient intracellular delivery even at low temperature and in the presence of metabolic inhibitors." Proc Natl Acad Sci U S A **98**(15): 8786-8791.

Tseng, Y. L., J. J. Liu and R. L. Hong (2002). "Translocation of liposomes into cancer cells by cell-penetrating peptides penetratin and tat: a kinetic and efficacy study." Mol Pharmacol **62**(4): 864-872.

Uchibori, M., Y. Nishida, T. Nagasaka, Y. Yamada, K. Nakanishi and N. Ishiguro (2006). "Increased expression of membrane-type matrix metalloproteinase-1 is correlated with poor prognosis in patients with osteosarcoma." Int J Oncol **28**(1): 33-42.

van Kasteren, S. I., S. J. Campbell, S. Serres, D. C. Anthony, N. R. Sibson and B. G. Davis (2009). "Glyconanoparticles allow pre-symptomatic in vivo imaging of brain disease." Proc Natl Acad Sci U S A **106**(1): 18-23.

Virtanen, I., L. Laitinen and M. Korhonen (1995). "Differential expression of laminin polypeptides in developing and adult human kidney." J Histochem Cytochem **43**(6): 621-628.

Visse, R. and H. Nagase (2003). "Matrix metalloproteinases and tissue inhibitors of metalloproteinases: structure, function, and biochemistry." Circ Res **92**(8): 827-839.

Vives, E., P. Brodin and B. Lebleu (1997). "A truncated HIV-1 Tat protein basic domain rapidly translocates through the plasma membrane and accumulates in the cell nucleus." J Biol Chem **272**(25): 16010-16017.

von der Mark, H., M. Aumailley, G. Wick, R. Fleischmajer and R. Timpl (1984). "Immunochemistry, genuine size and tissue localization of collagen VI." Eur J Biochem **142**(3): 493-502.

Wadia, J. S., R. V. Stan and S. F. Dowdy (2004). "Transducible TAT-HA fusogenic peptide enhances escape of TAT-fusion proteins after lipid raft macropinocytosis." Nat Med **10**(3): 310-315.

Wallquist, W., M. Patarroyo, S. Thams, T. Carlstedt, B. Stark, S. Cullheim and H. Hammarberg (2002). "Laminin chains in rat and human peripheral nerve: distribution and regulation during development and after axonal injury." J Comp Neurol **454**(3): 284-293.

Walz, J., A. L. Burnett, A. J. Costello, J. A. Eastham, M. Graefen, B. Guillonneau, M. Menon, F. Montorsi, R. P. Myers, B. Rocco and A. Villers (2010). "A critical analysis of the current knowledge of surgical anatomy related to optimization of cancer control and preservation of continence and erection in candidates for radical prostatectomy." Eur Urol **57**(2): 179-192.

Walz, J., M. Graefen and H. Huland (2007). "Basic principles of anatomy for optimal surgical treatment of prostate cancer." World J Urol **25**(1): 31-38.

Weissleder, R. (2001). "A clearer vision for in vivo imaging." Nat Biotechnol **19**(4): 316-317.

Weissleder, R. (2010). Molecular imaging : principles and practice. Shelton, Conn., People's Medical Pub. House--USA.

Wender, P. A., D. J. Mitchell, K. Pattabiraman, E. T. Pelkey, L. Steinman and J. B. Rothbard (2000). "The design, synthesis, and evaluation of molecules that enable or enhance cellular uptake: peptoid molecular transporters." Proc Natl Acad Sci U S A **97**(24): 13003-13008.

Whitney, M., J. L. Crisp, E. S. Olson, T. A. Aguilera, L. A. Gross, L. G. Ellies and R. Y. Tsien (2010). "Parallel in vivo and in vitro selection using phage display identifies protease-dependent tumor-targeting peptides." J Biol Chem **285**(29): 22532-22541.

Whitney, M., E. N. Savariar, B. Friedman, R. A. Levin, J. L. Crisp, H. L. Glasgow, R. Lefkowitz, S. R. Adams, P. Steinbach, N. Nashi, Q. T. Nguyen and R. Y. Tsien (2013). "Ratiometric activatable cell-penetrating peptides provide rapid in vivo readout of thrombin activation." Angew Chem Int Ed Engl **52**(1): 325-330.

Whitney, M. A., J. L. Crisp, L. T. Nguyen, B. Friedman, L. A. Gross, P. Steinbach, R. Y. Tsien and Q. T. Nguyen (2011). "Fluorescent peptides highlight peripheral nerves during surgery in mice." Nat Biotechnol **29**(4): 352-356.

Wisniewski, J. R., A. Zougman, N. Nagaraj and M. Mann (2009). "Universal sample preparation method for proteome analysis." Nat Methods **6**(5): 359-362.

Woodward, M. P., W. W. Young, Jr. and R. A. Bloodgood (1985). "Detection of monoclonal antibodies specific for carbohydrate epitopes using periodate oxidation." J Immunol Methods **78**(1): 143-153.

Wu, A. P., M. A. Whitney, J. L. Crisp, B. Friedman, R. Y. Tsien and Q. T. Nguyen (2011). "Improved facial nerve identification with novel fluorescently labeled probe." Laryngoscope **121**(4): 805-810.

Yuan, F., M. Dellian, D. Fukumura, M. Leunig, D. A. Berk, V. P. Torchilin and R. K. Jain (1995). "Vascular permeability in a human tumor xenograft: molecular size dependence and cutoff size." Cancer Res **55**(17): 3752-3756.

Zhivov, A., M. Blum, R. Guthoff and O. Stachs (2010). "Real-time mapping of the subepithelial nerve plexus by in vivo confocal laser scanning microscopy." Br J Ophthalmol **94**(9): 1133-1135.